Hollow-Core FRP-Concrete-Steel Bridge Columns under Extreme Loading

Prepared by
Omar I. Abdelkarim
Ahmed Gheni
Sujith Anumolu
Song Wang
Mohamed ElGawady, Ph.D.
Missouri University of Science and Technology

Final Report Prepared for Missouri Department of Transportation
2015 April Project TR201408 Report cmr15-008

FINAL REPORT

Hollow-Core FRP-Concrete-Steel Bridge Columns under Extreme Loading

Prepared for
Missouri Department of Transportation
Research, Development and Technology

By

Omar I. Abdelkarim
Ahmed Gheni
Sujith Anumolu
Song Wang
Mohamed ElGawady, PhD

Missouri University of Science and Technology, Rolla, Missouri

January 2015

TECHNICAL REPORT DOCUMENTATION PAGE.

<table>
<tr><td colspan="2">1. Report No.: cmr 15-008</td><td>2. Government Accession No.:</td><td>3. Recipient's Catalog No.:</td></tr>
<tr><td colspan="3">4. Title and Subtitle: Hollow-Core FRP-Concrete-Steel Bridge Columns Under Extreme Loading</td><td>5. Report Date:

January, 2015</td></tr>
<tr><td colspan="3" rowspan="2"></td><td>6. Performing Organization Code:</td></tr>
<tr><td colspan="3">7. Author(s):
Omar I. Abdelkarim, Ahmed Gheni, Sujith Anumolu, and Mohamed ElGawady</td><td>8. Performing Organization Report No.:</td></tr>
<tr><td colspan="3">9. Performing Organization Name and Address:
Missouri Department of Transportation
Organizational Results
PO BOX 270, JEFFERSON CITY MO 65102</td><td>10. Work Unit No.:

11. Contract or Grant No.:
TR201408</td></tr>
<tr><td colspan="3">12. Sponsoring Agency Name and Address:

Missouri Department of Transportation
Research, Development and Technology
PO BOX 270, JEFFERSON CITY MO 65102</td><td>13. Type of Report and Period Covered:
Final Report.

14. Sponsoring Agency Code:</td></tr>
<tr><td colspan="4">15. Supplementary Notes:
The investigation was conducted in cooperation with the U. S. Department of Transportation, Federal Highway Administration.</td></tr>
<tr><td colspan="4">16. Abstract: This report presents the behavior of hollow-core fiber reinforced polymer – concrete - steel columns (HC-FCS) under combined axial-flexural as well as vehicle collision loads. The HC-FCS column consists of a concrete wall sandwiched between an outer fiber reinforced polymer (FRP) tube and an inner steel tube. Four large-scale columns including a conventionally reinforced concrete (RC) column having solid cross section and three HC-FCS columns were investigated during this study. Each column had an outer diameter of 24 inch and a column's height-to-diameter ratio of 4.0. The steel tube was embedded into reinforced concrete footing with an embedded length of 1.6 times the steel tube diameter. The FRP tube truncated at the top of the footing level; hence, it provides only confinement to the concrete. The hollow steel tube was the only reinforcement for shear and flexure inside the HC-FCS column. The HC-FCS column exhibited high lateral drift reaching 15.2% and failed gradually due to concrete crushing, steel tube local buckling, followed by FRP rupture. The reference RC-column failed at drift of 10.9% due to rebar rupture. Finite element models using LS-DYNA software were developed and validated against the experimental results of the investigated large-scale columns and experimental results of small-scale columns available in the literature. The proposed model was able to predict the behaviors of the investigated columns with good accuracy. Finite element modeling of vehicle collision with RC and HC-FCS bridge columns was also presented in this report. Evaluation of the peak dynamic force (PDF) and the equivalent static force (ESF) through an extensive parametric study were conducted. The AASHTO-LRFD design force was found to be non-conservative when the column was collided with heavy vehicles of a weight more than 35 kips or high-speed vehicle more than 70 mph. A new equation for estimating the ESF based on the vehicle's mass and velocity was developed. This approach will allow Departments of Transportation (DOTs) to design different bridge columns to different impact force demands depending on the anticipated truckloads and velocities. In general, the PDF values of the HC-FCS columns were lower than those of the RC column when they were subjected to vehicle collision.</td></tr>
<tr><td colspan="2">17. Key Words:
Bridge Columns, Precast Columns, Composite Columns, Hollow-Core Columns, Vehicle Collision, LS-DYNA</td><td colspan="2">18. Distribution Statement:
No restrictions. This document is available to the public through National Technical Information Center, Springfield, Virginia 22161.</td></tr>
<tr><td>19. Security Classification (of this report):
Unclassified.</td><td>20. Security Classification (of this page):
Unclassified.</td><td>21. No of Pages:
184</td><td>22. Price:</td></tr>
</table>

Form DOT F 1700.7 (06/98).

EXECUTIVE SUMMARY

This study has developed an innovative resilient, durable, and quickly-constructed precast hollow-core fiber reinforced polymer-concrete-steel (HC-FCS) bridge column. The cross-section of the HC-FCS column consists of concrete shell sandwiched between an inner steel tube and an outer fiber reinforced polymer (FRP) tube. The inner steel tube was embedded into the concrete footing while the outer FRP is discontinued at the footing top surface level, i.e., the FRP tube provides confinement and stay-in-place formwork only. Hence, the system ductility is mainly attributed to the steel tube and high-confinement of the concrete shell. The HC-FCS column has the following several distinct advantages over columns constructed out of reinforced concrete (RC). The HC-FCS column uses 60 to 75% less concrete material since it has hollow-core. The HC-FCS column, also, requires reduced freight cost when implemented with precast construction. The inner steel and outer FRP tubes provide a continuous confinement for the concrete shell; hence, the concrete shell achieves significantly higher strain, strength, and ductility compared to unconfined concrete. The HC-FCS represents a compact engineering system; the steel and FRP tubes together act as stay-in-place formworks. The steel tube acts as flexural and shear reinforcement. The concrete shell will delay the local buckling of the steel tube and hence make more efficient use of the steel tube. The HC-FCS column has high corrosion resistance since the steel tube is well protected by the corrosion-free outer FRP tube and concrete core. The report focuses on investigating the behavior of HC-FCS columns under combined axial-flexural loads. Moreover, the behavior of the column under vehicle impact was investigated as well. Finally, design guidelines were developed. The behavior of the HC-FCS columns under different extreme load conditions were compared to those of conventional concrete having solid cross section. The report also introduce for the first time a design equation to predict the equivalent static impact force of vehicle collision with bridge columns which can be implemented in AASHTO-LRFD.

The report includes eleven chapters. Chapter 1 introduces a literature review on the FRP and its applications, behavior of hollow-core columns, and vehicle collision with bridge columns. Chapter 2 explains the behavior of the HC-FCS columns under axial loading. Chapter 3 details the construction, detailing, testing protocol, and results of four large-scale columns under constant axial load and static cyclic lateral loads. Chapter 4 contains the flexural and shear strength guidelines of the HC-FCS columns. Chapter 5 presents finite element analysis of the HC-FCS columns and an extensive parametric study to clarify the behavior under lateral loading. Chapter 6 explains the vehicle collision with RC columns through an extensive parametric study to clarify the behavior. Chapter 7 investigates the vehicle collision with HC-FCS columns through a parametric study to clarify the behavior. Chapter 8 presents the comparison between the behavior of RC and HC-FCS columns under vehicle collision. Chapter 9 contains conclusions and recommendations for future work. Finally, Chapters 10 and 11 contain the references and summary of large-scale columns' results, respectively.

Based on the results of this study, the research team recommends the HC-FCS columns for bridge construction. However, to facilitate this implementation, additional work is required in order to tailor the steel and FRP tubes as well as to develop construction details for column/girder connection. Further work is also required to address the shear, torsion, and development length of the inner steel tube. Finally, the behavior of the HC-FCS column having thin steel tube needs also further investigation.

ACKNOWLEDGEMENTS

The authors would like to acknowledge the many individuals and organizations that made this research project possible. The authors wish to extend a very sincere thank you to the Missouri Department of Transportation (MoDOT). In addition to their financial support, the authors appreciate MoDOT's vision and commitment to innovative concepts and pushing the boundaries of current practice. In particular, the success of this project would not have been possible without the support, encouragement, and patience of Mr. Andrew Hanks. The authors also wish to extend a sincere thank you to MoDOT's Technical Advisory Group for their thorough review of the draft final report and many insightful comments, namely Andrew Hanks, Dennis Heckman, and Gregory Sanders. Special thanks also to Mr. Bill Stone for his flexibility, insight, and continued support of the project.

The authors would also like to thank the Mid-America Transportation Center (MATC) which provided valuable match funding from the United States Department of Transportation through RITA. The authors also extend their appreciation to the National University Transportation Center (NUTC) at Missouri University of Science and Technology (Missouri S&T).

The authors would also like to thank the companies that provided material contributions necessary for the successful completion of this project, including Pittsburgh Pipe and Atlas Tube. Appreciation extended for Fyfe CO. LLC for partially donating some of the materials used in the experimental work.

Finally, the authors would like to thank Missouri S&T for their valuable contributions to the research. The authors also appreciate the tireless staff of the Department of Civil, Architectural, and Environmental Engineering and the Center for Infrastructure Engineering Studies. Their assistance both inside and out of the various laboratories was invaluable to the successful completion of this project.

TABLE OF CONTENTS

LIST OF ILLUSTRATIONS

LIST OF TABLES

1. LITERATURE REVIEW

1.1 Concrete-filled tube columns

A significant amount of research was recently devoted to developing accelerated bridge construction (ABC) systems. These ABC systems offer several benefits, including reduced construction time, minimal traffic disruptions, reduced life-cycle costs, improved construction quality, and improved safety (Dawood et al. 2012). Concrete-filled steel tubes (CFSTs) are widely used as bridge columns in Japan, China, and Europe to not only accelerate construction but also to obtain superior seismic performance. In the US, CFSTs are used as piles and bridge piers. Their application, however, is limited, primarily, as a result of inconsistent design code provisions (Moon et al. 2013). Incorporated CFST members have several advantages over either steel or reinforced concrete (RC) members. The steel tubes act as a stay-in-place formwork, flexural and shear reinforcement, and a confinement to the inside concrete core, increasing the member's ductility and strength. The tubes prevent concrete spalling so that the concrete core continues to function as a bracing for the steel tube. Therefore, the concrete core delays both local and global buckling under compression loads (Hajjar 2000).

The CFST members dissipate more energy than those made from either traditional steel or RC members. On a strength-per-dollar basis, CFST members are cheaper than traditional steel members; they are comparable in price to traditional RC members. A concrete core can be reinforced with steel rebar to further improve the member's performance while facilitating connections to other members. Limited performance data is available, however, for steel rebar reinforced CFST columns (Moon et al. 2013; Hajjar 2000).

FRP tubes have gained acceptance as an alternative to steel tubes in CFSTs. Concrete-filled fiber tubes (CFFT) have benefits that are similar to those of CFSTs. However, unlike steel tubes, FRP tubes have a lighter weight-to-strength ratio and a higher corrosion resistance than steel tubes have. Several researchers investigated the seismic behavior of CFFT columns (Zhu et al. 2006). Shin and Andrawes (2010) investigated the behavior of CFFTs that were confined by a shape memory alloy. ElGawady et al. (2010) and ElGawady and Sha'lan (2011) conducted static cyclic tests on both segmental precast post-tensioned CFFT columns and two-column bents. Upon conducting finite element analysis, ElGawady and Dawood (2012) and Dawood and ElGawady (2013) developed a design procedure for precast post-tensioned CFFTs.

1.2 Hollow-core columns

Hollow-core concrete columns are often used for very tall bridge columns in seismic areas including California, New Zealand, Japan and Italy et al. Hollow-core cross-sections reduce the mass of the column which reduces the bridge self-weight contribution to the inertial mode of vibration during an earthquake. The hollow-core columns also reduce the foundations dimensions, thereby reducing the construction costs substantially. These advantages have increased the use of hollow-core columns instead of similar solid members.

Mander et al. (1983) investigated hollow-core concrete columns that have two layers of longitudinal and transverse reinforcement placed near in-/outside faces and cross ties placed throughout the wall's thickness (Fig. 1.1). These columns can exhibit a ductile behavior (Fig. 1.2). However, they increase the labor cost making it not cost-effective construction option.

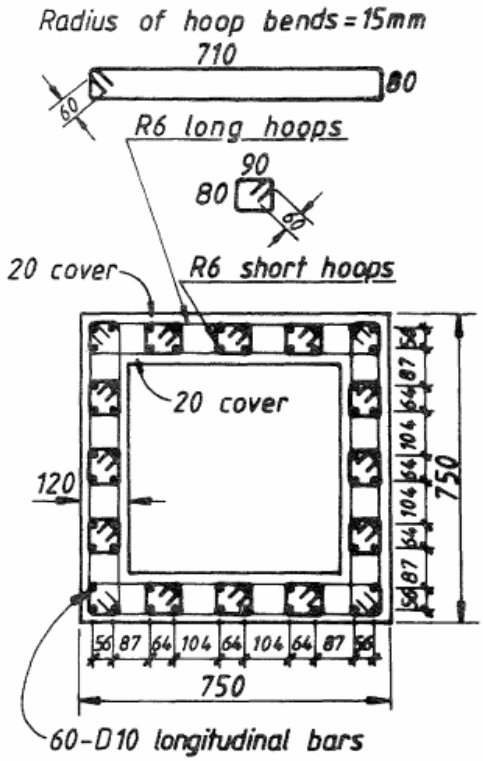

Figure 1.1: Cross-section of the hollow-core concrete column with two layers of reinforcement (Mander et al. 1983)

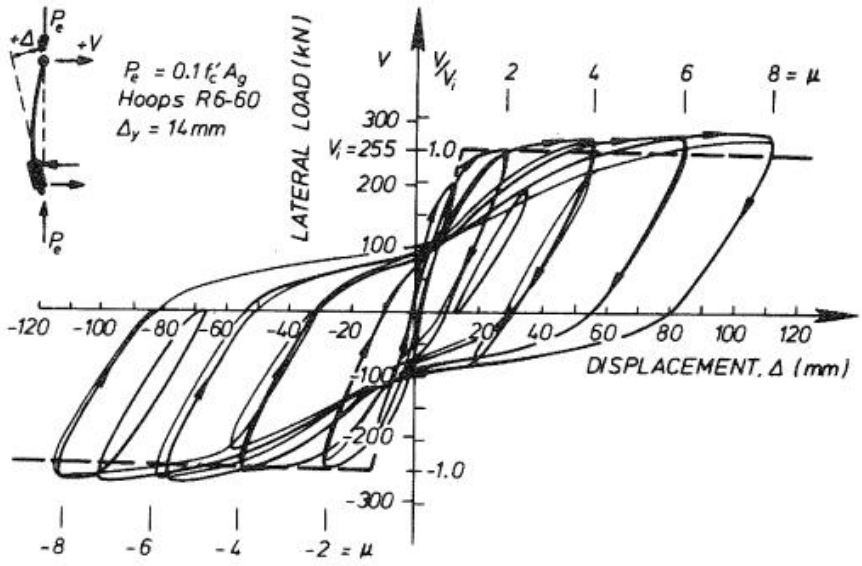

Figure 1.2: Load-displacement relationship of the hollow-core concrete column with two layers of reinforcement (Mander et al. 1983)

Hoshikuma and Priestley (2000) investigated hollow-core concrete columns that contain one layer of longitudinal reinforcement (Fig. 1.3). The peak lateral force occurred at a ductility of approximately 2.0. It dropped significantly at a ductility of 3.5 in the push direction (where the inside concrete was crushed, see Fig. 1.4). The lateral force began to deteriorate at a ductility of 3.3 in the pull direction. Both test observations and experimental hysteretic responses indicate that the failure that occurred inside the face concrete severely degraded the response. Therefore, the ultimate ductility capacity was 3.3, with a safe design limit of 2.2, providing a 50% reserve of displacement capacity. This study indicated that the lack of the hollow-core concrete columns with one layer reinforcement is the low curvature ductility due to early concrete spalling because of the void.

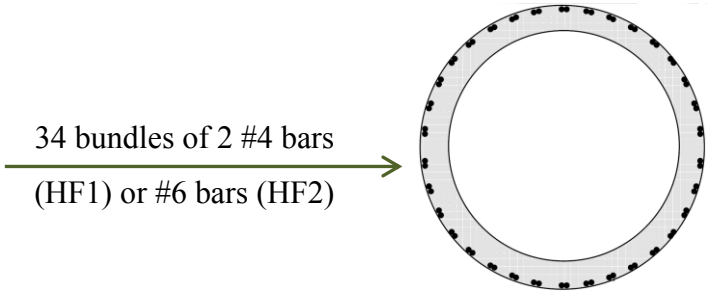

Figure 1.3: Cross-section of the hollow-core concrete column with one layer of reinforcement (Hoshikuma and Priestley 2000)

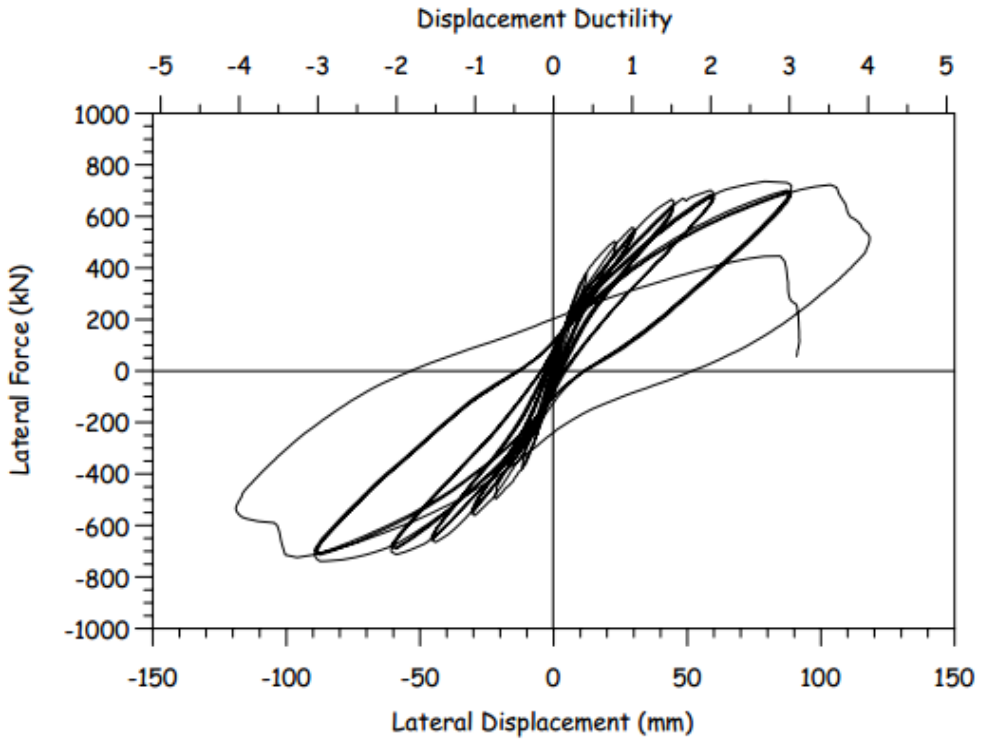

Figure 1.4: Load-displacement relationship of the hollow-core concrete column with two layers of reinforcement (Hoshikuma and Priestley 2000)

Montague (1978) combined the benefits of concrete-filled tube columns with the benefits of hollow-core concrete columns to develop a double-skin tubular column (DSTC). These columns consist of a concrete wall that is sandwiched between two generally concentric steel tubes; they have been studied extensively in Asia (Shakir-Khalil & Illouli 1987; Yagishita 2000). More recently, Teng et al. (2004) used FRP as an outer tube and the steel as an inner tube in the double-skin tubular elements. This system combines and optimizes the benefits of all three materials: FRP, concrete, and steel in addition to the benefits of the hollow-core concrete columns to introduce hollow-core FRP-concrete-steel columns (HC-FCS).

A number of investigators have studied the behavior of HC-FCS columns, in the form of beams and columns, under different static and cyclic loading conditions (Teng et al. 2005, 2007; Yu et al. 2006, 2010; Wong et al. 2008; Lu et al. 2010; Huang et al. 2013; Abdelkarim and ElGawady 2014a; Abdelkarim and ElGawady 2014b; Li et al. 2014a; Li et al. 2014b). The results of the conducted experimental tests under axial compression, flexure, and combined axial compression and flexure showed high concrete confinement and ductility (e.g., see Figs. 1.5 and 1.6).

Han et al. (2010) tested HC-FCSs in a beam-column arrangement, under cyclic flexural loading, with constant axial compression loading. The column's elastic stiffness increased as the applied axial load increased. The post-elastic stiffness increased as the FRP stiffness increased. The elastic stiffness, however, did not. The column's residual bending strength (after the FRP ruptured) increased as the applied axial load level increased. Zhang et al. (2012) and Ozbakkaloglu and Idris (2014) investigated the behavior of small-scale HC-FCSs under combined axial compression and lateral cyclic loading. The experimental tests results revealed a high concrete confinement and ductility.

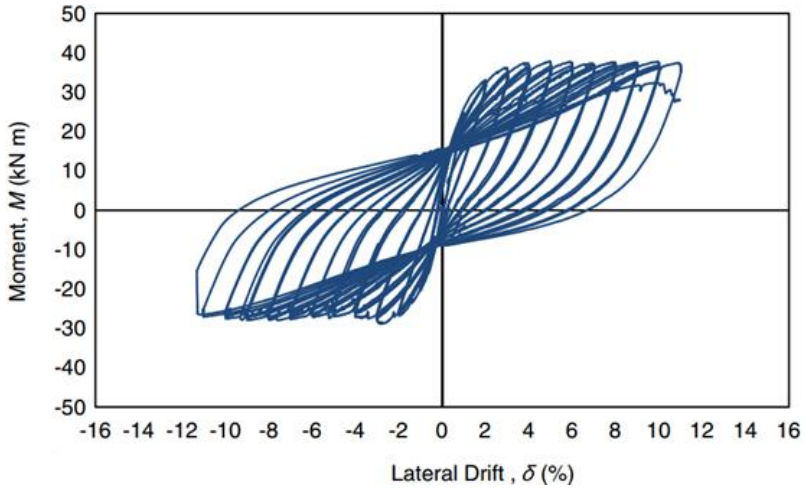

Figure 1.5: Moment-lateral drift relationship of HC-FCS column (Ozbakkaloglu and Idris 2014)

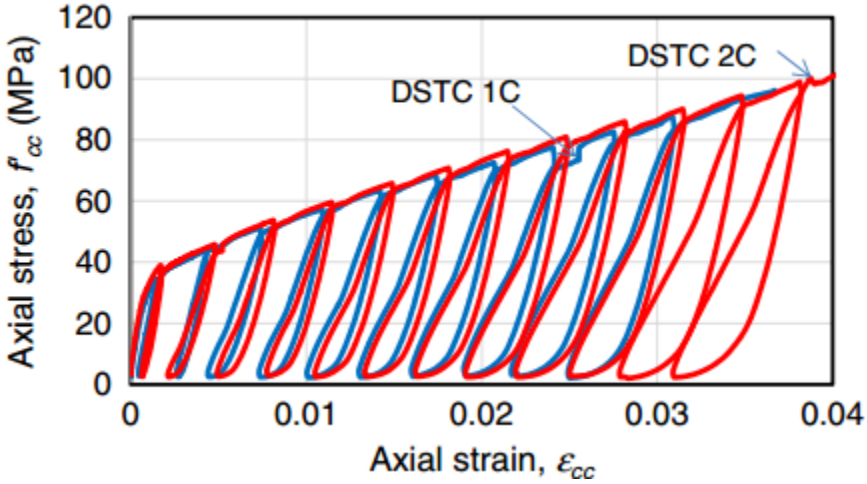

Figure 1.6: Axial strain-axial stress relationship of HC-FCS column (Albitar et al. 2013)

1.3 Impact analysis of vehicle collision

Accidents can have serious repercussions with regard to both human life and transportation systems. Many vehicle collision events involving bridge piers have been reported throughout the US (see Fig. 1.7; Buth et al. 2010). These collisions often result in either a complete or a partial bridge collapse (Harik et al. 1990; Agrawal 2011, 2013). For example, two trains collided at a rail intersection just outside of Scott City in southeast Missouri in May of 2013. Numerous train cars were derailed, and seven people were injured (Fig. 1.8). The derailed cars hit a highway overpass, causing it to collapse. The preliminary estimated cost to replace the overpass was approximately $3 million (McGrath 2013).

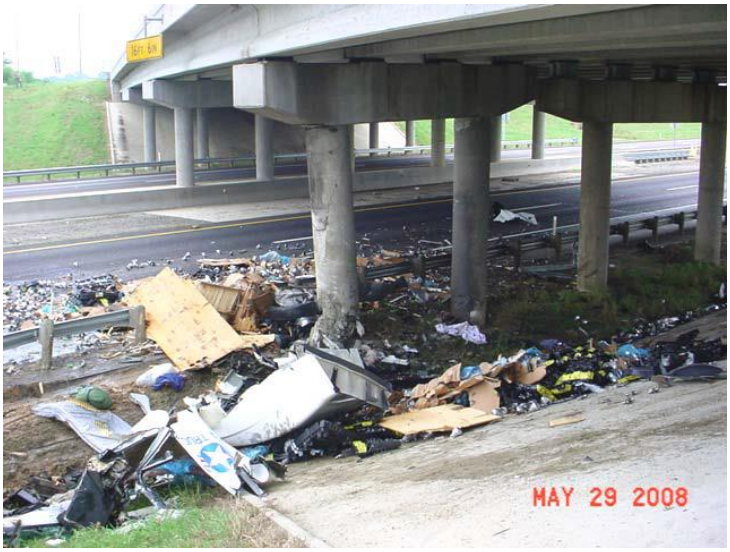

Figure 1.7: Truck-tractor-trailer accident–FM 1401 Bridge, Texas, 2008 (Buth 2010)

Figure 1.8: Trains accident-overpass outside of Scott City, Missouri, 2013 (McGrath 2013)

Numerous researchers have used LS-DYNA software to investigate the modeling of concrete columns under extreme loading (Abdelkarim and ElGawady 2014b; Sharma et al. 2012; Fouche and Bruneau 2010; Thilakarathna et al. 2010). El-Tawil et al. (2005) used this software to examine two bridge piers that had been impacted by different trucks at different velocities. Both the peak dynamic force (PDF: the maximum contact force of the vehicle collision on the bridge column) and the equivalent static force (ESF) were evaluated. The American Association of State Highway and Transportation Officials- Load and Resistance Factor Bridge Design Specifications 5th edition (AASHTO-LRFD 2010) mandates that both abutments and piers located within a distance of 30 ft from the roadway's edge must be designed to allow for a ESF of the collision load of 400 kips. El-Tawil et al. (2005) suggested that the AASHTO-LRFD could be non-conservative and that the ESF should be higher than 400 kips.

Buth et al. (2011) experimentally studied the collision of tractor-trailers into a rigid column that was constrained at both ends. Numerical models were used to conduct a parametric study on single unit trucks (SUTs). The investigated parameters included the pier's diameter, the vehicle's weight, the vehicle's velocity, and the cargo's state (rigid vs. deformable). Based on the results gathered during this study, the ESF of the AASHTO-LRFD was increased to 600 kips applied to a bridge pier in a direction of zero to 15 degrees with the edge of the pavement in a horizontal plane, at a distance of 5.0 ft above ground.

Sharma et al. (2012) used a performance-based response to investigate the effect of a vehicle's impact on a reinforced concrete column. They suggested that four different damage levels and three different performance levels be used to evaluate the column's response. Agrawal et al. (2013) investigated the effects of different seismic design details on a pier's response to vehicle impact loading. They proposed that a new procedure be used to calculate the ESF; this procedure is based on the vehicle's mass and velocity. A proposed equation was used to calculate the PDF. The ESF was calculated by dividing the calculated PDF by the damage ratio (which is dependent on the required performance level being 2, 5, and > 5 for minor, moderate, and high damage levels, respectively). This procedure produced variable values of ESF rather than the constant ESF recommended by AASHTO-LRFD.

No consensus exists among researchers with regard to calculating an ESF from a PDF. Three approaches to investigating the ESF were considered during the course of this research. In the first approach (SB_{ESF}; Stiffness-Based ESF) the ESF was defined as the force needed to produce

the same maximum displacement by a collision event at the point of impact (El-Tawil et al. 2005). In the second approach (EC_{ESF}; EuroCode ESF) the ESF was calculated by a Eurocode:

$$ESF = \frac{KE}{\delta_c + \delta_d} \tag{1.1}$$

$$KE = \frac{1}{2}\, m\, v_r^2 \tag{1.2}$$

where KE is the vehicle's kinetic energy, m = the vehicle's mass, v_r = the vehicle's velocity, δ_c = the vehicle's deformation, and δ_d = the column's deformation. The third approach (PTMSA; Peak of Twenty-five Milli Second moving Average) was recommended by Buth et al. (2011) referenced to the 50 millisecond moving average frequently used in automotive crash analyses.

1.4 Classification of impact

The material response under external loading could be defined by both the loading time and the strain rate. Here, the strain rate is the change in a material's strain with regard to time. Sierakowsi and Chaturved (1997) stated that the static load typically occurs within a time duration that is more than 10^4-10^6 seconds and a strain rate that is lower than 10^{-8}-10^{-6} s^{-1}. However, the impact load typically occurs within a time duration that is between 10^{-6} and 10^{-4} and a strain rate that is between 10^2 and 10^4 s^{-1}.

The structural system's response could be defined by the pulse duration relative to the structure's natural period. If the pulse duration is lower than a quarter of the structure's natural period, the system's response is impacted. However, if the pulse duration is larger than four times the structure's natural period, the system's response is quasi-static.

In a vehicle collision event with bridge piers, the bridge pier (the body that is struck) is considered to be the target while the vehicle (the body that impacts the target) is considered to be the projectile. The collision's relative degree of softness/hardness classifies the type of impact that occurs. Therefore, the impact type can be classified by the projectile/target interaction into the following categories: hard/soft, hard/hard, soft/hard, and soft/soft. This classification significantly affects the induced dynamic contact force between the projectile and the target. If a soft projectile interacts with a rigid target, the stress waves propagate within the projectile upon contact, damaging

the projectile. When this interaction occurs, the projectile absorbs most of the impact's kinetic energy in the form of plastic deformation. If a hard projectile interacts with a soft target, the stress waves propagate within the target upon contact. Hence, the target absorbs most of the impact's kinetic energy in the form of plastic deformation. Consequently, absorbing the kinetic energy from the projectile's mass and velocity is the key parameter when preparing the impact analysis.

1.5 FRP application in aerospace engineering versus civil engineering

Fiber-reinforced polymer (FRP) is outstanding in its high strength-to-mass ratio, easy construction and high resistance to environmental exposure, and has been used for retrofitting existing structures and new infrastructure construction in civil engineering area during the past decades. The FRP that is used to retrofit old structures is the FRP wrap in which the fibers are typically oriented in a circumferential direction. For new construction like concrete filled FRP cylinders, prefabricated FRP tubes are employed which are typically thicker than FRP cloths and there's no overlapping zone. Even though the FRP materials exhibited greater durability to environmental exposure than conventional materials (i.e., concrete and steel), the rigorous estimate of the resistance of FRP composite structures to severe environmental exposures and their service life cycles still face uncertainties. This study included a review of technical literatures that discussed on FRP composite's durability when subjected to various environmental exposures. The review began with FRP applications in aerospace engineering vs. civil engineering and the reasons why the durability of FRP used in civil engineering needs to be studied. Next the durability of each constitution component (fiber, matrix and fiber/matrix interface) was presented, followed by the effects of various environmental exposures on FRP at the composite level. The accelerated aging methodology and findings for FRP confined concrete cylinders were reviewed at the end.

The first known FRP product was a boat hull manufactured in the mid-1930s as part of a manufacturing experiment using a fiberglass fabric and polyester resin laid in a foam mold (ACI 2007). The defense industry began to use these FRP composite materials, particularly in aerospace and naval applications in the early 1940s. The U.S. Air Force and Navy capitalized on FRP composite's high strength-weight ratio, noncorrosive, nonmagnetic, and nonconductive characteristics.

FRP composite products were first used to reinforce concrete structures in the mid-1950s. Since then, FRP composite applications in civil engineering have evolved from temporary

structures to the restoration of historic buildings. A major development in FRP used for civil engineering area has been the application of externally bonded FRP in rehabilitation and strengthening concrete structures.

The application of FRP composites in civil engineering, however, is not a direct transfer from that in aerospace engineering. The FRP materials used in aerospace engineering are far more advanced than those needed in public infrastructures. Those advanced FRP materials are cured at very high temperature and provide excellent quality and properties. The FRP used in aerospace engineering is typically cured above 100°C, producing higher glass transition temperature in the resin and more durable joints. At the same time, these FRP materials are quite expensive. On the other hand, most infrastructures just need cost-effective materials for construction and rehabilitation purposes. In civil engineering application, resin acted as binders for fibers can be adequately cured at ambient temperatures and still offers comparable quality. The properties are more desirable and also practical. This efficient fabrication method helps reduce costs and increase popularity in civil market.

The primary obstacle that hinders the wide application of FRP composites in civil infrastructures is the long-term durability performance, especially when the structure is undergoing combined harsh environmental conditions. Even though the FRP system has been used in aerospace engineering for almost a century and demonstrated good durability characteristics, those FRP possesses much better quality than the one currently used in civil infrastructures and its excellent durability performance cannot be directly applied to the civil engineering case. This is why many researchers did a lot of research and study during the past few decades to investigate the durability of this new material in civil engineering applications.

1.6 Durability of Material Components

1.6.1 *Matrix*

The ester group, which is the weakest bond in polyester and vinylester matrices, is vulnerable to hydroxyl ions by hydrolysis process as demonstrated in the following equation (Chen et al. 2007):

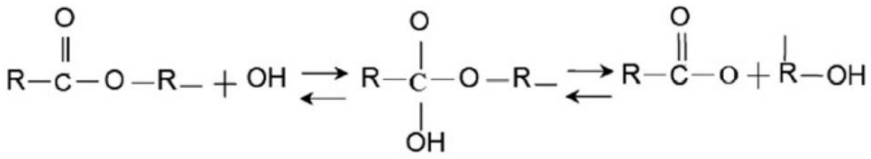

(1.3)

Compared to polyester, vinylester matrix is inert to the hydrolysis process because it contains much fewer ester units (Robert and Benmokrane 2013), and it is also resistant to water absorption (Balazs and Borosnyoi 2001). The epoxy matrix is unaffected by the hydrolysis reaction because no ester group is present in the molecular structure. However, the epoxy resin can absorb moisture typically from 1% to 7% by weight. This absorbed water would plasticize the matrix, induce differential swelling stresses and micro cracking, and generally degrades the physical properties (Soles et al. 1998). In terms of protecting the fiber from harsh concrete pore solution, it is reported that vinylester and epoxy resin are more advantageous than polyester because of the low diffusibility, high resistance to alkaline attack and quite tough in resisting microcrack development (Benmokrane et al. 2002). Kootsookos et al. (2001) placed four types of FRP composite materials, including glass/polyester, glass/vinylester composites, carbon/polyester, and carbon/vinylester, into seawater for up to 289 days. They observed that glass composites are less stable in seawater than carbon composites, polyester-based composites are less durable in seawater than are vinylester-based composites, and this is due to the susceptibility of the polyester resin to hydrolysis. They also found that some degradation of the polyester-and vinylester-based composites appeared to occur by leaching out unreacted chemicals from the resin matrix into the seawater. The extent of this process increased as the amount of under-curing resin increased.

1.6.2 *Fiber*

Bare glass fibers in a high pH cement solution are degraded rapidly with a loss in toughness and strength, and through a series process of pitting, etching, leaching, and embrittlement. In general, the degradation mechanisms for glass fibers due to concrete pore solution are: (1). Chemical attack by the alkaline cement environment, and (2) concentration and growth of hydration products between individual fibers. These hydration products include solid calcium hydroxide and possible some calcium carbonate which formed a layer on the fiber's surface. It is due to the transport of calcium ions contained in the solution towards the fiber-solution interface and also the gradual extracting/leaching of silica ions from the glass fiber. The latter results from a hydroxylic

attack on the glass fibers deteriorate the fibers' integrity. The hydration process that takes place in the cement solution can also lead to both pitting and roughness on the fiber's surface, which act as flaws and severely reduce the fiber properties in the presence of moisture. While resin can act as a protection layer to prevent glass fiber from direct contact to cement solution, the solution which carries alkaline salts and other detrimental ions, however, can eventually diffuse through the bulk resin, or wick through fiber-matrix interface, and deteriorate the fibers (Cheikh and Murat 1988; Karbhari et al. 2002). Glass fibers become damaged in a pure high pH alkaline solution (pH>10) when the hydroxyl ions break the Si-O bonds in the glass network, as shown in the following equation (Charles 1959; Yilmaz 1992):

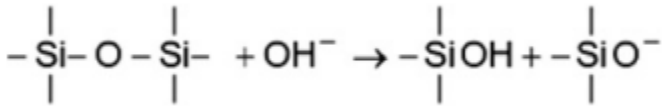

(1.4)

Several researchers have studied the durability of glass fibers in an acid solution and the loss of surface area of the glass fibers was observed during long-term immersion (Evans and Ainsworth 1988; Jones and Wheatley 1983). Glass fibers are generally immune to pure water, but chloride ions can deteriorate glass fibers through leaching and etching (Balazs and Borosnyoi 2001).

Aramid fibers are particularly susceptible to moisture absorption while Carbon fibers are known to be inert to chemical environments and do not absorb water (Chen et al. 2007). Micelli and Myers (2008) submerged CFRP sheets in an HCL solution for 2000 hours and then tested in tension. The maximum reduction measured on the strength and stiffness was only 20%, indicating the carbon fibers had a high chemical resistance. The carbon fibers are, however, vulnerable to electrolytic solutions. Alias and Brown (1992) showed that the carbon fiber composite materials in a seawater (3.5% NaCl) solution and in contact with metals experienced significant damage due to blistering and dissolution of the matrix under galvanic action.

1.6.3 *Fiber/Matrix Interface*

The degradation mechanism for the interface between the fiber and the matrix is quite complicated. The interface is an inhomogeneous layer that is approximately one micron thickness. It is the weakest bond and most vulnerable part in the composite microstructure (Chen et al. 2007).

Three degradation mechanisms of interface between fiber and matrix include: (1) matrix osmotic cracking; (2) interfacial debonding; and (3) delamination (Bradshaw and Brinson, 1997).

1.7 Various Environmental Exposures on FRP Composite

1.7.1 *Moisture*

In general, moisture decreases the glass transition temperature of the polymer matrix due to plasticization by means of interrupting Van Der Waals bonds between polymer chains. It leads to the degradation of matrix-dominated mechanical properties of the composite (Wolff 1993). The matrix could also be damaged by cracking and microcracking when the volume expands during moisture absorption. Ashbee and Wyatt (1969) reported that the change of resin's volume when subjected to boiling water was initiated by swelling after the resin was immersed in water for a very short time, but then superseded by shrinkage later. The volume shrinkage could be explained by two possible mechanism: either (1) extra cross-linking was formed, increasing the resin's density; or (2) the low molecular weight material was leached from the bulk resin, followed by a closing-in behavior of the adjacent polymer to fill the holes left behind by extracted molecules. The above two mechanisms lead to a more rigid and brittle behavior for the resin, but the water would act as a plasticizer later on, decreasing the Tg and elastic modulus of the resin if it was kept in the water for a longer time period (Lima et al. 2009). Researchers have conducted a number of experiments to investigate the moisture effect on durability of FRP composites. Chen et al. (2007) reported that the continuous immersion of GFRP in a wet solution resulted in greater degradation than wet and dry cycles. McBagonluri et al. (2000) conducted tensile tests on glass/vinylester composite coupons that were subjected to cyclic moisture aging in both freshwater and saltwater. They found that the quasi-static tensile strength of the FRP specimens was reduced by 24% at a moisture concentration of 1% by weight. More importantly, this degradation was shown to be permanent and cannot be reversible even the sample was dried. Gentry et al. (1998) concluded that an aqueous environmental condition affects more in strength than modulus for glass/polyester and glass/vinylester composite materials. Tucker and Brown (1989) examined the moisture effect on the FRP composite under high pressure to investigate the performance of FRP structures in deep sea. They found that the high pressure did not change the diffusion rate of the composite materials. It did, however, raise the equilibrium moisture, further deteriorating the strength and stiffness of the composite materials.

A number of researchers have studied the impact of saltwater on an FRP composite. It was reported that the FRP's degradation when immersed in saltwater is more attributed to FRP's moisture content than salt concentration. It was observed that the rate of strength decrease for samples in a saline solution is lower than that in distilled water, because the massive salt molecules in a saline solution impedes water absorption (D'Almieda 1991). A salt solution can also cause blistering on an FRP composite's surface due to osmotic effects (ACI 2007).

Silva et al. (2014) conducted more comprehensive durability tests on epoxy-based GFRP and CFRP composite laminates. These composites were subjected to salt fog cycles with 5% salinity, tap water wet/dry cycles, 5% saltwater wet/dry cycles, and freezing/thawing cycles with 10% RH. They found that saltwater wet/dry cycles reduced Tg of epoxy more severely than either salt fog or freezing/thawing cycles. The adhesion between the fiber and the matrix degraded more rapidly during both wet/dry cycles and salt fog cycles than it did during freezing/thawing cycles. Thus, moisture was the primary factor, rather than either salinity or low temperatures, in degrading the FRP composite.

1.7.2 *High Temperatures*

High temperatures affect the viscoelastic response of the resin, which led to the decreased modulus (ACI 2007). The glass transition temperature (Tg) is one of the most important properties of resin when considering environmental temperature. The resin's mechanical properties will be degraded dramatically if the service temperature approaches Tg. Both moisture and high temperature have a significant affect on Tg, but depending on materials' curing temperature. A reduced Tg will be observed for high-temperature-cured materials due to the plasticisation effects of hygrothermal exposure. However, the post-cure induced by elevated temperature hygrothermal exposure will increase Tg for low-temperature-cured materials. This increase will become greater when the ageing temperature is enhanced (Earl and Shenoi 2004). If materials are high-temperature cured properly, the high temperature condition deteriorates the composite material more significantly than low temperature effect. Fabio et al (2012) found that CFRP laminates tested at a temperature of +70°C and an RH of 65% had a significant decrease in tensile strength and ultimate strain, approximately equal to 30%, but no significant change was observed in stiffness.

1.7.3 *Low Temperatures*

Compared to high temperature effect, freezing/thawing cycles barely affect the ultimate strength and strain of CFRP laminates, with only a slight decrease (9% and 13%) for 210 cycles (Fabio et al. 2012). Miguel et al. (2006) found that exposure to freeze-thaw cycles had little effect on the longitudinal tensile properties of the saturated FRP tubes. Low temperatures make the resin stiffer, but the composite may suffer from internal stresses resulting from thermal coefficient mismatch of fibers and resins (Dutta and Hui 1996). The internal stresses will cause microcracks on the resin's surface which will induces more moisture and aggressive agents into the resin. Typically, wet freeze-thaw conditioning deteriorates the FRP composite more severely than dry freeze-thaw condition. While freezing/thawing cycles deteriorate composite materials, a constant freeze temperature improves the composite's properties. Rivera and Karbhari (2001) subjected vinylester-based GFRP and CFRP materials to a constant freeze temperature (-10°C). They found that both the tensile strength and the modulus increased for all of the specimens.

1.7.4 *Ultraviolet (UV) Light*

Surface oxidation occurs when resin materials are exposed to ultraviolet (UV) light, as evidenced by the increase in oxygen-containing functional groups. Surface oxidation can potentially cause degradation in mechanical properties of resin materials (Chin et al. 1997). More specifically, UV exposure primarily affects the surface region to a depth of approximately 10 micrometers. The degradation mechanism involves cross-linking that spoils the surface's aesthetic appearance. The combined UV exposure and high humidity was shown to severely deteriorate the FRP composite's surface and led to reduced fracture toughness, as the flaws on the surface can serve as stress concentrators and initiate fracture of the whole composite at stress levels much lower than those of unexposed material portion (Ashbee 1989; Moore and Epps 1992; Underwood and Kapusta 1991).

1.8 Accelerated conditioning and prediction methodology

Currently, Fick's law and Arrhenius relation are the two theories most often used to estimate the long-term performance of FRP materials, where the latter gains more popularity. Tannous and Saadatmanesh (1998) used Fick's law to determine the mass diffusion coefficient (D).

A number of researchers have applied Arrhenius law to generate the prediction curve for FRP composite structures in marine areas or those affected by deicing salt. Experiments have been conducted on the long-term performance of concrete-filled GFRP tube cylinders and concrete embedded GFRP bars in salt solution for up to one year (Robert and Fam 2012; Robert and Benmokrane 2013). Elevated temperatures were used as the accelerated aging factor to accelerate corrosion. They found that for both GFRP tubes and GFRP bars, no significant change occurred on the microstructure of the FRP cross-section, glass transition temperature of the resin showed no difference and chemical structure remained basically the same for the resin. The prediction curves revealed that the GFRP bar retained 77% of its tensile strength after 100 service years in salt water at a mean annual temperature of 10°C, and hoop tensile strength of the GFRP tubes decreased by 30% after 48 service years at a mean annual temperature of 6°C. Several researchers have investigated the reliability of prediction curves that are based on Arrhenius relation. Phani and Bose (1987) concluded that the reduction in strength of an FRP composite as a result of hydrothermal effects is a rate process, in which the temperatures influence only the rate constant. This finding supports the primary assumption of Arrhenius law that only one degradation mechanism dominates the entire reaction process. Additionally, this mechanism will not change with time and temperature. On the other hand, the elevated temperature used in accelerated aging tests cannot be too high or close to the glass transition temperature of the resin. Robert et al. (2010) suggested that the limitation for vinylester-based GFRP composite materials should be 60°C, which is also the recommended value by ACI (2007).

Bank et al. (2003) proposed a method to predict the long-term behavior of FRP materials and generate an estimated service life curve based on Arrhenius law. Arrhenius law gives the dependence of the rate constant (k) of a chemical reaction on the absolute temperature T (in kelvin) and can be expressed in the following equation:

$$k = A \exp\left(\frac{-E_a}{RT}\right) \tag{1.5}$$

where k = degradation rate (1/time); A = constant relative to the material and degradation process; Ea = activation energy of the reaction; R = universal gas constant; and T = temperature in Kelvin. This relation can be alternatively expressed as:

$$\ln\left(\frac{1}{k}\right) = \frac{E_a}{R}\frac{1}{T} - \ln(A) \tag{1.6}$$

It can be observed from the above equation that the logarithm of time needed for a material property to reach a given value is a linear function of (1/T) with the slope of (Ea/R). Specimens experience different elevated temperatures in fully-saturated conditions and last for different durations. The strength property retention of the specimens after each duration period for different temperatures will be tested and a regression relation can be generated, which can be extrapolated to estimate the strength retention for other different environmental temperatures and different service life time. It is noted that there are limitations when applying Arrhenius law to estimate the long-term behavior. First, only one chemical degradation mechanism dominants the entire reaction and this mechanism will not change with time and temperature during exposure. Second, the conditioning temperatures cannot be too close to the glass transition temperature of the resin matrix, because the resin is believed to change the mode when approaching its glass transition temperature. Finally, in order to see any noticeable change in the properties of an FRP composite as a function of temperature, the FRP must be conditioned in an aqueous environment and not dry. This law is powerful to predict the long-term performance of materials in a high moisture state during their service life, and the performance of dry materials must be better.

1.9 Durability of concrete-filled FRP tube (CFFT) cylinders

Up to now, few studies have been focused on the durability of FRP confined concrete cylinders subjected to various environmental exposures. In addition to the environmental corrosion on the outer FRP, the confining pressure acted by the outer FRP on the concrete core is another consideration for hybrid system level. Both moisture and elevated temperature can cause hydrothermal swelling of the FRP wraps. This swelling can lead to residual hoop strain in the FRP wrap and diminish the confining effect on the concrete core. Actually, the coefficients of thermal expansion (CTEs) for FRP composites are quite different from those of concrete or steel. The CTE of GFRP is generally higher than that of concrete and steel, while the CTEs of CFRP and AFRP are generally smaller than that of concrete and steel in fiber direction (ACI 2007). However, in the transverse direction, the CTEs of GFRP, CFRP and AFRP are all higher than that of concrete and steel, especially for AFRP which possesses approximately 5-8 times higher value (Balazs and

Borosnyoi 2001). The reduced confinement on concrete is indicated by the decreased critical stress, ultimate strength, and ultimate strain of the hybrid system (Kshirsagar et al. 2000).

Micelli and Myers (2008) conducted durability tests on concrete cylinders that were wrapped with either GFRP or CFRP sheets. The cylinders were subjected to either combined freeze-thaw cycles, moisture cycles and high temperature cycles, or immersed into an NaCl solution with 15% by mass. They found that GFRP confined concrete cylinders, after being exposed to either environmental conditioning or an NaCl solution, exhibited a moderate decrease in ultimate strength. The ductility, however, was significantly reduced by more than 40%. CFRP confined concrete cylinders, however, did not show any significant change in ultimate strength, though they did lose 30% of their axial strain after they were immersed in the NaCl solution.

Pando et al. (2002) presented an ongoing research of long-term moisture effect on CFFT cylinders. The methodology used in the study is firstly to track the moisture absorption in the FRP materials and estimate the strength of FRP tube for a given period of time. Then a confinement model based on reduced tube strength and stiffness was used to evaluate the residual strength of the CFFT piles. Fam et al. (2002) also conducted moisture affect tests on concrete-filled GFRP piles. They submerged GFRP cylinders with two different laminate structures into freshwater for up to one year. They noted that the degradation for GFRP cylinders were about 13 to 20% and the degradation rate was reduced over time. Robert and Fam (2012) carried out durability prediction experiments on GFRP tube cylinders that were subjected to saltwater immersion. It was observed that there was no significant change on microstructure of FRP composite, and no change on thermal or chemical structure of epoxy matrix. They also found the hoop tensile strength of the GFRP tube was estimated to decrease by 30% after 48 service years at a mean annual temperature of 6°C.

Fam et al. (2008) conducted freezing-thawing cycles tests on both low-strength concrete and medium-strength concrete filled FRP tubes while under sustained axial loading, and carried out compression test on cylinders before and after exposure. They found that sustained load and freezing-thawing conditions increased compressive strength of the CFFT cylinders with low-strength concrete. They proposed that both the creep effect and the dilation that occurred during the thawing process induced extra radial strain in the concrete core, thus triggering more active confining pressures from the outer FRP tube. These behaviors were not observed, however, in CFFT specimens with medium-strength concrete. This was due to the brittle nature and low dilation capacity of medium to high strength concrete. Such difference between low strength concrete core

and high strength concrete core agrees well with the authors' previous work (Mandal et al. 2005), where FRP tube was proved to enhance the strength and ductility more effectively on low strength concrete than high strength concrete.

Several researchers have also studied the behavior of CFFT cylinders under mechanical loading. Naguib and Mirmiran (2002) studied the long-time shrinkage and creep behavior of CFFT cylinders under sustained axial loading and found that (1). the shrinkage of the concrete core in CFFT cylinders was quite negligible; (2). The concrete core's creep coefficient decreased as the FRP tube's elastic modulus increased.

Besides those actual experiments, American Concrete Institute (ACI) committee 440 was also attempted to quantify the degradation of FRP composite system due to different service environments. They provided a table of environmental reduction factors for FRP composite system based on fiber type and environmental exposure type (ACI 2008).

When designing FRP composite structures, FRP material properties should consider the effect of environmental exposure that will result in a reduced value rather than data provided by manufactures. The ultimate design tensile strength of FRP composite should be determined by using the environmental reduction factor given the table above for the appropriate fiber type and exposure condition.

$$f_{fu} = C_E f_{fu}^{*} \tag{1.7}$$

Similarly, the ultimate design strain should also be reduced by environmental reduction factor.

$$\varepsilon_{fu} = C_E \varepsilon_{fu}^{*} \tag{1.8}$$

The elastic modulus is typically unaffected by environmental conditions, and the design value is the same as the data reported by the manufacture.

$$E_f = f_{fu} / \varepsilon_{fu} \tag{1.9}$$

The environmental reduction factors given in the above table are conservative estimates that are based on the relative durability of each fiber type. These values will be refined as more research

information is developed and becomes available. The methodology regarding the use of these factors, however, will remain unchanged.

Table 1.1: Environmental reduction factor for various FRP systems and exposure conditions

Exposure conditions	Fiber type	Environmental reduction factor C_E
Interior exposure	Carbon	0.95
	Glass	0.75
	Aramid	0.85
Exterior exposure (bridges, piers, and unenclosed parking garages)	Carbon	0.85
	Glass	0.65
	Aramid	0.75
Aggressive environment (chemical plants and wastewater treatment plants)	Carbon	0.85
	Glass	0.5
	Aramid	0.7

2. SMALL SCALE HC-FCS COLUMNS UNDER STATIC CYCLIC AXIAL LOADING

2.1 Test Specimens

In total, sixteen specimens were investigated during the course of this research (Table 2.1 and Fig. 2.1). The prepared and tested cylinders included thirteen hybrid HC-FCS cylinders and three CFFT cylinders. The sixteen specimens were sorted in four groups. HC-FCSs were prepared with inner steel tubes of three different diameters of 2, 3, and 4 inch. Each specimen had outer FRP tube with fiber oriented at ± 45° or hybrid of ± 45°/0°. By definition CFFT has no steel tube. The FRP tubes in group 1 were prepared using prefabricated GFRP. All of the FRP tubes in groups 2, 3, and 4 were manufactured using a manual wet layup process. The last wrapped layer of FRP tubes of groups 2, 3, and 4 were provided with overlap of 30% of the cylinder's perimeter to prevent premature debonding failure. The FRP tubes in group 2 were prepared using glass fiber oriented at ± 45°, however the FRP tubes of groups 3 and 4 were prepared using hybrid fiber oriented at ± 45°/0°. All of the specimens were tested under axial static cyclic loading.

Figure 2.1: Ready for concrete pouring of HC-FCSs and CFFTs

All of the specimens had an outer diameter of 8.25 inch and a height of 16 inch except that of the group 1 which had an outer diameter of 8.45 inch and a height of 12 inch.

2.2 Material Properties

Table 2.2 shows the mix design of the used concrete. The average cylindrical concrete compressive strength (f_c') at 56 days is 8,000 psi for five standard cylinders 6 inch x 12 inch. One of these cylinders was tested under cyclic loading as explained later in this report and the others were tested under monotonic loading with a displacement rate of 0.02 inch/min.

Table 2.1: Specimens descriptions

Group No.	Specimen Name (number of specimens)	Specimen height (inch)	Outer FRP tube (thickness (inch))	Inner steel tube D_i (t_s) (inch)	Concrete cylindrical strength f_c' (psi)
1	DS-PG45-64 (3)	12	Prefabricated GFRP tube $\pm$ 45^o (0.125)	4.0 (0.063)	6,746
2	DS-GIII45-64 (1) DS-GIII45-39 (1) DS-GIII45-32 (1) CFFT-GIII45 (1)	16	GFRP- Three layers $\pm$ 45^o (0.10)	4.0 (0.063) 3.0 (0.077) 2.0 (0.063) -	8,000
3	DS-GII45-GI0-64 (1) DS-GII45-GI0-39 (1) DS-GII45-GI0-32 (1) CFFT-GII45-GI0 (1)	16	Hybrid GFRP- Two layers $\pm$ 45^o + One Layer 0^o (0.118)	4.0 (0.063) 3.0 (0.077) 2.0 (0.063) -	8,000
4	DS-GI45-GII0-64 (1)	16	Hybrid GFRP- One layer $\pm$ 45^o + Two Layers 0^o (0.134)	4.00 (0.063)	8,000

Table 2.2: Concrete mixture proportions

w/cm	Cement (lb/yd^3)	Fly Ash (lb/yd^3)	Water (lb/yd^3)	Fine aggregate (lb/yd^3)	Coarse aggregate (lb/yd^3)	HRWRA (lb/yd^3)	VEA (lb/yd^3)
0.38	590	295	336	1411	1411	3.6	1.2

Standard coupons were cut longitudinally from the steel tube for tensile tests according to ASTM A1067. The steel coupon tests were conducted under a displacement control of 0.03 inch/min. A strain gauge was attached to the mid height of the steel coupons (Fig. 2.2(a)). All steel coupons failed by yielding neck. The average stress-strain curve of steel coupons is shown in Figure 2.3. The results showed that the yield stress, ultimate stress, and the Young's modulus of the steel tubes are 90,000 psi, 90,000 psi, and 29,000 ksi, respectively. Table 2.3 summarizes the steel tube properties.

Three hollow steel tubes similar to those used in the HC-FCSs were tested under monotonic axial compression. Two strain gauges in the hoop direction and two vertical strain gauges were

mounted on the outer surfaces of steel tubes as shown in Figure 2.2 (b). Steel tubes A and B were failed by the local buckling in the elephant's foot mode at ultimate loads 67.80 kips and 66.50 kips, respectively. These are corresponding to stresses of 85.78 ksi and 89.42 ksi, respectively. However the steel tube C failed by global buckling and the local buckling in the elephant's foot mode at load 18.55 kips corresponding to a stress of 45.81 ksi. Failure load of tube C was significantly lower than the other tubes because the global buckling occurred early (Fig. 2.2 (c)).

According to ASTM D3039, longitudinal and radial coupons were cut from the one layer FRP tubes. One horizontal and one vertical strain gauge were attached to the mid height of the longitudinal FRP coupon as shown in Figure 2.4 (a). Two strain gauges were attached to the mid of the radial disk as shown in Figure 2.4 (b). Under tensile tests with a displacement loading rate of 0.05 inch/min, all FRP coupons whether longitudinal or radial failed by debonding between the two 45^o plies [$\pm 45^o$] without fiber rupture as shown in Figure 2.4. The ultimate stress was 10,500 psi (Fig. 2.5). The saturated FRP with fiber orientation at 45^o has a structure depends on fibers in two perpendicular directions [$\pm 45^o$] and adhesive material between them. Therefore this type of laminates works globally. As a result, the fibers did not work in the coupon tests as the width of the strip is only 1.0 inch so there is no fibers continuity. Table 2.4 summarizes the properties of the manual wet layup GFRP which were referenced based on the manufacturer's data sheet. Table 2.5 summarizes the properties of the prefabricated GFRP tube were referenced based on the coupon test results.

(a) (b) (c)

Figure 2.2: (a) steel coupon during tensile test, (b) Steel tube A during compression test; (c) Failure modes of the steel tubes A, B, and C

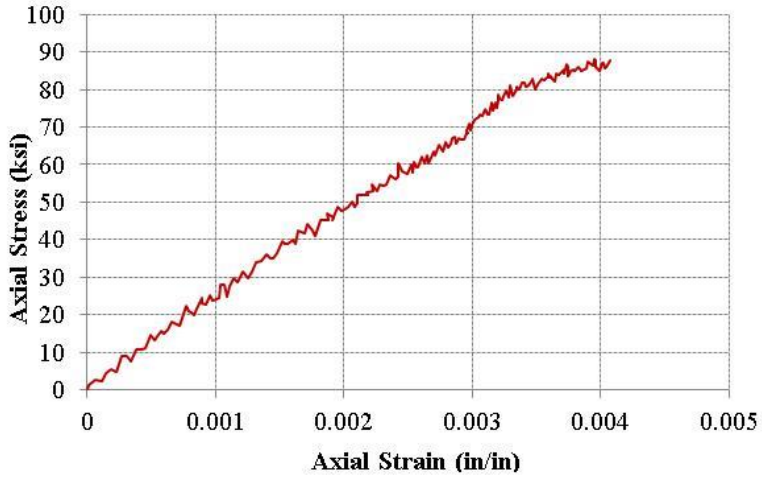

Figure 2.3: Axial strain-stress curve for steel coupon tensile test

Table 2.3: Properties of steel tubes

Material	Young's modulus, E (ksi)	Yield stress (psi)	Ultimate stress (psi)	Ultimate strain
Steel	29,000	90,000	90,000	0.40 %

Table 2.4: Properties of saturated FRP according to manufacturer's data

Material	Nominal thickness/layer (inch)	Young's modulus, E (ksi)	Tensile strength (psi)	Ultimate strain
GFRP-45^{o}	0.034	2,700	40,500	1.50 %
GFRP-0^{o}	0.050	3,790	83,400	2.20 %

Table 2.5: Properties of the prefabricated GFRP tubes

Material	Nominal thickness/layer (inch)	Hoop Young's modulus, E (ksi)	Hoop tensile strength (psi)	Axial Young's modulus, E (ksi)	Axial tensile strength (psi)
Prefabricated GFRP	0.125	2,028	21,350	1,523	8,430

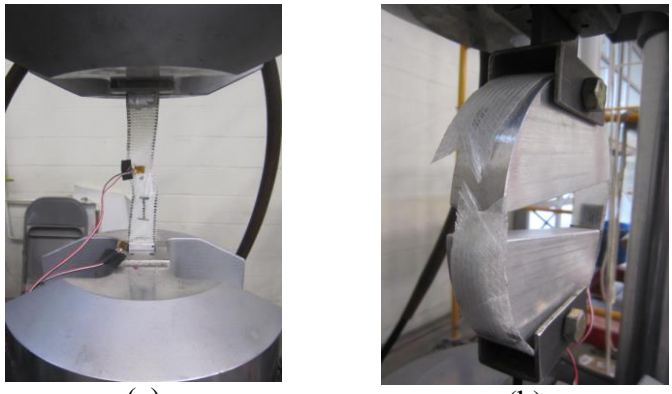

(a) (b)

Figure 2.4**:** (a) Longitudinal FRP coupon; (b) Radial FRP coupon

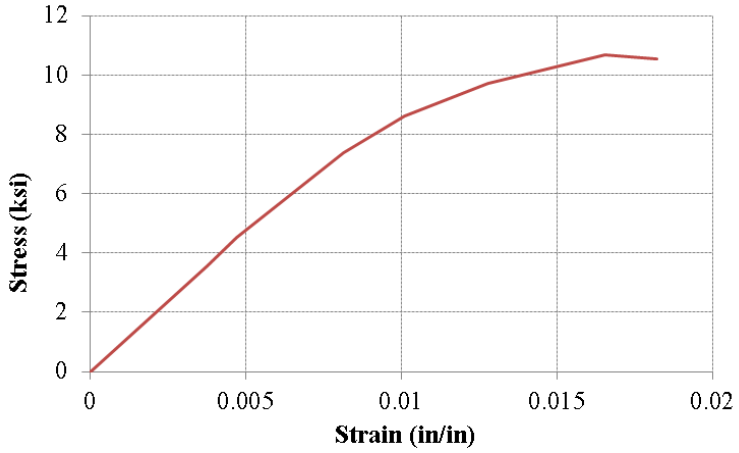

Figure 2.5: Strain-stress curve for FRP radial coupon

2.3 Experimental set-up and instrumentation

Compression tests were carried out using MTS machine with a loading rate of 0.02 inch/min. All test data, including the strains, loads, and displacements, were recorded simultaneously using a data acquisition system. Two horizontal and two vertical strain gauges were installed on the outer surface at the mid-height of the FRP tube. Likewise two horizontal and two vertical strain gauges were installed on the outer surface at the mid-height of the steel tube. In addition, two string potentiometers were attached on the outer surface of the FRP tube to obtain the axial deformation of the middle region of 5.5 inch for each specimen. Another radial string potentiometer was installed around the outer surface of the cylinder at the mid height in order to measure the average hoop strain.

2.4 Loading Schemes

All of the specimens were tested under compression loading on cyclic scheme as shown in Figure 2.6. The cyclic compression involved full loading/unloading cycles, where the unloading of each cycle was designed to terminate at a 100 lb (near zero) and the reloading of each cycle was designed to terminate at the unloading displacement of the same cycle. The loading scheme followed nine steps started at axial strain of 0.125 % and was increased gradually until failure of the specimen. Each loading step repeated three cycles.

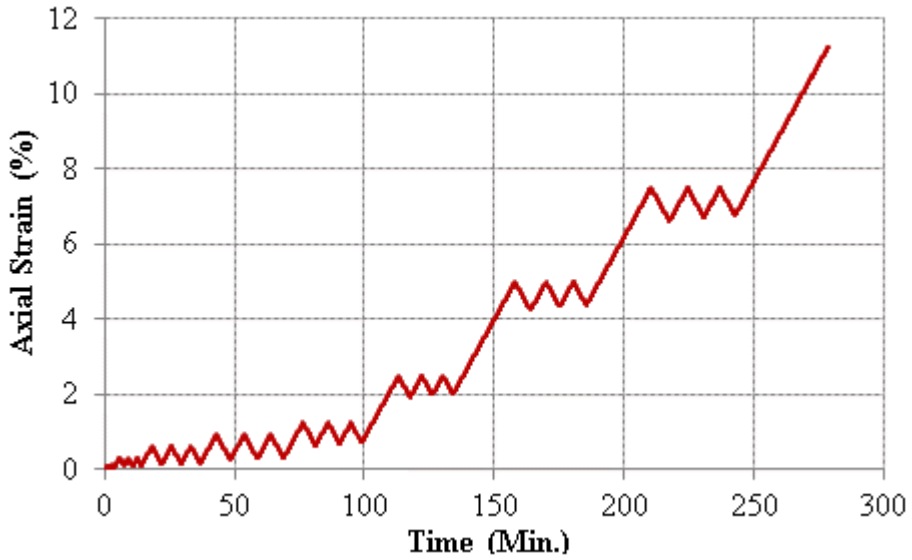

Figure 2.6**:** Cyclic loading scheme

2.5 Results and discussions of compression tests

2.5.1 *General Behavior*

The envelope axial strain-load and the hoop strain-load curves of the cyclic curves of groups 1 to 4 are shown in Figure 2.7. The axial strains were obtained from the average readings of the two string potentiometers. The radial strains were calculated using the difference in length of radial string potentiometers versus the initial reading. All cylinders of group 1 failed right after the outer FRP tube ruptured; no damage or buckling occurred on the inner steel tubes (Figs. 2.7(a) and 2.8(a)). The concrete between the two tubes, however, was crushed into multiple columns before the GFRP tube ruptured. This failure mode may have occurred for two reasons: 1) the shape and size of the concrete block was very slim and easily broken; 2) not adequate horizontal confinement was exerted on the concrete from the inner steel tube. Theoretically, the inner steel tube moved

outward and was in contact with the concrete block at initial elastic stage due to larger Poisson's ratio of steel than concrete. The concrete began to expand faster after elastic stage due to the development of cracks, and concrete block separated from the inner steel tube (Yu, T. et al. 2010).

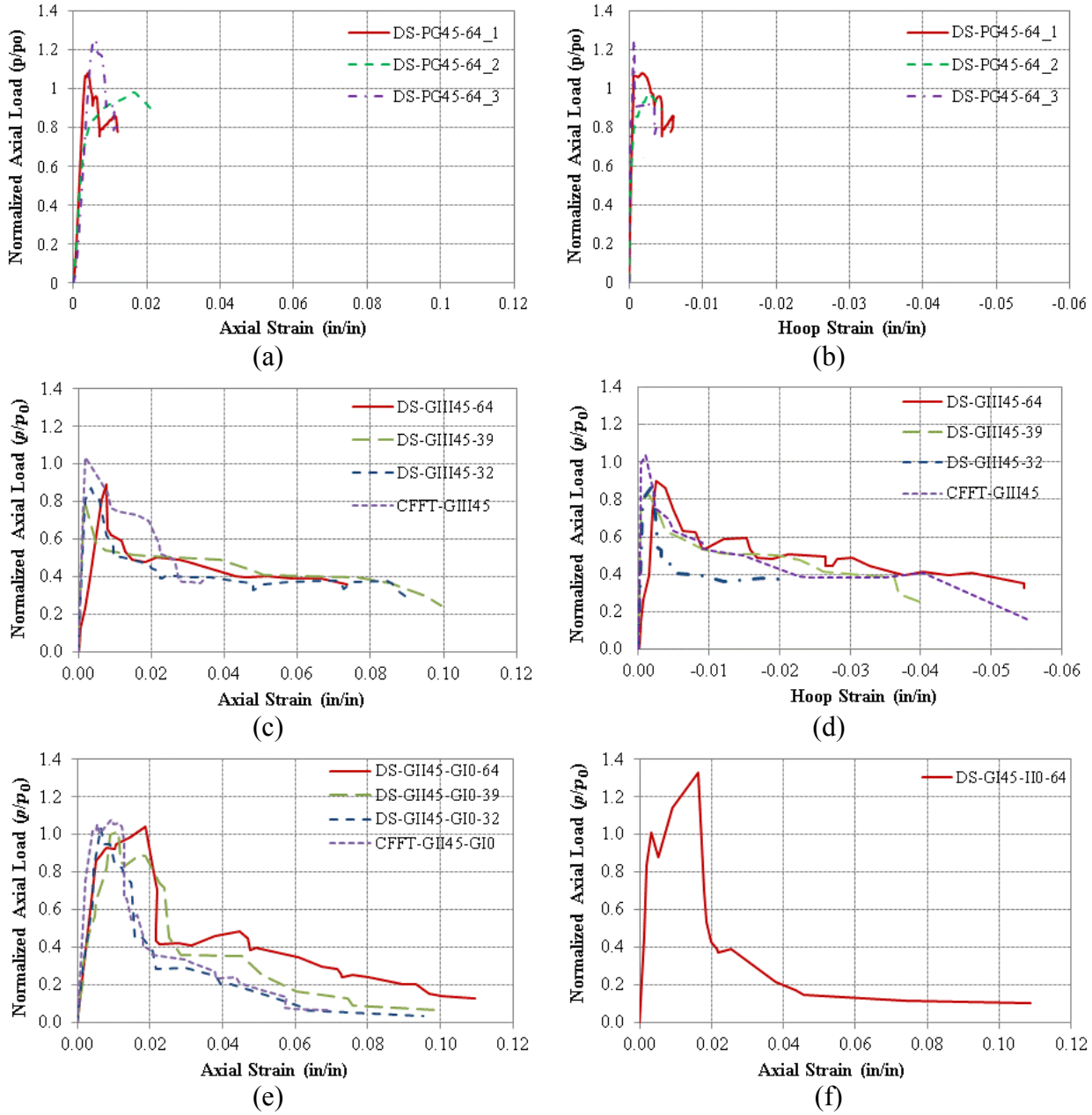

Figure 2.7: Axial strain-normalized axial load and hoop strain-normalized axial load relations for groups 1 to 4: (a) and (b) group 1, (c) and (d) group 2, (e) group 3, and (f) group 4

All of the specimens of group 2 failed due to steel tube buckling (Figs. 2.8(b) and 2.8(c)). The angle-ply FRP has an ability to give high ductility by the reorientation phenomenon (Au and

Buyukozturk 2005). Under axial loading, the angular fiber reoriented from the initial case (±45) toward the hoop direction without rupture. Therefore, most of the cylinders of groups 2 and 3 reached to the ultimate load without fiber rupture. As shown in Figure 2.7(c) that all of the specimens in group 2 had similar overall behavior. All of them reached to the maximum MTS machine axial displacement without FRP rupture.

All of the specimens in group 2 were ruptured before reaching the maximum applied axial strain except DS-GIII45-64 as the maximum applied strain was lower than the others. It can be concluded that the GFRP was reorienting during the axial loading hence the fibers were going closer to the hoop direction after the reorientation. Therefore the specimens in group 2 achieved higher capacities than the ones in group 1.

All of the specimens of groups 3 and 4 of hybrid FRP failed by fiber rupture (Fig. 2.8(d)). The capacities of all cylinders of these groups were higher than the nominal capacity (Figs. 2.7 (e) and 2.7(f)). The initial stiffness of the HC-FCS cylinders was almost the same however the CFFT had higher initial stiffness. When the outer unidirectional FRP layers ruptured, the axial strength dropped to 35-40% of the capacity at axial strain approximately of 0.02. After that, the angle-ply FRP layers kept the residual strength to approximately strain of 0.04 because of the fiber reorientation. Then, the axial strength reduced slowly with the increase of the axial strain up to approximately of 0.11.

(a) (b) (c) (d)

Figure 2.8: (a) Group 1 failed specimen, (b) Group 2 failed specimen (c) Steel tube local buckling, (d) Group 3 failed specimen

2.5.2 *FRP Axial-hoop strains relation*

The relation between the axial and hoop strain is considered as the key parameter which controls the effectiveness of the confinement of FRP. As all specimens were similar in the relation of the axial and hoop strains, the specimen DS-GIII45-32 was considered for representing this relation. Figure 2.9 shows the axial strain-axial load curve and the hoop strain-axial load curve of such specimen. It was noted that the axial and hoop strains were increasing simultaneously. During the first cycles, before ultimate load, the hoop and axial strains were increasing with high rate. It means the expansion of the concrete under axial loading was outward only. At ultimate load, the failure occurred due to the steel tube local buckling. After the local buckling of the steel tube and up to axial strain of 10,000 microstrain, the hoop strain was increasing with low rate. It means the concrete expansion was in the outward and inward directions. After the axial strain 10,000 microstrain, the effect of local buckling almost stopped as the local buckling occurred at many places in the steel. Therefore, the load slightly increased and the hoop strain was increasing with a moderate rate up to the maximum applied strain.

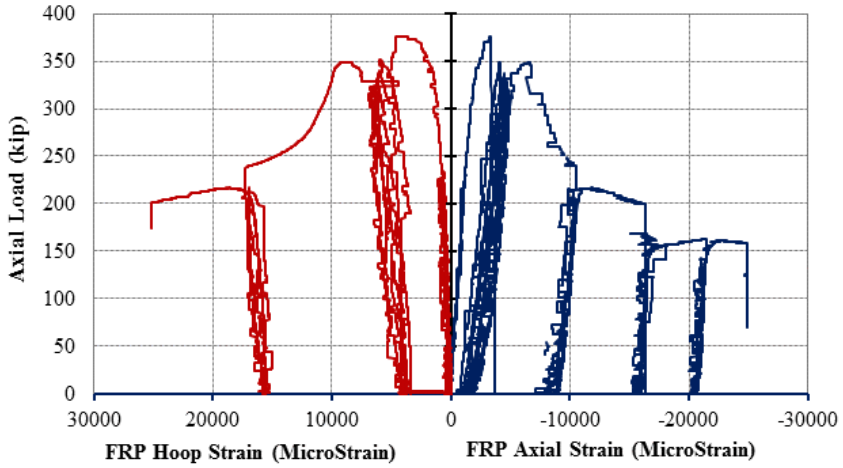

Figure 2.9: Axial load-strain curve of DS-GIII45-32

2.5.3 *Local buckling of the steel tubes*

The diameter-to-thickness (D_i/t_s) ratio is very significant parameter for HC-FCS columns. Researchers studied HC-FCS columns with D/t ratio (Ozbakkaloglu 2014, Yu 2010 and 2004, and Wong 2007) as listed in Table 2.6. In general in the previous studies, an increase in capacity for such cylinders was achieved or at least no reduction in capacity. Hence, this report presents higher values of the D_i/t_s ratio started with 32 up to 64. The capacity of the tested cylinders ranged by

factors of 0.76 to 1.30 from the nominal capacity P_o which was calculated as follows (AASHTO-LRFD 2012):

$$P_o = A_s f_y + 0.85 f_c'(A_c - A_s) \quad (2.1)$$

where A_s = the cross-sectional area of the steel tube or the longitudinal steel reinforcements, A_c = the cross sectional area of the concrete column, f_y = the yield stress of the steel tube or the longitudinal steel reinforcements, and f_c' = the cylindrical concrete's unconfined compressive stress.

The reduction can be explained because of the steel local buckling. However, the vertical strain in the steel tubes of the tested cylinders before local buckling was around 600-800 microstrain which was very low value. That exhibited the low contribution of the steel tube in axial capacity and hence a reduction in capacity occurred.

Normalized D_i/t_s can be defined as the ratio between the D_i/t_s to the D_i/t_s of AISC manual for the steel hollow section under compression as per the following equation:

$$\text{Normalized } ({}^{D_i}/_{t_s}) = {}^{D_i}/_{t_s} / (0.07 \frac{E}{F_y}) \quad (2.2)$$

The local buckling occurs when the D_i/t_s ratio is higher than that of the AISC manual value. The D_i/t_s ratio for the tested cylinder relative to that of the AISC manual value was between 1.37 and 2.74. However this ratio in the cylinders of literature relative to that of the AISC manual was lower than 1.00 as shown in Figure 2.10. That explained occurring the local buckling in the tested cylinders even in the cylinders with steel tube D_i/t_s ratio equals to 32. According to these results presented in this report, the contribution of the steel tube in the nominal capacity calculation should be adjusted therefore this research in continuing for this scope.

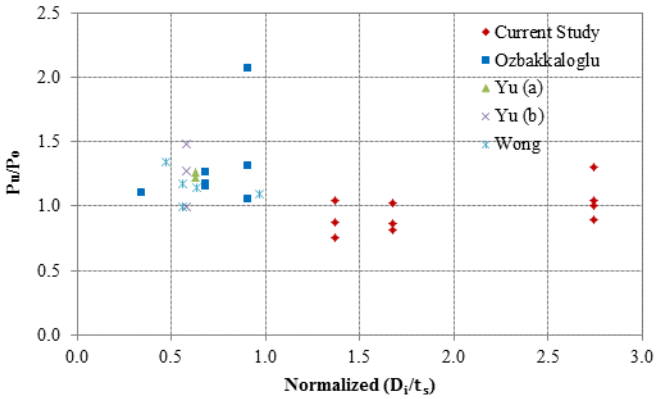

Figure 2.10: Actual steel diameter-thickness ratios relative to the AISC manual value versus increase in capacity

Table 2.6: Steel tube D/t ratio of HC-FCS columns of literature and of our work

	D_o (in)	D_i (in)	t_s (in)	D_i/t_s	$(D_i/t_s)_{AISC}$	Normalized (D_i/t_s)	P_u/P_o
Current Study	8.25 to 8.45	4.00	0.063	64.00	23.33	2.74	1.1
		4.00	0.063	64.00	23.33	2.74	0.89
		4.00	0.063	64.00	23.33	2.74	1.04
		4.00	0.063	64.00	23.33	2.74	1.30
		3.00	0.077	39.00	23.33	1.67	0.82
		3.00	0.077	39.00	23.33	1.67	1.02
		2.00	0.063	32.00	23.33	1.37	0.87
		2.00	0.063	32.00	23.33	1.37	1.04
Ozbakkaloglu (2013)	5.91	4.00	0.126	31.75	35.00	0.91	1.31
		4.00	0.126	31.75	35.00	0.91	2.07
		4.00	0.126	31.75	35.00	0.91	1.05
		3.00	0.126	23.78	35.00	0.68	1.16
		3.00	0.126	23.78	35.00	0.68	1.17
		1.50	0.126	11.91	35.00	0.34	1.10
		1.50	0.063	23.81	35.00	0.68	1.27
		1.50	0.063	23.81	35.00	0.68	1.16
Yu (a) (2012)	8.08	5.52	0.209	26.47	42.06	0.63	1.26
						0.63	1.23
Yu (b) (2004)	6.00	3.00	0.126	23.78	41.14	0.58	0.99
						0.58	1.27
						0.58	1.48
Wong (2007)	6.00	1.65	0.091	18.26	38.66	0.47	1.35
		2.99	0.130	23.03	41.14	0.56	0.99
		2.99	0.138	21.71	34.24	0.63	1.14
		3.46	0.083	41.90	43.29	0.97	1.10
		4.53	0.205	22.12	39.52	0.56	1.17

3. LARGE SCALE HC-FCS COLUMNS UNDER AXIAL-FLEXURAL LOADING

3.1 Test specimens

Four large scale columns were tested as free cantilevers under both constant axial compression load and cyclic lateral load. Each column had a circular cross-section with an outer diameter (D_o) of 24 inch and a height of 80 inch (Fig. 3.1). The lateral load was applied at a height (H) of 95 inch measured from the top of the footing resulting in shear-span-to-depth ratio of approximately 4.0. The first column was a conventional reinforced concrete (RC) column and the other columns were HC-FCS columns. Table 5.1 summarizes the columns' variables.

The columns' label used in the current experimental work consisted of three segments. The first segment is a letter F referring to flexural testing followed by the column's height-to-outer diameter ratio (H/D_o). The second segment refers to the column's outer diameter (D_o) in inches. The third segment refers to the GFRP matrix using E for epoxy and P for Iso-Polyster base matrices; this is followed by the GFRP thickness in 1/8 inch, steel thickness in 1/8 inch, and concrete wall thickness in inches. In the case of reinforced concrete column, the third segment is replaced with RC.

The F4-24-RC column had a longitudinal reinforcement of 8#7 corresponding to approximately 1.0% of the concrete cross-sectional area and it had a transverse spiral reinforcement of #4 @ 3 inch corresponding to volumetric reinforcement ratio of 1.0%. The concrete cover beyond the spiral reinforcement was 0.5 inch (Fig. 3.1(a)).

The F4-24-E324 column consisted of an outer filament wound GFRP tube having a wall thickness (t_{FRP}) of 0.375 inch, an inner steel tube having an outer diameter (D_i) of 16 inch and a wall thickness (t_s) of 0.25 inch with steel tube diameter-to-thickness (D_i/t_s) ratio of 64, and the concrete wall thickness (t_c) was 4 inch (Fig. 3.1(b)). The F4-24-P124 column was similar to the F4-24-E324 except the outer filament GFRP tube was made with a matrix of Iso-polyester with a wall thickness of 0.125 inch (Fig. 3.1(c)). The F4-24-E344 column was similar to the F4-24-E324 except the thickness of the inner steel tube was 0.5 inch (Fig. 3.1(d)). The inner steel tube of all of the HC-FCS columns was extended inside the footing and the column loading stub using an embedded length (L_e) of 25 inch representing 1.6 D_i while the FRP tube was stopped at the top of the footing

and at the bottom of the column's loading stub. The steel tube was hollow inside. All HC-FCS columns did not include any shear or flexure reinforcement except the steel tube.

Each column's footing had length, width, and thickness of 60 inch, 48 inch, and 34 inch, respectively. The footing of the F4-24-RC column had bottom reinforcements of 7#7, top reinforcements of 4#7, and shear reinforcement of #4@ 2.5 inch (Fig. 3.1(a)). The footing of the columns F4-24-E324 and F4-24-P124 had bottom reinforcements of 7#7, top reinforcements of 6#7, and shear reinforcement of #4 @ 2.5 inch (Figs. 3.1(b) and 3.1(c)). The footing of the column F4-24-E344 had bottom reinforcements of 7#8, top reinforcements of 6#8, and shear reinforcement of #4 @ 2.5 inch (Fig. 3.1(d)).

Table 5.2 summarizes the concrete mixture proportions of the columns' components. Pea gravel of maximum aggregate size of 3/8 inch and high range water reducers (HRWR) were used for the columns only to increase the workability. Table 5.3 summarizes the unconfined concrete cylindrical strengths (f_c') of the columns and the footings at 28 days and the days of the tests. Table 5.4 summarizes the properties of the steel rebars and tubes, used during this experimental work, based on the manufacturers' data sheets. Table 5.5 summarizes the properties of the FRP tubes, used during this experimental work, based on the manufacturers' data sheets.

Table 3.1: Summary of the columns' variables

Column		F4-24-RC	F4-24-E324	F4-24-P124	F4-24-E344
Nominal outer diameter (D_o, inch)			24		
Nominal inner diameter (D_i, inch)		N.A.		16	
Steel tube thickness (t_s, inch)		N.A.	0.25	0.25	0.5
FRP tube	Matrix	N.A.	Epoxy	Iso-polyester	Epoxy
	Thickness (t_{FRP}, inch)	N.A.	0.375	0.125	0.375
Longitudinal reinforcement		8#7	N.A.	N.A.	N.A.
Transverse reinforcement		spiral #4 @ 3 inch	N.A.	N.A.	N.A.

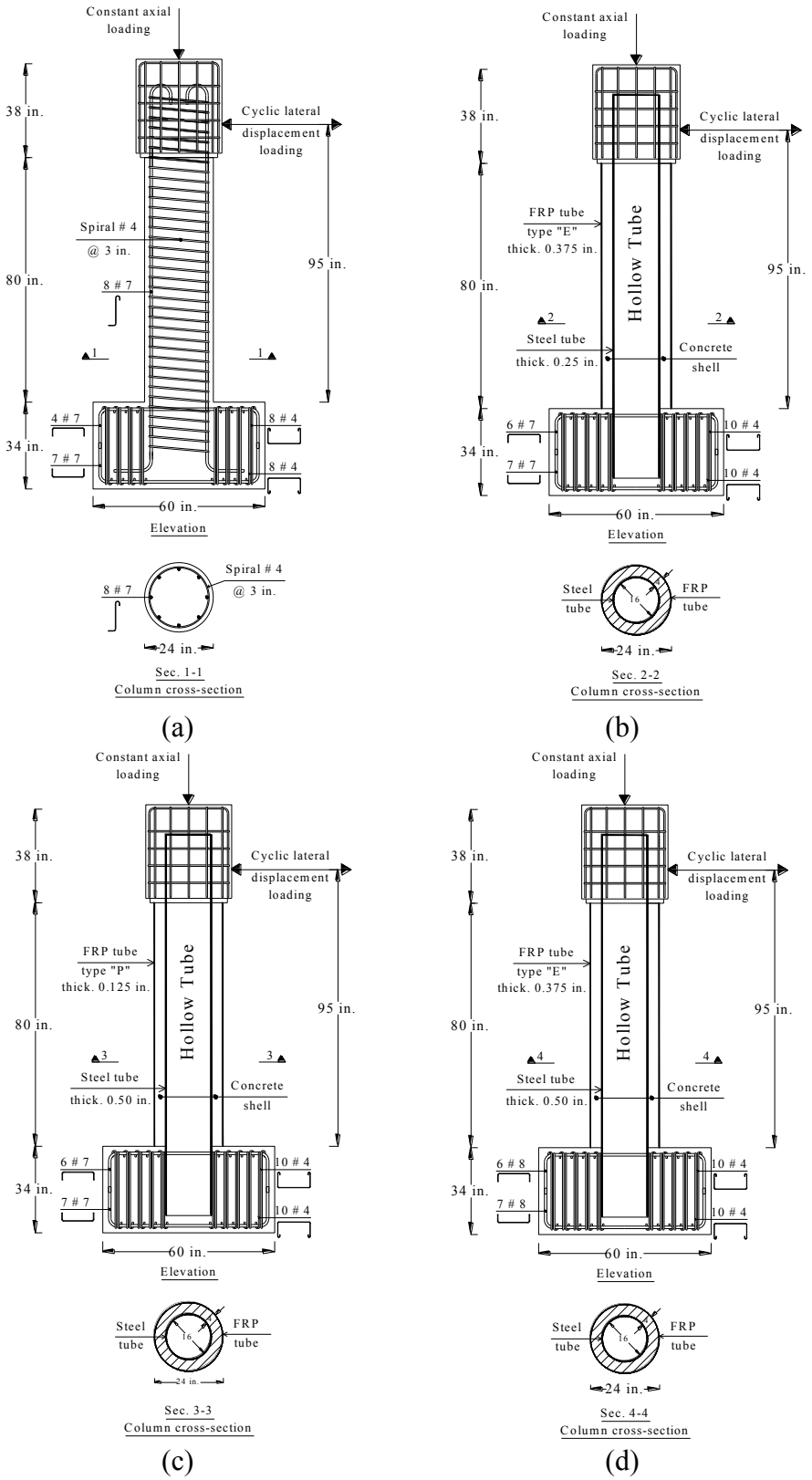

Figure 3.1: Reinforcement details of the investigated columns: (a) F4-24-RC column, (b) F4-24-E324 column, (c) F4-24-P124 column, (d) F4-24-E344 column

Table 3.2: Concrete mixture proportions

w/c	Cement (lb/yd^3)	Fly Ash (lb/yd^3)	Water (lb/yd^3)	Fine Aggregate (lb/yd^3)	Coarse Aggregate (lb/yd^3)	HRWR* (lb/yd^3)
0.5	590	170	380	1,430	1,430	1.90

*HRWR was used only for the column

Table 3.3: Summary of the unconfined concrete strength of the columns and the footings

	F4-24-RC		F4-24-E324		F4-24-P124		F4-24-E344	
	Column	Footing	Column	Footing	Column	Footing	Column	Footing
f_c' at 28 days (psi)	4,725	5,300	4,725	5,300	5,770	8,117	5,770	8,117
f_c at the day of the test (psi)	5,075	5,480	5,215	5,640	6,235	8,910	7,787	8,605

Table 3.4: Steel properties of the rebars and steel tubes

	Elastic modulus (E, ksi)	Yield stress (f_y, psi)	Ultimate stress (f_u, psi)	Ultimate strain (ε_u, inch/inch)
Steel rebar	29,000	60,000	90,000	0.08
Steel tube	29,000	42,000	58,000	0.23

Table 3.5: FRP tubes properties

	Axial compression elastic modulus (E_a, ksi)	Axial ultimate stress (f_{ar}, psi)	Hoop elastic modulus (E_h, ksi)	Hoop rupture stress (f_{hr}, psi)
Epoxy tube	677	12,150	3,020	40,150
Iso-polyester tube	1,400	17,900	2,200	40,000

3.2 Bill of quantities-per-foot

Table 3.6 summarizes the weight and the cost of the conventional reinforced concrete column (F4-24-RC) and HC-FCS column having thinner FRP tube (F4-24-P124) column. The table focuses on the column that has thinner FRP tube since it is more appropriate for Missouri from a seismic prospective. The thinner FRP tube was manufactured using Iso-polyster resin. Using epoxy based resin would slightly increase the price given in Table 3.6. The F4-24-P124 column could be built with a minimum concrete wall thickness for constructability as will be explained in Chapter 4.

Table 3.6: Summary of bill of quantities-per-foot of F4-24-RC and F4-24-P124 columns

Item	F4-24-RC			F4-24-P124 with minimum concrete wall thickness		
	Quantity (unit/ft.)	Weight (lb/ft.)	Amount (US $/ft.)	Quantity (unit/ft.)	Weight (lb/ft.)	Amount (US $/ft.)
Concrete	3.2 ft^3/ft	448	11.9	1.1 ft^3/ft	154	4.1
Long. rebars	8#7	16.5	14.5	N.A.	N.A.	N.A.
Spirals	4#4	17.5	28.2	N.A.	N.A.	N.A.
Steel tube	N.A.	N.A.	N.A.	1	55	52
FRP tube	N.A.	N.A.	N.A.	1	9	50
Summation	N.A.	482	54.6	N.A.	218	106.1
Normalized to F4-24-RC	N.A.	100%	100%	N.A.	45%	194%

For the case of minimum concrete wall thickness, the F4-24-P124 column's weight-per-foot was 45% of that of the F4-24-RC column. The weight of the full-scale of the HC-FCS column can be reduced further compared to its counterpart RC columns. For instance, the weight of a HC-FCS column having 5 ft. diameter can be 35% of the weight of its counterpart RC-column. The material price of the HC-FCS column can be also reduced if the material used in the construction is tailored for the column's applications and the design is refined. For example, the steel tube thickness can be significantly reduced; however, the effects of such reduction on the local and global buckling of the column need to be investigated. The FRP tube used in this project is an over the counter tube having fiber oriented at ±53°. However, an optimization of the fiber angle can significantly reduce the thickness and the price of the tube. In addition, the current project uses FRP tube having constant thickness along the height of the column. However, using variable FRP thickness along the height of the column would also reduce the cost of the FRP tube. As shown in the table, the dollar-per-foot of F4-24-P124 column's materials was 194% of that of the F4-24-RC column. However, the price comparison based on the material prices only is not a fair comparison as the main benefit

of using HC-FCS columns is the constructability and superior structural performance as they much lower workmanship, and a significant shorter time for construction compared to the RC-columns. Finally, the freight costs of the materials used in the case of HC-FCS will be approximately 35% of those of the RC column.

3.3 Construction sequence in the field

There are two options to construct the HC-FCS columns. The first option; building the precast HC-FCS column in the precast yard, then install it on the reinforcement cage of the footing, and finally cast-in-place the concrete footing (Fig. 3.2). The second option; building the precast HC-FCS column in the precast yard during casting-in-place of the footing with a certain void, then install the precast column into the footing's void, and finally grouting the gap between the footing and the steel tube (Fig. 3.3). The void diameter (D'_o) is larger than the column's diameter (D_o) to free access for grouting. Option "1" has lower number of tasks for construction but the tasks are series while option "2" has higher number of tasks for construction but the tasks are parallel. Option "1" was considered during the current study because of the easy of construction in the lab.

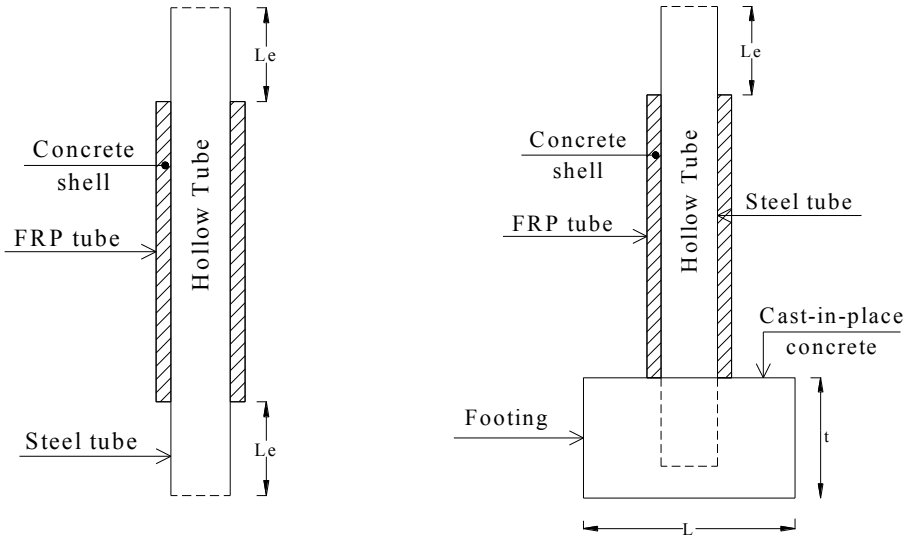

Step 1: Build pre-cast HC-FCS column

Step 2: Install pre-cast column on the footing cage then cast-in-place the footing

Figure 3.2: Construction of HC-FCS column: Option "1"

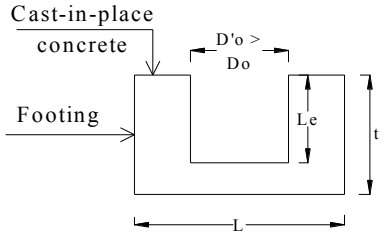

Step 1: Build pre-cast HC-FCS column as in OPTION "1"

Step 2: Cast-in-place the footing with void of dimensions D_o' x L_e

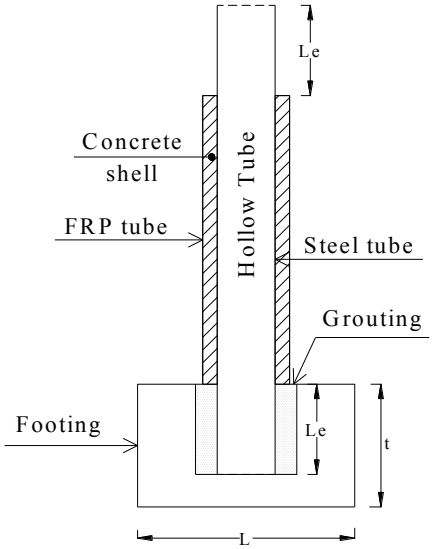

Step 3: Install pre-cast column on the footing's void then concrete grouting to fill the gap between the steel tube and the footing

Figure 3.3: Construction of HC-FCS column: Option "2"

3.4 Construction sequence of the investigated columns

The construction sequence of the four columns is presented as following:

- **Prepare reinforcement cages of the footings and the RC-column**

(a)

(b)

Figure 3.4: Preparing reinforcement cages: (a) footing, (b) RC-column

- **Install reinforcement cages into the formwork**

(a) (b)

Figure 3.5: Install reinforcement cages into formwork: (a) footing, (b) RC-column

- **Install steel tube into footing**

The embedded length (L_e) of the steel tube into the footing, measuring from the top of footing to the bottom of the steel tube into the footing, was 25 inch which was approximately 1.6 times the diameter of the steel tube (D_i).

(a) (b) (c)

Figure 3.6: Install the steel tube into the footing: (a) moving the steel tube, (b) putting the steel tube into the footing, (c) verticality check of the steel tube

- **Concrete pouring of the footing**

Figure 3.7: Concrete pouring of the footing

- **Install the formwork of the RC-column and the FRP tube for the HC-FCS column**

Figure 3.8: Install the formwork of the RC-column and the FRP tube for the HC-FCS column

- **Concrete pouring of the column**

Figure 3.9: Concrete pouring of the columns

- **Install the formwork of the columns' loading stub above the scaffolding**

Figure 3.10: Install the formwork of the columns' heads

- **Install the reinforcement cage of the column's loading stub and concrete pouring**

Install reinforcement cage

3D-view

Top view

Concrete pouring

Figure 3.11: Install the reinforcement cage of the column head and concrete pouring

- **Paint the concrete surfaces**

Figure 3.12: Paint the concrete surfaces

3.5 Instrumentations

5.4.1 Measuring displacement and curvature of the column

Fifteen Linear-variable-displacement-transducers (LVDTs) and string potentiometers (SPs) were employed for the measurement of displacement and curvature of the column. Two more LVDTs were attached on the footings for measuring the rocking and sliding of the footings. The effect of the rocking and sliding were subtracted from calculating displacement and curvature of the columns. A layout of the LDVTs and SPs is depicted in Fig. 3.13. All of the LVDTs and SPs were attached to a reference column in order to collecting the net readings from the LDVDTs and SPs. Four LVDTs were mounted each on the north and south faces for the curvature measurement at the plastic end region.

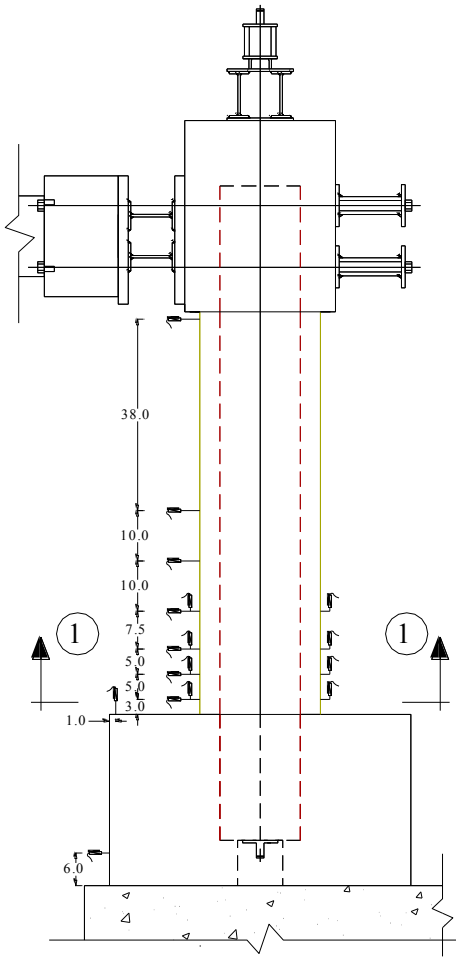

Figure 3.13: Layout of the LVDTs and SPs

5.4.2 Measuring strains on the longitudinal rebar of the RC-column

Fourteen strain gauges were installed on the north and south longitudinal steel rebars of the RC-column (Fig. 3.14).

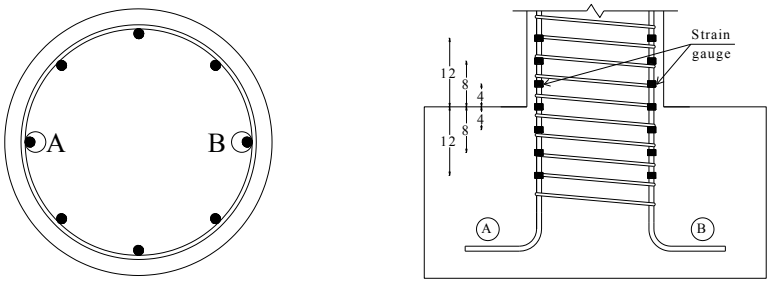

Cross-section Elevation

Figure 3.14: Install strain gauges on two longitudinal rebars of the RC-column

5.4.3 Measuring strains on the FRP tubes

Forty-eight strain gauges were installed on each FRP tube at six levels with spacing of 5 inch (Fig. 3.15). Four horizontal and four vertical strain gauges were installed at each level.

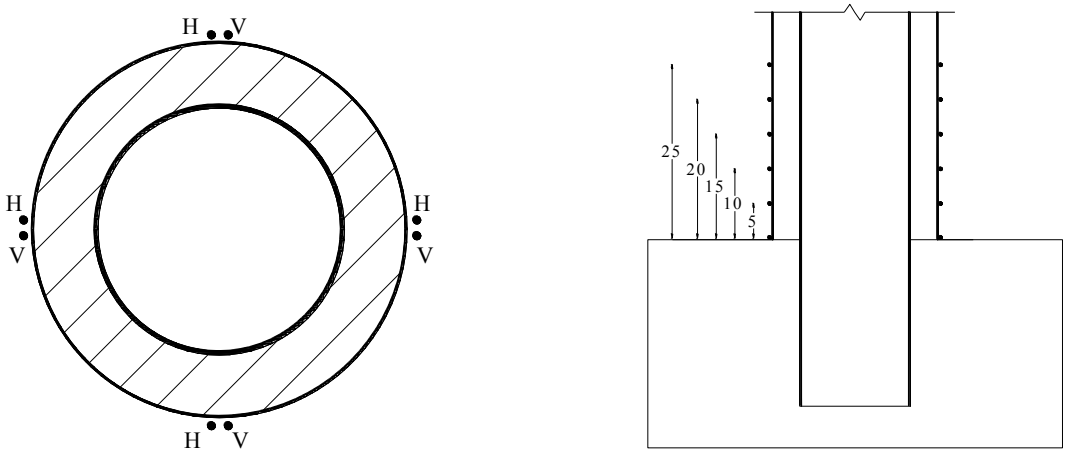

Cross-section Elevation

Figure 3.15: Install strain gauges on FRP tubes

5.4.4 Measuring strains on the concrete shell of the HC-FCS columns

One vibrating wire strain gauge (VWSG) was installed at the south direction in the concrete wall thickness of each column F4-24-P124 and F4-24-E344 to measure concrete micro changes in a gauge length (Fig. 3.16). The concrete strain was calculated by dividing the change in length measured by VWSG by the gauge length of it. VWSG was temporary supported to the steel tube with weak glue until the concrete pouring of the column.

Figure 3.16: Install vibrating wire strain gauges in the concrete wall thickness

5.4.5 Measuring strains on the steel tubes

Seventy-two strain gauges were installed inside each steel tube at nine levels with spacing of 5 inch (Fig. 3.17). Four horizontal and four vertical strain gauges were installed at each level.

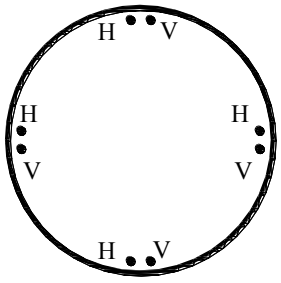

H: horizontal strain gauge
V: vertical strain gauge

(a)

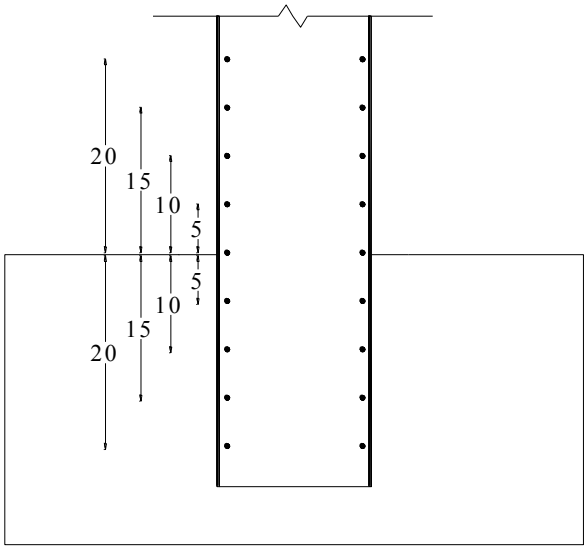

(b)

(c) (d)

Figure 3.17: Install strain gauges inside steel tubes: (a) arrangement in cross-section, (b) arrangement along the height, (c) inserting strain gauges into steel tube, and (d) final view

5.4.6 Monitoring the steel tube buckling and sliding using webcams

Two webcams were hanged inside the steel tubes to monitor buckling and sliding of each steel tube of the columns F4-24-P124 and F4-24-E344 (Figs. 3.18 and 3.19). One of the webcams was hanged vertically at 20 inch from the top of the footing level to show the buckling of the steel tube at the footing level. The other webcam was hanged horizontally at 3 inch below the top of the steel tube to show the sliding of the top of the steel tube on the concrete tube.

Figure 3.18: Install webcams inside the steel tubes

3.6 Loading protocol and test setup

Constant axial load (P) of 110 kips representing to 5% of the RC-column axial capacity (P_o) was applied to all of the columns using six external prestressing strands 0.5 inch at the east and west of the center of the columns (Fig. 3.19). The prestressing strands were supported by a rigid steel beam atop the column and the column's footing. The prestressing force was applied using two automatic hydraulic jacks as the hydraulic pressure can be automatically controlled to keep the prestressing force constant during the test. The P_o was calculated by eqn. (2.1)

After applying the axial load, cyclic lateral load was applied in a displacement control using two hydraulic actuators connected to the column loading stub (Fig. 3.19). The loading regime is based on the recommendations of FEMA 2007 where the displacement amplitude a_{i+1} of the step i+1 is 1.4 times the displacement amplitude of the proceeding step (ai). Two cycles were executed for each displacement amplitude. Figure 3.20 illustrates the loading regime of the cyclic lateral displacement. Each loading cycle was applied in 100 sec. corresponding to loading rate ranged from 0.01 inch/sec. to 0.05 inch/sec.

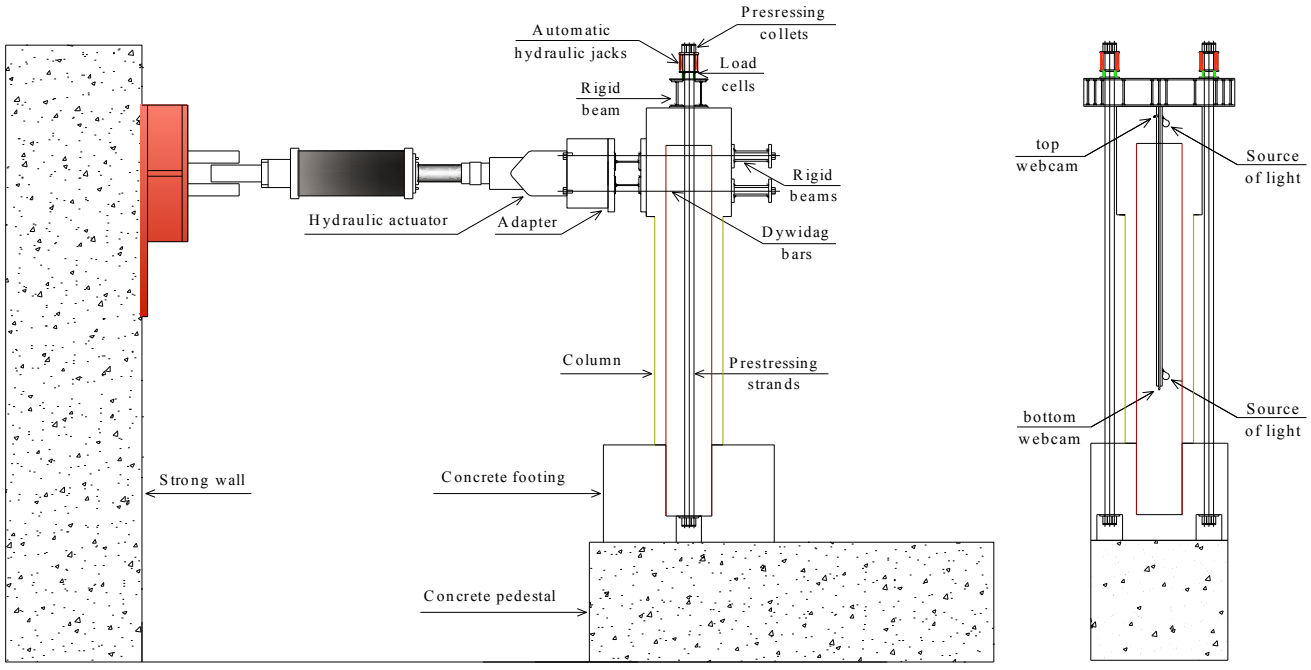

(a) (b)

Figure 3.19: Column test setup: (a) elevation, (b) sideview

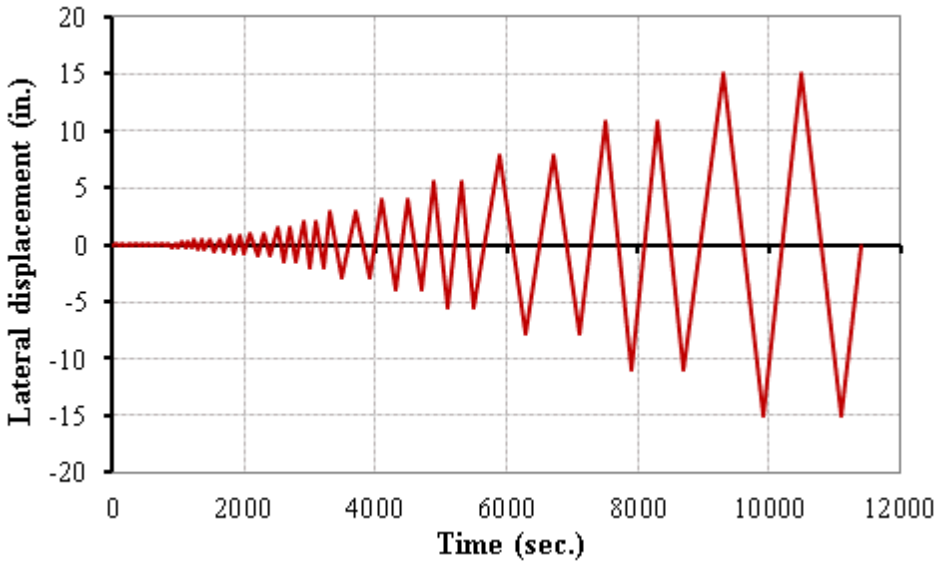

Figure 3.20: Lateral displacement loading regime

3.7 Results and discussion

Figure 3.21 illustrates the moment-lateral drift relation of all of the columns. The lateral drift (δ) of each column was obtained by dividing the lateral displacement measured from the actuators and corrected for any footing sliding, by the column's height of 95 inch. The moment (M) at the base of the column was obtained by multiplying the force collected from the actuators' loading cells by the column's height of 95 inch. Table 3.7 gives a summary of the maximum moments, the lateral drift at maximum moment, and the maximum lateral drift of each column. Appendix A illustrates all of the Force-curvature relations, lateral drift-steel strain relations, and lateral drift-FRP strain relations of all of the columns.

As shown in Fig. 3.21(a), the average peak moment capacity of the column F4-24-RC was 438 kip.ft at lateral drift of 5.1%. The stiffness of the column displayed gradual stiffness degradation up to a lateral drift of approximately 2.0%. Beyond that drift, significant stiffness softening started. The failure of the column occurred at lateral drift approximately 10.9% due to rupture of two rebars at the north and south side of the column (Fig. 3.22(a)). Failure was defined as the column loses at least 20% of its flexural capacity.

Two more rebars ruptured during cycling the column toward the second cycle of 10.9% lateral drift. At this stage, the column suffered severe damage in the form of concrete crushing and spalling, buckling and rupture of longitudinal rebars, and lateral deformation of the spiral reinforcement. It was worthy noted that the longitudinal rebars buckled in two different directions. One direction was the usual buckling going out of the column toward the radius of the column. Other longitudinal rebars buckled toward the circumferential direction indicating effective spiral confinement (Figs. 3.22(c)). The height of the damage area measured from the top of the footing ranged from 17 inch to 22 inch. However, the severe damage occurred within the first 9 inch from the top of the footing. The column's curvature was compatible with the column damage as it was high within the first 8 inch (Fig. 3.23(a)). However, the column was still able to carry the applied axial load. Figure 3.24(a) illustrates the force-curvature relation of the F4-24-RC column. The steel rebars was suffered high tensile and compressive strains (Fig. 3.25(a)).

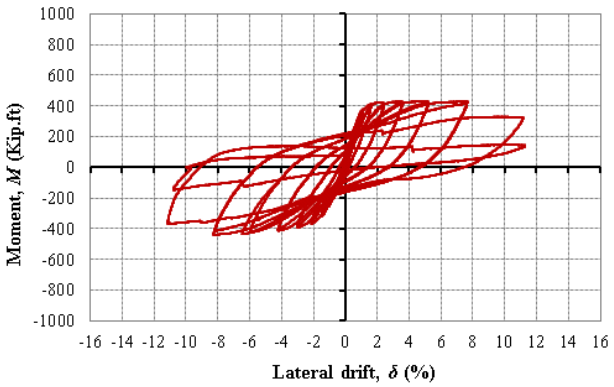

(a)

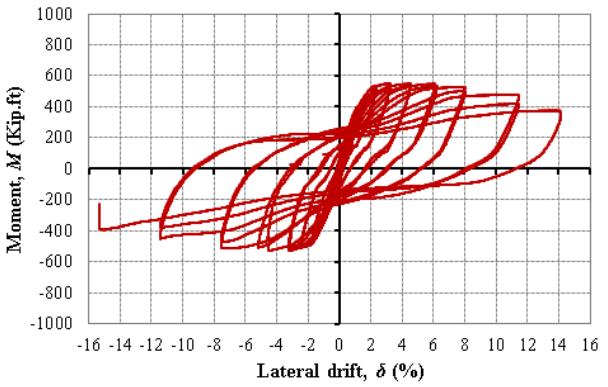

(b)

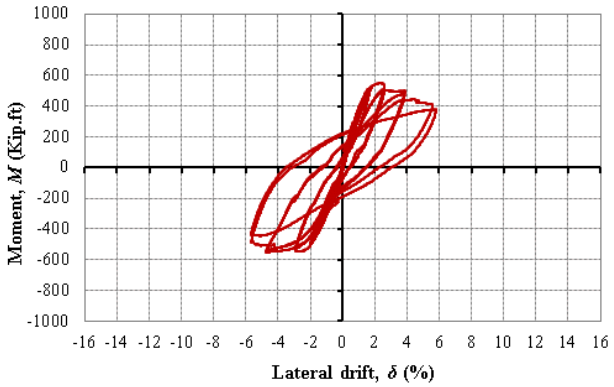

(c)

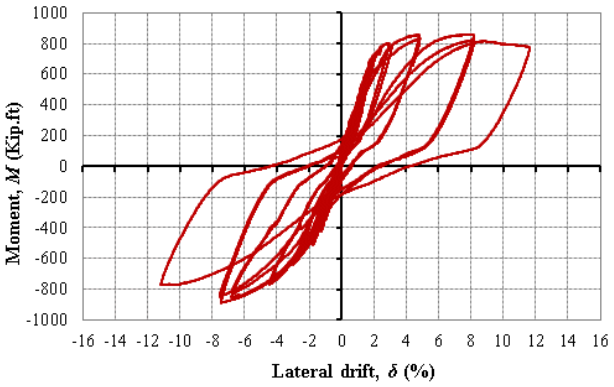

(d)

Figure 3.21: Moment-lateral drift relation: (a) F4-24-RC column, (b) F4-24-E324 column, (c) F4-24-P124 column, and (d) F4-24-E344 column

For the F4-24-E324 column, the average moment capacity of the column was 540 kip.ft at lateral drift of 2.8% (Fig. 3.21(b)). Gradual stiffness degradation occurred until drift of 2%; beyond that the column suffered significant stiffness softening. The peak lateral strength of the column remained approximately constant till a drift of approximately 6.0%. Beyond that the column's flexural strength gradually decreased till drift of 10.9%. At this drift ratio the column suffered 11% strength reduction. The failure of the column was considered at lateral drift of 13% when the strength reduction exceeded 20%. Cycling continued beyond that and the FRP ruptured at lateral drift of 15.2% (Fig. 3.22(b)). The direction of the FRP rupture followed closely the fiber direction i.e. 53^{o} (Fig. 3.22(d)). The residual moment after the FRP rupture was 232 kip.ft corresponding to 43% of the peak moment capacity of the column. After testing the column, it was observed that the column's concrete shell was almost powder along the bottommost 6 inch. This indicates that the steel and FRP tubes were able to confine the concrete shell and the concrete reached its ultimate strain before the rupture of the FRP tube. The column's curvature was compatible with the column damage as it was high within the first 8 inch (Fig. 3.23(b)). Figure 3.24(b) illustrates the force-curvature relation of the F4-24-E324 column. The steel tube was suffered high tensile and compressive strains (Figs. 3.25(b) and 3.26(a)). Figures 3.27(a) and 3.28(a) illustrate the vertical and hoop FRP strains.

The opening of the interface joint between the column and footing was measured as 2.75 inch at lateral drift of 14.1%. This sliding resulted from sliding of the FRP tube on the concrete shell, the sliding of the concrete shell on the steel tube, the sliding of the concrete surfaces on each other at the damage zone, and the concrete pull-out from the footing.

For the F4-24-P124 column, the average moment capacity of the column was 551.7 kip.ft at lateral drift of 2.6% (Fig. 3.21(c)). Gradual stiffness degradation occurred until drift of 2%; beyond that the column suffered significant stiffness softening. The failure of the column was considered at lateral drift of 5.8% when the strength reduction was approximately 20% combined with severe FRP rupture (Fig. 3.22(e)). The camera inside the steel tube showed that no visible steel tube buckling was noted. Figure 3.23(c) illustrates that the high column's curvature was within the first 8 inch from the top of the footing. Figure 3.24(c) illustrates the force-curvature relation of the F4-24-P124 column. The steel tube was suffered high tensile and compressive strains (Figs. 3.25(c)

and 3.26(b)). Figures 3.27(b) and 3.28(b) illustrate the vertical and hoop FRP strains. Figure 3.29(a) illustrates the concrete strain-lateral drift relation. The concrete behaved linearly up to approximately lateral drift of 1.0%.

For the F4-24-E344 column, the average moment capacity of the column was 874.5 kip.ft at lateral drift of 7.7% (Fig. 3.21(c)). The column suffered significant stiffness softening after approximately lateral drift of 8%. The column's footing suffered severe damage due to the steel tube pullout (Figs. 3.22(f)). The damage indicated that the embedded length of the steel tube was not enough for that column which explains that the steel tube embedded length is not related only to its diameter but it is related also to its thickness. The column lost approximately 15% of its flexural capacity at lateral drift of 11.6%. Figure 3.23(d) illustrates that the high column's curvature was within the first 8 inch from the top of the footing. Figure 3.24(d) illustrates the force-curvature relation of the F4-24-E344 column. The steel tube was suffered high tensile and compressive strains (Figs. 3.25(d) and 3.26(c)). Figures 3.27(c) and 3.28(c) illustrate the vertical and hoop FRP strains. Figure 3.29(b) illustrates the concrete strain-lateral drift relation. The concrete behaved linearly up to approximately lateral drift of 1.0%.

(a)

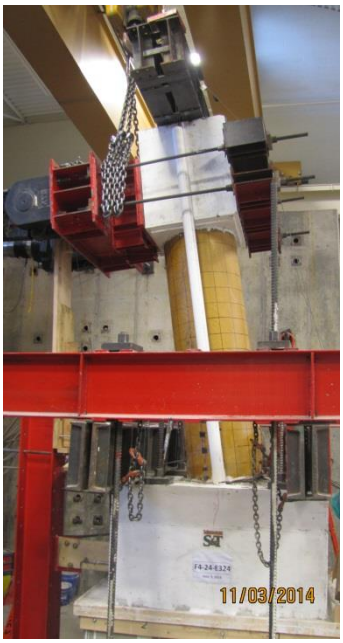

(b)

(c)

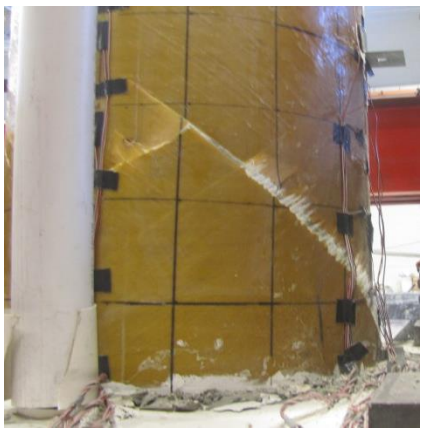

(d)

(e)

(f)

Figure 3.22: Columns' failure: (a) F4-24-RC at 11.5% lateral drift, (b) F4-24-E324 at 15.2% lateral drift, (c) F4-24-RC damage area, (d) F4-24-E324 FRP rupture, (e) F4-24-P124 FRP rupture, (f) F4-24-E344 column's footing damage due to steel tube pullout

Table 3.7: Summary of the columns' results

Column	Average maximum moment (kip.ft.)	Lateral drift at the maximum moment	Lateral drift at failure
F4-24-RC	438.0	5.1%	10.9%
F4-24-E324	540.0	2.8%	13.0%
F4-24-P124	551.7	2.6%	5.8%
F4-24-E344	874.5	7.7%	11.6%

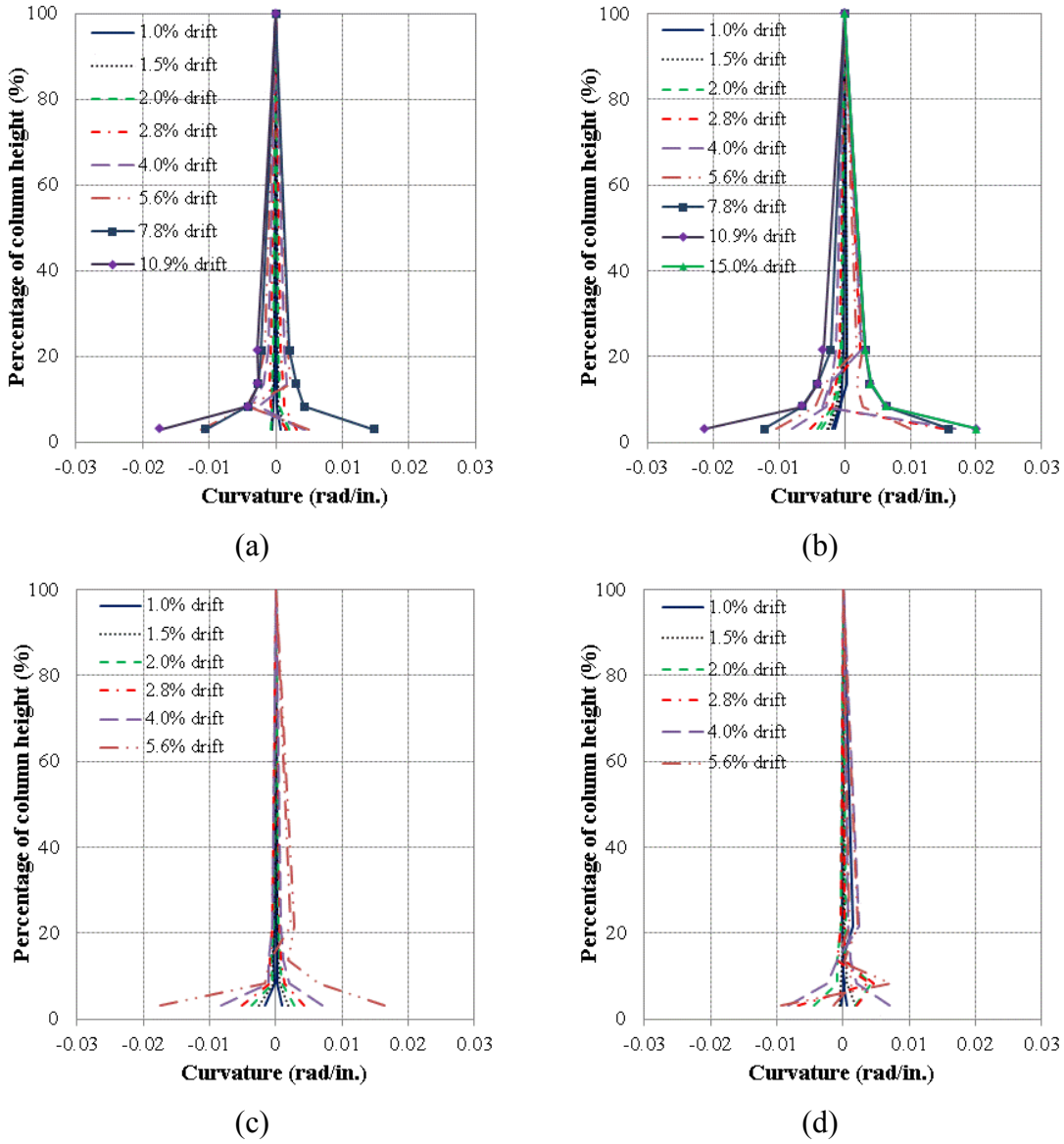

Figure 3.23: Curvature along the height: (a) F4-24-RC column, (b) F4-24-E324 column, (c) F4-24-P124 column, and (d) F4-24-E344 column

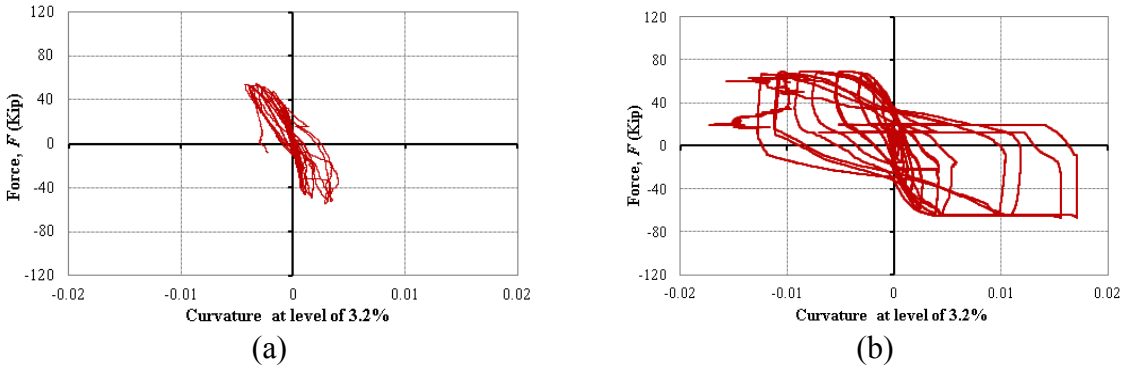

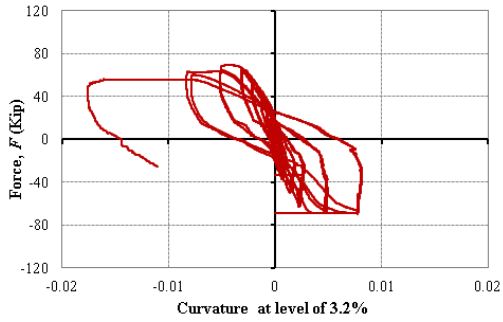

(c)

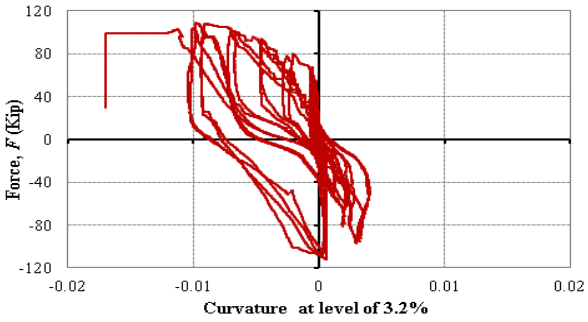

(d)

Figure 3.24: Force-curvature relation at the level of 3.2% of the column's height: (a) F4-24-RC column, (b) F4-24-E324 column, (c) F4-24-P124 column, and (d) F4-24-E344 column

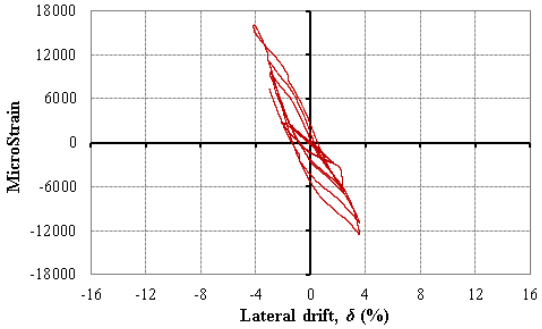

(a)

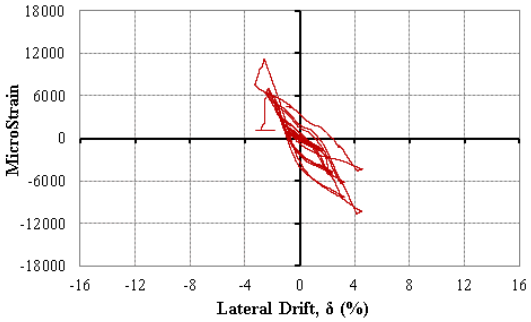

(b)

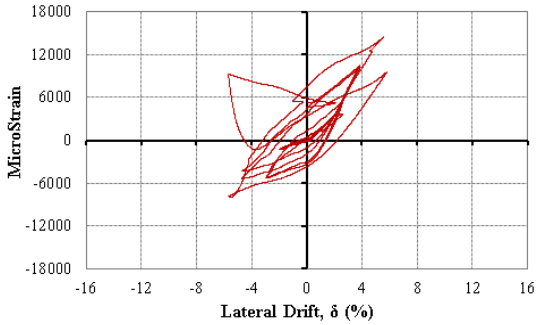

(c)

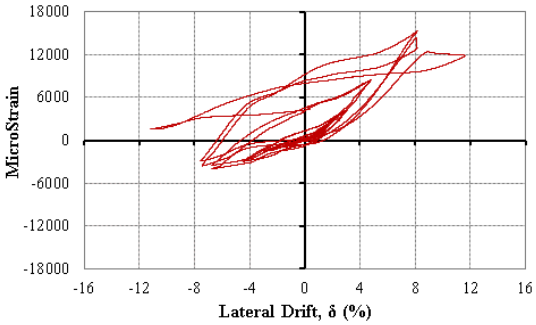

(d)

Figure 3.25: Lateral drift-vertical steel strain relation for: (a) the F4-24-RC column at 4 inch from the top of the footing, (b) the F4-24-E324 column at 10 inch from the top of the footing, (c) the F4-24-P124 column at 10 inch from the top of the footing, (d) the F4-24-E344 column at 10 inch from the top of the footing

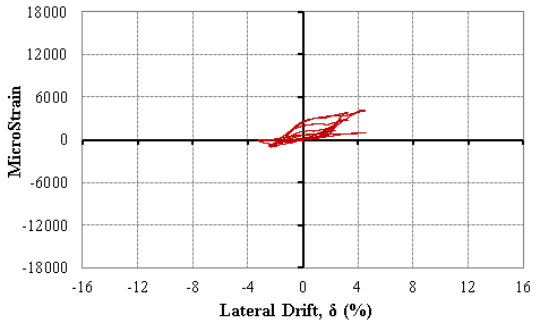

(a)

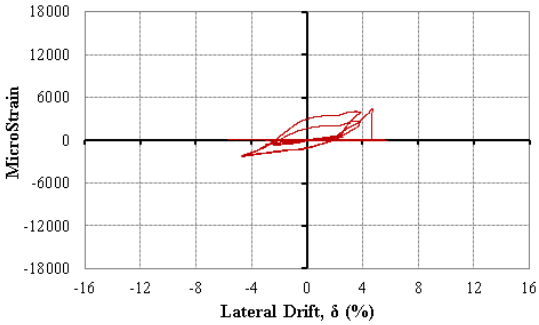

(b)

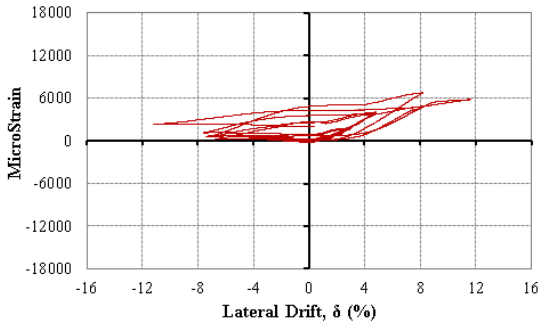

(c)

Figure 3.26: Lateral drift-hoop steel strain relation for: (a) the F4-24-E324 column at 10 inch from the top of the footing, (b) the F4-24-P124 column at 10 inch from the top of the footing, (c) the F4-24-E344 column at 10 inch from the top of the footing

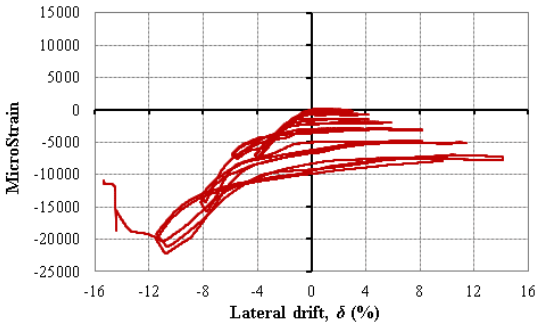

(a)

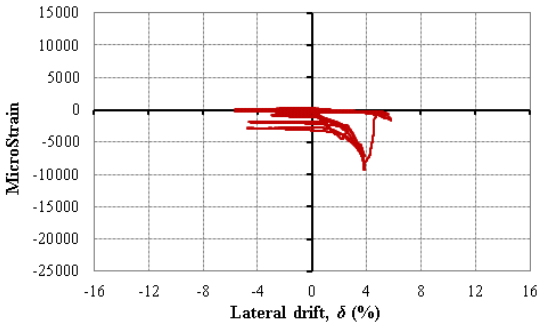

(b)

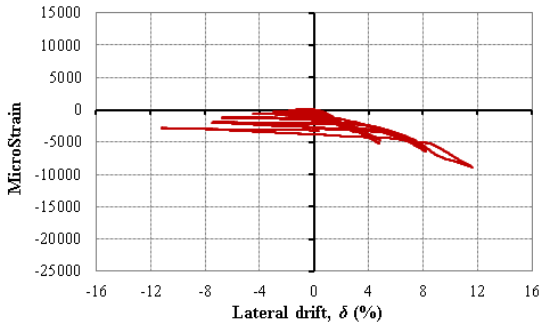

(c)

Figure 3.27: Lateral drift-vertical FRP strain relation for: (a) the F4-24-E324 column at 5 inch from the top of the footing, (b) the F4-24-P124 column at 5 inch from the top of the footing, (c) the F4-24-E344 column at 5 inch from the top of the footing

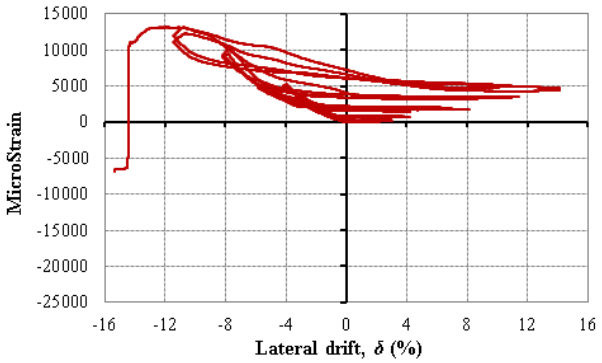

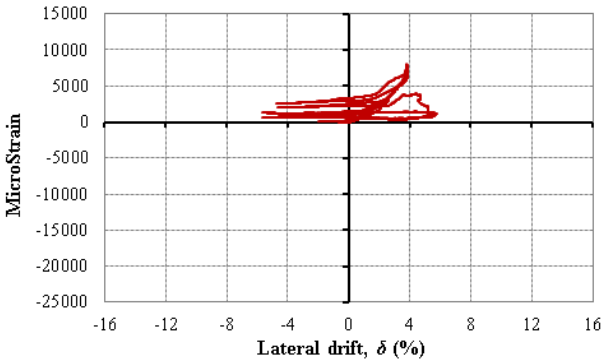

(a) (b)

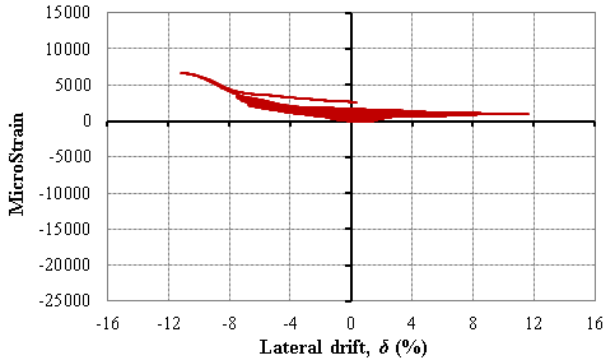

(c)

Figure 3.28: Lateral drift-hoop FRP strain relation for: (a) the F4-24-E324 column at 5 inch from the top of the footing, (b) the F4-24-P124 column at 5 inch from the top of the footing, (c) the F4-24-E344 column at 5 inch from the top of the footing

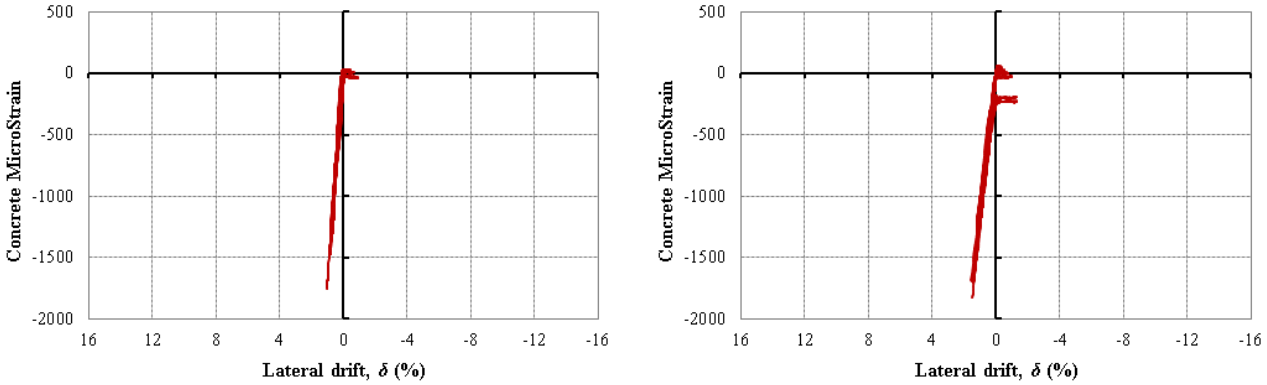

(a) (b)

Figure 3.29: Lateral drift-concrete strain relation for: (a) the F4-24-P124 column and (b) the F4-24-E344 column

4. FLEXURAL AND SHEAR STRENGTHS OF HC-FCS COLUMNS

4.1 Flexural guidelines

This section presents guidelines for the selection of the HC-FCS columns dimensions and their flexural strength. These flexural strength expressions were validated with the experimental and finite element results described in chapters 3 and 5, respectively. The dimensions and flexural strength are as follows:

1- Determine an initial size of the column's outer diameter (D_o).

2- Compute the minimum concrete wall thickness (t_c) based on constructability. Currently, based on the limited test data, it is recommended to select t_c as follows:

$$t_c = 0.10\ D_o \tag{4.1}$$

3- Compute the outer diameter of the steel tube (D_i) using Equation 4.2.

$$D_i = D_o - 2\ t_c \tag{4.2}$$

It is worth noting that increasing the steel tube diameter will decrease the column weight. However, it will increase the column's flexural strength as the lever arm of the tensile forces in the steel tube increases.

4- Compute the thickness of the steel tube (t_s) using Equation 4.3.

$$t_s = \frac{D_i}{64} \tag{4.3}$$

The steel tube's thickness is controlled by the diameter-to-thickness ratio (D_i/t_s). Thinner steel tubes are more susceptible to local buckling. However, thicker steel tube would increase the column's weight, cost, and strength. The tubes that were investigated during the current research have maximum D_i/t_s of 64. Hence, until further research is available, it is recommended to keep D_i/t_s to 64.

5- Compute the FRP tube thickness (t_{FRP}) using Equations 4.4 and 4.5 for low and high seismic regions, respectively.

$$t_{FRP} = 0.035 \frac{D_o f_c'}{f_t} \quad (4.4)$$

$$t_{FRP} = 0.105 \frac{D_o f_c'}{f_t} \quad (4.5)$$

Where f_t is the ultimate hoop tensile stress of the FRP tube and f_c' is the cylindrical unconfined concrete compressive strength at 28 days. A minimum f_t value of 40,000 psi is recommended.

The FRP tube represents the concrete confinement which allows the column to reach higher lateral drift before failure. Two FRP tube's thicknesses were investigated during the course of this study. Both thicknesses were able to display large lateral drifts of 13.0% and 5.8% before rupture. Hence, until further research is carried out, the lateral confinement pressure used in the test columns were used to develop recommendations for the FRP thickness.

6- Compute the column's flexural strength

Nonlinear analysis, considering Navier-Bernoulli's assumptions and strains compatibility, was used to calculate the flexural strength of HC-FCS columns. The main assumptions in the analysis were as follows: a) The plane section remained plane both before and after deformation occurred; b) Full composite action between the steel tube and concrete; c) The stress-strain relationship of steel was assumed elastic-perfectly plastic; d) the stress-strain relationship of concrete in the FRP-concrete-steel double skin sections (developed by Yu et al. 2006) was adopted. Moment-curvature analysis (including the applied axial load effects) was conducted and the bending strength was determined for each column.

The concrete compressive strain at the extreme fibers (ε_c) was initially assumed. Then, the distance from the neutral axis to the compressive extreme fibers (c) was incrementally increased until attaining force equilibrium ($\Sigma F_x = 0$). During the previous step, the compression and tension sides of cross-section were divided to 100 horizontal strip segments based on the polar angle of each side (Fig. 4.1). The stresses and forces in compressive confined concrete, steel in compression, and steel in tension were calculated at each c value. Consequently, the bending moment and the curvature were computed. The bending moment was computed around the plastic centroid which is the center of gravity (C.G.) of the cross-section as it is a symmetrical section. The concrete

compressive strain at the extreme fibers (ε_c) was incrementally increased up to ultimate strain (ε_{cu}; Yu et al. 2006). The analytical procedure is presented in the following steps:

a- Compute the sectors' polar angles ($\theta_1, \theta_2 \& \theta_3$)

$$\theta_1 = \frac{\alpha_1}{(n)}\ , \theta_2 = \frac{\alpha_2}{(n)} \& \ \theta_3 = \frac{\alpha_3}{(n)} \tag{4.6}$$

where n is the number of strip segments = 100 in this study

b- Compute the strain in each strip segment

$$\varepsilon_{c1n} = \frac{c - R_o\,(1 - cos\left(\alpha_{1n} + \frac{\theta_1}{2}\right))}{c}\,\varepsilon_c \tag{4.7}$$

c- Compute the force of the whole concrete compression segment as if there is no void

$$C_{C1} = 4\,R_O^2 \int_0^{\alpha_1} sin^2\left(\alpha_{1n} + \frac{\theta_1}{2}\right) \sin\left(\frac{\theta_1}{2}\right) * \sigma_{c1n} \tag{4.8}$$

d- Compute the concrete stress σ_{c1n} using Yu et al. (2006) model (Fig. 4.2)

e- Compute the strain in each virtual strip segment inside the void as if there is a concrete infill

$$\varepsilon_{c2n} = \frac{c - (R_o - R_i\,cos\left(\alpha_{2n} + \frac{\theta_2}{2}\right))}{c}\,\varepsilon_c \tag{4.9}$$

f- Compute the force of the virtual strip segment inside the void

$$C_{C2} = 4\,R_i^2 \int_0^{\alpha_2} sin^2\left(\alpha_{2n} + \frac{\theta_2}{2}\right) \sin\left(\frac{\theta_2}{2}\right) * \sigma_{c2n} \tag{4.10}$$

g- Compute the concrete stress σ_{c2n} using Yu et al. (2006) model (Fig. 4.2)

h- Subtract C_{C2} from C_{C1} to get the actual compression force in the concrete shell (C_C)

$$C_C = 4\,(R_O^2 \int_0^{\alpha_1} sin^2\left(\alpha_{1n} + \frac{\theta_1}{2}\right) \sin\left(\frac{\theta_1}{2}\right) * \sigma_{c1n} - R_i^2 \int_0^{\alpha_2} sin^2\left(\alpha_{2n} + \frac{\theta_2}{2}\right) \sin\left(\frac{\theta_2}{2}\right) * \sigma_{c2n}) \tag{4.11}$$

i- Compute the compressive force of each segment of steel tube

$$C_{scn} = 2\int_0^{\alpha_2} t_s * R_i * \frac{\theta_2}{n} * \frac{c-(R_o - R_i\, cos\left(\alpha_{2n}+\frac{\theta_2}{2}\right))}{c}\varepsilon_c * E_s \tag{4.12}$$

where t_s and E_s are the thickness and the Young's modulus of the steel tube

j- Compute the tensile force of each segment of steel tube

$$T_{stn} = 2\int_0^{\alpha_3} t_s * R_i * \frac{\theta_3}{n} * \frac{(R_o - c) + R_i\, cos\left(\alpha_{3n}+\frac{\theta_3}{2}\right))}{c}\varepsilon_c * E_s \tag{4.13}$$

k- After attending the force equilibrium ($\Sigma F_x = 0$), compute the column's flexural strength

$$M_n = \int_0^{\alpha_1} C_{c1n} * R_o * cos\left(\alpha_{1n}+\frac{\theta_1}{2}\right) - \int_0^{\alpha_2} C_{c2n} * R_i * cos\left(\alpha_{2n}+\frac{\theta_2}{2}\right) + \int_0^{\alpha_2} C_{scn} * R_i * cos\left(\alpha_{2n}+\frac{\theta_2}{2}\right) + \int_0^{\alpha_3} T_{stn} * R_i * cos\left(\alpha_{3n}+\frac{\theta_3}{2}\right) \tag{4.14}$$

where M_n is the nominal flexural strength of the column

m- Check the column design comparable to the ultimate applied loads

$$0.9\, M_n \geq M_u \tag{4.15}$$

where M_u is the factored applied moment on the column due to external loads

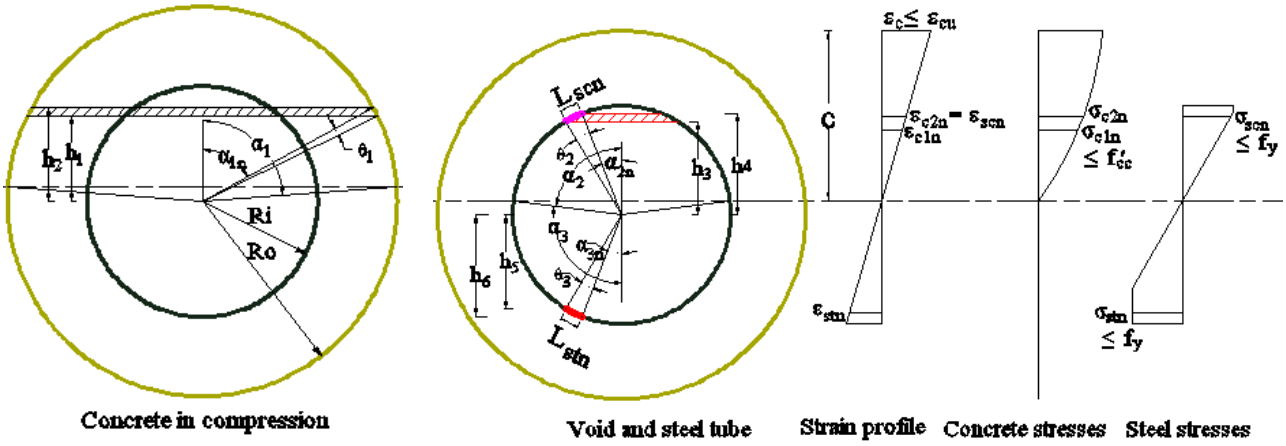

Figure 4.1:Cross-sectional analysis

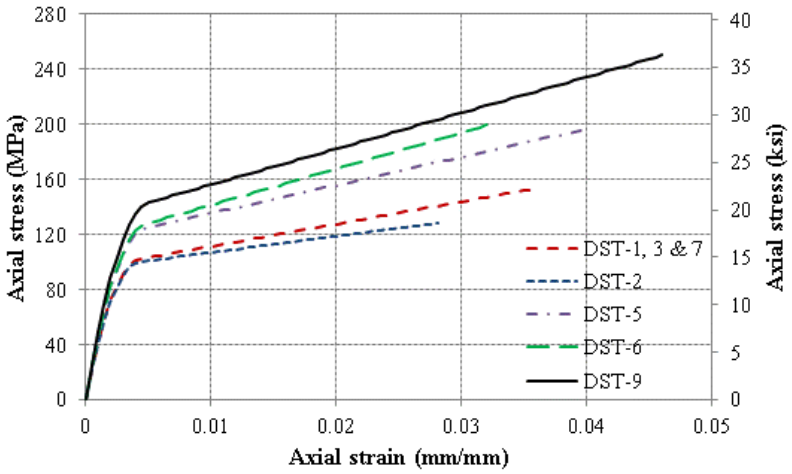

Figure 4.2: Stress-strain curves of the test columns based on the model of Yu et al. (2006)

The bending strengths calculated using the analytical procedure for the tested columns F4-24-E324, F4-24-P124, and F4-24-E344 are presented in Table 4.1 and Figure 5.3. The specimens tested by Ozbakkaloglu and Idris (2014) are presented in Table 4.2 and Figure 5.4. The analytical procedure overestimated the strength for all of the specimens. The analytical results were multiplied by the strength reduction factor (φ) of 0.9 and the errors using the factored analytical results were presented in tables 4.1 and 4.2. The error in the strength prediction increased as the number of FRP layers increased. However, the error decreased as the steel tube D/t ratio increased.

Table 4.1: Summary of the tested large scale columns' results versus simplified analytical method

Column	$M_{capacity}$		Percentage of error*	Percentage of error considering φ factor*
	EXP.	Analytical		
	kip-ft	kip-ft		
F4-24-E324	540.0	604.8	12.0	0.8
F4-24-P124	551.7	586.4	6.3	4.3
F4-24-E344	874.5	1,025.2	17.2	5.5

*The percentage of the absolute value of the difference between the experimental and the analytical ultimate moments divided by the experimental ultimate moment

Table 4.2: Summary of Ozbakkaloglu and Idris (2014) experimental results versus simplified analytical method

Column	$M_{capacity}$		Percentage of error*	Percentage of error considering φ factor*
	EXP.	Analytical		
	kip-ft	kip-ft		
DST-1	26.9	27.1	0.5	9.5
DST-2	21.1	23.5	11.5	0.4
DST-3	24.0	24.7	2.8	7.5
DST-5	30.0	31.2	3.9	6.5
DST-6	31.0	31.4	1.4	8.7
DST-7	29.3	34.9	19.4	7.5
DST-9	30.3	35.6	17.6	5.8

*The percentage of the absolute value of the difference between the experimental and the analytical ultimate moments divided by the experimental ultimate moment

4.2 Shear guidelines

This section presents the shear strength of the HC-FCS columns depending on the steel tube only until further investigation would be conducted to identify the contribution of the other column's aspects. The shear strength of the steel tube could be determined according to American Institute of Steel Construction (AISC) manual as follows:

a- Compute the critical stress "F_{cr}" as the larger of Equations 4.16 and 4.17

$$F_{cr} = \frac{1.6\,E}{\sqrt{\frac{L_v}{D_i}}\left(\frac{D_i}{t_s}\right)^{1.25}} \leq 0.6\,F_y \tag{4.16}$$

$$F_{cr} = \frac{0.78\,E}{\left(\frac{D_i}{t_s}\right)^{1.5}} \leq 0.6\,F_y \tag{4.17}$$

Where E = Young's modulus of steel = 29,000 ksi, L_v = half the span of the steel tube, F_y = the yield stress of the steel tube, D_i = the outer diameter of the steel tube, and t_s = the steel tube thickness

b- Compute the shear capacity of the steel tube "V_n" using Equation 4.18

$$V_n = \frac{1}{2} (\pi D_i t_s) F_{cr} \quad (4.18)$$

c- Check the shear capacity comparable to the factored shear demand "V_u" using Equation 4.19

$$0.9 V_n \geq V_u \quad (4.19)$$

5. FINITE ELEMENT MODELING

This chapter describes the finite element modeling of HC-FCS's behavior under a constant axial compression load and lateral pushover. The LS-DYNA software was used to design and verify the models against the experimental results gathered from seven HC-FCS columns tested by Ozbakkaloglu and Idris (2014). These columns had a concrete compressive strength (f'_c) that was between 13,775 psi and 18,850 psi. Either aramid (AFRP) or carbon (CFRP) was used to manufacture the FRP tubes (see Table 5.1). The columns were tested under axial loads (P) between 92.2 kips and 155.1 kips. These loads were corresponding to 0.34 to 0.45 of the columns nominal axial capacity (P_o) where P_o was calculated by eqn. (2.1).

Table 5.1: Summary of columns variables (reproduced after Ozbakkaloglu and Idris 2014)

Column	f'_c	FRP tube		Inner steel tube	P	P/P_o
	(psi)	Material	n*	t (inch)	(kips)	
DST-1	13,775	AFRP	3	0.126	122.5	0.45
DST-2	13,775	AFRP	2	0.126	92.2	0.34
DST-3	13,775	AFRP	3	0.126	92.2	0.34
DST-5	16,675	AFRP	4	0.126	140.5	0.45
DST-6	16,675	CFRP	5	0.126	140.5	0.45
DST-7	13,775	AFRP	3	0.217	151.7	0.45
DST-9	18,850	AFRP	6	0.126	155.1	0.45

*n: number of FRP layers

These models were next used to conduct a parametric study investigating the effects of the applied axial load level, concrete strength, concrete wall thickness, the steel tube's diameter-to-

thickness ratio (D/t), and the number of FRP layers on the HC-FCS column's behavior. Analytical models will be presented later in Chapter 4 to predict the column's flexural strength.

5.1 Model description

5.1.1 Geometry

The columns under consideration in this study were tested as free cantilevers under both a constant axial compression load and cyclic lateral loading. The tested columns were symmetrical about the vertical plane. Thus half of each column was modeled and analyzed in LS-DYNA (Figs. 5.1 and 5.2). Each column had a circular cross-section with an outer diameter of 5.90 inch and an inner diameter of 3.50 inch. The column's height (measured from the top of the footing to the top of the column) was 47.25 inch; the lateral load (measured from the top of the column's footing) was applied at a height of 39.37 inch. A steel tube was extended inside the footing while the FRP tube was stopped at the top of the footing. The FRP tube of specimen DST-2 stopped at 0.79 inch above the top of the footing. The specimens did not include any flexural reinforcement except the steel tubes. Each FE model had 5,248 elements and 6,840 nodes. A sensitivity analysis was conducted before the final form of the finite element model to optimize the elements' sizes achieving an acceptable accuracy.

Each column's concrete core was modeled by solid elements. These elements had a height of 0.98 inch. Both the outer FRP tube and the inner steel tube were simulated by shell elements. A typical element height for the FRP tube was 0.98 inch; each steel tube was 0.98 inch x 0.34 inch. A rigid cylinder, modeled by solid elements, was placed on top of the concrete column to apply the axial load. Each column was supported on a concrete footing, which was also modeled by solid elements. All solid elements were modeled with constant-stress and one-point quadrature integration to reduce the computational time. Hourglass control was used to avoid spurious singular modes for solid elements. The hourglass value for all models was taken as the default value of 0.10.

Contact elements surface-to-surface were used to simulate the interface between the concrete column and the FRP tube. They were also used between the concrete column and the steel tube. This type of contact considers slip and separation that occurs between master and slave contact pairs. Hence, slip/debonding will be displayed if either occurs between the concrete wall's surface and the tube's surface. This type of contact was used between the concrete footing and the steel tube.

Node-to-surface contact elements were used between the loading stub and the concrete wall, the FRP tube, and the steel tube. Similarly, this contact type was used to simulate the contact between the concrete wall and the FRP tube to the footing. The coefficient of friction for all of the contact elements was taken as 0.6.

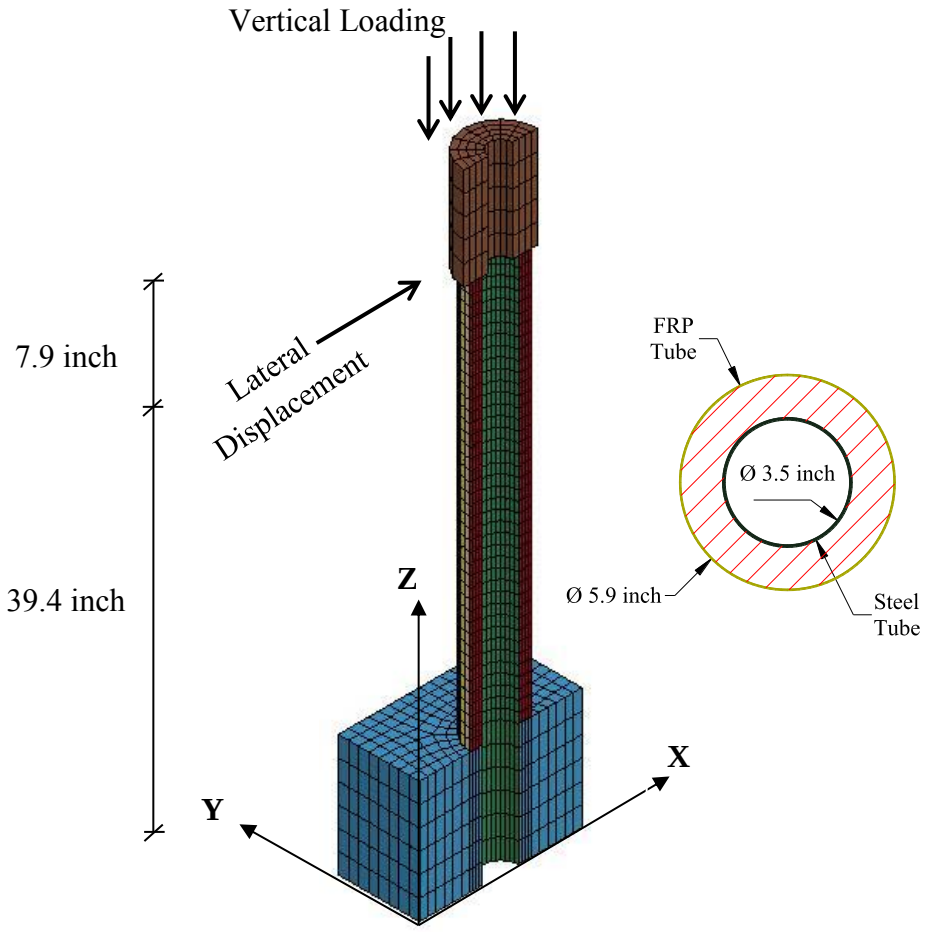

Figure 5.1: 3D view of simulated HC-FCS column

5.1.2 Material models

a. Concrete

Different material models are available in LS-DYNA to simulate concrete materials. The Karagozian and Case Concrete Damage Model Release 3 (K&C model) was used in this study because it exhibited good agreement with the experimental results gathered in previous studies

(Ryu et al. 2014). This model, developed from the theory of plasticity, has three shear failure surfaces: yield, maximum, and residual (Malvar et al. 1997).

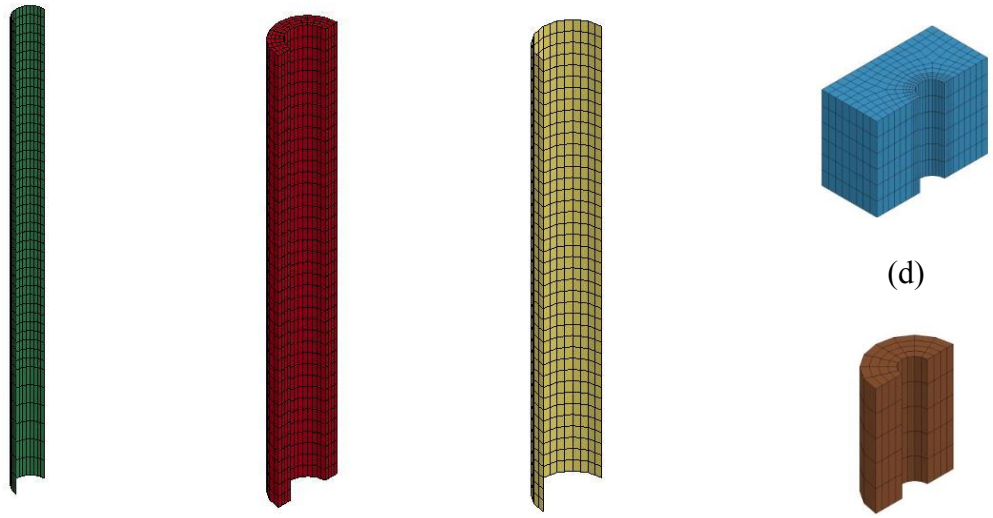

(a) (b) (c) (d) (e)

Figure 5.2: model components: (a) Steel tube, (b) Concrete column, (c) FRP tube, (d) Concrete footing, and (e) Loading stub

This study used the automatic generation option for the failure surface, where f_c' was the main input to the model. Another input to the model, the fractional dilation parameter (ω), considers any volumetric change in concrete. The fractional dilation parameter was taken as the default value of 0.50. The equation of state (EOS), which controls the compressive behavior of the concrete under triaxial stresses, was automatically generated, given f_c' and ω.

b. FRP tube

The FRP material used was modeled as an orthotropic material using "002-orthotropic_elastic" material. Such material model uses total Lagrangian-based to model the elastic-orthotropic behavior of solids, shells, and thick shells. This material is defined by several engineering constants: elastic modulus (E), shear modulus (G), and Poisson's ratio (PR), in the three principle axes (a, b and c). The fiber orientation is defined by a vector. Table 5.2 is a summary of FRP's properties. The following characteristics, based on Ozbakkaloglu and Idris (2014) were implemented in the FE. The elastic moduli of the AFRP and CFRP tubes in the hoop directions (E_a) were 18,226 ksi and 36,404 ksi, respectively. The ultimate tensile strain of the AFRP and CFRP

tubes in the hoop directions was 0.0212 and 0.0144, respectively. The major Poisson's ratio was 0.25. The shear moduli of the AFRP and CFRP tubes in the transverse directions (G_{ab}) was 1,341 ksi and 1,392 ksi, respectively. The failure criterion for the FRP, defined as "000-add_erosion," was assigned the ultimate strain of FRP in "EFFEPS" card.

Table 5.2: Summary of orthotropic material properties for FRP tubes

Material properties	AFRP tube	CFRP tube
Elastic modulus in the hoop direction (Ea; ksi)	18,226	36,404
Ultimate tensile hoop strain	0.0212	0.0144
Shear modulus (Gab; ksi)	1,341	1,392
Poisson's ratio (PR)	0.25	0.25

c. Steel tube

The material model "003-plastic_kinamatic" was used to identify the steel tube's elasto-plastic stress-strain curve. Three parameters were needed to define this material model according to the material's properties: the elastic modulus (E), the yield stress (SIGY), and Poisson's ratio (PR). The elastic modulus and the yield stress were 29,725 ksi and 50,750 psi, respectively, for all columns except DST-7. A different steel tube with a different thickness was used in this column. Thus, its elastic modulus and yield stress were different: 29,906 ksi and 59,813 psi, respectively.

5.1.3 Boundary conditions and loading

Displacement in the Y direction and rotations about both the X and Z axes at the plane of symmetry were restrained. Displacements and rotations in all directions at the nodes of the footing's bottom were prevented.

The loading was applied in two different steps. An axial compressive load was applied to the top of the loading stub during the first step. These loads were half of those listed in Table 5.1 due to symmetry. During the second step, lateral displacement was applied at the middle nodes of the common surface, between the column and the loading stub, until failure occurred due to rupture of the FRP tube or compression failure.

5.2 Results and discussions

The lateral drift of each of the tested large scale columns was obtained by dividing the lateral displacement, measured at 95 inch above the footing top, by 95 inch. The moment at the base of the column was also obtained from FE analysis; the sum of the reactions at the footing level was multiplied by a column height of 95 inch. The moment versus drift of the tested large scale columns (obtained from FE analyses) is plotted in Fig. 5.3. This figure also depicts the experimental drift versus the moment for each column. Table 5.3 includes a summary of the finite element results versus the experimental results for all columns. This table also includes the error in predicting the ultimate moment of each test specimen. This error was calculated as the absolute value of the difference between the experimental and the FE ultimate moments divided by the experimental ultimate moment. The error was between 9.5% and 25.1%. All simulated columns behaved in a manner similar to the tested columns up to failure.

The lateral drift of each of Ozbakkaloglu's columns was obtained by dividing the lateral displacement, measured at 39.37 inch above the footing top, by 39.37 inch. The moment at the base of the column was also obtained from FE analysis; the sum of the reactions at the footing time was multiplied by a column height of 39.37 inch. The moment versus drift (obtained from FE analyses) is plotted in Fig. 5.4. This figure also depicts the experimental drift versus the moment for each column. Table 5.4 includes a summary of the finite element results versus the experimental results for all columns. This table also includes the error in predicting the ultimate moment of each test specimen. This error was calculated as the absolute value of the difference between the experimental and the FE ultimate moments divided by the experimental ultimate moment. The error was between 1.3% and 8.9%. All simulated columns behaved in a manner similar to the tested columns up to failure.

Overall, the FE models were able to capture the test specimen's behavior (Fig. 5.4). Column DST-1 reached peak bending strengths of 26.9 kip-ft and 24.9 kip-ft during the experimental work and the FE analysis, respectively (Fig. 5.4a). The difference between the experimental strength and the FE strength was 7.4%. The column reached its peak strength at drifts of 5.8% and 5.7% during the experimental and FE analysis, respectively. However, during the experimental work and beyond a drift of 6.0%, the column failed abruptly when the FRP tube ruptured. This column failed by compression failure during the FE analysis at a lateral drift of 8.9%.

The FE predicted the initial stiffness until a drift of 1.0% (see Fig. 5.4a). At that drift, both the experimental and the FE analysis revealed a significant nonlinear behavior up to failure. The FE analysis revealed that the nonlinear behavior began when the concrete column began to uplift at the footing level. This connection had no continued reinforcement and, therefore, had no tensile strength. Thus, at some point during flexural loading, the connection between the column and the footing uplifted at the tension side. As a result, the contact area of the column with the footing reduced nonlinearly as the neutral axis shifted toward the compression zone (Fig. 5.5). As the neutral axis continued to shift, the compression in the concrete increased caused the concrete volumetric dilation to increase. This increase, in turn, increased the strain in the FRP tube.

Table 5.3: Summary of the tested large scale columns' results vs. finite element results

Column	$M_{capacity}$ (kip-ft)		Percentage of error*
	EXP.	FE	
F4-24-E324	540.0	488.2	9.6
F4-24-P124	551.7	412.9	25.2
F4-24-E344	874.5	713.3	18.4

*The percentage of the absolute value of the difference between the experimental and the FE ultimate moments divided by the experimental ultimate moment

Table 5.4: Summary of Ozbakkaloglu and Idris (2014) experimental results vs. finite element results

Column	$M_{capacity}$ (kip-ft)		Percentage of error*	Mode of failure	
	EXP.	FE		EXP.	FE
DST-1	26.9	24.9	7.4	FRP rupture	Compression failure
DST-2	21.1	22.7	7.6	FRP rupture	FRP rupture
DST-3	24.0	23.7	1.3	FRP rupture	FRP rupture
DST-5	30.0	28.8	4.0	FRP rupture	Compression failure
DST-6	31.0	29.2	5.8	FRP rupture	Compression failure
DST-7	29.3	31.9	8.9	FRP rupture	FRP rupture
DST-9	30.3	32.3	6.6	N/A*	Compression failure

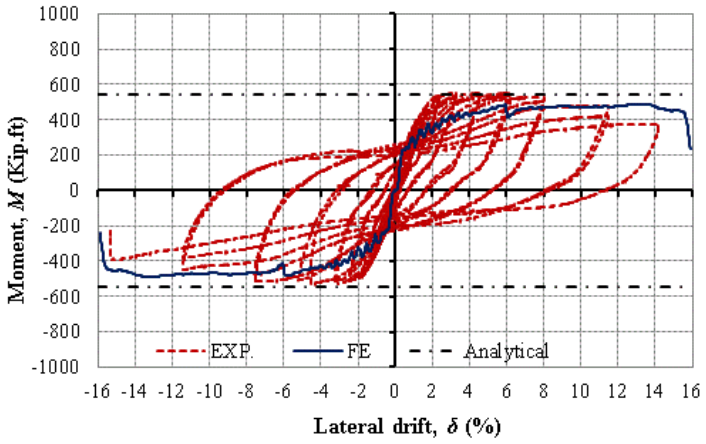

(a)

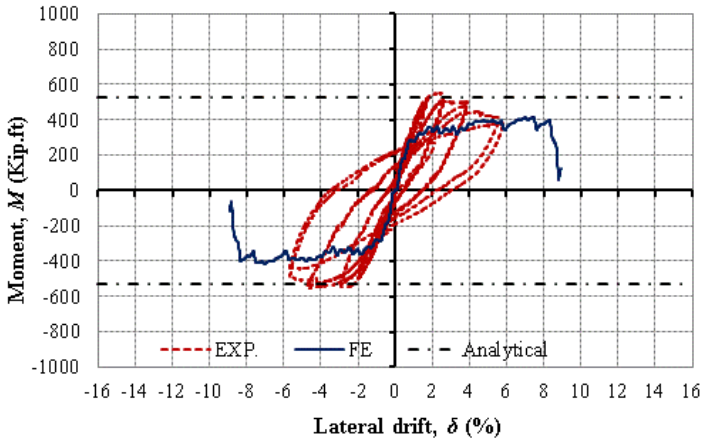

(b)

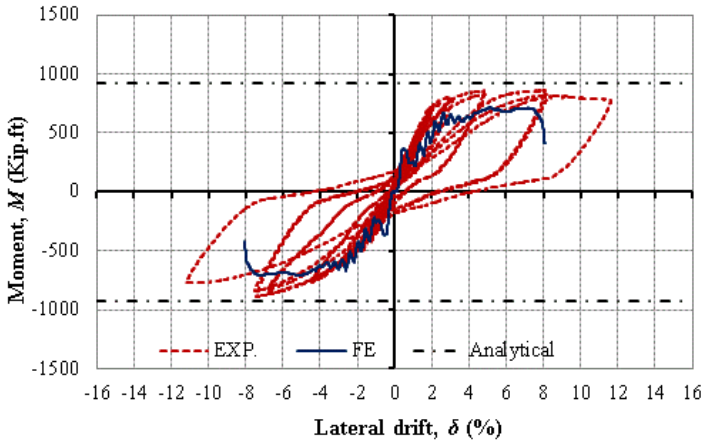

(c)

Figure 5.3: Experimental hysteretic vs. FE backbone curves and analytical results for the HC-FCS large scale columns: (a) F4-24-E324 column, (b) F4-24-P124 column, and (c) F4-24-E344 column

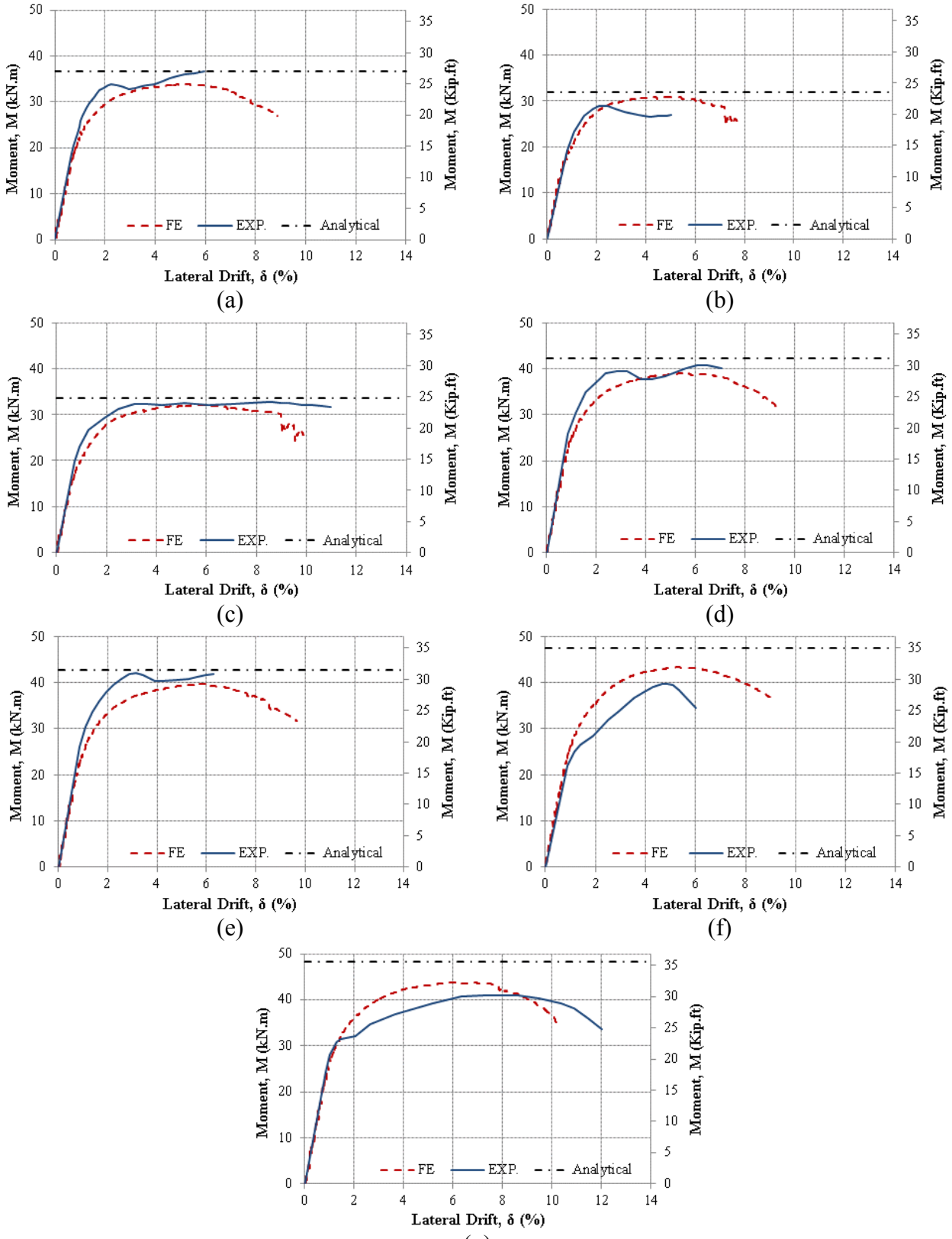

Figure 5.4: Experimental (Ozbakkaloglu and Idris 2014 ©ASCE) vs. FE backbone curves for specimens: (a) DST-1, (b) DST-2, (c) DST-3, (d) DST-5, (e) DST-6, (f) DST-7, (g) DST-9

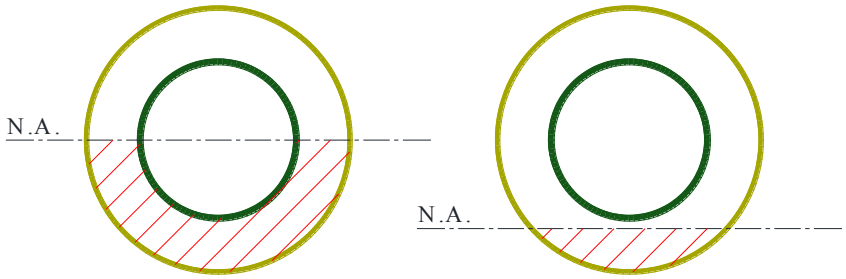

Figure 5.5: Moving of neutral axis (N.A.) under lateral loading (hatched area is the compression side)

The FE analysis revealed a confined concrete compressive strength (f'_{cc}) of 25,810 psi just before failure (Fig. 5.6). This value indicates that the concrete's strength increased 87%, signaling good confinement. Yu et al. (2010) developed a confinement model for HC-FCS. For the given cross-section, this model predicted an f'_{cc} that was equal to 23,235 psi, a value close to the f'_{cc} observed during the FE analysis.

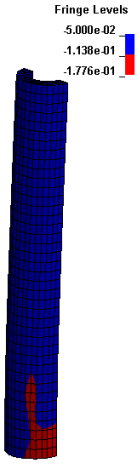

Figure 5.6: Maximum confined concrete stress of the column DST-1 in GPa. (1 GPa = 145 ksi)

The strain profile of the FRP tube at the bottom 17.7 inch of column DS-1 was obtained from the FE analysis and is compared with the experimental profile at a lateral drift of 5.0% (Fig. 5.7). Three strain profiles taken from the FE are plotted in Fig. 5.7. These profiles represent the peak, average, and minimum strains, respectively. The average profile of the strains obtained from the FE is close to those obtained during the experimental work. Both the FE and the experimental work revealed a strain concentration at the bottom 1.97 inch.

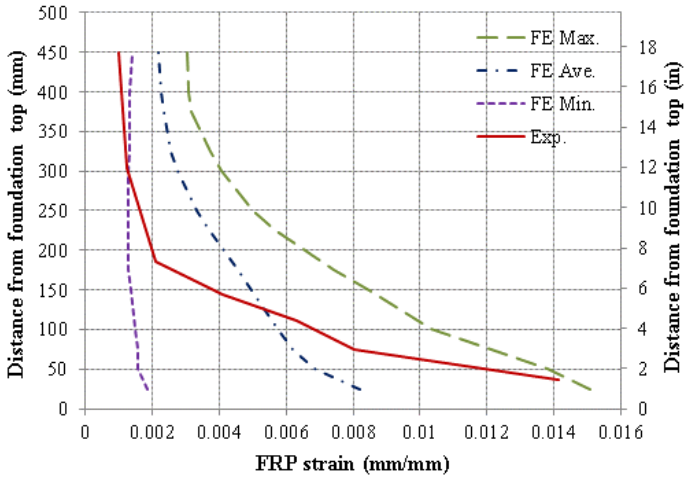

Figure 5.7: FE vs. experimental (Ozbakkaloglu and Idris 2014 ©ASCE) strain profile of the FRP tube of column DST-1

Column DST-2 reached a bending strength of 21.1 kip-ft and a lateral drift of 5.0% during the experimental work (Fig. 5.4b); it reached a bending strength of 22.7 kip-ft and a drift of 7.8% during the FE analysis. This represents an error of 7.6% in predicting the bending strength. During the experimental work, strength degradation occurred after a 2% lateral drift. This degradation was the result of a 0.8 inch gap that was present between the FRP tube and the footing during the experimental work. Hence, a slight difference occurred in the behavior between the FE results and the experimental results after 2.0% lateral drift. The FE model demonstrated both a higher moment capacity and a higher lateral drift. This column failed by FRP rupture in both the experimental and the FE studies.

Column DST-3 reached bending strengths of 24.0 kip-ft and 23.7 kip-ft during the experimental work and the FE analysis (Fig. 5.4c), respectively. These values correspond to an error of 1.3%. Both the FE and the experimental analysis revealed that failure occurred when the FRP ruptured. The FE analysis predicted the column's behavior accurately up to a drift of 9.0%. Beyond that level, the FE analysis exhibited slow strength degradation while the experimental work presented a nearly constant strength. Degradation in the bending strength during FE analysis occurred as a result of local buckling in the steel tube.

Columns DST-5 and DST-6 failed during the experimental work at bending strengths of 30.0 kip-ft and 31.0 kip-ft, respectively (Figs. 5.4(d) and 5.4(e)). The FE analyses of both columns predicted peak bending loads of 28.8 kip-ft and 29.2 kip-ft, respectively. This corresponds to errors

of 4.0% and 5.8% for the columns DST-5 and DST-6, respectively. However, while the experimental work showed that these columns failed at drifts of 6.0% and 7.0% for DST-5 and DST-6, respectively, the FE analyses showed that these columns failed at drifts of 9.4% and 9.7%. Both columns failed numerically as a result of compression failure at a confined concrete strength of 26,100 psi.

During FE analysis, local buckling in the steel tube occurred at a lateral drift of 5.7%. Hence, the concrete stresses increased considerably because of the significant reduction in the participation of the steel tube to bending resistance. The experimental work revealed a strength reduction, likely due to steel buckling, at a drift of 5.0%. The FRP also ruptured, however, after the steel buckled.

Column DST-7 reached a bending strength of 29.3 kip-ft during the experimental work. The FE analysis results were in close agreement with the experimental results; the column reached a bending strength of 31.9 kip-ft (Fig. 5.4f), corresponding to an error of 8.9%. The FE analysis and the experimental work revealed stiffness degradation at a lateral drift of 5.0% and 5.5%, respectively. Moreover, the post-elastic stiffness of column DST-7 was significantly higher than that of all other specimens. This column was displaced laterally up to 6.0% experimentally and up to 9.0% numerically. The FRP rupture occurred experimentally within the first 4.0 inch from the footing's top. The FE model simulated this behavior very well, as illustrated in Fig. 5.8. The FRP failed more gradually, however, during the numerical analysis. Both the FE and the experimental work revealed significantly higher post-elastic due to the thicker steel tube and higher yield stress.

Column DST-9 reached bending strengths of 30.3 kip-ft and 32.3 kip-ft during the experimental and FE analysis, respectively, (see Fig. 5.4g) corresponding to an error of 6.6%. The FE analysis predicted the column's behavior accurately up to failure. The column failed experimentally at a 12.0% lateral drift without any visible fiber rupture. It could not, however, endure more applied lateral load. Likewise, the column failed numerically because of the concrete strength degradation, up to compression failure, without fiber rupture, at a lateral drift of 10.2%. The FE analysis revealed that the maximum confined concrete strength for this column was 32,625 psi with an increase in the unconfined concrete strength of 73.0%.

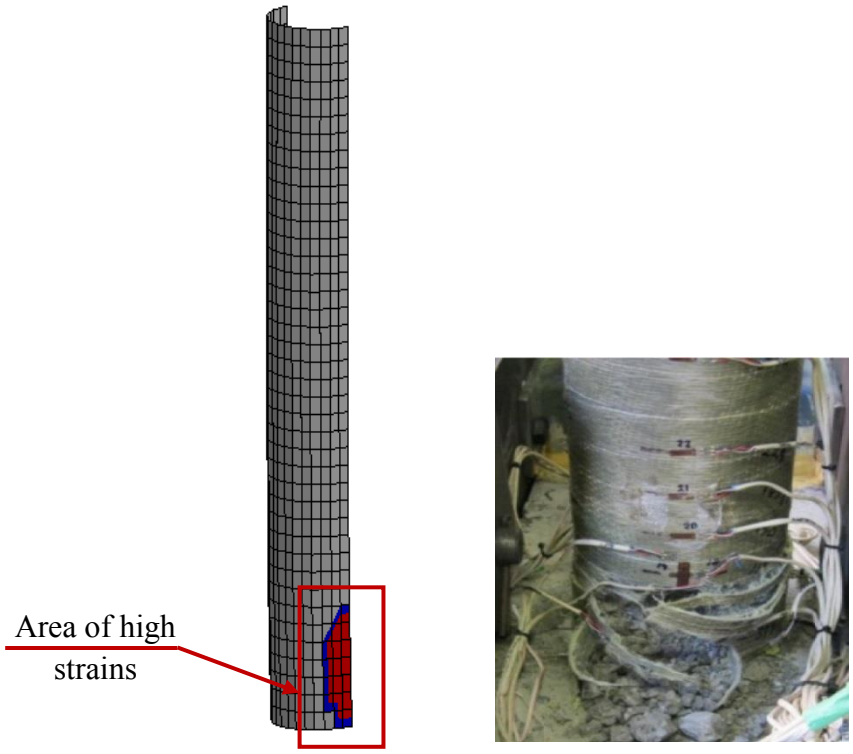

(a) (b)

Figure 5.8: Fiber rupture of FRP tube of the column DST-7; (a) FE result and (b) Experimental result (Ozbakkaloglu and Idris 2014 ©ASCE)

5.3 Parametric study

The HC-FCS column is a new system that has only recently been investigated. The FE models developed in this work were used to examine the effects of the applied axial load level, concrete wall thickness, and unconfined concrete nominal compressive strength (f_c'). They were also used to study both the diameter-to-thickness of the steel tube (D/t) as well as the number of FRP layers on the HC-FCS column's strength, ultimate drift, and mode of failure. The FE model of column DST-1 was used as the reference for this parametric study. Each parameter was studied independently, resulting in an analysis of 36 columns. The results from this study provided an in-depth understanding of HC-FCS's behavior under combined vertical and lateral loadings.

The columns' overall behavior was as follows. Steel tubes yielded under tension and compression. This yielding was followed by an onset of local buckling at the section just above the concrete footing. Two modes of failure were observed; both modes were triggered by local buckling of the steel. This buckling led to stiffness degradation of the steel tube, placing higher compression demands on the concrete.

The first mode of failure displayed by columns with a higher FRP confinement ratio, defined as the ratio of the ultimate FRP confining pressure normalized by f_c'; the onset of local steel buckling was followed by a propagation of local buckling leading to excessive compressive load demand on concrete and gradual failure of the system due to steel/concrete failure. This mode of failure is referred to here as compression failure. The second mode of failure displayed by columns having lower confinement ratio, the onset of the local buckling placed higher compression and dilation demands on the concrete where the FRP can't effectively confine the concrete leading to abrupt rupture of the FRP. This mode of failure is referred to here as FRP failure. A specimen was identified as having failed when either the specimen's lateral resistance dropped by 20% of its peak strength or the FRP ruptured, whichever occurred first.

Table 5.5 includes summary of the parametric study results collected. The backbone curves and the change in bending strengths of the investigated columns are presented in Figs. 5.9 and 5.10, respectively. Different limit states are given in Fig. 5.9. These states include the onset of compression and tension yielding in the steel tube, the presence of local buckling in the steel tube, and FRP rupture if occurred. The ultimate lateral drift (δ) for each column is also presented in Figs. 5.9 and 5.10.

5.3.1 Effects of axial load level on the behavior of HC-FCS

The behavior of four columns, namely, DST-1, DST-2A, DST-3A, and DST-4A were studied with different values of applied axial load levels of 45%, 30%, 15% and 7.5% of Po, respectively, where P_o was defined by equation 1. As shown in Figs. 5.9(a), 5.10(a) and Table 5.5, the effects of the axial load on the nominal moment capacity, ultimate drifts, and modes of failure were substantial with the nominal bending strength increased with increasing the applied axial load level. Decreasing the applied axial load level by 83% i.e., from 45%P_o to 7.5% P_o decreased the bending strength by 39% i.e., from 33.8 kN.m (24.9 kip-ft) for the DST-1 to 20.7 kN.m (15.2 kip-ft) for the DST-4A. This behavior resembled the behavior of conventional reinforced concrete short columns under the combined effect of small applied axial load and large bending moment where increasing the applied axial load would increase the moment capacity of the column.

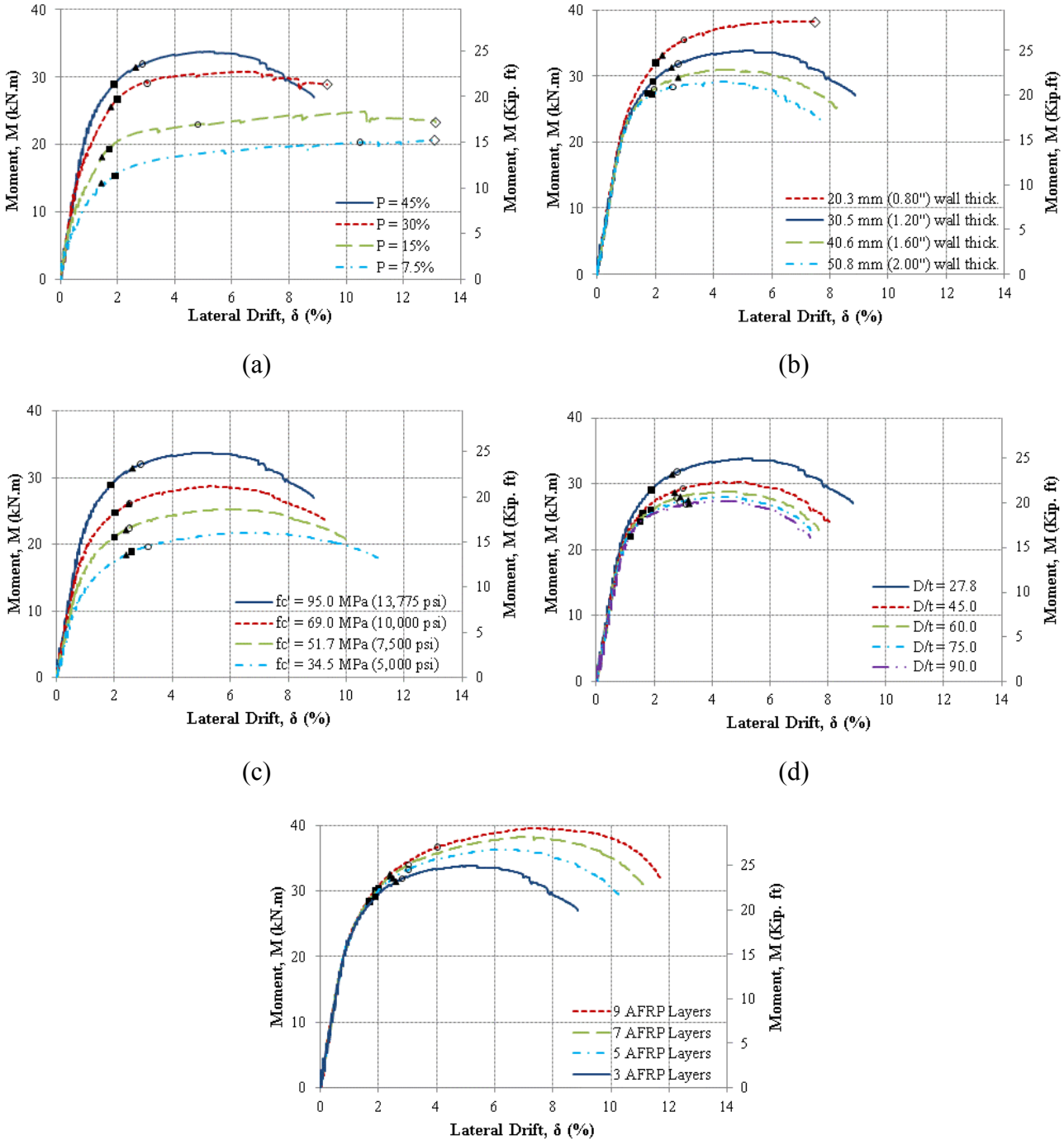

Figure 5.9: Lateral drift vs. Moment for finite element parametric study: (a) Load level change, (b) Concrete wall thickness change, (c) Concrete strength change, (d) D/t for steel tube change, (e) Number of FRP layers change

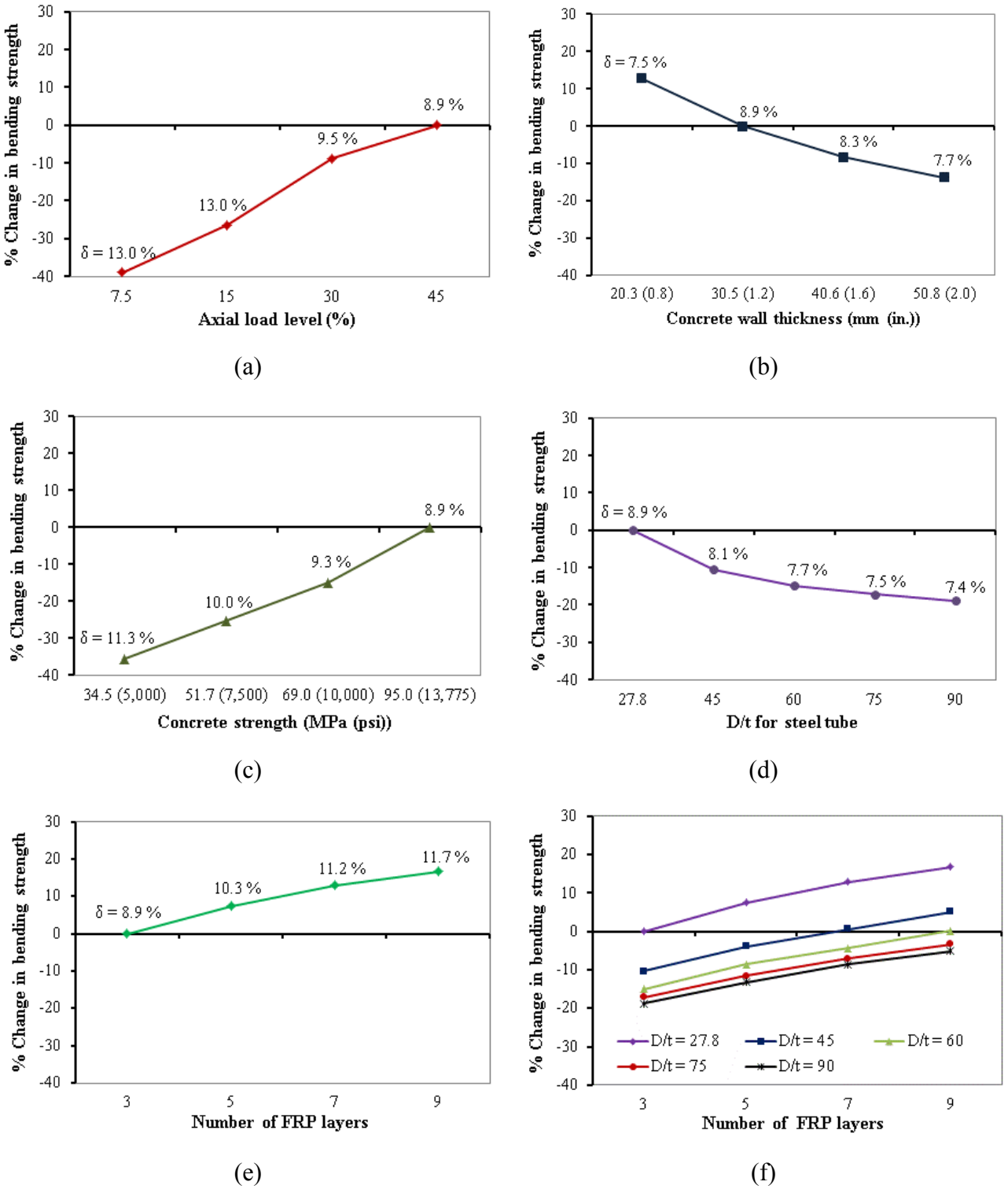

Figure 5.10: % change of the bending strength and the maximum lateral drift versus; (a) Loading level, (b) Concrete wall thickness, (c) Concrete strength, (d) D/t for steel tube, (e) Number of FRP layers, (f) Number of FRP layers with different steel tube D/t

Table 5.5: Summary of the parametric study results

Group	Model name	Description		FE results		Analytical results
				$M_{capacity}$	Lateral drift	$M_{capacity}$
				kip-ft		kip-ft
A	DST-1	Load Level	45.0% P_o	24.9	8.9	27.1
	DST-2A		30.0% P_o	22.7	9.5	23.9
	DST-3A		15.0% P_o	18.4	13.0	19.2
	DST-4A		7.5% P_o	15.2	13.0	16.3
B	DST-1	Wall thick	1.2 inch	24.9	8.9	27.1
	DST-2B		0.8 inch	28.1	7.5	29.3
	DST-3B		1.6 inch	22.9	8.3	24.8
	DST-4B		2.0 inch	21.5	7.7	23.2
C	DST-1	f_c'	13,775 psi	24.9	8.9	27.1
	DST-2C		10,000 psi	21.2	9.3	23.3
	DST-3C		7,500 psi	18.6	10.0	20.5
	DST-4C		5,000 psi	16.0	11.3	18.3
D	DST-1	$\frac{D}{t}$	27.8	24.9	8.9	27.1
	DST-2D		45.0	22.3	8.1	23.6
	DST-3D		60.0	21.3	7.7	22.0
	DST-4D		75.0	20.7	7.5	20.9
	DST-5D		90.0	20.2	7.4	20.3
E	DST-1	Number of FRP layers	3	24.9	8.9	27.1
	DST-2E		5	26.8	10.3	29.8
	DST-3E		7	28.2	11.2	31.7
	DST-4E		9	29.1	11.7	33.1

These specimens failed in two distinct failure modes. Column DST-1 failed as a result of compression failure when an axial load of 45% P_o was applied while the other columns failed as a result of FRP failure. As explained earlier, local buckling of the steel tubes triggered failures of the columns. Expectedly, the higher the applied axial is the smaller drift at local buckling. Columns that had been subjected to axial loads of 15% P_o or higher locally buckled at drifts of 3% to 5%; the steel tube in column DST-4A locally buckled at a drift of 10.6%. After local buckling occurred, it propagated leading to a gradual degradation in concrete confinement and, ultimately, failure of the columns. This propagation of the local buckling was relatively quick in columns that had higher levels of applied axial loads (i.e., 30% P_o and 45% P_o). Excessive local buckling placed higher compressive stress demands on the concrete while the steel tube was not able to effectively confine the concrete leading to gradual concrete crushing at smaller drifts. For example, the concrete in column DST-1sustained an axial compressive stress of 187% f_c'. Degradation in concrete stresses occurred beyond that point.

Columns that were subjected to low axial loads (i.e., DST-4A) experienced a delay in local buckling, allowing the concrete to remain effectively confined and the concrete sustained axial compressive stress of 240% f_c'. These high stresses led to excessive dilation demands on the FRP and, ultimately, abrupt FRP rupture. As shown in Figs. 5.9(a) and 5.10(a), the lateral drift capacity significantly increased as the applied axial load level decreased. Moreover, the backbone curves reflect the differences in the modes of failure. Compression failure occurred quite gradually. Thus, the backbone curve displayed a post-peak descending branch while the FRP failure displayed abrupt termination of the backbone curves.

The applied axial load level also had a significant effect on the initiation of the nonlinear behavior, tensile yielding of the tubes, and stiffness degradation. Nonlinear behavior initiated when uplift began on the tension side of the footing-column connection (Fig. 5.11). Thus, for columns subjected to lower level of applied axial load, the interface joint opened early leading to early stiffness degradation and early yielding of the steel tubes. The steel tubes in this group exhibited tensile yielding at drifts between 1.4% and 2.6%. Expectedly, the higher the applied axial load is the higher drift at tensile yielding of the tube.

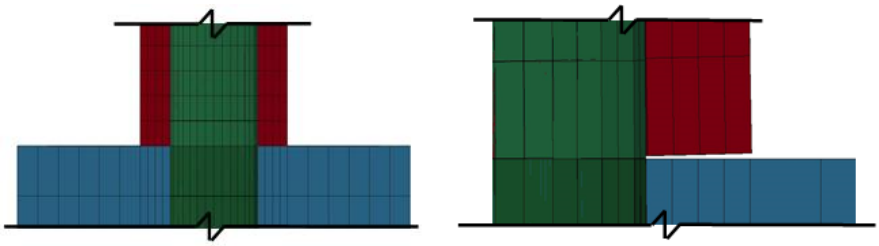

(a) (b)

Figure 5.11: Column-footing connection (a) closed connection, (b) uplift of the heel of the connection

5.3.2 Effects of concrete wall thickness on the behavior of HC-FCS

Four columns, namely, DST-1, DST-2B, DST-3B, and DST-4B were studied with different concrete wall thicknesses of 1.2 inch, 0.8 inch, 1.6 inch, and 2.0 inch, respectively. As shown in Figs. 5.9(b) and 5.10(b) as well as table 5.5, as the concrete wall thickness decreased, the column strength increased. Decreasing the concrete wall thickness by 60% i.e., from 2.0 inch to 0.8 inch increased the bending strength 30% i.e., from 21.5 kip-ft in column DST-4B to 29.8 kip-ft in column DST-2B.

The increase in the strength of columns having smaller wall thickness occurred since the lever arm between the tensile forces in the steel tube and the compression forces in concrete and steel tube increased with decreasing the concrete wall thickness. Moreover, since all columns have the same FRP and steel rigidities, confinement of columns having smaller concrete wall thickness was relatively higher. The concrete in the case of column DST-2B sustained compressive stresses up to 25,382 psi while the concrete in columns DST-3B and DST-4B sustained peak stresses of 24,366 psi and 23,351 psi, respectively.

Local buckling occurred at drifts of 2% to 3%. Columns with a thicker concrete wall thickness locally buckled at higher drifts since the initial axial stresses on the steel tubes due to the applied axial load will be smaller on columns having thicker concrete wall. Moreover, for columns having thicker concrete walls (DST-3B and DST-4B), the confinement was not as effective as the columns having thinner concrete walls. Hence, for columns DST-3B and DST-4B, concrete reached their peak stresses at smaller drifts of 3% to 5% when the columns began to approach their peak strengths. This was followed by concrete strength gradual degradation and the local buckling in the steel tubes propagated rapidly leading to compression failure in the columns. Column that had a

smaller concrete wall thickness (i.e., column DST-2B) were more confined, leading to the gradual propagation of local steel buckling. Hence, the concrete sustained higher stresses and placed higher dilation demand on the FRP, causing the FRP to rupture.

It is worth noting that the steel tubes in all of the specimens, except specimen DST-4B, yielded in tension. The steel tube in specimen DST-4B had the thickest concrete wall was the only tube in the specimens presented in this manuscript that did not reach tensile yielding.

5.3.3 Effects of column concrete strength (f'_c) on the behavior of HC-FCS

Four columns, namely, DST-1, DST-2C, DST-3C, and DST-4C were studied with different concrete compressive strengths (f'_c) of 13,775 psi, 10,000 psi, 7,500 psi, and 5,000 psi, respectively. As shown in Figs. 5.9(c) and 5.10(c) as well as table 5.5, by increasing the concrete compressive strength, the bending strength increased while the lateral drift decreased. Increasing the concrete compressive strength by 175% i.e. from 5,000 psi to 13,775 psi increased the bending strength by 56% i.e. from 16.0 kip-ft for column DST-4C to 24.9 kip-ft for column DST-1 and the maximum lateral drift decreased from 11.3% for column DST-4C to 8.9% for column DST-1.

The concrete's compressive strength had an insignificant effect on the onset of steel tube local buckling. All tubes locally buckled at drifts of 2.5% to 3.0%. However, once locally buckled the rate of strength degradation in the compression steel in the columns that have lower values of f'_c was slightly slower than those having higher values of f'_c. This occurred since for a given number of FRP layers, the lower the concrete compressive strength is the highest confinement effectiveness and ductility.

Expectedly, the concrete in column DST-4C, which had a f'_c of 5,000 psi, sustained compressive stress up to 248% f'_c at a drift of approximately 6.1%, while the concrete in column DST-1, which had a f'_c of 13,775 psi, sustained compressive stress up to 187% f'_c at a drift of 5%. Beyond these drifts, the columns strengths decreased gradually due to compression failure.

5.3.4 Effects of D/t ratio of the steel tube on the behavior of HC-FCS

Five columns, namely, DST-1, DST-2D, DST-3D, DST-4D, and DST-5D were studied with the diameter-to-thickness (D/t) of 27.8, 45.0, 60.0, 75.0 and 90.0, respectively. As shown in Figs. 5.9(d), and 5.10(d) as well as table 5.5, the bending strength decreased linearly and the drift decreased nonlinearly as the D/t increased. Increasing the D/t by 224% (i.e., from 27.8 to 90.0)

decreased the bending strength by 19% from 24.9 kip-ft to 20.2 kip-ft for columns DST-1 and DST-5D, respectively. Similarly, the drift decreased by 17% from 8.9% to 7.4% for columns DST-1 and DST-5D, respectively.

All of the columns in this group failed by compression failure. Similar to the other columns, local buckling occurred at drifts of 2.8% to 3.1% and tensile yielding at drifts of 2.6% to 3.2%. Local buckling propagated quite slowly for thicker steel tubes allowing their columns to display higher ultimate drifts than thinner steel tubes. Local buckling led to concrete crushing.

5.3.5 Effects of the number of FRP layers on the behavior of HC-FCS

Four columns, namely, DST-1, DST-2E, DST-3E, and DST-4E had 3, 5, 7, and 9 FRP layers, respectively. Expectedly, both the bending strength and the lateral drift increased as the number of layers increased as shown in Figs. 5.9(e) and 5.10(e) as well as Table 5.5. However, the increase in the lateral drift was more pronounced than the increase in the bending strength. Increasing the FRP layers by 200% (i.e., from 3 to 9 layers) increased the bending strength by 17% i.e., from 24.9 kip-ft to 29.1 kip-ft while increased the lateral drift by 31% i.e., from 8.9% to 11.7%. All of the specimens in this set failed due to compression failure.

Increasing the number of FRP layers increased the confined concrete strength and stiffness, which increased the concrete contribution to the lateral load resistance mechanism delaying the onset of the steel tube local buckling. For column DST-1 local buckling occurred at a drift of 2.8%; tripling the number of FRP layers in column DST-4E, the local buckling occurred at a drift of 4.0%. Moreover, while the concrete in column DST-1, which has 3 layers of FRP, sustained an axial stress up to 187% f_c', column DST-3E, which has 7 layers of FRP, sustained an axial stress up to 205% f_c'. Increasing the number of FRP layers to 9 layers did not improve the concrete confinement compared to the column having 7 layers since confinement does not depend exclusively on FRP rigidity but also on the steel rigidity. Since the steel rigidity was the same in this set of column, there seems that there is a threshold on FRP rigidity beyond which increasing FRP rigidity does not significantly improve the column behavior. Finally, local buckling in the steel tubes led to a gradual reduction in the steel tube compressive stresses leading to more axial load demand on the concrete in compression. For columns with low number of FRP layers, once local buckling occurred, concrete began to dilate more rapidly loosing the confinement effect. In the case

of DST-4E, beyond the initiation of local buckling concrete was still well-confined sustaining the high compressive stresses.

Table 5.6: Results summary of number of FRP layers versus steel tube D/t ratios

Group	Model name	Description		FE $M_{capacity}$	Analytical $M_{capacity}$
		Number of FRP layers	D/t	kip-ft	kip-ft
F	DST-1	3	27.8	24.9	27.1
	DST-2E	5		26.8	29.8
	DST-3E	7		28.2	31.7
	DST-4E	9		29.1	33.1
	DST-2D	3	45	22.3	23.6
	DST-2F	5		23.9	25.6
	DST-3F	7		25.1	27.0
	DST-4F	9		26.2	28.0
	DST-3D	3	60	21.3	22.0
	DST-5F	5		22.8	23.7
	DST-6F	7		23.9	24.9
	DST-7F	9		25.0	25.8
	DST-4D	3	75	20.7	20.9
	DST-8F	5		22.1	22.5
	DST-9F	7		23.2	23.6
	DST-10F	9		24.1	24.4
	DST-5D	3	90	20.2	20.3
	DST-11F	5		21.7	21.7
	DST-12F	7		22.8	22.7
	DST-13F	9		23.7	23.5

5.3.6 Effects of the number of FRP layers combined with D/t ratio

The number of FRP layers versus D/t ratios of the steel tubes was investigated last. Twenty columns were investigated numerically as stated in Table 5.6. Four different numbers of FRP layers of 3, 5, 7, and 9 were studied in a matrix with five steel tube D/t ratios of 27.8, 45.0, 60.0, 75.0, and 90.0. The bending strength increased as the number of layers increased regardless of the steel tube D/t ratio as presented in Fig. 5.10(f). However, the bending strength decreased as the steel tube D/t ratio increased for the same number of FRP layers. The relationship between the number of FRP layers and the bending strength was nearly linear, regardless of the steel tube D/t ratio. It is worthy noted that, for a given number of FRP layers, the rate of increase in the bending decrease with increasing D/t ratio.

6. ANALYSIS OF VEHICLE COLLISION WITH REINFORCED CONCRETE BRIDGE COLUMNS

6.1 Research significance

While several studies investigated the issue of vehicle impact with concrete columns, few studies investigated the effect of the different construction detailing and vehicle parameters on the performance of the column. This report used detailed finite element analyses to investigate the effects of 13 different parameters including the concrete material model, unconfined compressive strength (f_c'), material strain rate, percentage of longitudinal reinforcement, hoop reinforcement, column span-to-depth ratio, column diameter, the top boundary conditions, axial load level, vehicle velocity, vehicle mass, clear zone distance, and soil depth above the top of the column footing on the dynamic and static impact forces. Comparisons between the ESF of the AASHTO-LRFD 600 kips and the ESF calculated using different approaches are presented as well. Furthermore, the constant impact load used in AASHTO-LRFD does not consider the vehicle mass nor the velocity. Hence, it may be anticipated that the given impact load will be conservative in some occasions and unconservative in other occasions. This report presents a new equation to directly calculate the ESF given the vehicle's mass and velocity without the need to run crash analysis. Similarly, a simplified equation for the Eurocode equation is presented to directly calculate the ESF without a crash analysis.

6.2 Verifying the finite element modeling of a vehicle colliding with a bridge pier

Experiments conducted on vehicle collisions with concrete columns are both difficult and expensive. Finite element analysis (FEA) is considered an attractive approach because it is economical, reliable, and easy to implement. The FEA of a collision event requires a combination of vehicle and concrete structure modeling.

Bridge pier models similar to the one used by El-Tawil et al. (2005) was developed during the course of this study. The models were subjected to the impact loads similar to those used by El-Tawil et al. (2005). The results from El-Tawil et al. (2005) were used to verify the developed models. In these models, the bridge pier was 32.6 ft tall (see Figs. 6.1 and 6.2) and it was supported by a reinforced concrete pile cap that was 10.0 ft x 7.0 ft x 3.5 ft. The pile cap was supported by six prestressed piles that were 18 inch in diameter and 30 ft in length.

Fully integrated 8-node brick elements, with elastic material (mat. 001), were used to simulate the substructure (pier and pile cap). Beam_orientation-type truss elements (ELFORM_3) were used to model all of the reinforced bars. These elements shared nodes with the concrete elements. A Hughes-Liu beam element type (ELFORM_2) was used to simulate the pile so that the soil/structure interaction could be examined. The piles were supported by four discrete lateral spring elements. These elements were modeled by a spring inelastic material (mat. S08). This material provided a compression response only. Bowles' (1988) equations for soil's compressive stiffness were used to calculate the modulus of the subgrade's reaction to the soil. The springs were spaced 17.4 inch apart.

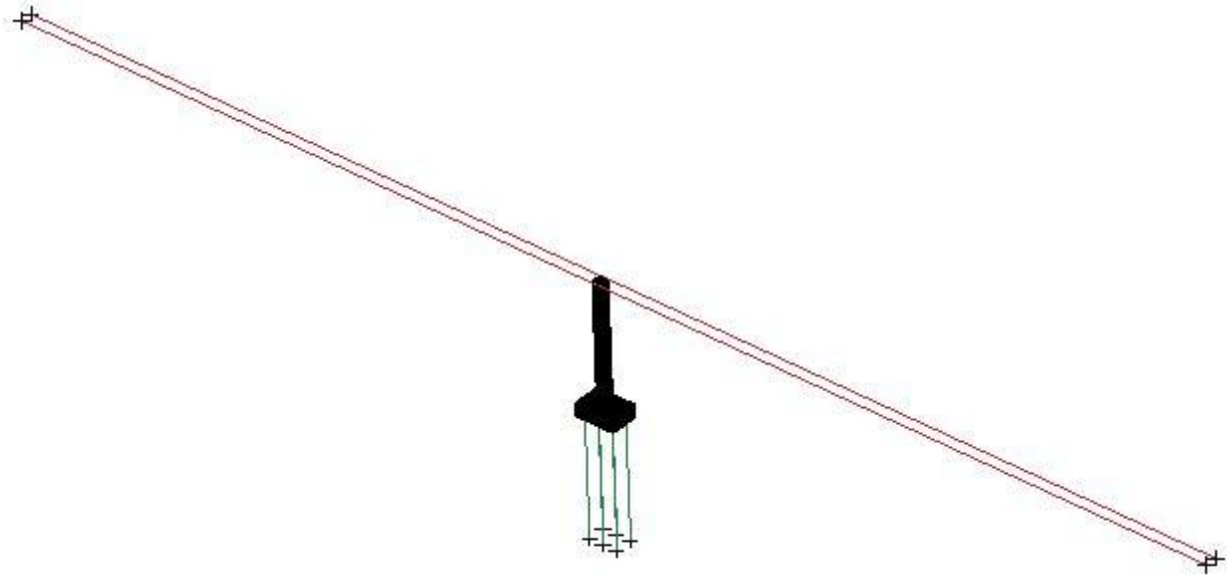

Figure 6.1: 3D- view of the FE model for verification against El-Tawil's et al. (2005) results
Note: soil subgrade springs are not shown for simplicity

The bridge superstructure was composed of a composite steel-concrete box girder. Thirty-six Belytschko-Schwer resultant beam-type (ELFORM_2) elements were used to simulate two adjacent steel girders. This superstructure's transformed steel cross-sectional area was 124 in^2. The strong moment of inertia (the I_{yy} about the vertical axis) was 2.0×10^5 in^4, and the weak moment of inertia (the I_{zz} about the horizontal axis) was 6.7×10^4 in^4. The superstructure's two unequal spans were 175 ft and 165 ft, respectively. This superstructure was assumed to be pinned at the far ends. The Hughes-Liu beam-type element (ELFORM_2) was used to simulate the bridge bearings located

under the superstructure. These bearings were 1.5 inch thick and 8 inch x 8 inch in the cross-section. The bridge bearing's shear modulus was 88.0 psi.

A Chevrolet pickup's reduced finite element model was used to study the vehicle's collision with a bridge pier (Fig. 6.3a). A surface-to-surface contact element was used between the vehicle and the bridge pier in the finite element models; the coefficient of friction was 0.3. The vehicle model was developed by the National Crash Analysis Center (NCAC) of The George Washington University under a contract with both the Federal Highway Administration (FHWA) and the National Highway Traffic Safety Administration (NHTSA) of the U.S. Department of Transportation (DOT).

The collision event of the Chevrolet pickup with the bridge pier, at a velocity of 69 mph, with a time of 0.05 seconds is illustrated in Figure 6.3b. The FE results from this study, in general, were close to the results reported by El-Tawil et al. (2005), as illustrated in Fig. 6.4 and Table 6.1. The percentages of difference between the PDFs from this study and those from the El-Tawil et al. (2005) study for vehicle velocities of 34 mph, 69 mph, and 84 mph were between 0.6% and 9.2% (Fig. 6.4). These differences occurred as a result of the number of uncertainties such as a column's concrete cover, mesh size, the column component's material models, the vehicle nose's location at the column's face, and the values of modulus of the subgrade's reaction of the soil springs. These parameters were not accurately described in El-Tawil et al. (2005).

The percentages of difference between the ESFs from this study and those from the El-Tawil et al. (2005) study for vehicle velocities of 34 mph, 69 mph, and 84 mph were between 6.4% and 14.5% (Fig. 6.4).

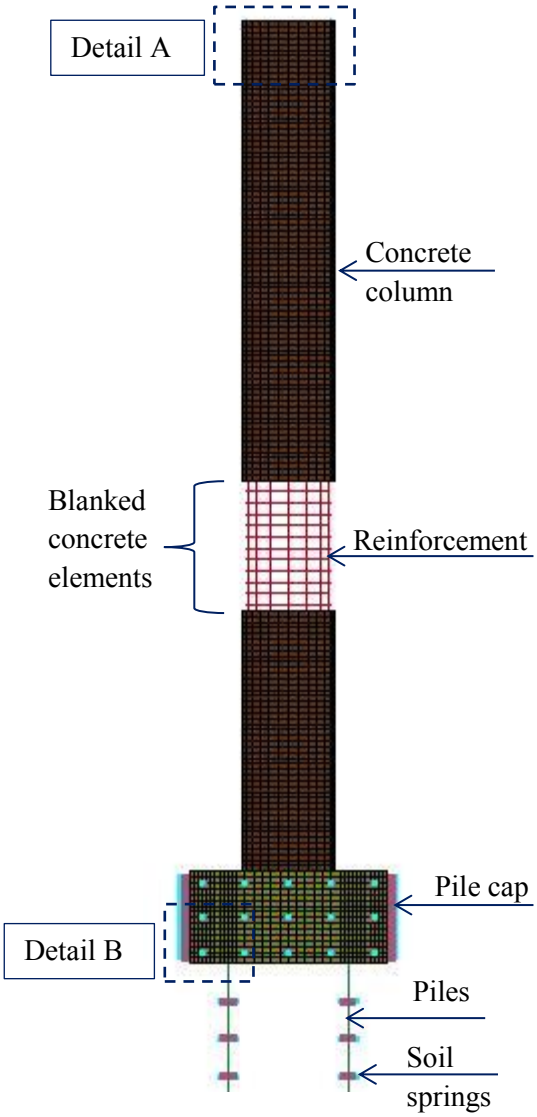

Bridge pier sideview

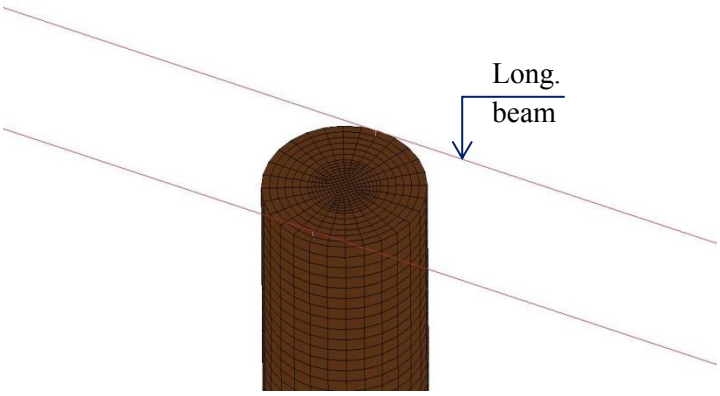

Detail A: Superstructure-substructure connection

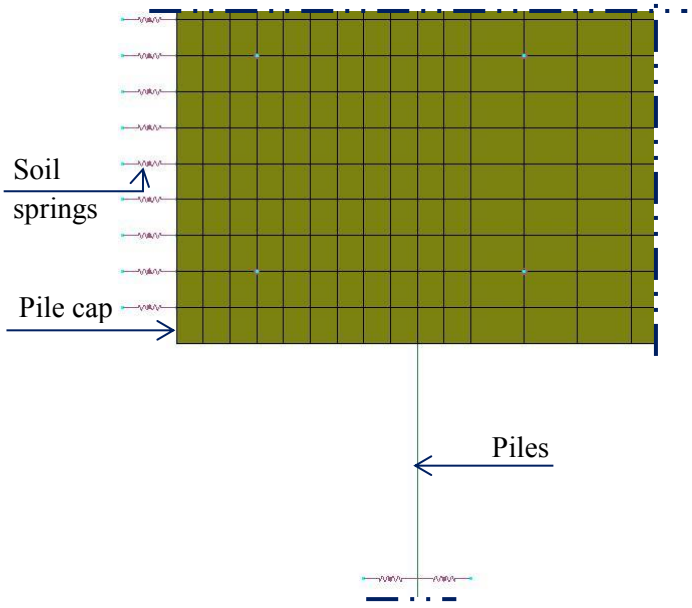

Detail B: Soil springs with piles and pile cap

Figure 6.2: Components of the FE model for verification against El-Tawil's et al. results (2005)

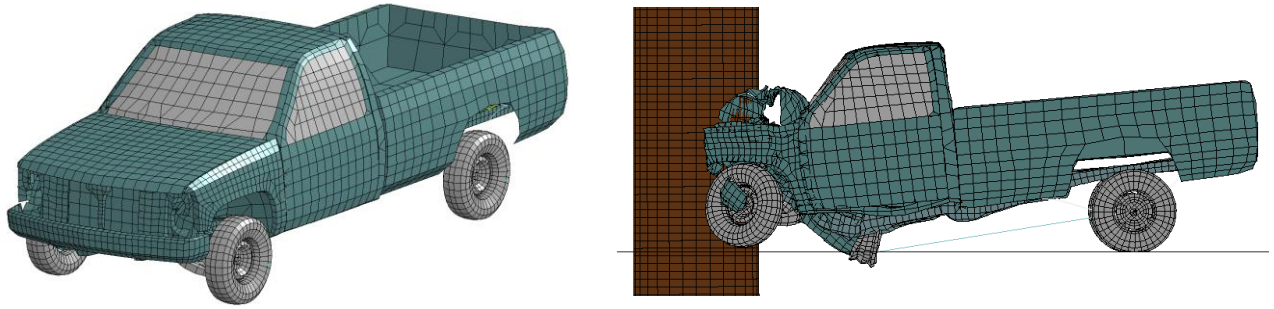

(a) (b)

Figure 6.3: The reduced FE model of Chevrolet pickup: (a) 3D-view, (b) Side view of the collision event of the reduced FE model of Chevrolet pickup with bridge pier (velocity = 69 mph and time = 0.05 second)

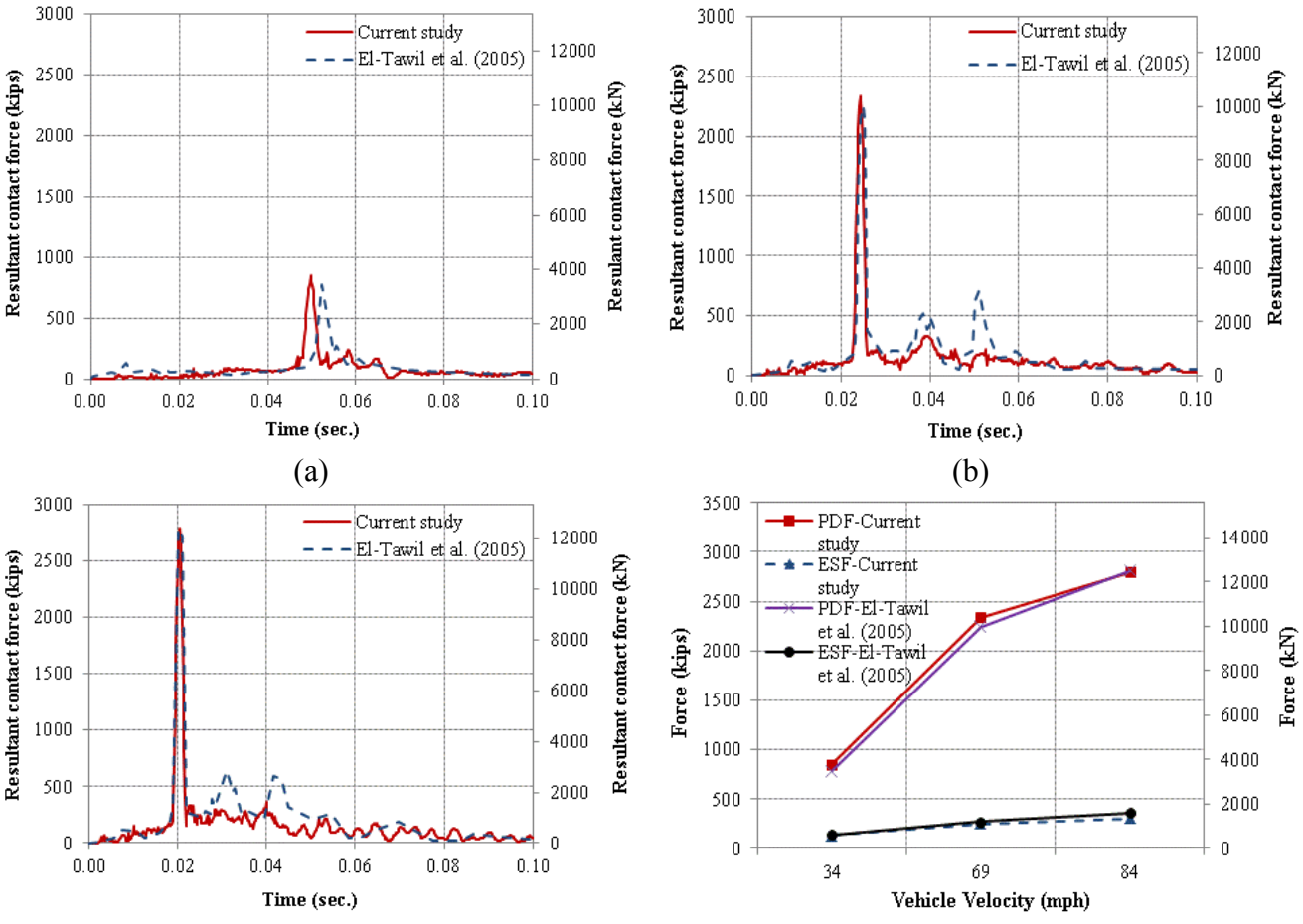

Figure 6.4: FE results from current study versus those from El-Tawil et al. (2005) FE results; (a) vehicle velocity of 34 mph, (b) vehicle velocity of 69 mph, (c) vehicle velocity of 84 mph, and (d) PDF and ESF versus the vehicle velocities

Table 6.1: Summary of FE results of current study versus El-Tawil et al. (2005)

Vehicle velocity, mph	PDF (kips)		Difference (%)	ESF (kips)		Difference (%)
	Current study	El-Tawil et al. (2005)		Current study	El-Tawil et al. (2005)	
34	851	779	9.2	131	140	6.4
69	2,337	2,245	4.1	248	269	7.8
84	2,792	2,810	0.6	306	358	14.5

6.3 Modeling the Parametric Study

Once the model was verified, a parametric study was conducted to numerically investigate the RC-column's behavior during a vehicle collision. The LS-DYNA was used to examine 13 different parameters including the following:

- Concrete material model (elastic, nonlinear, and rigid)
- Unconfined compressive strength (f_c') ranging from 3,000 psi to 10,000 psi
- Material strain rate (SR; considered and not considered)
- Percentage of longitudinal reinforcement ($\rho_s = A_s/A_c$) ranging from 1% to 3%
- Hoop reinforcement ranging from #4@2.5 inch to 5@12 inch corresponding to volumetric reinforcement ratio of 0.54% to 0.17%
- Column span-to-depth ratio (S/D) ranging from 2.5 to 10.0
- Column diameter (D) ranging from 4.0 ft to 7.0 ft
- Column top boundary condition (free, superstructure, and hinged)
- Axial load level (P/P_o) ranging from 0% to 10%
- Vehicle velocity (v_r) ranging from 20 mph to 70 mph
- Vehicle mass (m) ranging from 4.4 kips to 65 kips
- Clear zone distance (L_c) ranging from 0.0 ft to 30 ft
- Soil depth above the top of the column footing (d_s) ranging from 1.7 ft to 5.0 ft

Thirty-three columns (from C0 to C32) were investigated. Column C0 was used as a reference column. The ranges of selected variables for the columns with regard to the examined parameters are summarized in Table 6.2. It should be noted that some of the selected parameters may be not common in practice. However, they were used to fully understand the performance of the columns under a wide spectrum of parameters.

6.3.1 Geometry

The columns investigated in this study were supported on a concrete footing which had fixed boundary condition at its bottom. All of the columns, but C17 and C18 were hinged at the top ends. Column C17 was free at the top end while column C18 had superstructure attached at its top as explained in the verification section. Each column had a circular cross-section with a diameter (D) that was between 4.0 ft and 7.0 ft with 5.0 ft being the common diameter (Fig. 6.5). The column's height (H) ranged from 12.5 ft to 50.0 ft with 25.0 ft being the common height. The column span-to-depth ratios (S/D) ranged from 2.5 to 10 with 5.0 being the common span-to-depth ratio. The soil depth above the top of the footing (d_s) ranged from 1.7 ft to 4.9 ft with 3.3 ft being the common soil depth.

The percentage of longitudinal steel reinforcement (ρ_s) ranged from 1.0% to 3.0% with 1.0% being the common percent. The hoop reinforcement size ranged from #4 to #6 with #5 being the common hoop reinforcement size. The hoop reinforcement spacing ranged from 2.5 inch to 12 inch with 4 inch being the common hoop reinforcement spacing.

The column's axial load (P) ranged from 0% to 10% of P_o with 5% of P_o being the common axial load where P_o was calculated by eqn. (2.1).

6.3.2 Columns' FE modeling

One-point quadrature solid elements were used to model each column's concrete core. These elements had an average dimension of 4.3 inch x 2.2 inch x 2.5 inch A rigid cylinder that was 7.9 inch height, modeled by solid elements, was placed atop the concrete column to avoid excessive local damage to the column's top when the axial loads were applied. Solid elements were used to model the concrete footing.

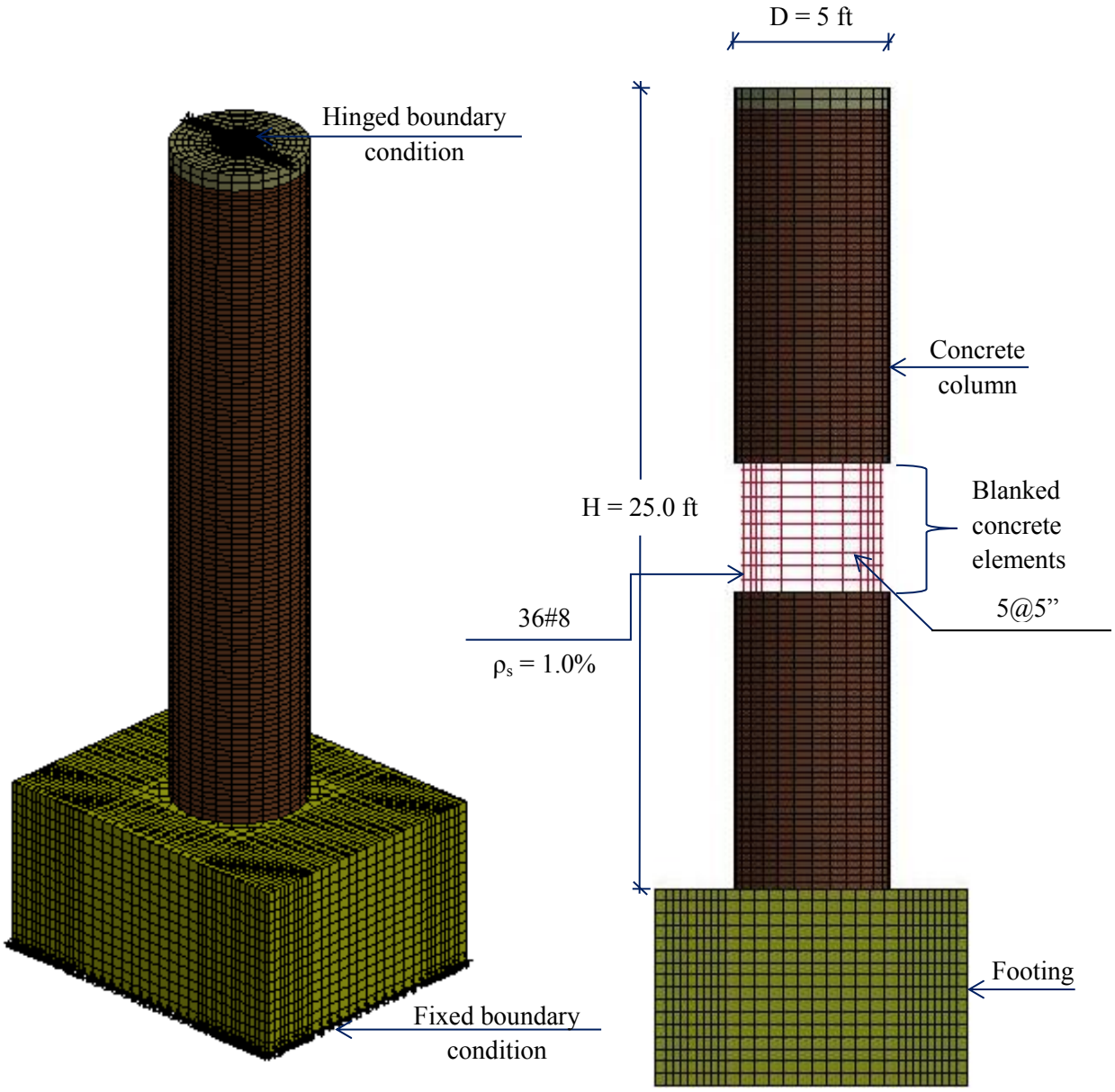

Figure 6.5: F.E. model of the bridge pier “C0” for the parametric study; (a) 3D-view, (b) detailed side view of the pier components

Table 6.2: Summary of the examined columns' parameters

Column	Conc. Mat.	$f'c$ (psi)	SR	ρ_s	Hoop RFT	S/D	D (ft)	Top Bound. Cond.	P/P$_0$	v_r (mph)	m (kip)	L_C (ft)	d_s (ft)
C0	NL	5,000	C	1%	#5 @ 4 inch	5	5.0	Hinged	5%	50	16	0.5	3.3
C1	EL												
C2	RIG												
C3	NL	3,000											
C4		7,000											
C5		10,000											
C6		5,000	NC										
C7			C	2%									
C8				3%									
C19				1%	#4 @ 2.5 inch								
C10					#6 @ 6 inch								
C11					#5 @ 12 inch								
C12					#5 @ 4 inch	2.5							
C13						10							
C14						5	4.0						
C15							6.0						
C16							7.0						
C17							5.0	Free					
C18								Super-structure					
C19								Hinged	0%				
C20									10%				
C21									5%	70			
C22										35			
C23										20			
C24										50	4.4		
C25											35		
C26											65		
C27											16	0	
C28												1.0	
C29												10.0	
C30												30.0	
C31												0.5	1.7
C32													4.9

NL = nonlinear material (mat72RIII), EL = elastic material (mat001), RIG = rigid material (mat020), SR = strain rate, NC = Not Considered, C = Considered, ρ_s = the percentage of longitudinal steel reinforcement in the column's cross-section =A_s/A_c(A_s = the cross-sectional area of the longitudinal steel reinforcements, A_c = the cross sectional area of the concrete column), S/D = span-to-depth ratio, D = column diameter, P = applied axial load, P_o = column axial compressive capacity, v_r = vehicle velocity, m = vehicle mass, L_c = clear distance in front of vehicle's nose, d_s = soil depth above the column footing.

An hourglass control was used to avoid spurious singular modes (e.g., hourglass modes). The hourglass value for each of the models was taken as the default value 0.10, with an hourglass control type_4 (Flanagan-Belytschko stiffness form). Both longitudinal and the hoop reinforcements were modeled by beam_orientation elements. All of the beam elements within the reinforcement were constrained with the concrete column and the footing by "Lagrange in solid." The column's concrete cover was defined to spall at an axial compressive strain exceeding 0.005 (Caltrans 2006).

6.3.3 Material models

Two different concrete material models have been used in the literature to assess the impact forces on bridge columns, namely, the elastic isotropic material mat001 and rigid material model mat020. Using an elastic material allows the evaluation of the impact force assuming that the column will remain elastic (El-Tawil et al. 2005). Using rigid material model does not allow any deformations to take place in the columns (Buth et al. 2010). Since both material models respond elastically, the energy dissipation by the inelastic deformation in the column is ignored. Thus, the impact forces calculated with these two material models represent the impact forces' upper bounds. The AASHTO-LRFD, However, considers vehicle impact to be an extreme load. Therefore, a column's nonlinear behavior is both expected and allowed. Hence, this research investigated the effect of three different concrete material models including elastic (mat001), rigid (mat020), and nonlinear (mat72RIII) on the response of bridge column to vehicle impact.

For elastic material, the elastic modulus and Poisson's ratio are the only parameters required to define this material model. These parameters were also used for the rigid material in determining the sliding interface parameters of the contact elements between the vehicle and the column. The elastic modulus, E, was calculated according to ACI-318 (2011) and considering the dynamic increase factor (DIF) factor ($E = 4{,}750\sqrt{\text{DIF} * f_c'}$) and the Poisson's ratio was taken as 0.20 (Mehta and Monteiro 2006). The DIF factor is explained later in this section.

A nonlinear concrete material model (mat72RIII) was used for all columns and footings but C1 and C2 and their footings examined in this study. The model had three shear failure surfaces: yield, maximum, and residual (Malvar et al. 1997). Given f_c' and ω, the yield failure surfaces of this model were generated automatically. The fractional dilation parameter (ω) that takes into

consideration any volumetric change occurring in the concrete was taken as the default value of 0.50.

Loading strain rates may play an essential role in a structure's response. The DIF is typically used to describe the increase in concrete's strength under dynamic loading as compared to static loading (Malvar and Ross 1998; Bischoff and Perry 1991; Williams 1994; Fu et al. 1991). Malvar and Ross (1998) modified the CEB model code for use with strain rate effects and implemented the modified model into an LS-DYNA format (CEB-FIP 1990). For example, when concrete has a compressive strength (f_c') of 5,000 psi is subjected to a compressive load with a strain rate of 100 s^{-1} (common for impact loading), the DIF will be 2.21 in compression and 7.52 in tension (Sierakowsi and Chaturved 1997). The effect of a high strain rate is quite significant with regard to concrete's tensile strength compared to concrete's compressive strength. This occurred since tension cracks do not have enough time to propagate through concrete because the loading time is too short.

6.3.4 Steel reinforcement

An elasto-plastic constitutive model, mat003-plastic_kinamatic, was used for steel reinforcement. The following five parameters were needed to define this material model: the elastic modulus (E), the yield stress, Poisson's ratio, the tangent modulus, and the ultimate plastic strain. These parameters were assigned the following values: 29,000 ksi, 60,900 psi, 0.30, 160 ksi, and 0.12, respectively (Caltrans 2006). To consider strain rate effect, Cowper-Symonds's (1957) model was adopted. Parameters p and c were assigned as a means for identifying the strain rate effect. The constants p and c were taken as 5 and 40, respectively (Yan and Yali 2012). Substituting these two constants into Cowper-Symonds's equation at a strain rate of 100 s^{-1} produces a dynamic yield stress that is 2.20 times the static yield stress. The elastic modulus of steel does not considerably change under impact loading (Campbell 1954).

6.3.5 Vehicles FE models

Two vehicle models were used in this study: a Ford reduced model (35,353 elements) single unit truck (SUT) and a detailed model (58,313 elements) Chevrolet C2500 Pickup (Fig. 6.6). These

models were downloaded from the NCAC website. Experimental tests involving head-on collisions were conducted to verify each model (Zaouk et al. 1996; Mohan et al. 2003).

Different vehicle impact speeds were investigated during this research ranging from 20 mph to 70 mph with 50 mph being the common velocity. The mass of the vehicle ranged from 4.4 kips to 65 kips with 18 kips being the common mass. The Chevrolet C2500 Pickup was used as the vehicle for the mass of 4.4 kips and the Ford SUT was used for the other models. The Ford SUT's mass increased by increasing the value of the added mass. Automatic_surface_to_surface contact elements by parts with the contact factor SOFT=1 were used between the vehicle and the RC-column (Bala 2001).

If the bridge pier was located inside the clear zone (the total roadside border area, starting at the edge of the traveled way, available for safe use by an errant vehicle) without a crashworthy barrier, the design of the pier must include the collision force (KDoT 2013). The effect of the clear zone distance (L_c) was examined here by changing the distance between the vehicle's nose and the column's face. The clear zone distance ranged from 0.0 ft to 30.0 ft with 0.5 ft being the common clear zone distance.

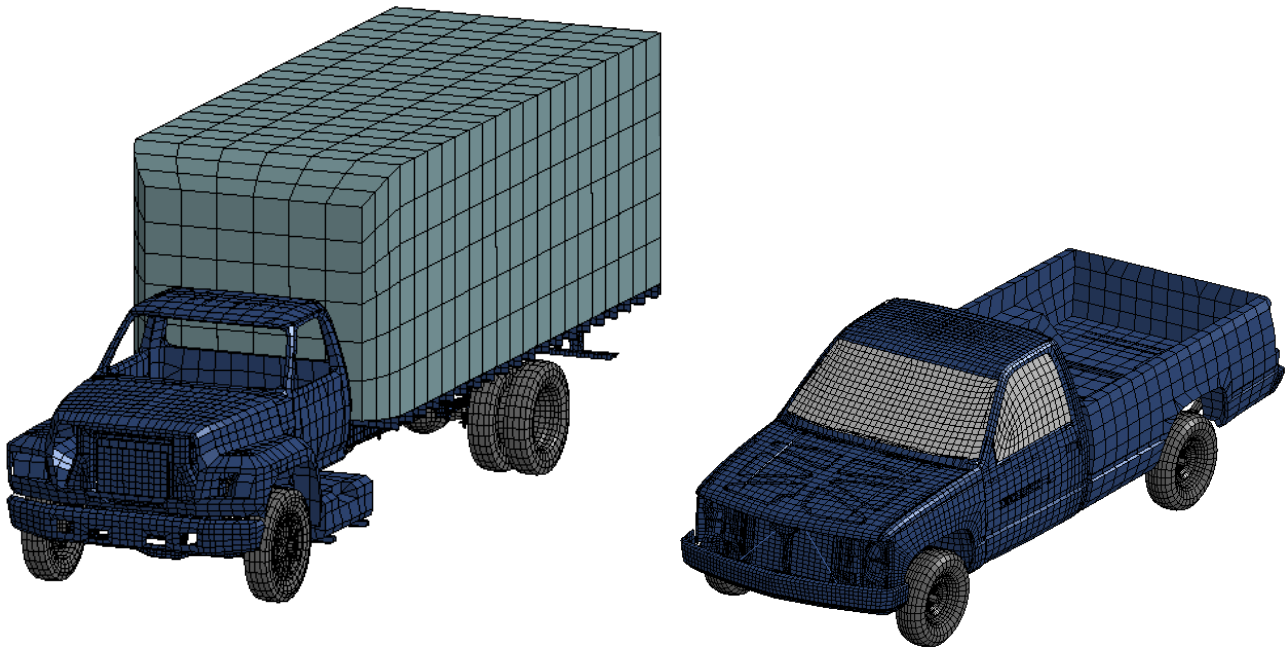

(a) (b)

Figure 6.6: 3D-view of the FE model: (a) the Ford single unit truck, (b) Chevrolet pickup detailed model

6.4 Results and Discussion of the Parametric Study

6.4.1 Performance levels

While there has been few researchers attempted to assign limit states to bridge columns under vehicle impact (Agrawal et al. 2013; Sharma et al. 2012); there has been no consensus among researchers on the damage state at the different limit states. During the course of this report, the authors defined three different limit states. Performance level P1 assigned when no bar buckling took place during the analysis. The performance level P2, heavy damage, assigned when less than 20% of the longitudinal rebar buckled. The performance level P3 assigned when at least 20% of longitudinal rebar buckled which is considered as column's failure. Figure 6.7a and Table 6.3 present the performance levels of all of the columns. Approximately 73%, 15%, and 12% of the columns were assigned to performance levels P1, P2 and P3, respectively. The columns C14, C21, C25, and C26 failed under the vehicle impact load. These impact cases are characterized by small column diameter of 4 ft, high speed vehicle of 70 mph, heavy mass of 35 kips and 65 kips. The columns C3, C6, C12, C17, and C30 suffered heavy damage. These impact cases characterized by low concrete strength of 3,000 psi, excluding strain rate effect, low column's aspect ratio of 2.5, free top boundary condition, and long clear zone distance of 30 ft.

6.4.2 General comparisons

Figure 6.7b and Table 6.3 present the ESF and the columns' shear capacity normalized by the ESF of the AASHTO-LRFD (600 Kips) for all of the columns. In addition, Table 6.3 summarizes the PDFs normalized by the ESF of the AASHTO-LRFD for all of the columns. As shown in the figure and table, the differences between the ESF approaches were highly varied from case to case. The differences between the maximum and the minimum values of ESF calculated using the different approaches for a given column ranged from 7% (C2) to 140% (C14). Furthermore, the SB_{ESF} represents the upper bound for 73% of the cases while EC_{ESF} represents the lower bound for 85% of the columns. The SB_{ESF} of 27% of the examined columns exceeded or equal the ESF of the AASHTO-LRFD (600 kips). The ESF calculated using the PTMSA exceeded the ESF of the AASHTO-LRFD for 9% of the examined columns. In general, the ESF of the Eurocode (EC_{ESF}) was typically lower than the ESF of the AASHTO-LRFD except for the columns C25 and C26 of the heavy vehicles of masses more than 35 kips.

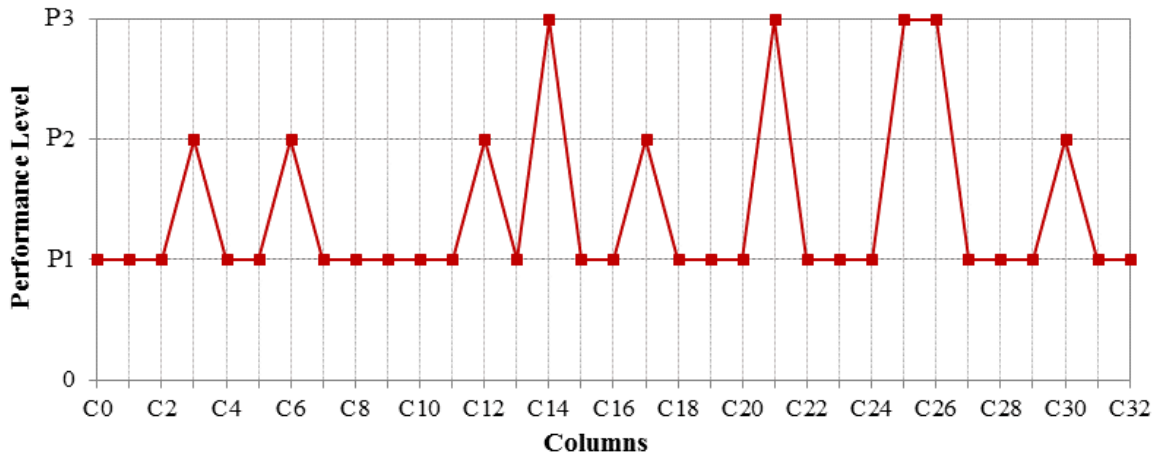

(a)

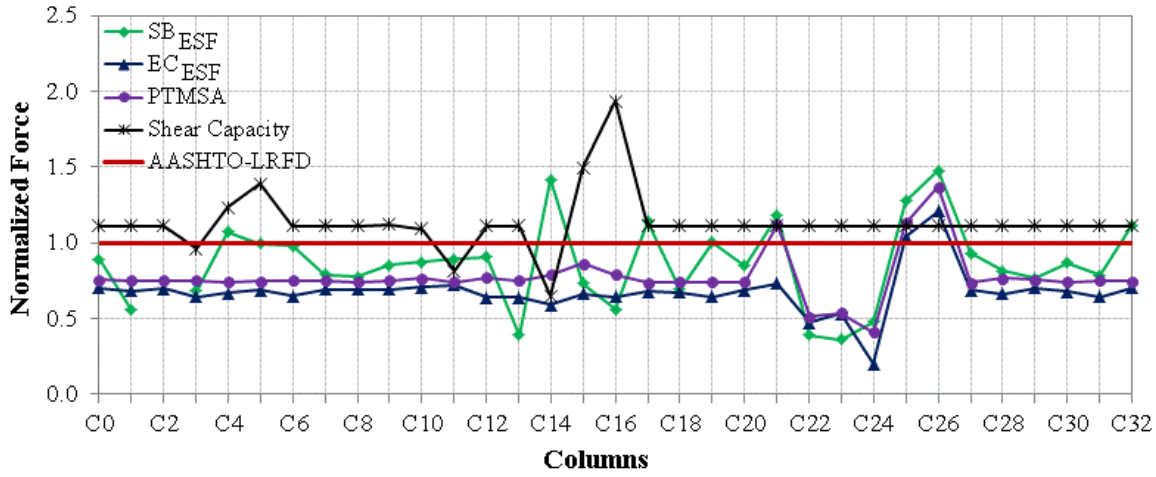

(b)

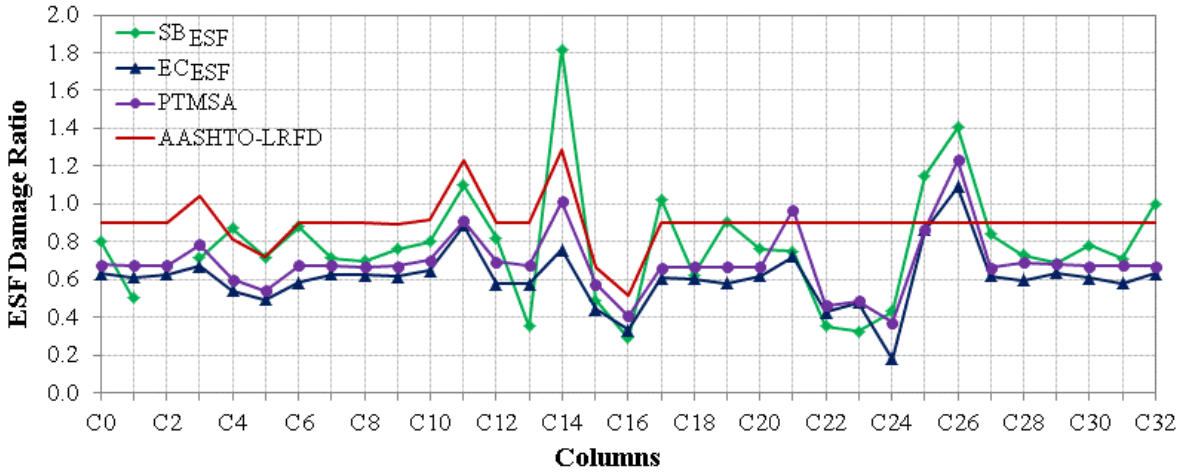

(c)

Figure 6.7: (a) Performance levels of the examined columns according to the results of FE, (b) Normalized forces to the ESF of AASHTO-LRFD (600 kips), and (c) Damage ratio of the dynamic and static forces for the examined columns

The results of FE will be used as a basis for comparing the best approach in calculating the ESF. Columns that reach performance level P3 will be called "failed columns" while all other columns will be called "unfailed columns." Among the investigated approaches, if the ESF according to a given approach is higher than the shear capacity of this column, the column will be considered failed column. Otherwise, it is unfailed column. Equations 6.1 and 6.2 summarize these characteristics as following:

Safety according to FE =

$$true\ value\ of \begin{cases} P_1\ or\ P_2 & (unfailed\ column) \\ P_3 & (failed\ column) \end{cases} \quad (6.1)$$

Safety according to the different approaches =

$$true\ value\ of \begin{cases} ESF \leq shear\ capacity & (unfailed\ column) \\ ESF > shear\ capacity & (failed\ column) \end{cases} \quad (6.2)$$

Figures 6.7a and 7b as well as Table 6.3 and 6.4 indicated that PTMSA approach was the best approach for predicting the columns' performance. This approach predicted that four columns failed which is in 100% agreement with the FE results where their PTMSAs were higher than the columns' shear capacities. The PTMSA was lower than the column's shear capacity for all unfailed columns.

The SB_{ESF} approach predicted that 6 of the columns would fail which is higher number of columns compared to the results of the FE analyses. The SB_{ESF} approach correctly predicted that columns C14, C21, C25, and C26 would fail. However, the SB_{ESF} indicated that columns C11 and C17 would fail. Columns C11 and C17 reached to performance level P1 and P2, respectively according to the FE analyses. Hence, the SB_{ESF} approach over predicted the impact force on columns C11 and C17 at least by 10% and 2%, respectively. These two columns are characterized by unfailed columns.

EC_{ESF} approach predicted that 2 of the columns would fail which is lower number of columns compared to the results of the FE analyses. The EC_{ESF} approach correctly predicted that columns C14 and C26 would fail. However, The EC_{ESF} indicated that columns C21 and C25 would not fail. Columns C21 and C25 reached to performance level P3 according to the FE analyses. Hence, the EC_{ESF} approach under predicted the impact force on columns C21 and C25 at least by 34% and 6%, respectively. These two columns are characterized by failed columns. The EC_{ESF} correctly predicted the column's failure for the columns are associated with impact with the

heaviest vehicle of 65 kips which represents the highest kinetic energy and for the case of the lowest column's diameter of 4 ft with low shear capacity.

The AASHTO-LRFD predicted that one of the columns would fail which is lower number of columns compared to the results of the FE analyses. The AASHTO-LRFD approach correctly predicted that column C14 would fail. However, the AASHTO-LRFD indicated that columns C21, C25, and C26 would not fail. Columns C21, C25, and C26 reached to performance level P3 according to the FE analyses. Hence, the AASHTO-LRFD approach under predicted the impact force on columns C21, C25, and C26 at least by 10% for all of them. These three columns are characterized by failed columns. The AASHTO-LRFD correctly predicted the failure of the lowest diameter column of 4.0 ft. The AASHTO-LRFD indicated that columns C3 and C11 would fail. However, columns C3 and C11 reached to performance level P2 and P1, respectively according to the FE analyses. Hence, the AASHTO-LRFD over predicted the impact force on columns C3 and C11 at least by 2% and 13%, respectively. These two columns are characterized by unfailed columns.

Figure 6.7c illustrated the damage ratios defined as the ESFs normalized by each column's shear capacity calculated according to AASHTO-LRFD (2012). The design of approximately 21% of the columns would be controlled by the shear force caused by vehicle impact.

6.4.3 Concrete material models

This section investigated the effects of the selection of concrete material model on the PDF and ESFs. Three material models mat001, mat020, and mat72RIII representing elastic, rigid, and nonlinear behavior were used for this investigation. The typical time-impact force relationship is illustrated in Fig. 6.8a. The first peak force occurred when the vehicle's rail collided with the column. The second peak force on the columns, which was the largest, was produced by the vehicle's engine. The third peak occurred when the vehicle's cargo (in the Ford SUT only) struck the cabinet and the engine. The fourth peak was produced when the rear wheels left the ground. The PDFs for columns C0, C1, and C2 were 834 kips, 936 kips, and 963 kips, respectively. Each of the columns reached their PDF nearly at the same time (0.04) seconds and had zero impact force beyond 220 milliseconds. The PDF of column C2, which was modeled using a rigid material, was approximately 15% higher than that of column C0, which was modeled using a nonlinear material. This finding was expected as no deformations were allowed to take place in the concrete material of

column that was modeled using a rigid material. Hence, no impact energy was dissipated. Column C1, which was modeled using elastic material, had a slightly lower PDF value than that of column C2.

Figure 6.8b illustrates the normalized ESFs and PDFs of the columns C0, C1, and C2. The normalized ESF for columns C0, C1, and C2 ranged from 0.7 to 0.9. Column C2 was a rigid column; hence, the SB_{ESF} could not be calculated. The values' PTMSA and EC_{ESF} for all of the columns were nearly constant regardless of the material model.

The system's kinetic energy before collision occurred was 18,408 kip.inch (Fig. 6.8c). This was absorbed entirely during the first 150 milliseconds in the form of column and vehicle deformations. Converting part of the kinetic energy into thermal energy (in the form of heat) was excluded from this study.

The vehicle's net displacement was calculated by substituting the clear zone distance from the total displacement (Fig. 6.8d) to obtain the deformation that occurred throughout the vehicle's body. The maximum net displacement of vehicles in FE models C0, C1, and C2 was 44.2 inch, 45.5 inch, and 44.4 inch, respectively.

The FE results are reliable if the initial kinetic energy completely transformed into internal energy, hourglass energy, and residual kinetic energy (El-Tawil 2004). Figure 6.9 illustrates the quantities of the different energies obtained from column C0. The hourglass energy was lower than 2% of the total energy. Therefore, neither the constant stress solid elements nor the hourglass control affected accuracy of results.

Table 6.3: Summary of the normalized PDFs ESFs, and shear capacity of all of the columns and their performance levels

Column	PDF	SB_{ESF}	EC_{ESF}	PTMSA	Shear capacity	Performance level
C0	1.4	0.9	0.7	0.8	1.1	P1
C1	1.6	0.6	0.7	0.7	1.1	P1
C2	1.6	N/A	0.7	0.7	1.1	P1
C3	1.1	0.7	0.6	0.8	1.0	*P2*
C4	1.4	1.1	0.7	0.7	1.2	P1
C5	1.4	1.0	0.7	0.7	1.4	P1
C6	1.1	1.0	0.7	0.8	1.1	*P2*
C7	1.4	0.8	0.7	0.7	1.1	P1
C8	1.5	0.8	0.7	0.7	1.1	P1
C9	1.5	0.9	0.7	0.8	1.1	P1
C10	1.5	0.9	0.7	0.8	1.1	P1
C11	1.3	0.9	0.7	0.7	0.8	P1
C12	1.1	0.9	0.6	0.8	1.1	*P2*
C13	1.1	0.4	0.6	0.8	1.1	P1
C14	1.3	1.4	0.6	0.8	0.7	**P3**
C15	1.5	0.7	0.7	0.9	1.5	P1
C16	1.4	0.6	0.6	0.8	1.9	P1
C17	1.4	1.1	0.7	0.7	1.1	*P2*
C18	1.5	0.7	0.7	0.7	1.1	P1
C19	1.1	1.0	0.6	0.7	1.1	P1
C20	1.4	0.8	0.7	0.7	1.1	P1
C21	3.2	1.2	0.7	1.1	1.1	**P3**
C22	0.8	0.4	0.5	0.5	1.1	P1
C23	0.6	0.4	0.5	0.5	1.1	P1
C24	1.5	0.5	0.2	0.4	1.1	P1
C25	2.2	1.5	1.0	1.1	1.1	**P3**
C26	2.8	1.6	1.2	1.4	1.1	**P3**
C27	1.5	0.9	0.7	0.7	1.1	P1
C28	1.5	0.8	0.7	0.8	1.1	P1
C29	1.2	0.8	0.7	0.8	1.1	P1
C30	1.5	0.9	0.7	0.7	1.1	*P2*
C31	1.5	0.8	0.6	0.8	1.1	P1
C32	1.5	1.1	0.7	0.7	1.1	P1

Table 6.4: Summary of the prediction of the different approaches including AASHTO-LRFD

Prediction	SB_{ESF}	EC_{ESF}	PTMSA	AASHTO-LRFD
% correctly predicted	94.0%	94.0%	100.0%	85.0%
% over predicted	9.0%	0.0%	0.0%	6.0%
% under predicted	0.0%	6.0%	0.0%	9.0%
No. of predicted failed columns	4 out of 4	2 out of 4	4 out of 4	1 out of 4

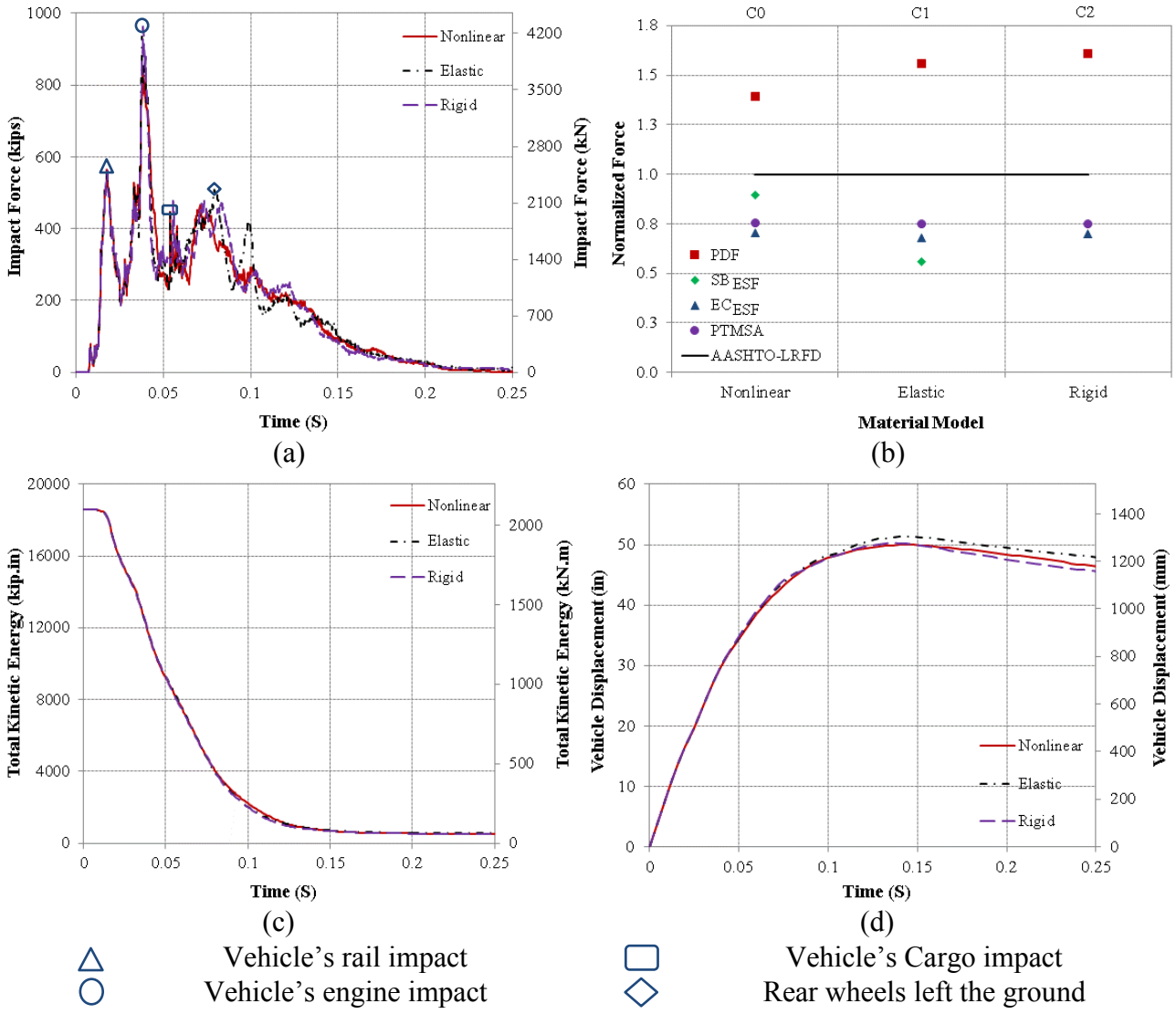

Figure 6.8: Effects of various concrete material models: (a) Time-Impact force, (b) PDF vs. ESF vs. AASHTO-LRFD, (c) Time-Total kinetic energy, and (d) Time-Vehicle displacement.

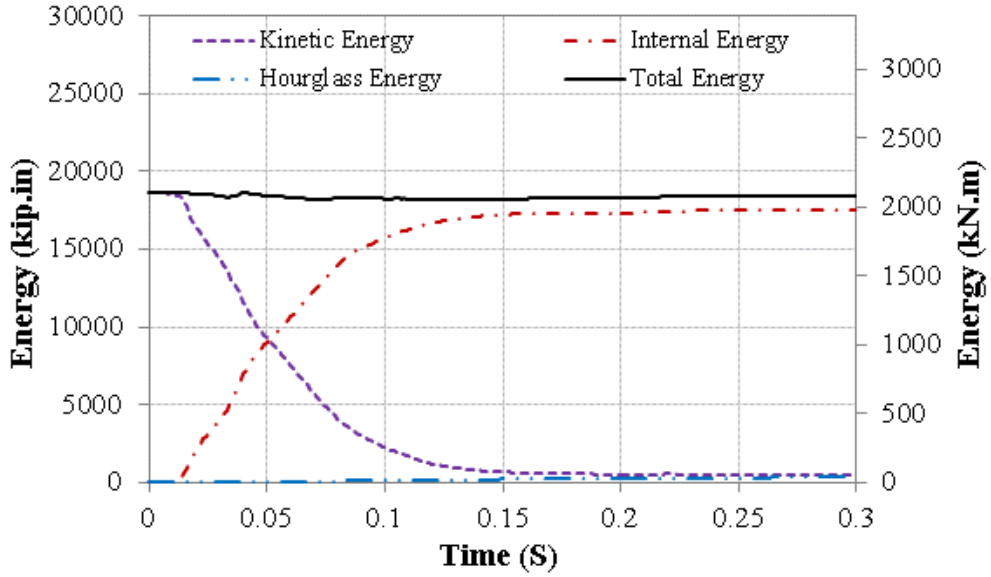

Figure 6.9: Time-energies relations of the FE model C0

6.4.4 Unconfined compressive strength (f'_c)

Four values of f'_c ranging from 3,000 psi to 10,000 psi were investigated during this section. Changing f'_c did not significantly affect the values of PDF except when the f'_c was considerably low for column C3 (Fig. 6.10a). The PDF value of column C3 having f'_c of 3,000 psi, was 20% lower than that of the other columns. The lower concrete strength in C3 led to early concrete spalling and bucking to several longitudinal bars, which dissipated a portion of the impact force. Column C4 was one of the few columns where the calculated SB_{ESF} was higher than the ESF of the AASHTO-LRFD because the elastic modulus was high. The SB_{ESF} of the column C5, having f'_c of 10,000 psi, was lower than that of the column C4, having f'_c of 7,000 psi, because the displacement of the column C5 significantly reduced due to the high stiffness. The values' PTMSA and EC_{ESF} for all of the columns were nearly constant regardless of the f'_c.

6.4.5 Strain rate effect

The PDF increased significantly when the strain rate effect was included (Fig. 6.10b). The PDF of column C0, which was modeled including the strain rate effect, was approximately 27% higher than that of column C6, which was modeled excluding the strain rate effect. Including the strain rate effect, the column's strength and stiffness increased leading to higher dynamic forces.

However, this higher stiffness resulted in smaller SB_{ESF} because the column's displacement significantly reduced. There is no significant effect of strain rate effect on EC_{ESF} and PTMSA.

6.4.6 Percentage of longitudinal reinforcement

Three values of longitudinal reinforcement ratios ranging from 1% to 3% were investigated during this section. In general, the PDF slightly increased when the percentage of longitudinal reinforcement increased (Fig. 6.10c). Tripling the percentage of longitudinal reinforcement increased the PDF by 10% only. It increased because the column's flexural strength and stiffness slightly increased with increasing the flexural steel ratio. When the percentage of longitudinal reinforcement increased, SB_{ESF} decreased while the EC_{ESF} and PTMSA were constant.

6.4.7 Hoop reinforcement

Four volumetric hoop reinforcement ratios ranging from 0.54% (#4@2.5 inch) to 0.17% (#5@12 inch) were investigated during this section. The PDF decreased when the volume of hoop reinforcement decreased leading to increasing concrete damage which dissipated significant portion of the impact energy (Fig. 6.10d). The PDF decreased by 12% when the volume of hoop reinforcement decreased by 67%. When the hoop reinforcement decreased, SB_{ESF} slightly increased because the column's displacement increased while the EC_{ESF} and PTMSA were constant.

6.4.8 Column span-to-depth ratio

Three values of column span-to-depth ratio ranging from 2.5 to 10 were investigated during this section. The relationship between the PDF and the column's span-to-depth ratio was nonlinear (Fig. 6.10e). The PDF of column C0, having span-to-depth ratio of 5, was higher than that of columns C12 and C13, having span-to-depth ratios of 2.5 and 10, respectively. This was because the column C12 had high local damaged buckling of several rebars leading to energy dissipation and the column C13 had the lowest stiffness leading to energy dissipation through high column's displacement.

The SB_{ESF} and EC_{ESF} were related, overall, nonlinearly to the span-to-depth ratio. The SB_{ESF} of column C13 was significantly lower than the other columns because of its low column stiffness. The PTMSA and EC_{ESF} are approximately constant regardless of the span-to-depth ratio.

6.4.9 Column diameter

Four values of column's diameter ranging from 4.0 ft to 7.0 ft were investigated during this section. The PDF of all of the columns, except for Column C16, slightly increased when the column diameter increased (Fig. 6.10f). The PDF of the column C16, having a diameter of 7.0 ft, was lower than that of the column C15, having a diameter of 6.0 ft because of the rebars' buckling. While column C14 of the diameter of 4.0 ft failed under the impact loading because of the severe rebar buckling that occurred (Fig. 6.11)

The SB_{ESF} tended to rapidly decrease when the column diameter increased which significantly increased column stiffness and significantly decreased the lateral displacement. The SB_{ESF} was slightly higher than the PDF of column C14 having the lowest column diameter. This column had high lateral displacement due to its small stiffness combined with relatively high PDF leading to the highest SB_{ESF}. This was one of the few columns where SB_{ESF} exceeded that of AASHTO-LRFD. All of the approaches including the AASHTO-LRFD could anticipate the failure of the column as the ESFs exceeded the shear capacity. The AASHTO-LRFD (2012) stated that "Field observations indicate shear failures are the primary mode of failure for individual columns and columns that are 30.0 inch in diameter and smaller are the most vulnerable," while this study indicated that columns that are 48.0 inch in diameter and smaller are the most vulnerable for shear failure. Both the EC_{ESF} and the PTMSA for all columns increased slightly when the column's diameter increased.

6.4.10 Top boundary conditions

Three column's top boundary conditions including free, hinged, and superstructure (similar to the one explained in section of verification of the FE modeling in this report) were investigated during this section. Changing the column's top boundary condition slightly changed the PDF values because the PDF was induced in a very short period of time (Fig. 6.12a). However, the maximum lateral displacement at the point of impact of column C17 having free top boundary condition, was significantly higher than those of columns C0 and C18 having hinged and superstructure top conditions, respectively. The existence of the superstructure's in column C18 resulted in a top boundary condition similar to that in column C0. Hence, column C17 had higher SB_{ESF} compared to C0 and C18. The column C17 was one of the few columns where SB_{ESF} exceeded that of AASHTO-LRFD. Changing the top boundary condition did not change the EC_{ESF} and PTMSA.

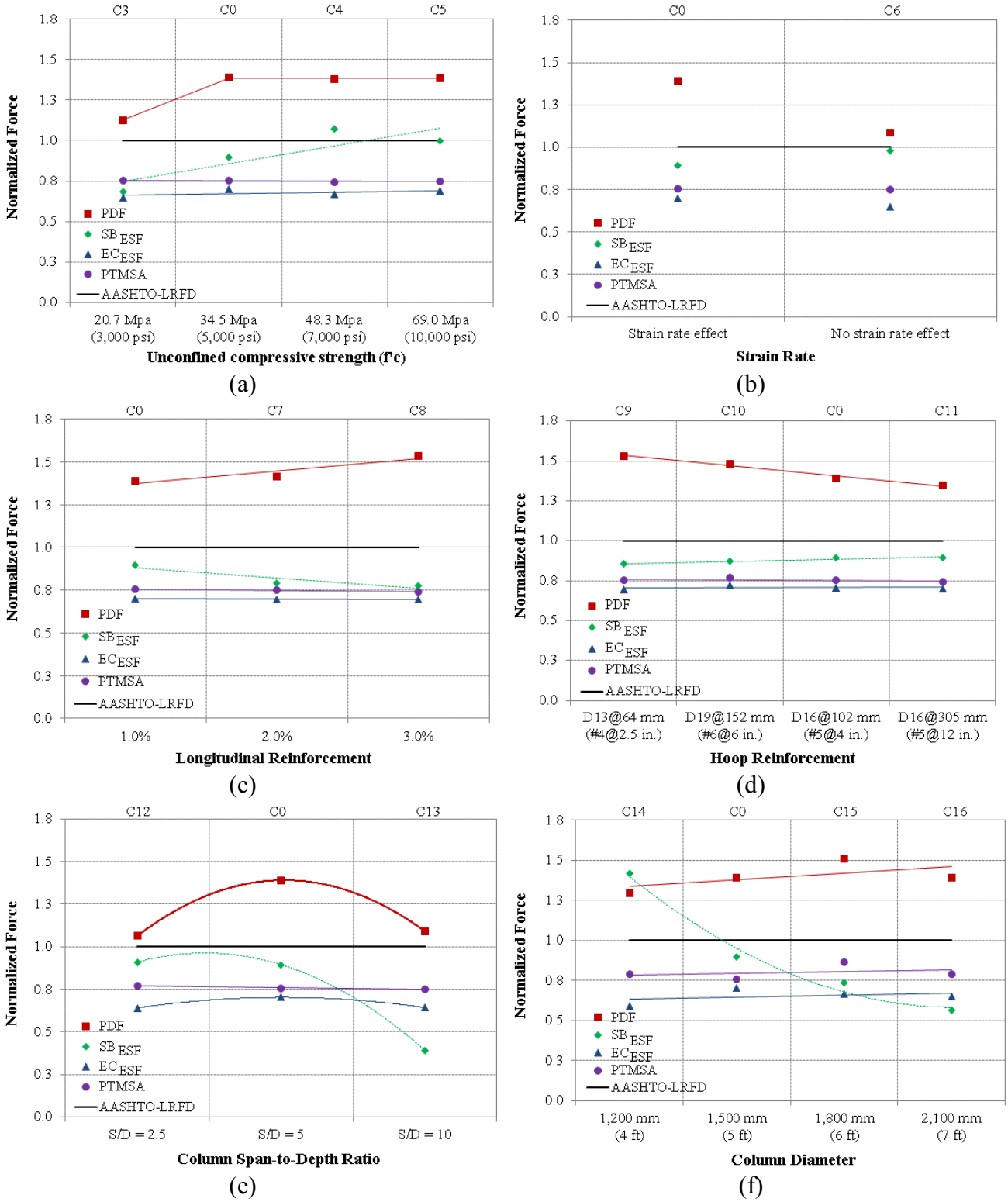

Figure 6.10: Effects of (a) f_c', (b) strain rate, (c) longitudinal reinforcements ratio, (d) hoop reinforcements ratio, (e) span-to-depth ratio, and (f) column diameters on PDF and ESF

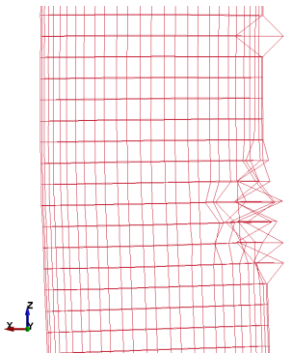

Figure 6.11: Buckling of rebars of the column C14 having a diameter of 4 ft- scaled 50 times

6.4.11 Axial load level

Three values of axial load level ranging from 0 to 10% of the column's axial capacity (P_o) were investigated during this section. The PDF typically increased when the axial load level increased (Fig. 6.12b). Column C19, sustained zero axial load, had a PDF that was approximately 25% lower than that of column C20, sustained an axial load that was 10% the P_o. The high axial compressive stresses on the column delayed the tension cracks due to the vehicle impact and hence increased the column's cracked stiffness leading to higher dynamic forces. The PTMSA and EC_{ESF} are approximately constant regardless of the axial load level.

6.4.12 Vehicle velocity

Four vehicle velocities ranging from 20 mph to 70 mph were investigated during this section. The PDF tended to increase nonlinearly when the vehicle's velocity increased (Fig. 6.12c). It is of interest that the increase in the PDF is not proportional to the square of the velocity as in the case of elastic impact problems. Damage to the columns reduces the rate of increase in the PDF. For example, the PDF increased by approximately 500% when the vehicle's velocity increased from 20 mph to 70 mph.

All of the ESFs approximately linearly increased with increasing the vehicle velocity. The PTMSA and SB_{ESF} are the only approaches could expect the failure of the column C21 having the vehicle's velocity of 70 mph. However, the AASHTO-LRFD and EC_{ESF} under predicted the ESF of the collision of vehicles with high speed with the RC-columns.

6.4.13 Vehicle mass

Four vehicle masses ranging from 4.4 kips to 65 kips were investigated during this section. In general, both the PDF and ESF increased linearly when the vehicle's mass increased (Fig. 6.12d). However, the rate of increase is slower than what is anticipated in elastic impact problems. For example, the PDF increased by approximately 101% when the vehicle's mass increased from 4.4 kips to 65 kips. The PDF almost did not change when the vehicle mass increased from 4.4 kips to 18 kips because the energy dissipation in the form of inelastic deformations whether in the vehicle or in the column did not significantly change as the kinetic energy was not considerably high.

All approaches for calculating ESF resulted in higher values compared to that of the AASHTO-LRFD when the column was collided with heavy vehicles of a weight more than 35 kips. The PTMSA and SB_{ESF} predicted the failure of the columns when they were collided with heavy vehicles of a weight more than 35 kips. However, the EC_{ESF} predicted only the column's failure when the vehicle of a weight of 65 kips collided the column. The AASHTO-LRFD under predicted the columns' failure when they were collided with heavy vehicles of a weight more than 35 kips.

6.4.14 Clear zone distance

Five clear zone distances ranging from zero to 30 ft were investigated during this section. In general, the PDF decreased when the clear zone distance increased (Fig. 6.12e). The PTMSA and EC_{ESF} are approximately constant regardless of the clear zone distance while SB_{ESF} generally decreased when the clear zone distance increased.

6.4.15 Soil depth above the top of the column footing

Three values of the soil depth above the top of the column footing ranging from 1.7 ft to 4.9 ft were investigated during this section. In general, the change in the soil depth above the column footing did not significantly affect the PDF (Fig. 6.12f). However, SB_{ESF} linearly increased when the soil depth above the column footing increased. For large soil depth, the SB_{ESF} was 20% higher than that of AASHTO-LRFD because the vehicle impact was closed to the mid of the column leading to high displacement. The PTMSA and EC_{ESF} are approximately constant regardless of the soil depth.

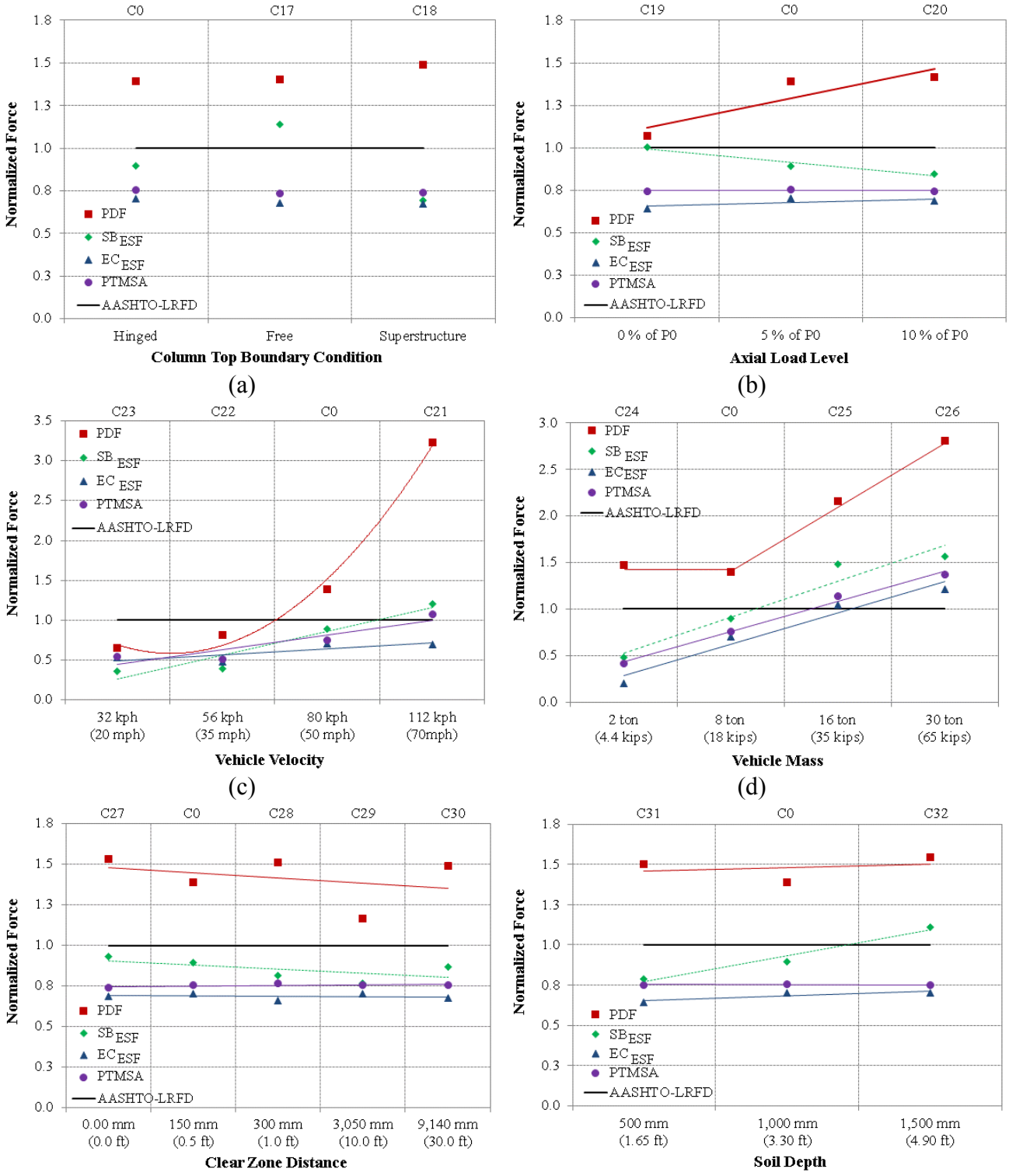

Figure 6.12: effects of (a) top boundary conditions, (b) axial load level (c) vehicle velocities, (d) vehicle masses, (e) clear zone distance, and (f) soil depth above the top of column footing on PDF and ESF

6.5 Proposed variable ESF for adoption by AASHTO-LRFD

AASHTO-LRFD uses constant value for ESF regardless of vehicle and/or columns characteristics. However, all other approaches use variable ESF depends on the column and/or vehicle characteristics. While the AASHTO-LRFD approach for ESF is quite simple, Figs 6.7, 6.8 and 6.9 as well as Tables 6.3 and 6.4 showed that in some cases AASHTO-LRFD is quite conservative and in other cases such as those involving heavy trucks and high speeds the AASHTO-LRFD under predict the impact loads. However, the other approaches require a cumbersome FE analysis and iterative design. Hence, having a simple equation to predict the ESF without a cumbersome FE and iterative analysis would represent a significant improvement over the current AASHTO-LRFD approach. Figures 6.11 and 6.12 reveal that vehicle mass and velocity are the most influential parameters on the impact problems while the other parameters either have insignificant effect or limited effects. Hence, it seems reasonable to develop a vehicle impact load as a function of mass and velocity of the vehicle. This approach will allow Departments of Transportation (DOTs) to design different bridge columns to different impact forces depends on the anticipated truck loads and velocities. Vehicles' information can be identified by the database of roads' survey which defines the mass and velocity of the frequent trucks on a specific road. Therefore, the ESF of the impact should be classified by the type of road that the bridge pier serves. Since PTMSA correctly predicted the performance of all the columns investigated in this study, it was selected to be the basis for the newly developed equation. Based on the FE results of PTMSA of the parametric study and using CurveExpert Professional software and SAS software, a new equation for estimating kinetic energy-based equivalent static force KEB_{ESF} is developed and presented in equation (6.3) as below:

$$KEB_{ESF} = 2.1\sqrt{m\, v_r^2} = 3\sqrt{KE} \tag{6.3}$$

where KEB_{ESF} = proposed ESF to AASHTO-LRFD (kip), m = the vehicle mass in kip, v_r = the vehicle velocity in mph, and KE = kinetic energy of the vehicle in kip.mph^2.

The results of the proposed equations were compared with the FE results of PTMSA. The ESFs of additional fourteen columns collided with SUT trucks of different masses ranged from 18 kips to 90 kips were calculated and compared with the results of equation (6.3). Figure 6.13 illustrates the relation between the vehicle kinetic energy of the vehicles and normalized PTMSA as

well as between normalized KEB_{ESF} and the vehicle kinetic energy for all of the forty-seven columns investigated in this study. As shown in the figure, up to KE of approximately 1,844 kip.ft, AASHTO-LRFD overpredicated ESF. However, beyond that AASHTO-LRFD is quite conservative. In some cases the RC-columns were subjected to impact loads are almost the double of the ESF of the AASHTO-LRFD. Also, shown in the figure are the upper and lower limits referring to $\pm$ 10% of the KEB_{ESF} in order to visualize the error of equation (6.3) versus the PTMSA results. The proposed equation KEB_{ESF} showed good agreement with averages, standard deviations, and coefficient of variation of 1.1, 8.7, and 8.2, respectively. Figure 6.15 illustrates the normalized forces using the proposed equation (6.3) for the investigated columns comparing to the columns' shear capacity and AASHTO-LRFD ESF. The figure showed that the KEB_{ESF} could predict the columns' performance by 100% and 4 out of 4 of the failed columns.

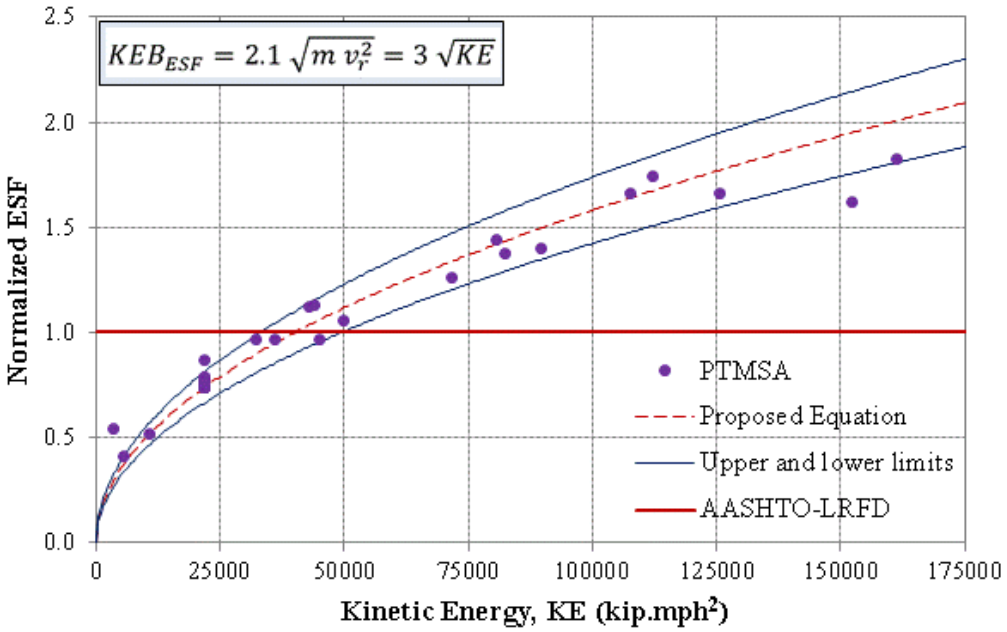

Figure 6.13: Kinetic energy-ESF relation for the proposed equation of KEB_{ESF} and the FE results

6.6 Proposed simplified ESF for adoption by Eurocode

Based on equation (1.1), the EC_{ESF} depends on the vehicle and column deformation as well as the KE. The FE analyses showed that the column displacement is much smaller than the vehicle displacement and can be ignored. Hence, the EC_{ESF} depends on weight and speed of the vehicle. Based on the FE results of EC_{ESF} of the parametric study and using CurveExpert Professional

software and SAS software, a new simplified equation for estimating momentum-based equivalent static force MB_{ESF} is developed and presented in equation (6.4) as below:

$$MB_{ESF} = 13\sqrt{m\, v_r} = 13\sqrt{P_m} \quad (6.4)$$

where MB_{ESF}= proposed ESF to Eurocode (kip), m = the vehicle mass in kip, v_r = the vehicle velocity in mph, and P_m = the momentum of the vehicle in kip.mph

The results of the proposed equations were compared with the FE results of EC_{ESF}. The ESFs of additional fourteen columns collided with SUT trucks of different masses ranged from 18 kips to 90 kips were calculated and compared with the results of equation (6.4). Figure 6.14 illustrates the relation between the momentum of the vehicles and normalized EC_{ESF} as well as between normalized MB_{ESF} and the vehicle momentum for all of the forty-seven columns investigated in this study. Also, shown in the figure are the upper and lower limits referring to $\pm$ 10% of the MB_{ESF} in order to visualize the error of equation (6.4) versus the EC_{ESF} results. The proposed equation MB_{ESF} showed good agreement with averages, standard deviations, and coefficient of variation of 2.9, 6.3, and 2.2, respectively. Figure 6.15 illustrates the normalized forces using the proposed equation (6.4) for the investigated columns comparing to the columns' shear capacity and AASHTO-LRFD ESF. The figure showed that the MB_{ESF} could predict the columns' performance by 94% and 2 out of 4 of the failed columns.

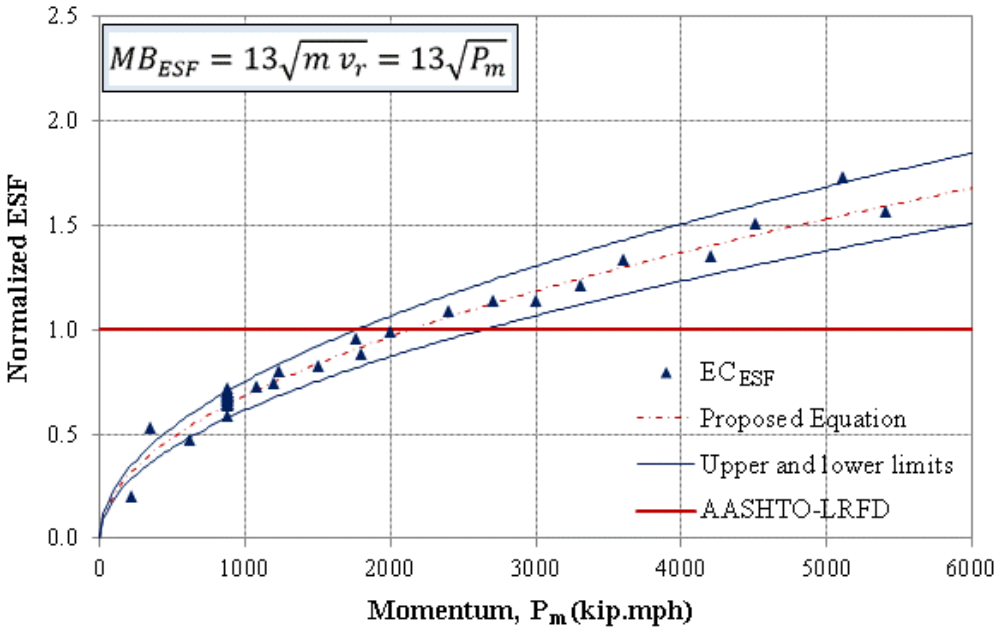

Figure 6.14: Momentum-normalized ESF relation for the proposed equation of MB_{ESF} and the FE results

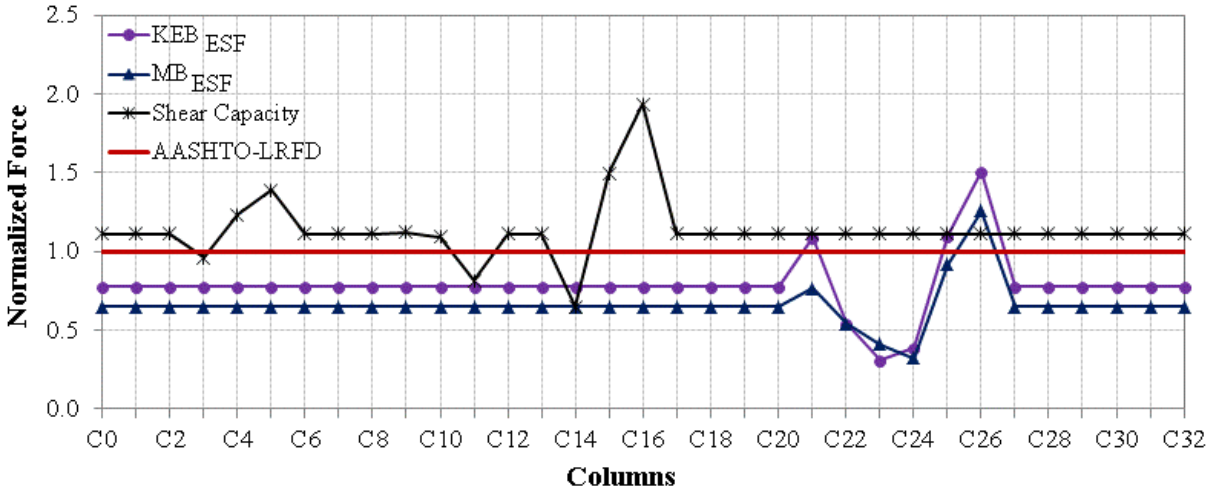

Figure 6.15: Normalized forces of KEB_{ESF} and MB_{ESF} versus the normalized shear capacity and the ESF of AASHTO-LRFD

7. ANALYSIS OF VEHICLE COLLISION WITH HC-FCS BRIDGE COLUMNS

7.1 Research Significance

However, several studies investigated the behavior of the reinforced concrete bridge columns under vehicle impact; very few studies investigated the behavior of other types of bridge columns under vehicle impact. This manuscript used detailed finite element analyses to investigate the behavior of the hollow-core FRP-concrete-steel (HC-FCS) columns under vehicle impact. Comparisons between the ESF of the AASHTO-LRFD (600 kips) and the ESF calculated using different approaches are presented as well.

7.2 Parametric Study

A parametric study was conducted to numerically investigate the behavior of the HC-FCS columns under a vehicle collision. Eleven columns were explored, named C0 to C10. Column C0 was used as a reference column. LS-DYNA was used to examine four different parameters. These parameters included the following:

- Vehicle velocity (v_r) ranging from 20 mph to 70 mph
- Vehicle mass (m) ranging from 4.4 kips to 65 kips
- Unconfined compressive strength (f_c') ranging from 3,000 psi to 10,000 psi
- Material strain rate (SR; considered and not considered)

7.3 FE modelling of HC-FCSs

Figures 7.1a and 7.1b illustrate the FE modeling details of the HC-FCS columns. The inner steel tube was extended inside the footing using an embedded length (L_e) while the FRP tube was stopped at the top of the footing. The steel tube was hollow inside. All of the columns did not include any shear or flexure reinforcement except the steel tube. The columns investigated in this study were supported on a concrete footing which had fixed boundary condition at its bottom. All of the columns were hinged at the top ends. Each column had an outer diameter (D_o) of 5.0 ft. The inner steel tube had a diameter (D_i) of 4.0 ft. and a thickness of 1.05 inch with a diameter-to-thickness ratio (D_i/t_s) of 45. The embedded length of the steel tube inside the footing (L_e) was 6 ft.

representing 1.5 D_i. The thickness of the outer FRP tube was 0.23 inch. The column's height was 25.0 ft. with a span-to-depth ratio (S/D_o) of 5.0. The soil depth above the top of the footing (d_s) was 3.3 ft. Four values of f_c' ranging from 3,000 psi to 10,000 psi were investigated during this study. Axial load (P) was applied on the column representing to 5% of P_o where P_o was calculated by eqn. (2.1).

One-point quadrature solid elements were used to model the sandwiched concrete. A rigid cylinder that was 7.9 inch height, modeled by solid elements, was placed atop the column to avoid excessive local damage to the column's top when the axial loads were applied. Solid elements were used to model the concrete footing. An hourglass control was used to avoid spurious singular modes (e.g., hourglass modes). The hourglass value for each of the models was taken as the default value 0.10, with an hourglass control type_4 (Flanagan-Belytschko stiffness form).

Contact elements surface-to-surface were used to simulate the interface between the concrete column and the FRP tube. They were also used between the concrete column and the steel tube. This type of contact considers slip and separation that occurs between master and slave contact pairs. Hence, slip/debonding will be displayed if either occurs between the concrete wall's surface and the tube's surface. This type of contact was used also between the concrete footing and the steel tube. Node-to-surface contact elements were used between the bottom edges of the FRP tube and the steel tube, and the concrete footing. The coefficient of friction for all of the contact elements was taken as 0.6.

A nonlinear concrete material model (mat72RIII) was used for all columns and footings in this study. An elasto-plastic constitutive model, mat003-plastic_kinamatic, was used for steel tube. The following parameters were needed to define this material model: the elastic modulus (E), the yield stress, and Poisson's ratio. These parameters were assigned the following values: 29,000 ksi, 60,900 psi, and 0.30, respectively (Caltrans 2006). To consider strain rate effect, Cowper-Symonds's model was adopted. The strain rate effect was considered for all of the columns except the column C10.

The FRP material used was modeled as an orthotropic material using "002-orthotropic_elastic" material. This material is defined by several engineering constants: elastic modulus (E), shear modulus (G), and Poisson's ratio (PR), in the three principle axes (a, b and c).

The fiber orientation is defined by a vector. The following characteristics, based on the manufacturer "Grace Composites and FRP Bridge Drain Pipe" were implemented in the FE. The elastic modulus in the hoop direction (Ea), shear modulus in the transverse direction (Gab), and Poisson's ratio of the FRP tube were 3,020 ksi, 406 ksi, and 0.35, respectively. The failure criterion for the FRP, defined as "000-add_erosion," was assigned the ultimate strain of FRP in "EFFEPS" card. The ultimate tensile strain in the hoop direction was 0.013. To consider strain rate effect, Gama and Gillespie (2011) model was adopted.

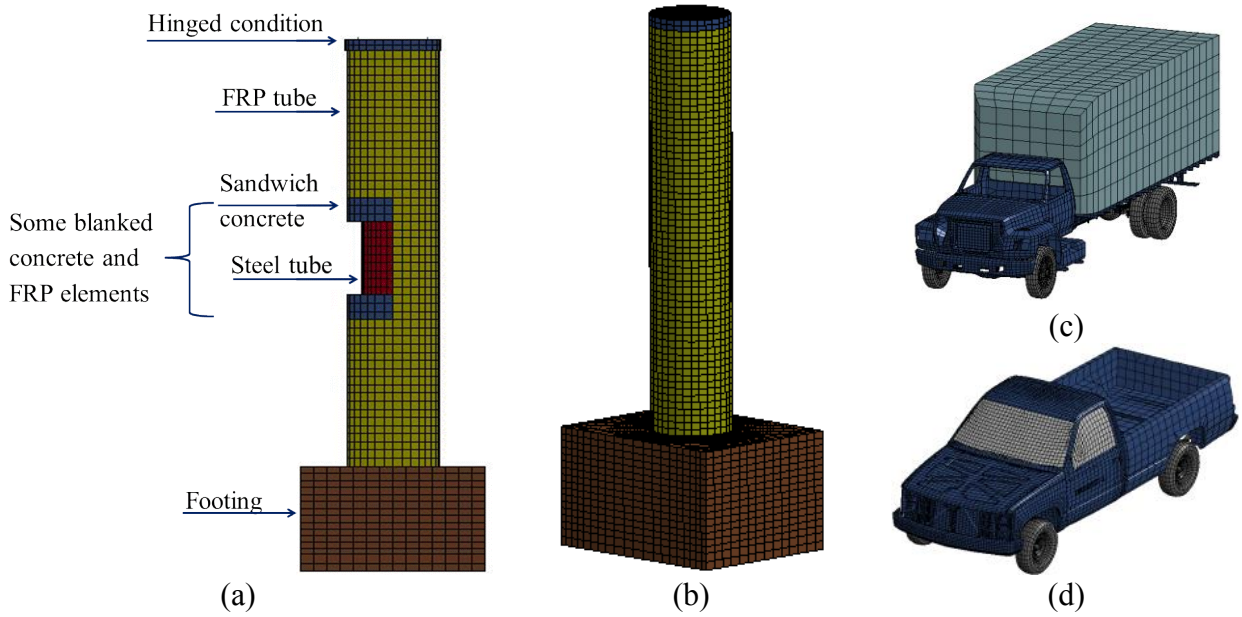

Figure 7.1: F.E. model of the bridge pier "C0" for the parametric study: (a) detailed side view of the pier components, (b) 3D-view, (c) FE model of the Ford single unit truck, (d) FE detailed model of the Chevrolet pickup

7.4 FE modelling of vehicles

Two vehicle models were used in this study: a Ford reduced model (35,353 elements) single unit truck (SUT) and a detailed model (58,313 elements) Chevrolet C2500 Pickup (Figure 7.1c and 7.1d). Different vehicle impact speeds were investigated during this research ranging from 20 mph to 70 mph with 50 mph being the common velocity. The mass of the vehicle ranged from 4.4 kips to 65 kips with 18 kips being the common mass. The Chevrolet C2500 Pickup was used as the vehicle for the mass of 4.4 kips and the Ford SUT was used for the other models. The Ford SUT's mass increased by increasing the value of the added mass. Automatic_surface_to_surface contact

elements by parts with the contact factor SOFT=1 were used between the vehicle and the column. The distance between the vehicle's nose and the column's face was taken as 0.5 ft.

7.5 Results and discussion of the parametric study

7.5.1 General comparisons

Figure 7.2 illustrates the vehicle collision with HC-FCS column. Figure 7.3 illustrates the ESFs and PDFs for all of the columns. As shown in the figure, the differences between the ESF approaches were highly varied from case to case. The SB_{ESF}, in general, represents the upper bound while EC_{ESF}, in general, represents the lower bound of the ESFs. In general, the ESF of the Eurocode (EC_{ESF}) was lower than the ESF of the AASHTO-LRFD except for the columns of the heavy vehicles of masses more than 35 kips.

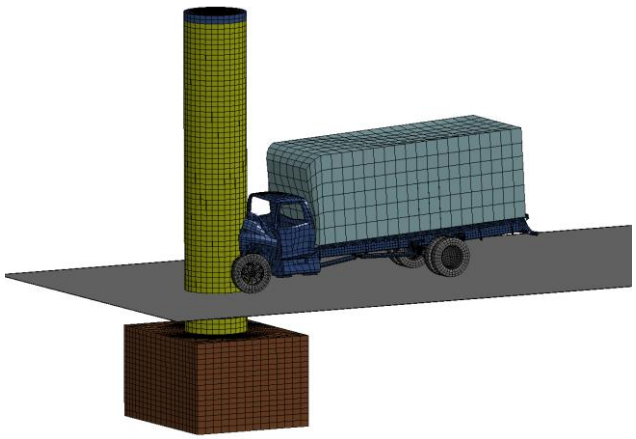

Figure 7.2: Vehicle collision with the HC-FCS column

7.5.2 Vehicle velocity

Four vehicle velocities ranging from 20 mph to 70 mph were investigated during this section. The PDF tended to increase nonlinearly when the vehicle's velocity increased (Figure 7.3a). The PTMSA and EC_{ESF} approximately linearly increased with increasing the vehicle's velocity. However, the SB_{ESF} increased nonlinearly when the vehicle's velocity increased. All of the ESFs were lower than or approximately equal to the ESF of the AASHTO-LRFD.

7.5.3 Vehicle mass

Four vehicle masses ranging from 4.4 kips to 65 kips were investigated during this section. In general, both the PDF and ESF increased linearly when the vehicle's mass increased (Figure 7.3b). The PDF almost did not change when the vehicle mass increased from 4.4 kips to 18 kips because the energy dissipation in the form of inelastic deformations whether in the vehicle or in the column did not significantly change as the kinetic energy was not considerably high. All approaches for calculating ESF resulted in higher values compares to that of the AASHTO-LRFD when the column was collided with heavy vehicles of a weight more than 35 kips.

7.5.4 Unconfined compressive strength (f'_c)

Four values of f'_c ranging from 3,000 psi to 10,000 psi were investigated during this section. The PDF slightly increased when the f'_c increased (Figure 7.3c). The PTMSA and the EC_{ESF} for all of the columns were nearly constant regardless of the f'_c. However, the SB_{ESF} slightly increased when the f'_c increased because of the increase of column's stiffness as the concrete modulus of elasticity increased.

7.5.5 Strain rate effect

The PDF slightly increased when the strain rate effect was included (Figure 7.3d). Including the strain rate effect, the column's strength and stiffness increased leading to higher dynamic forces. However, this higher stiffness resulted in smaller SB_{ESF} because the column's displacement significantly reduced. There is no significant effect of strain rate effect on EC_{ESF} and PTMSA.

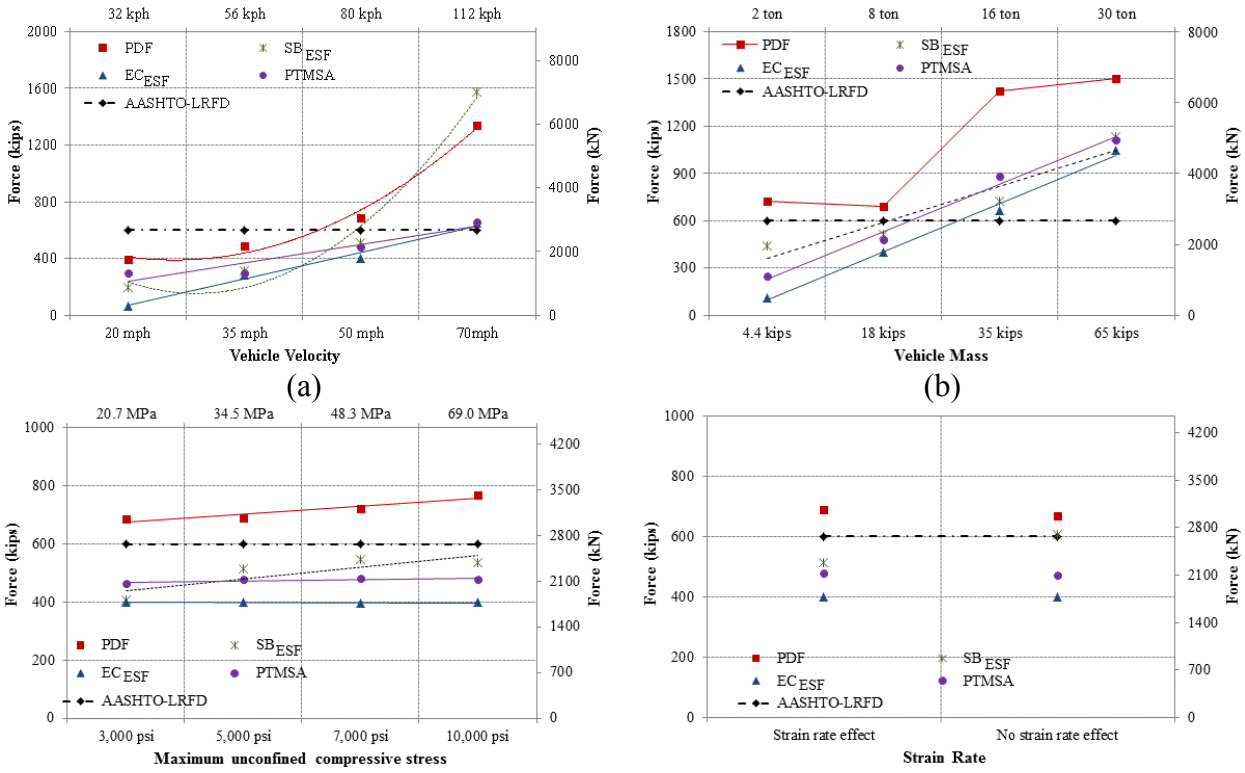

Figure 7.3: Effects of (a) vehicle velocity, (b) vehicle mass, (c) f'_c, and (d) strain rate on PDF and ESF

8. COMPARISONS BETWEEN RC AND HC-FCS BRIDGE COLUMNS UNDER VEHICLE COLLISION

This chapter represents the dynamic behavior of the HC-FCS columns comparable to the dynamic behavior of the RC columns under vehicle collision. Table 8.1 summarizes the examined columns' variables. The investigated HC-FCS and RC columns were designed to have the same flexural capacity to unify the comparison. Each column was collided with three different velocities of 70 mph, 50 mph, and 20 mph. Figure 8.1 illustrates the impact force versus time of each column under different velocities.

The PDFs of the HC-FCS and RC columns collided with vehicle's velocity of 70 mph were 1,532 kips and 2,515 kips, respectively (Fig. 8.1a). The PDF of the HC-FCS column was lower than that of the RC column by approximately 39% when it was collided with a vehicle's velocity of 70 mph. The PDFs of the HC-FCS and RC columns collided with vehicle's velocity of 50 mph were 632 kips and 878 kips, respectively (Fig. 8.1b). The PDF of the HC-FCS column was lower than that of the RC column by approximately 28% when it was collided with a vehicle's velocity of 50 mph. The PDFs of the HC-FCS and RC columns collided with vehicle's velocity of 20 mph were 392 kips and 388 kips, respectively (Fig. 8.1c). The PDFs of the HC-FCS and RC columns were almost the same when it was collided with a vehicle velocity of 20 mph.

The concrete spalling occurred during the vehicle collision with the RC column because of the high local strain (Fig. 8.2a). However, the FRP tube in the HC-FCS column protected the concrete from spalling and increased the ultimate compressive strain by approximately 5 times than that of the RC column (Fig. 8.2b).

Table 8.1: Summary of the examined columns' variables

Column	Diameter (ft)	Height (ft)	Steel tube/reinforcement		FRP tube	
HC-FCS column	5.0	25.0	Diameter (ft)	3.3	Diameter (ft)	5.0
			Thickness (inch)	0.25	Thickness (inch)	0.30
RC column	5.0	25.0	Rebars	24#11	N.A.	

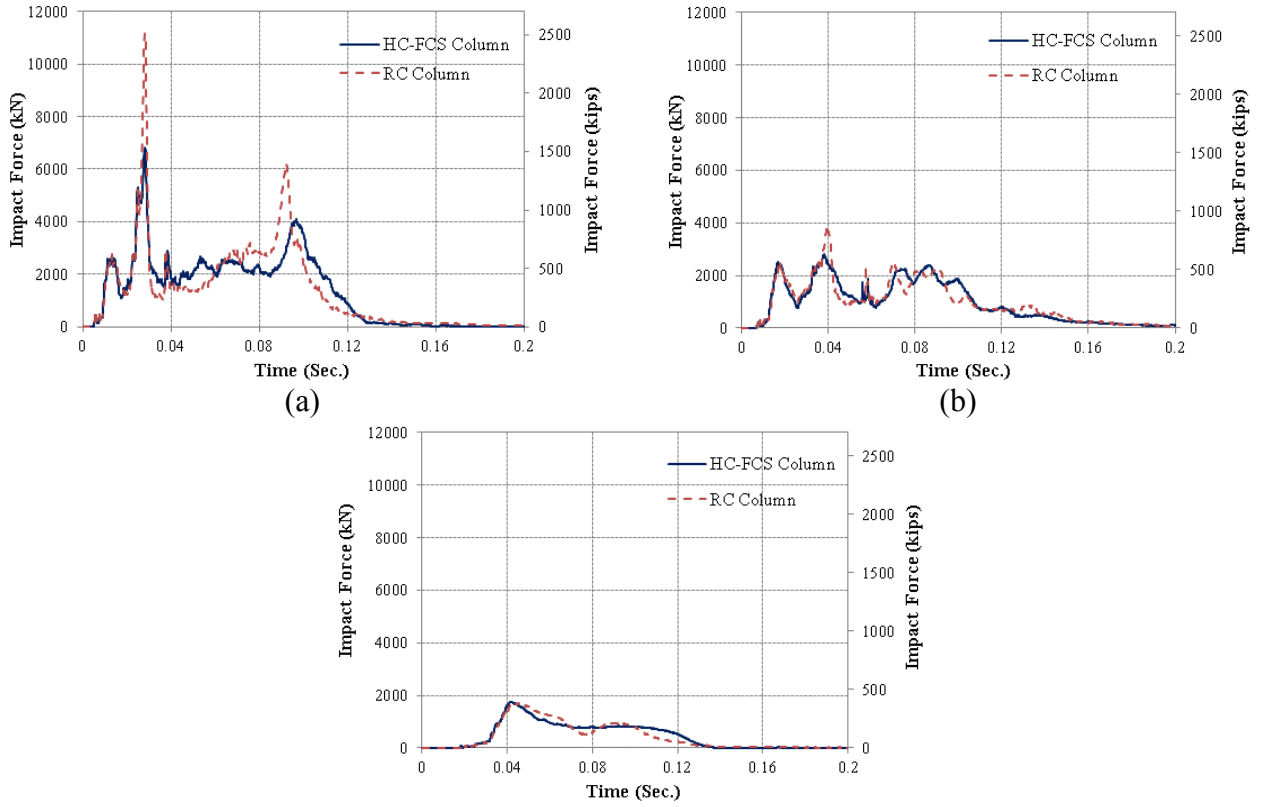

Figure 8.1: Time vs impact force for HC-FCS column and RC column under vehicle collision with a velocity of: (a) 70 mph, (b) 50 mph, and (c) 20 mph

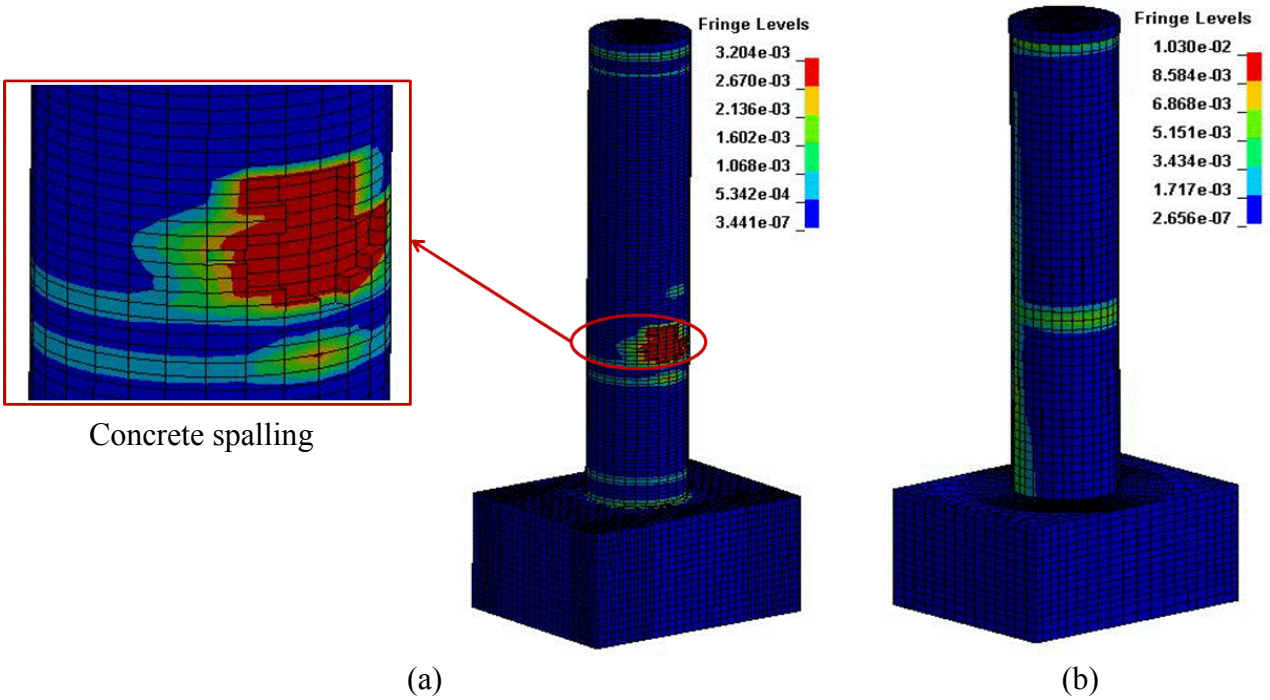

Figure 8.2: Column strain contour: (a) RC column and (b) HC-FCS column

9. CONCLUSIONS AND FUTURE WORK

9.1 Conclusions

This report presented the behavior of HC-FCS columns under axial, combined axial-flexural, and vehicle collision loading. The effects of using different steel tube diameter-to-thickness ratio (D/t), outer FRP tubes with different orientations, and different concrete wall thickness, on the behavior of HC-FCS columns under axial loading were investigated. HC-FCS columns with wet lay-up FRP tubes having $\pm$ 45° exhibited high level of axial strain capacity than that of the unconfined concrete. However, the increase in strength due to confinement was minimal.

HC-FCS columns with wet lay-up FRP tubes having $\pm$ 45° and 0° (hybrid FRP) exhibited high axial strengths and strains. The failure of the HC-FCS columns with hybrid FRP tubes consisted of two stages. The first stage was the rupture of the unidirectional FRP (outer tube) and then the second stage was the reorientation of the angle-plied FRP exhibiting high axial strains. HC-FCS columns having steel tubes of high D/t ratio was not effective in confining the concrete shell. The local buckling of the steel tube affected the overall hoop strain of the FRP tube.

Four large scale columns, a conventionally reinforced concrete (RC) column having solid cross section and three HC-FCS columns were investigated during this study. Each column had an outer diameter of 24 inch and a column's aspect ratio, height-to-diameter ratio, of 4.0. The steel tube was extended inside the footing with an embedded length of 1.6 times the steel tube diameter. While the FRP tube only confined the concrete wall thickness and truncated at the top of the footing level. The hollow steel tube was the only reinforcement for shear and flexure inside the HC-FCS column. The HC-FCS column exhibited high lateral drift reaching 15.2% and failed gradually due to concrete crushing, steel tube local buckling, followed by FRP rupture. The reference RC-column failed at drift of 10.9% due to rebar rupture.

A finite element models were developed and validated against experimental results of small-scale column available in the literature. The proposed model was able to predict the behaviors of the large-scale columns that were tested during this research. The Karagozian and Case Concrete Damage Model Release 3 (K&C model), with automatically generated

parameters, produces good results for concrete modelling, including high strength concrete. An analytical model based on Navier-Bernoulli's assumptions and strains compatibility was also used to predict the HC-FCS's strength. Based on the finite element analyses and analytical model, it is concluded that:

i. The behavior of HC-FCS column is complex and is controlled by the interaction of the stiffness of the steel tube, concrete wall, and FRP. Local buckling occurred in all of the specimens investigated using the finite element analyses, which triggered the rupture of the HC-FCS system. The rate of local buckling propagation depends on the FRP confinement ratio, the steel tube diameter/ steel tube thickness (D/t), concrete unconfined compressive strength, and the concrete wall thickness.
ii. Two modes of failure were defined, namely, steel/concrete compression failure and FRP rupture. Compression failure is relatively gradual while failure due to FRP rupture is quite abrupt.
iii. The bending strength increases as the applied axial load, concrete compressive strength, and number of FRP layers increase.
iv. Keeping the column outer diameter constant and decreasing the concrete wall thickness and/or D/t, increases the column flexural strength.
v. The columns' drifts increase as the applied axial load, unconfined concrete compressive strength, and steel tube D/t decrease. The columns' drifts increase as the FRP layers increase.
vi. The flexural strength slightly increases as the number of FRP layers increases regardless of the steel tube D/t ratio within the range of the parameters investigated in this study.

A detailed description of finite element modeling of vehicle collision with RC bridge columns using LS-DYNA software was presented in this report. Evaluation of the peak dynamic force (PDF) and the equivalent static force (ESF) through an extensive parametric study were conducted. The extensive parametric study investigated the effects of concrete material model, maximum unconfined concrete compressive stress (f_c'), material strain rate, percentage of longitudinal reinforcement, hoop reinforcement, column span-to-depth ratio, column diameter, the top boundary conditions, axial load level, vehicle's velocity, vehicle's mass, clear zone distance, and soil depth above the top of the column footing on the PDF and ESF. Three

approaches were considered during the course of this research to investigate the ESF. In the first approach, SB_{ESF}, the ESF was defined as the force needed to produce the same maximum displacement by a collision event at the point of impact. In the second approach, EC_{ESF}, the ESF was calculated by Eurocode. In the third approach, PTMSA, the ESF was defined as the peak of the 25 millisecond moving average. This study revealed the following findings:

- The AASHTO-LRFD was found to be non-conservative when the column was collided with heavy vehicles of a weight more than 35 kips or high speed vehicle more than 70 mph. In another terms, the AASHTO-LRFD nonconservative for KE higher than 1,800 kip.ft. The AASHTO-LRFD predicted 85% of the columns' performance and predicted only 1 out of 4 of the failed columns.
- A new equation for estimating the ESF based on the vehicle's mass and velocity ($KEB_{ESF} = 33\sqrt{m\ v_r^2}$) with accuracy more than 90% was developed. This approach will allow Departments of Transportation (DOTs) to design different bridge columns to different impact forces depends on the anticipated truck loads and velocities.
- This report simplified the Eurocode equation for estimating the ESF based on the vehicle's mass and velocity ($MB_{ESF} = 130\sqrt{m\ v_r}$) with accuracy more than 90%.
- Approximately 12% of the columns failed while 15% and 73% of the columns were assigned to performance levels P2 and P1, respectively.
- PTMSA approach was the best approach for predicting the columns' performance by 100% and 4 out of 4 of the failed columns while SB_{ESF} predicted 94% of the columns' performance and 4 out of 4 of the failed columns. Furthermore, EC_{ESF} predicted 94% of the columns' performance and 2 out of 4 of the failed columns.
- This study indicated that columns that are 48.0 inch in diameter and smaller are the most vulnerable for shear failure contradicting the AASHTO-LRFD (2012) which states that columns that are 30.0 inch in diameter and smaller are the most vulnerable.
- Different approaches predict different vehicle impact force values and there is no consensus among researchers on the best approach. For a given column and impact scenario, the difference between the estimated maximum and minimum impact force (ESF) ranged from 7% to 140%.
- The SB_{ESF} generally represents the upper bound for 73% of the impact cases while EC_{ESF} represents the lower bound for 85% of the columns.

- The impact demand forces according to SB_{ESF} and PTMSA exceeded the ESF of the AASHTO-LRFD by 27% and 9%, respectively. The ESF of the Eurocode (EC_{ESF}) was typically lower than the ESF of the AASHTO-LRFD.
- Generally, the PDF increases when the longitudinal reinforcement ratio, hoop reinforcement volumetric ratio, column diameter, axial load level, vehicle velocity, and vehicle mass increase and when the strain rate effect is considered. While it decreases when the damage of the column and the clear zone distance increase. However, it is not affected by changing f_c', column top boundary condition, and soil depth.
- The relation between the PDF and the column's span-to-depth ratio was nonlinear.

A detailed description of finite element modeling of vehicle collision with HC-FCS bridge columns using LS-DYNA software was presented in this report. Evaluation of the peak dynamic force (PDF) and the equivalent static force (ESF) through a parametric study were conducted. The parametric study investigated the effects of the vehicle velocity, vehicle mass, unconfined concrete compressive stress (f_c'), and material strain rate were carried out. The three approaches of estimating the ESF were investigated. This study revealed the following findings:

- The AASHTO-LRFD was found to be non-conservative when the column was collided with heavy vehicles of a weight more than 35 kips.
- The difference between the ESF calculated by the different approaches highly varied.
- The SBESF generally represents the upper bound of the ESF while EC_{ESF} represents the lower bound.
- The ESF of the Eurocode (EC_{ESF}) was typically lower than the ESF of the AASHTO-LRFD.
- Generally, the PDF increases when the f_c', vehicle velocity, and vehicle mass increase and when the strain rate effect is considered.

The dynamic behavior of the HC-FCS columns was compared to the dynamic behavior of the RC columns under vehicle collision. Each column was collided with three different velocities of 70 mph, 50 mph, and 20 mph. The PDFs were calculated and compared for each case. The PDF values of the HC-FCS columns were lower than those of the RC column by approximately 28% - 39% when they were collided with vehicles having velocities ranging from 50 mph to 70 mph. The vehicles mass was 18 kips. The PDFs of the HC-FCS and RC columns were approximately equal when they were collided with a vehicle having velocity of 20 mph.

Concrete spalling occurred during the vehicle collision with the RC column because of high local strains. However, the FRP tube in the HC-FCS column protected the concrete from spalling and increased the ultimate compressive strain by approximately 5 times than that of the RC column.

9.2 Future work

While an extensive research was carried out during the current project, including testing on small-scale cylinders, large-scale testing, analytical modeling, and finite element modeling under lateral and vehicle impact, there remain few issues that need to be addressed before field implementation of HC-FCS. Future work is required to address the following issues:

- Optimize the manufacturing of the FRP tube. This includes the effects of fiber orientation, resin type, and using thicker FRP tube at the potential plastic hinges.
- Flexural-shear interaction of HC-FCS. For short columns, there will be an interaction between the shear and flexural strength of the columns. This interaction may reduce the flexural capacity of the column.
- Shear strength of HC-FCS. The contribution of steel tube, concrete shell, and FRP tube to the shear strength need to be determined.
- Determine the required steel tube embedment length to achieve full fixation and avoid pull-out of the column from footing. The embedment length needs to be a function in tube diameter, yield strength, thickness, and concrete strength.
- Develop and test a cap-beam column connection.
- Torsion strength of the column. Skew and curved bridges may induce torsion on columns. The contribution of concrete, FRP tube, and steel tube to torsional resistance need to be investigated.
- Durability studies of the steel encased into the concrete and FRP tube is required.

10.REFERENCES

AASHTO, (2012), AASHTO-LRFD Bridge Design Specifications – Customary US Units, sixth edition, Washington, DC.

AASHTO, (2010), AASHTO-LRFD Bridge Design Specifications – Customary US Units, fifth edition, Washington, DC.

Abdelkarim, O. and ElGawady, M. (2014a). "Behavior of Hybrid FRP-Concrete-Steel Double-Skin Tubes Subjected to Cyclic Axial Compression." Structures Congress 2014: pp. 1002-1013.

Abdelkarim, O. and ElGawady, M. (2014b). "Analytical and Finite-Element Modeling of FRP-Concrete-Steel Double-Skin Tubular Columns." J. Bridge Eng., 10.1061/(ASCE)BE.1943-5592.0000700 , B4014005.

Agrawal, A. K., Liu, G., and Alampalli, S. (2013). "Effects of Truck Impacts on Bridge Piers." Advanced Materials Research, 639-640, pp.13-25.

Agrawal, A.K. (2011). "Bridge Vehicle Impact Assessment: Final Report." University Transportation Research Center and New York State Department of Transportation.

Alias, M.N. and R. Brown, 1992, Corosion, 48: 373-378.

American Concrete Institute (ACI) Committee 318 (2011). "Building Code Requirements for Structural Concrete (ACI 318-11) and Commentary (318R-11)." ACI, Farmington Hills, Mich., 509 pp.

American Concrete Institute (ACI) Committee 440 (2008). "Guide for the Design and Construction of Externally Bonded FRP Systems for Strengthening Concrete Structures." ACI 440.2R-08, 2008, Farmington Hills, MI.

American Concrete Institute (ACI) Committee 440 (2007). "Report on Fiber-Reinforced Polymer (FRP) Reinforcement for Concrete Structures." ACI 440R-07, 2007, Farmington Hills, MI.

Amir Fam, Andrew Kong, and Mark F. Green. (2008) "Effects of freezing and thawing cycles and sustained loading on compressive strength of precast concrete composite piles." PCI journal, V. 53, No. 1, January–February 2008, pp. 109–120.

Ashbee K and Wyatt R. (1969), "Water damage in glass fibre/resin composites." Proceedings of the Royal Society of London. Series A, Mathematical and Physical Sciences, Vol. 312, No. 1511 (Sep. 30, 1969), pp. 553-564.

Ashbee, K. H. G. 1989. Fundamental Principles of Fiber Reinforced Composites, Lancaster, PA: Technomic Publishing CO. Inc.

ASTM Standard A1067, 2012, "Test Coupons for Steel Castings," ASTM International, West Conshohocken, PA, 2012, 10.1520/A1067_A1067M-12A.

ASTM Standard D3039, 2008, Standard Test Method for Tensile Properties of Polymer Matrix Composite Materials," ASTM International, West Conshohocken, PA, 2008, 10.1520/D3039_D3039M-08.

Au, C. and Buyukozturk, O. (2005). ”Effect of Fiber Orientation and Ply Mix on Fiber Reinforced Polymer-Confined Concrete.” J. Compos. Constr., 9(5), 397–407.

Bala, S. (2001). “Contact Modeling in LS-DYNA.” Livermore Software Technology Corporation.

Balazs, G. and Borosnyoi, A. (2001). “Long-Term Behavior of FRP.” Composites in Construction: pp. 84-91. doi: 10.1061/40596(264)10.

Benmokrane, B., Wang, P., Ton-That, T., Rahman, H., and Robert, J. (2002). “Durability of Glass Fiber-Reinforced Polymer Reinforcing Bars in Concrete Environment.” J. Compos. Constr., 6(3), 143–153.

Bischoff, P.H., Perry, S.H., “Compressive Behavior of Concrete at High Strain Rates.” Materials and Structures, Vol. 24, 1991, pp. 425-450.

Bowles, J. (1988) “Foundation Analysis and Design.” McGraw-Hill Inc., United States of America, 1004 pp.

Bradshaw RD, Brinson LC. (1997). “Physical aging in polymer composites: an analysis and method for time aging time superposition.” Polymer Engineering & Science, Volume 37, Issue 1, pp. 31–44, January 1997.

Buth, C. E., Williams, W. F., Brackin, M. S., Lord, D., Geedipally, S. R., and Abu-Odeh, A. Y. (2010). “Analysis of Large Truck Collisions with Bridge Piers: Phase 1.” Texas Department of Transportation Research and Technology Implementation Office, 9-4973-1.

Buth, C. E., Brackin, M. S., Williams, W. F., and Fry, G.T. (2011). “Collision Loads On Bridge Piers: Phase 2.” Texas Department of Transportation Research and Technology Implementation Office, Report 9-4973-2.

California Department of Transportation. (2006). “Seismic Design Criteria”. California Department of Transportation, Rev. 1.4.

Campbell, J.D. (1954). “The yield of mild steel under impact loading.” Journal of the Mechanics and Physics of Solids, 3, 54-62.

Charles, RJ. (1959), “The strength of silicate glasses and some crystalline oxides [chapter 12]”.

Cheikh, A.Al. and Murat, M. (1988). “Kinetics of Non-Congruent Dissolution of E-Glass Fiber in Saturated Calcium Hydroxide Solution.” Cement and Concrete Research, Volume 18, Issue 6, November 1988, Pages 943–950.

Chen Y, Davalos JF, Ray I, Kim HY. (2007). “Accelerated aging tests for evaluation of durability performance of FRP reinforcing bars reinforcing bars for concrete structures” Composite Structures, Volume 78, Issue 1, March 2007, pp. 101–111.

Chin JW, Aouadi K, Nguyen T. (1997) “Effects of environmental exposure on fiber-reinforced plastic (FRP) materials used in construction.” J Compos Technol Res 1997; 19(4):205–13.

Comité Euro-International du Béton. (1993). “CEB-FIP Model Code 1990.” Redwood Books, Trowbridge, Wiltshire, UK.

Cowper, G. R. and Symonds, P. S. (1957). “Strain Hardening and Strain Rate Effects in Impact Loading of Cantilever Beams.” Brown University, App. Math. Report No. 28.

D’Almieda. J. R. M. 1991. Composite Materials, 15: 117-132.

Dawood, H., ElGawady, M. (2013). “Performance-based seismic design of unbonded precast post-tensioned concrete filled GFRP tube piers” Composites Part B: Engineering, Volume 44, Issue 1, Pages 357-367.

Dawood, H., ElGawady, M., and Hewes, J. (2012). “Behavior of Segmental Precast Post-Tensioned Bridge Piers under Lateral Loads.” ASCE Journal of Bridge Engineering, Vol. 17, No. 5, pp. 735-746.

Earl, J.S. and Shenoi, R.A. (2004). “Hygrothermal ageing effects on FRP laminate and structural foam materials.” Composites Part A: Applied Science and Manufacturing. Volume 35, Issue 11, November 2004, pp. 1237-1247.

ElGawady, M. and Dawood, H. (2012). “Analysis of segmental piers consisted of concrete filled FRP tubes.” Engineering Structures, Vol. 38, pp. 142-152.

ElGawady, M. and Sha’lan, A. (2011). ”Seismic Behavior of Self-Centering Precast Segmental Bridge Bents.” J. Bridge Eng., 16(3), 328–339.

ElGawady, M., Booker, A., and Dawood, H. (2010). ”Seismic Behavior of Posttensioned Concrete-Filled Fiber Tubes.” J. Compos. Constr., 14(5), 616–628.

El-Tawil, S., Severino, E., and Fonseca, P. (2005). “Vehicle Collision with Bridge Piers.” J. Bridge Eng., 10(3), 345-353.

Eurocode 1: Actions on structures – Part 1-1: General actions – Densities, self-weight, imposed loads for buildings, Final Draft prEN 1991-1-1, October 2002.

Evans, K. E. B. D. Caddock and K. L. Ainsworth. 1988, Journal of Material Science 23: 2926-2930.

Fabio Nardone, Marco Di Ludovico, Francisco J. De Caso y Basalo, Andrea Prota, Antonio Nanni, (2012) "Tensile behavior of epoxy based FRP composites under extreme service conditions" Composites Part B: Engineering Volume 43, Issue 3, April 2012, pp. 1468-1474.

Fakharifar, M., Sharbatdar, M. K., Lin, Z., Dalvand, A., Sivandi-Pour, A., & Chen, G. (2014). Seismic performance and global ductility of RC frames rehabilitated with retrofitted joints by CFRP laminates. Earthquake Engineering and Engineering Vibration, 13(1), 59-73. DOI: 10.1007/s11803-014-0212-6.

Fam, A. Z.; Schnerch, D.; and Rizkalla, S. H., 2002, "Moisture Effect on Durability of Concrete-Filled GFRP Tubular Piles." NCSU-CFL Report No. 02-04, Constructed Facilities Laboratory, North Carolina State University, Raleigh, NC.

Fouche, P., Bruneau, M. (2010). "Non-Linear Analysis of Multi-Hazard Performance of Cylindrical Concrete Filled Steel Tubes Bridge Piers." Proceedings of 8th International Conference on Short and Medium Span Bridges, Canada.

Francesco Micelli and Antonio Nanni, "Durability of FRP rods for concrete structures." Construction and Building Materials 18 (2004) pp. 491–503.

Fu, H.C., Erki, M.A., Seckin, M., "Review of Effects of Loading Rate on Reinforced Concrete," Journal of Stru. Eng., Vol. 117, No. 12, December 1991, pp. 3660-3679.

Gama, BA., Gillespie, JW. (2011). "Finite element modeling of impact, damage evolution and penetration of thick-section composites." International Journal of Impact Engineering, 38 (4), pp. 181-197.

Gentry, T.R., Bank, L.C., Barkatt, A., and Prian, L. (1998). "Accelerated Test Methods to Determine the Long-Term Behavior of Composite Highway Structures Subject to Environmental Loading." Journal of Composites Technology & Research, JCTRER, Vol. 20, No.1, January 1998, pp.38-50.

Hajjar J. (2000). "Concrete-filled steel tube columns under earthquake loads." Structural Engineering and Materials; 2(1):72–82.

Han, L.H., Tao, Z., Liao, F.Y., and Xu, Y. (2010). “Tests on Cyclic Performance of FRP-Concrete –Steel Double-Skin Tubular Columns.” Thin-Walled Structures, 4, 430-439.

Han L.H., Huang H., Tao Z. and Zhao X.L. (2006). “Concrete-filled double skin steel tubular (CFDST) beam-columns subjected to cyclic bending”, Engineering Structures, Vol.28, No.12, 1698–714.

Harik, I., Shaaban, A., Gesund, H., Valli, G., and Wang, S. (1990). ”United States Bridge Failures, 1951–1988.” J. Perform. Constr. Facil., 4(4), 272–277.

Holmes, T.M., Leatherman, G.L. and El-Korchi, T. (1991). “Alkali-Resistant Oxynitride Glasses.” Journal of Material Research, Vol. 6, No. 1, Jan 1991, pp. 152-158.

Huang, H., Han, L. H., Zhao, X. (2013). “Investigation on concrete filled double skin steel tubes (CFDSTs) under pure torsion” Journal of Constructional Steel Research, Volume 90, 221-234.

Joannie W. Chin, Khaled Aouadi, Michael R. Haight, William L. Hughes, and Tinh Nguyen, (2001), “Effects of Water, Salt Solution and Simulated Concrete Pore Solution on the Properties of Composite Matrix Resins Used in Civil Engineering Applications.” Polymer Composites, April 2001, vol. 22, no. 22, pp. 282-298.

Jones, F. R. J. W. Rock and A. R. Wheatley. 1983, Journal of Composite Materials, 14: 213-232.

Karbhari, V.M., Murphy K., and Zhang, S. (2002). “Effect of Concrete Based Alkali Solutions on Short-Term Durability of E-Glass/Vinylester Composites.” Journal of Composite Materials, September 2002, vol. 36 no. 17, pp. 2101-2121.

Kootsookos, A, Mouritz, A.P, St John, N.A. (2001). “Comparison of the Seawater Durability of Carbon- and Glass-Polymer composites.” ICCM-13, 2001, Beijing, China.

Lawrence C. Bank, T. Russell Gentry, Benjamin P. Thompson and Jeffrey S. Russell. (2003). “A model specification for FRP composites for civil engineering structures.” Construction and Building Materials 17(2003), pp. 405–437.

Li, W., Han,L. H., Chan, T. (2014a). “Tensile behaviour of concrete-filled double-skin steel tubular members” Journal of Constructional Steel Research, Volume 99, 35-46

Li, W., Han,L. H., Chan, T. (2014b). “Numerical investigation on the performance of concrete-filled double-skin steel tubular members under tension” Thin-Walled Structures, Volume 79, 108-118.

Lima Sobrinho, Ledjane; Ferreira, Marysilvia and Bastian, Fernando Luiz. (2009). “The effects of water absorption on an ester vinyl resin system.” Mat. Res. 2009, vol.12, n.3, pp. 353-361.

LS-DYNA. (2007). “Keyword user’s manual.” Livermore Software Technology Corporation, CA.

Lu, H., Zhao, X., Han, L. H. (2010). “Testing of self-consolidating concrete-filled double skin tubular stub columns exposed to fire” Journal of Constructional Steel Research, Volume 66, Issues 8–9, 1069-1080

Kansas Department of transportation. (2013). “Bridge LRFD Design Manual”.

Malvar, L. J. and Ross, C. A. (1998). “Review of Strain Rate Effects for Concrete in Tension.” ACI Materials Journal, 95, 735-739.

Malvar, L., Crawford, J., Wesevich, J., and Simons, D. (1997). “A plasticity concrete material model for DYNA3D.” Int. J. Impact Eng., 19(9–10), 847–873.

Mathieu Robert and Brahim Benmokrane (2013), “Combined effects of saline solution and moist concrete on long-term durability of GFRP reinforcing bars.” Construction and Building Materials. Volume 38, January 2013, pp. 274-284.

Mathieu Robert and Amir Fam, (2012), “Long-Term Performance of GFRP Tubes Filled with Concrete and Subjected to Salt Solution.” J. Compos. Constr., 16(2), 217–224.

McBagonluri, F., Garcia, K., Hayes, M., Verghese, K.N.E., Lesko, J.J. (2000). “Characterization of fatigue and combined environment on durability performance of glass/vinyl ester composite for infrastructure applications.” International Journal of Fatigue, Volume 22, Issue 1, January 2000, pp. 53–64.

McGrath, J.J. (2013). “Replacement of Missouri Route M Overpass Creamed by Freight-Train Crash in Scott County Estimated to Cost about $3 Million: Accident is the Third Railroad Mishap in Four Months in Rockview- May 26, 2013” International Business times, http://www.ibtimes.com/replacement-missouri-route-m-overpass-creamed-freight-train-crash-scott-county-estimated-cost-about, Accessed by July, 2014.

Mehta, K.P., Monteiro, P.J.M. (2006). “CONCRETE: Microstructure, Properties, and Materials” 3rd Edition, McGraw-Hill Inc., United States of America, 660 pp.

Micelli, F., and Myers, J.J. (2008), “Durability of FRP-confined concrete”. Proceedings of the ICE-Construction Materials, Volume 161, Issue 4, 01 November 2008, pp. 173-185.

Miguel A. Pando, Carl D. Ealy, George M. Filz, J.J. Lesko, and E.J. Hoppe, (2006), “A Laboratory and Field Study of Composite Piles for Bridge Substructures”. Report No. FHWA-HRT-04-043.

Miguel Pando, Jack Lesko, Amir Fam, and Sami Rizkalla. (2002). “Moisture Effect on Durability of Axially Loaded Concrete-Filled Tubular FRP Piles.” 2nd Int. Conf. on Durability of FRP Composites in Construction, CDCC 2002, Sherbrooke, May 29-31, pp. 25-37.

Mohan, P., Marzougui, D., Kan, C. (2003). “Validation of a Single Unit Truck Model for Roadside Hardware Impacts.” NCAC, The George Washington University.

Montague, P., (1978). “Experimental behavior of double-skinned, composite, circular cylindrical-shells under external-pressure”. Journal of Mechanical Engineering Science, 20(1), pp. 21–34.

Moon, J., Lehman, D., Roeder, C., and Lee, H. (2013). ”Strength of Circular Concrete-Filled Tubes with and without Internal Reinforcement under Combined Loading.” J. Structural Engineering, 139(12).

Moore, M. A. and H. H. Epps, 1992. Journal of Testing and Evaluation, 20(2): 139-143.

Ozbakkaloglu, T. and Idris, Y. (2014). ”Seismic Behavior of FRP-High-Strength Concrete–Steel Double-Skin Tubular Columns.” J. Struct. Eng., 140(6), 04014019.

Ozbakkaloglu, T. and Fanggi, B. (2013). "Axial Compressive Behavior of FRP-Concrete-Steel Double-Skin Tubular Columns Made of Normal- and High-Strength Concrete." J. Compos. Constr., 10.1061/(ASCE)CC.1943-5614.0000401 , 04013027.

Phani, K. K. and Bose, N. R. (1987), “Temperature Dependence of Hydrothermal Ageing of CSM-Laminate During Water Immersion.” Composites Science and Technology, Volume 29, Issue 2, 1987, pp. 79–87.

Piyush K. Dutta and David Hui, (1996), “Low-temperature and freeze-thaw durability of thick composites.” Composites Part B: Engineering. Volume 27, Issues 3–4, 1996, pp. 371-379.

Rivera, J. and Karbhari, V. M. (2001), “Characterization of Sub-Zero Response of Vinylester FRP in Civil Infrastructure Renewal.” The Eleventh International Offshore and Polar Engineering Conference, 17-22, June 2001, Stavanger, Norway.

Robert, M., Wang, P., Cousin, P., and Benmokrane, B. (2010). “Temperature as an Accelerating Factor for Long-Term Durability Testing of FRPs: Should There Be Any Limitations?” J. Compos. Constr., 14(4), 361–367.

Ryu, D., Wijeyewickrema, A., ElGawady, M., and Madurapperuma, M. (2014). "Effects of Tendon Spacing on In-Plane Behavior of Post-Tensioned Masonry Walls." J. Struct. Eng., 140(4), 04013096.

Sachin Kshirsagar, Roberto A. Lopez-Anido, and Rakesh K. Gupta, (2000), "Environmental Aging of Fiber-Reinforced Polymer-Wrapped Concrete Cylinders." ACI Material Journal, Volume 97, Issue 6, pp. 703-712.

Shakir-Khalil, H., and Illouli, S. 1987. "Composite columns of concentric steel tubes." Proc., Conf. on the Design and Construction of Non-Conventional Structures, Vol. 1, London, pp. 73–82.

Sharma, H., Hurlebaus, S., Gardoni, P. (2012). "Performance-based response evaluation of reinforced concrete columns subject to vehicle impact." Inter. Journal of Impact Eng., (43), 52-62.

Shin, M. and Andrawes, B. (2010). "Experimental Investigation of Actively Confined Concrete Using ShapeMemory Alloys". J. Eng. Struct. 32:3, 656-664.

Siddhwartha Mandal, Andrew Hoskin, and Amir Fam. (2005). "Influence of Concrete Strength on Confinement Effectiveness of Fiber-Reinforced Polymer Circular Jackets." ACI Structural Journal; May 2005, Vol. 102 Issue 3, p383.

Sierakowsi, R. L. and Chaturved, S. K. (1997). "Dynamic Loading and Characterization of Fiber-Reinforced Composites," John Wiley & Sons, Inc., New York, USA.

Silva, M., Cidade, M., Biscaia, H., and Marreiros, R. (2014). "Composites and FRP-Strengthened Beams Subjected to Dry/Wet and Salt Fog Cycles." J. Mater. Civ. Eng., 10.1061/(ASCE), 2014, MT.1943-5533.0001008 , 04014092.

Soles CL, Chang FT, Bolan BA, Hristov HA, Gidley DW, Yee AF. (1998). "Contributions of the nanovoid structure to the moisture absorption properties of epoxy resins." Journal of Polymer Science Part B: Polymer Physics. Volume 36, Issue 17, pp. 3035–3048, December 1998.

Tannous FE, Saadatmanesh H. (1998). "Environmental effects on the mechanical properties of E-glass FRP rebars." ACI Materials Journal, Volume 95, Issue 2, pp. 87-100.

Teng, J. G., Yu, T., Wong, Y. L., and Dong, S. L. (2007). "Hybrid FRP concrete-steel tubular columns: Concept and behavior." Constr. Build. Mater., 21(4), 846–854.

Teng, J.G., Yu, T., Wong, Y.L., and Dong, S.L. (2005). "Innovative FRP-Steel-Concrete Hybrid Columns." Advances in Steel Structures, 1, 545-554.

Teng, J.G., Yu, T., and Wong, Y.L. (2004). "Behavior of Hybrid FRP-Concrete-Steel Double-Skin Tubular Columns." Proc. 2nd Int. Conf. on FRP Composites in Civil Engineering, Adelaide, Australia, 811-818.

Thilakarathna, H.M.I., Thambiratnam, D.P., Dhanasekar, M., Perera, N. (2010). "Numerical simulation of axially loaded concrete columns under transverse impact and vulnerability assessment." Inter. Journal of Impact Eng., (37), 1100-1112.

Tucker, W. C. and R. Brown. 1989. Journal of Composite Materials, 23: 787-797.

Underwood, J. H. and A. A. Kapusta. 1991. Journal of Composites Technology and Research, 13: 179-182.

Wassim Naguib and Amir Mirmiran. (2002). "Time-Dependent Behavior of Fiber-Reinforced Polymer Confined Concrete Columns under Axial Loads." ACI Structural Journal, V. 99, No. 2, March-April 2002.

Williams, M.S., "Modeling of Local Impact Effects on Plain and Reinforced Concrete." ACI Structural Journal, Vol. 91, No. 2, March-April 1994, pp. 178-187.

Wolff, E. G. 1993, Sample Journal, 29(3):11-19.

Wong, Y. L., Yu, T., Teng, J. G., and Dong, S. L. (2008). "Behavior of FRP-confined concrete in annular section columns." Compos. B Eng., 39(3), 451–466.

Yagishita F, Kitoh H, Sugimoto M, Tanihira T, Sonoda K. (2000). "Double-skin composite tubular columns subjected cyclic horizontal force and constant axial force." Proceedings of the Sixth ASCCS Conference, Los Angeles, USA, March 22–24, pp. 497–503.

Yan, X. and Yali, S. (2012). "Impact Behaviors of CFT and CFRP Confined CFT Stub Columns." J. Compos. Constr., 16(6), 662–670.

Yilmaz, V.T. (1992). "Chemical attack on alkali-resistant glass fibers in a hydrating cement matrix: characterization of corrosion products." Journal of Non-Crystalline Solids, Volume 151, Issue 3, 2 December 1992, pp. 236–244.

Yu, T., Cao, Y., Zhang, B. & Teng, J. G. (2012). Hybrid FRP-concrete-steel double-skin tubular columns: Cyclic axial compression tests. 6th International Conference on FRP Composites in Civil Engineering (pp. 1-8).

Yu, T., Teng, J., and Wong, Y. (2010). "Stress-Strain Behavior of Concrete in Hybrid FRP-Concrete-Steel Double-Skin Tubular Columns." J. Struct. Eng., 136(4), 379–389.

Yu, T., Wong, Y., Teng, J., Dong, S., and Lam, E. (2006). "Flexural Behavior of Hybrid FRP-Concrete-Steel Double-Skin Tubular Members." J. Compos. Constr., 10(5), 443–452.

Yu, T., Wong, Y.L., Teng, J.G., and Dong, S.L., (2004). “Structural behavior of hybrid FRP-concrete-steel double-skin tubular columns.” ANCER Annual Meeting: Networking of Young Earthquake Engineering Researchers and Professionals, Honolulu, Hawaii

Zaouk, A., Bedewi N.E., Kan, C.D., Marzougui, D. (1996). ”Validation of a Non-Linear Finite Element Vehicle Model Using Multiple Impact Data.” International Mechanical Engineering Congress and Exposition, Atlanta, GA.

Zaouk, A. K., Bedewi, N. E., Kan, C. D., and Marzoughi, D. (1996). “Evaluation of a Multi-purpose Pick-up Truck Model Using Full Scale Crash Data with Application to Highway Barrier Impact.” 29th Inter. Sym. on Auto. Tech. and Auto., Florence, Italy.

Zhang, B., Teng, J. G. and Yu, T. (2012). “Behaviour of hybrid double-skin tubular columns subjected to combined axial compression and cyclic lateral loading.” Sixth International Conference on FRP Composites in Civil Engineering (pp. 1-7). Rome, Italy.

Zhao, X., Bai, Y., Al-Mahaidi, R., and Rizkalla, S. (2014). ”Effect of Dynamic Loading and Environmental Conditions on the Bond between CFRP and Steel: State-of-the-Art Review”. J. Compos. Constr. 18, Special Issue: 10th Anniversary of IIFC, A4013005. 2014.

Zhu, Z., Ahmad, I., and Mirmiran, A. (2006). “Seismic performance of concrete-filled FRP tube columns for bridge substructure.” J. Bridge Eng., 11(3), 359–370.

11.APPENDIX A: SUMMARY OF COLUMNS RESULTS

11.1 F4-24-RC column

11.1.1 Force-Curvature relations

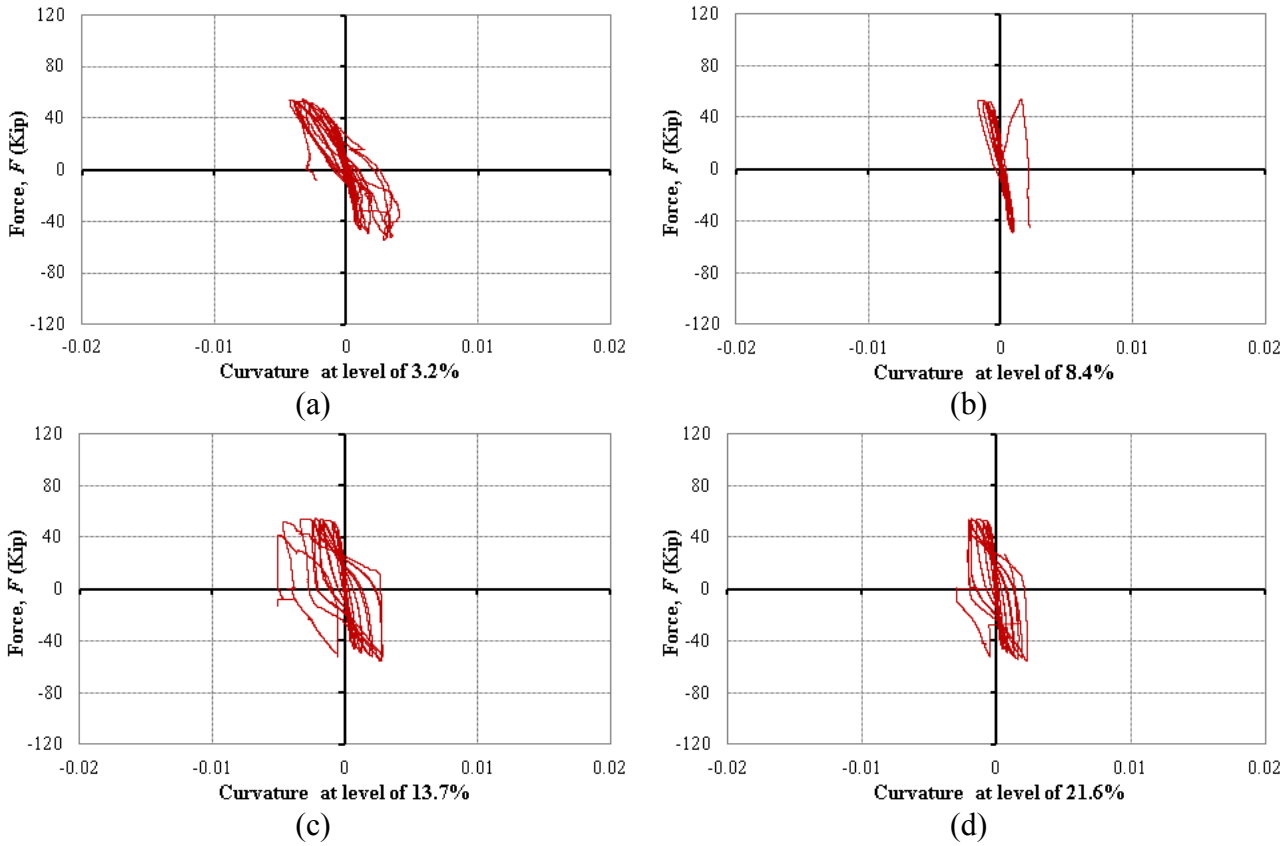

Figure 11.1: Force-curvature relation of the F4-24-RC column: (a) at level of 3.2% of the column's height, (b) at level of 8.4% of the column's height, (c) at level of 13.7% of the column's height, and (d) at level of 21.6% of the column's height

11.1.2 Lateral drift-steel strain relations

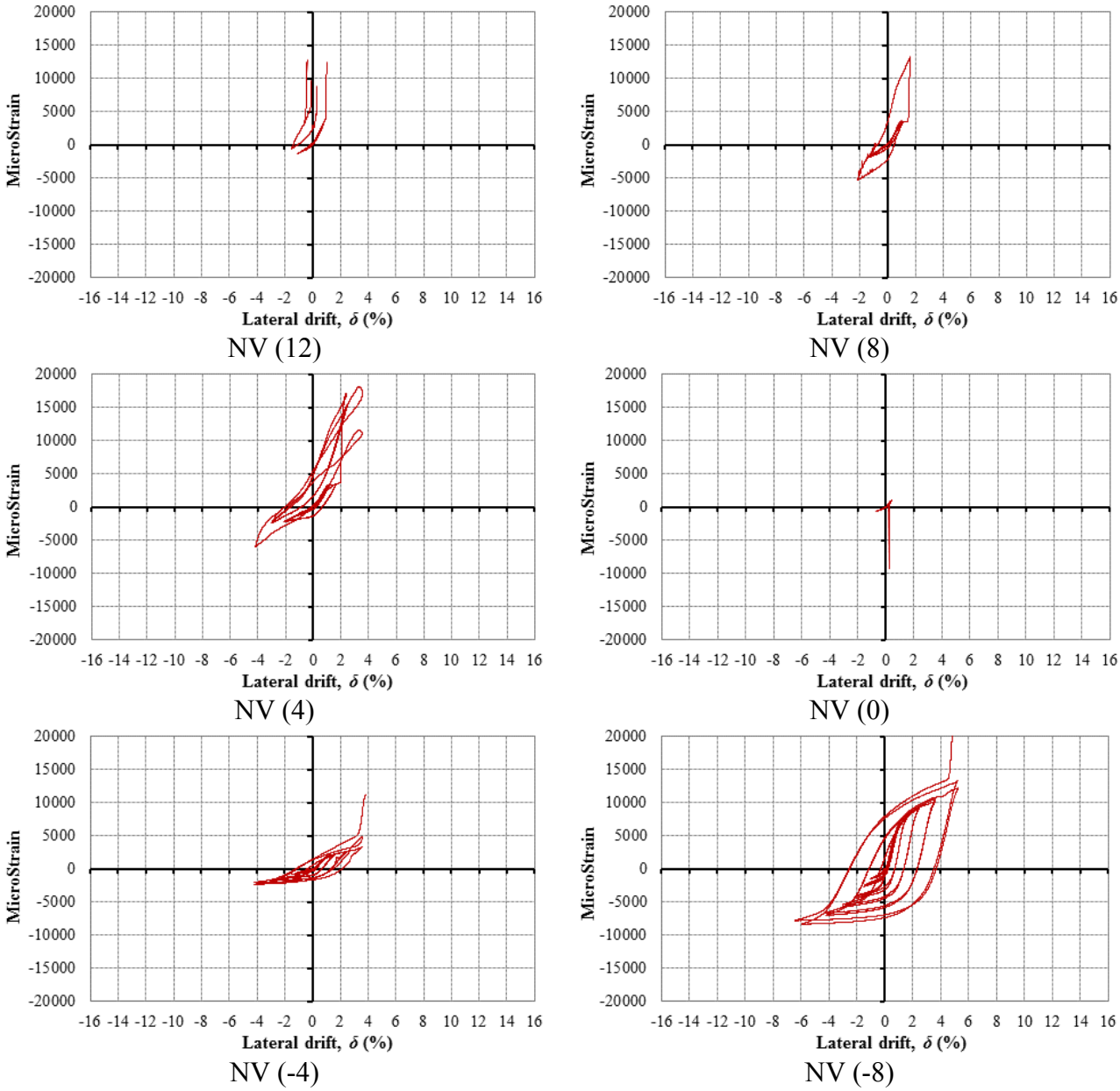

Figure 11.2: Lateral drift-steel rebar microstrain relation in the north direction
N: north, S: south, E: east, W: west, V: vertical, and H: horizontal

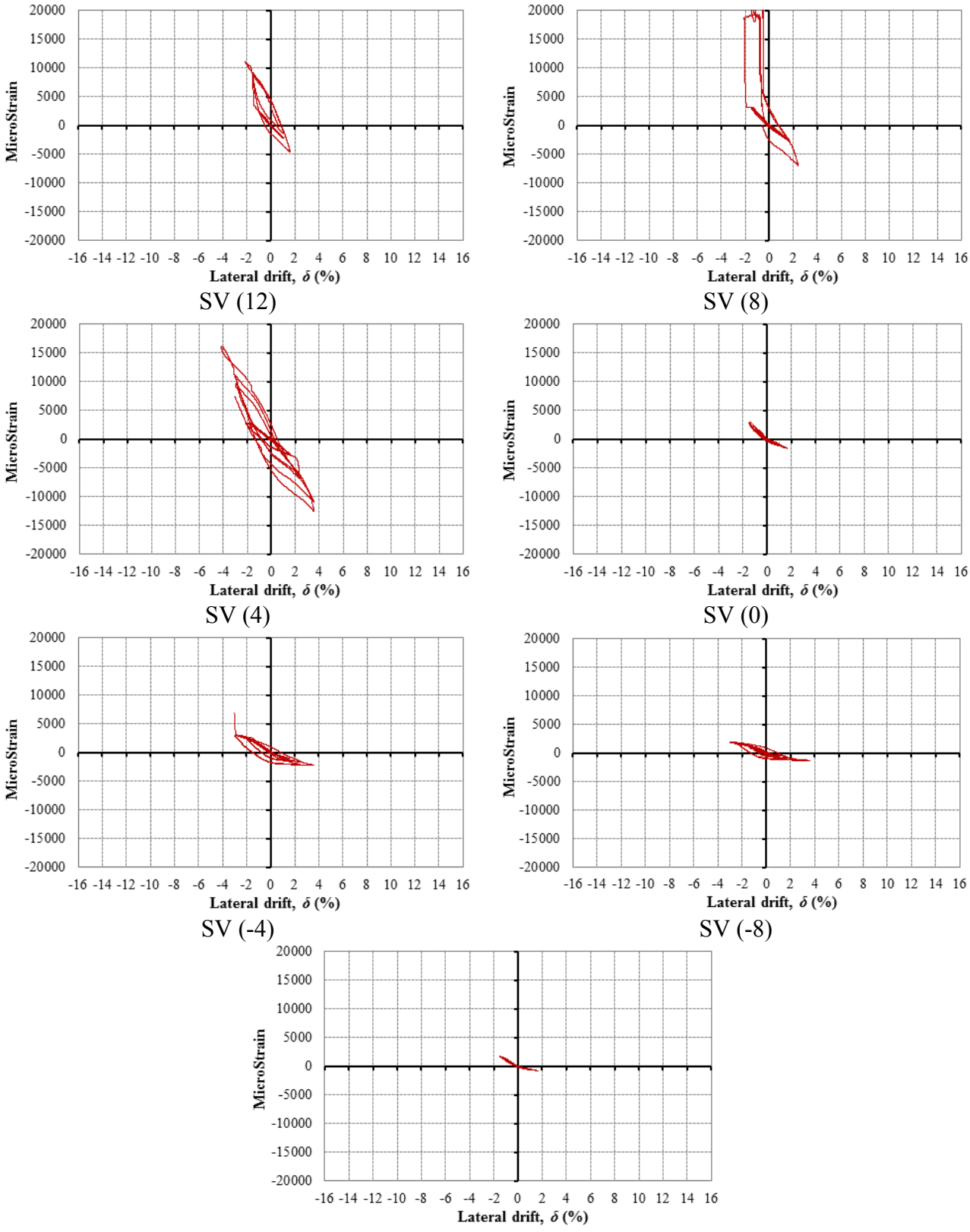

Figure 11.3: Lateral drift-steel rebar microstrain relation in the north direction
N: north, S: south, E: east, W: west, V: vertical, and H: horizontal

11.2 F4-24-E324 column

11.2.1 Force-curvature relations

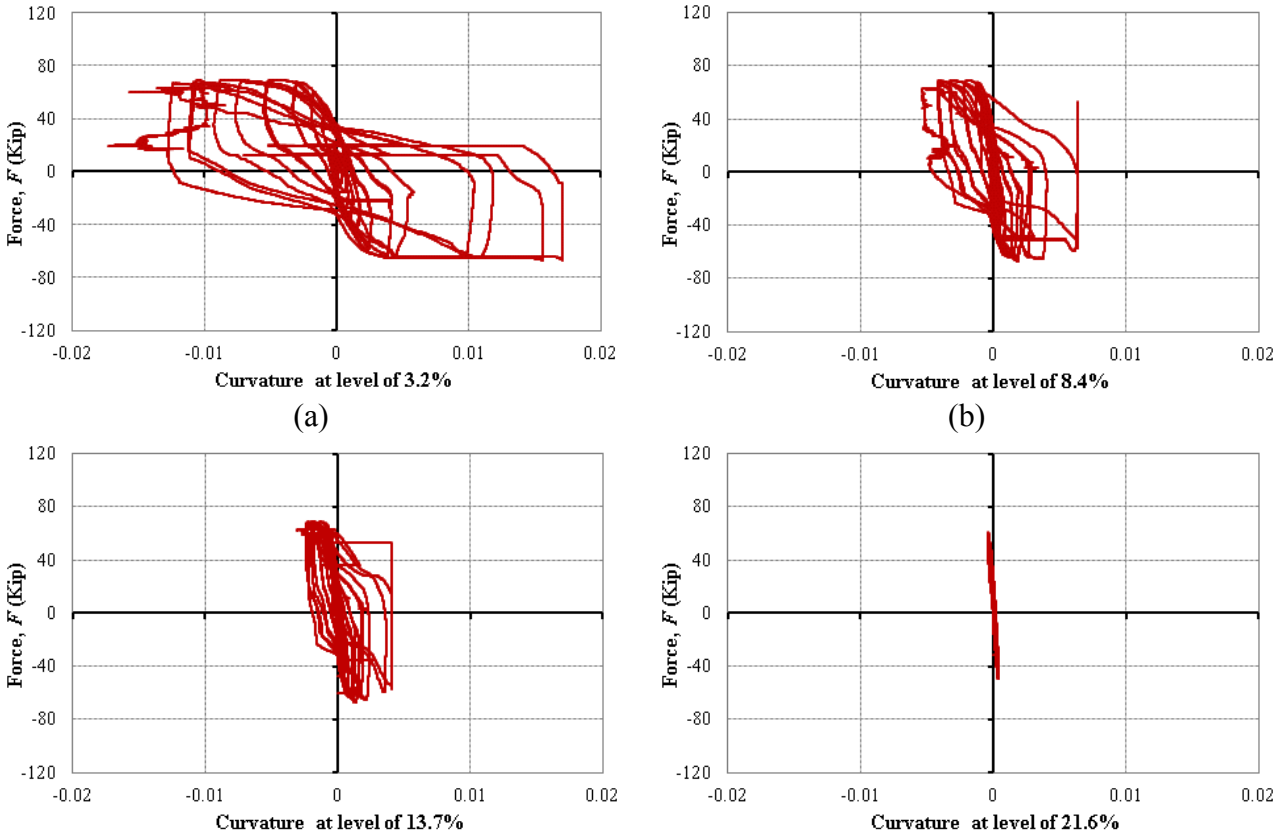

Figure 11.4: Force-curvature relation the F4-24-E324 column: (a) at level of 3.2% of the column's height, (b) at level of 8.4% of the column's height, (c) at level of 13.7% of the column's height, and (d) at level of 21.6% of the column's height

11.2.2 Lateral drift-steel strain relations

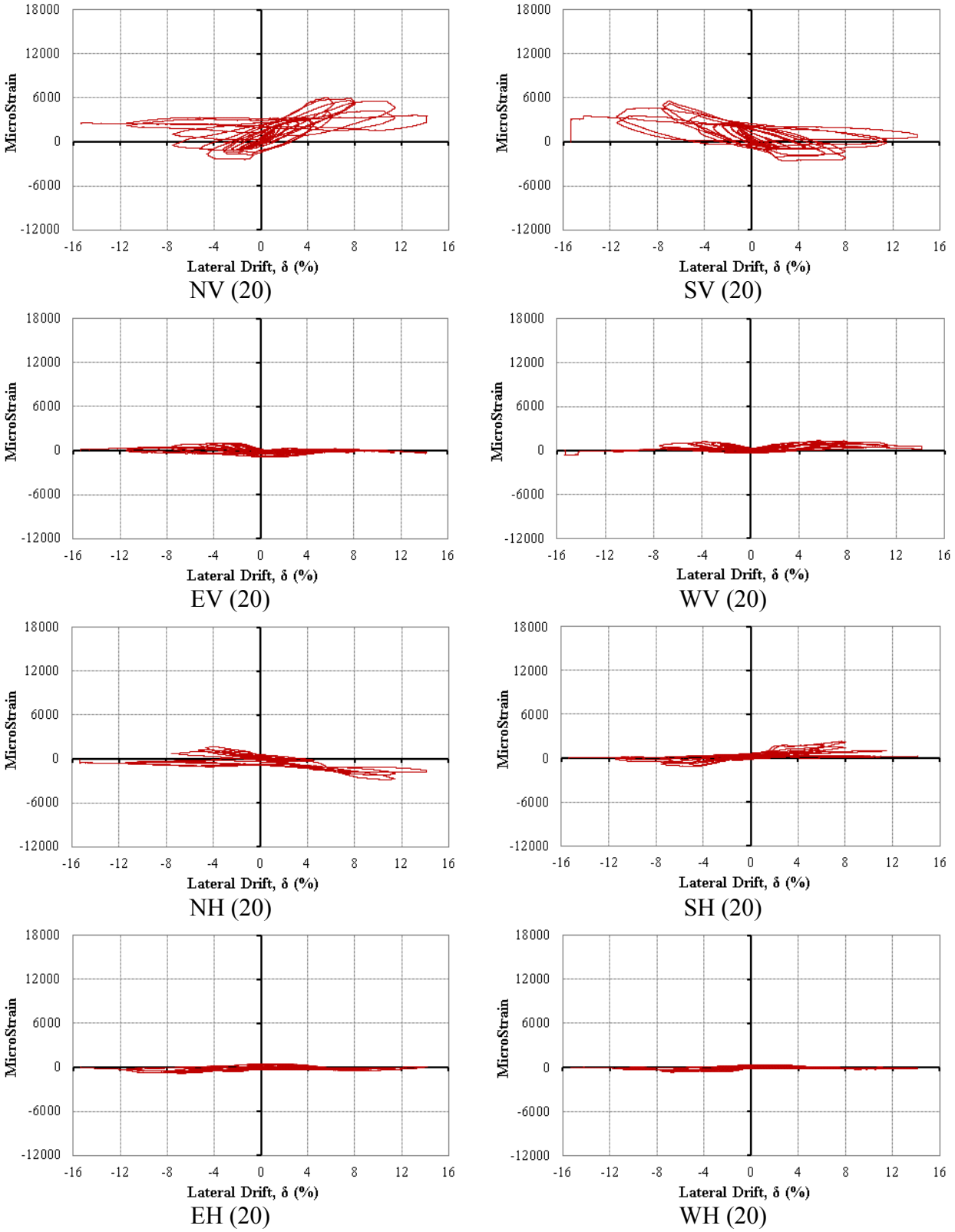

Figure 11.5: Lateral drift-steel tube microstrain relation at 20 inch above the top of the footing
N: north, S: south, E: east, W: west, V: vertical, and H: horizontal

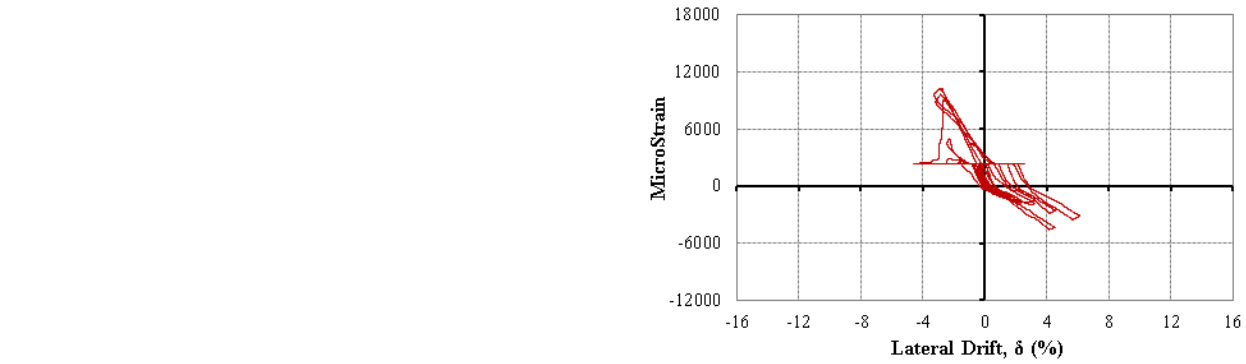

SV (15)

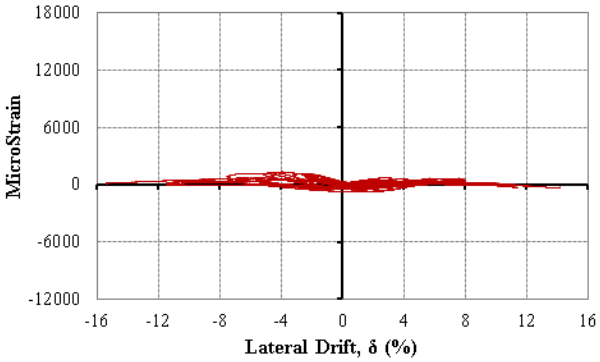

EV (15)

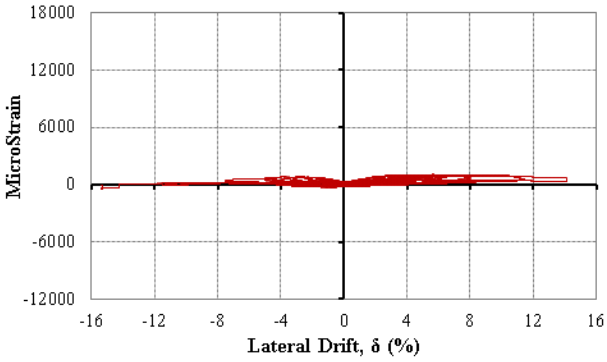

WV (15)

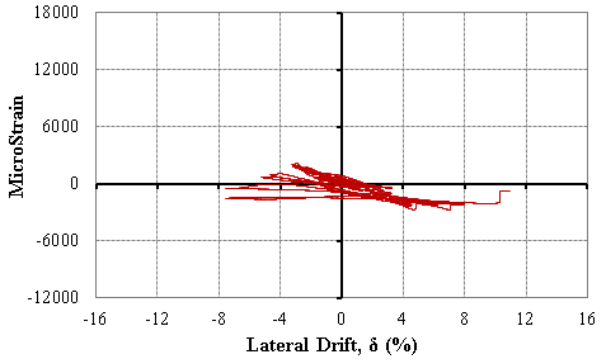

NH (15)

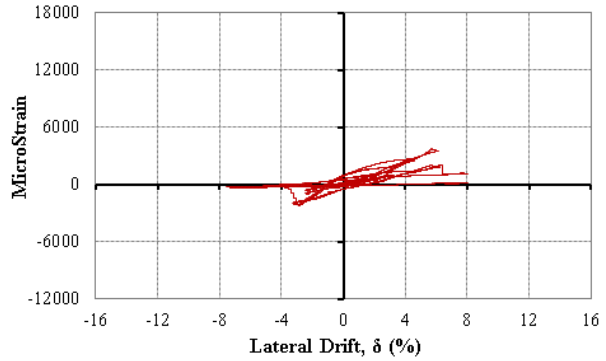

SH (15)

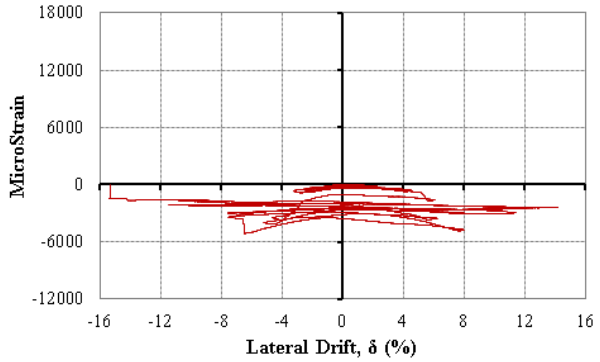

EH (15)

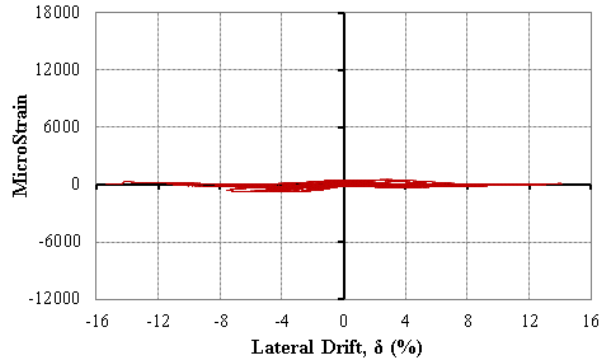

WH (15)

Figure 11.6: Lateral drift-steel tube microstrain relation at 15 inch above the top of the footing
N: north, S: south, E: east, W: west, V: vertical, and H: horizontal

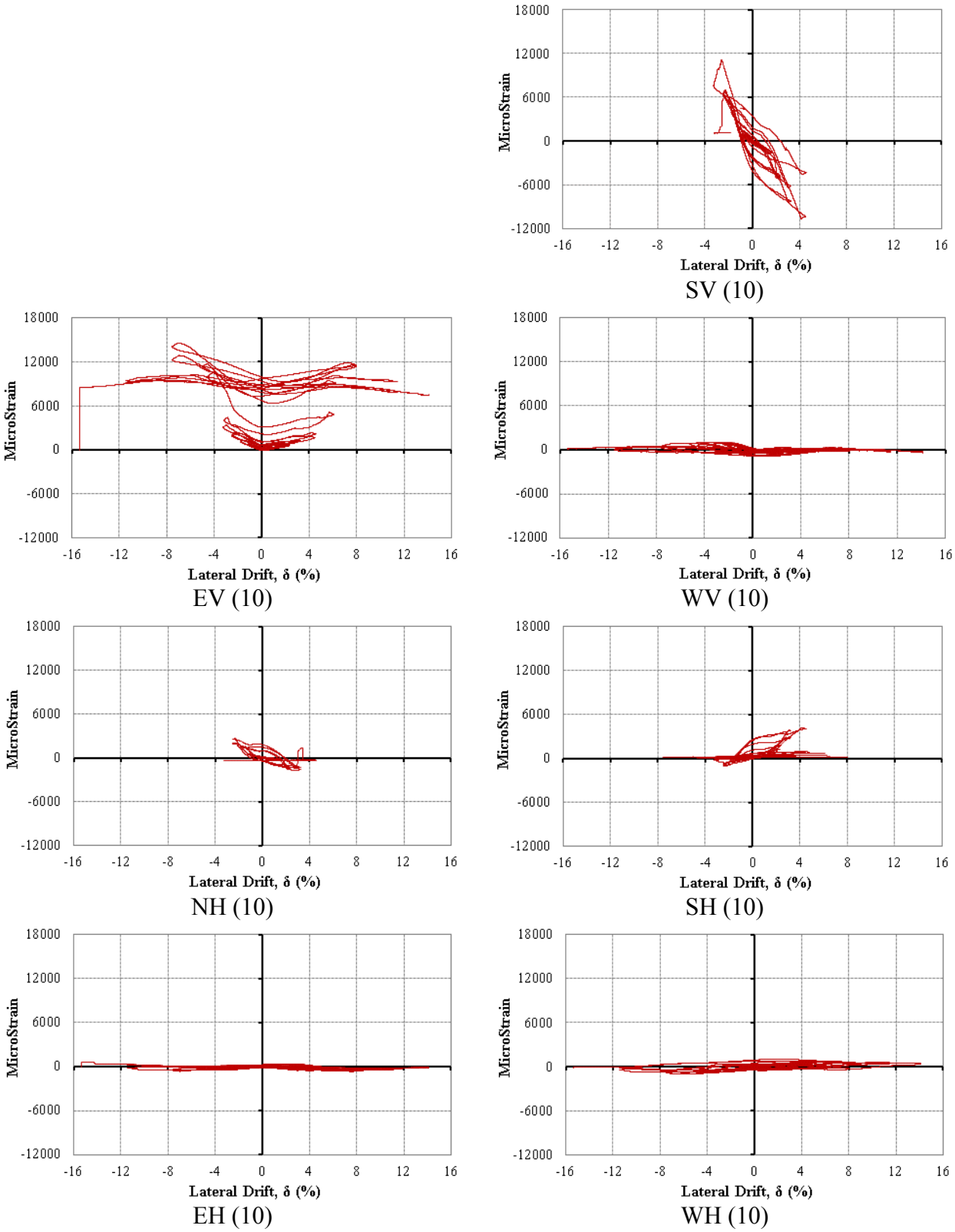

Figure 11.7: Lateral drift-steel tube microstrain relation at 10 inch above the top of the footing
N: north, S: south, E: east, W: west, V: vertical, and H: horizontal

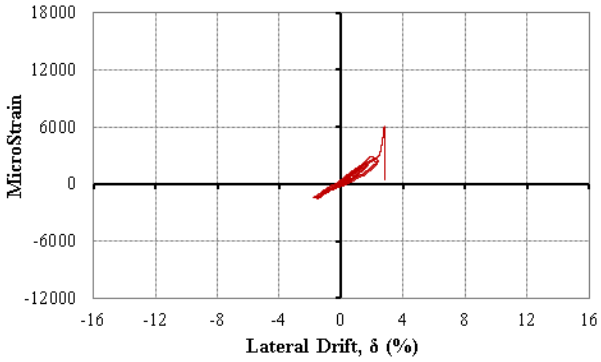

NV (5)

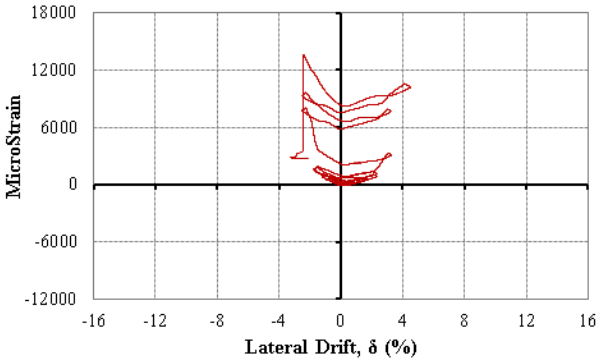

EV (5)

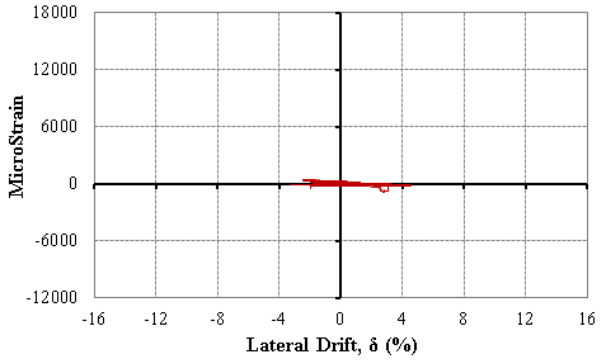

NH (5)

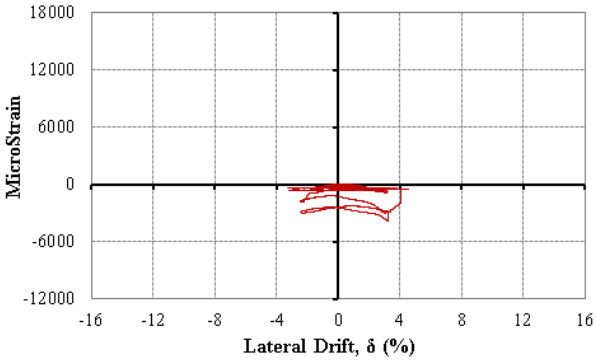

SH (5)

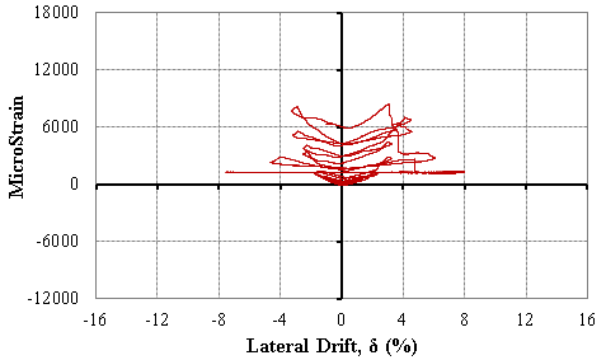

EH (5)

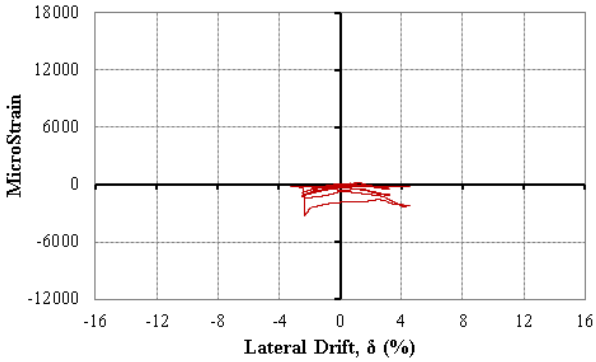

WH (5)

Figure 11.8: Lateral drift-steel tube microstrain relation at 5 inch above the top of the footing
N: north, S: south, E: east, W: west, V: vertical, and H: horizontal

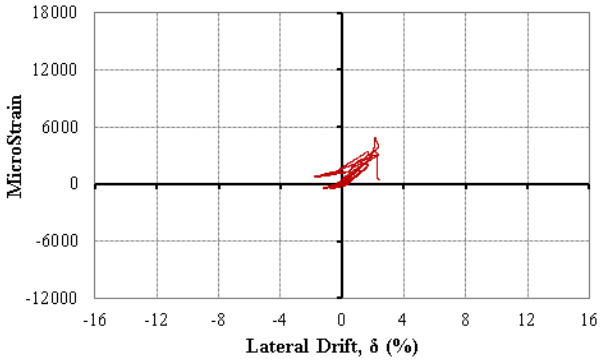

NV (0)

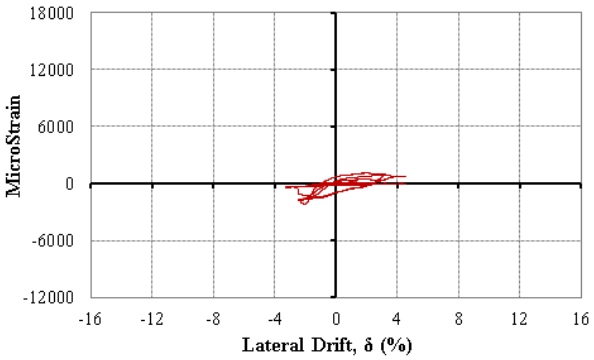

SV (0)

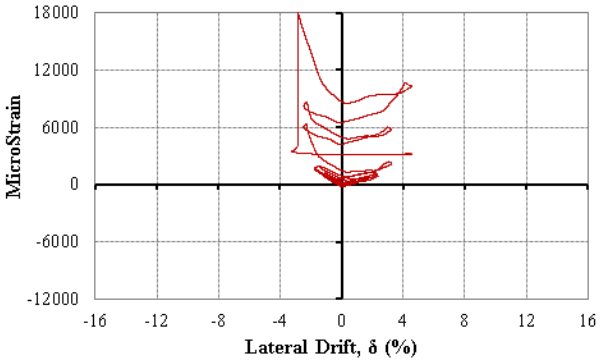

EV (0)

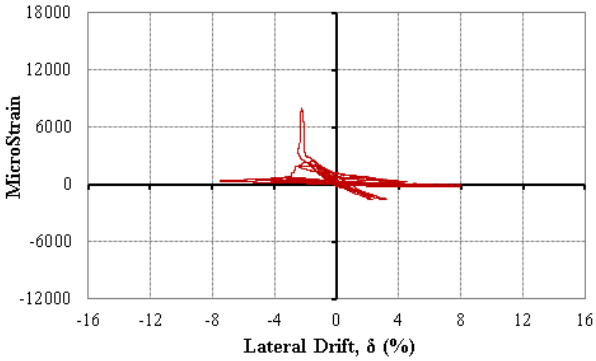

SH (0)

Figure 11.9: Lateral drift-steel tube microstrain relation at the level of the top of the footing
N: north, S: south, E: east, W: west, V: vertical, and H: horizontal

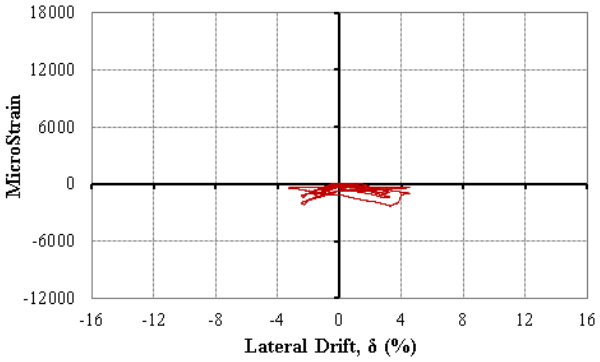

NV (-5)

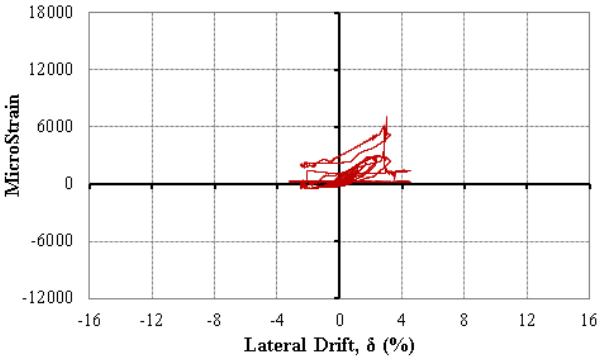

SV (-5)

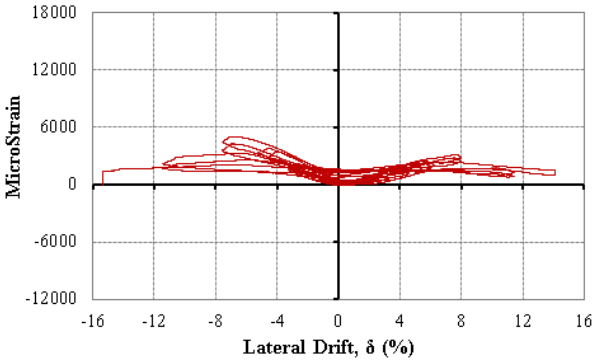

EV (-5)

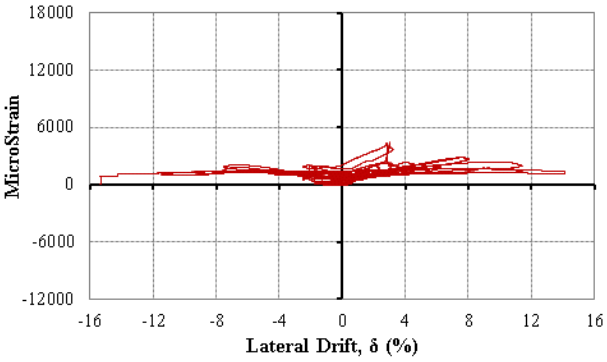

WV (-5)

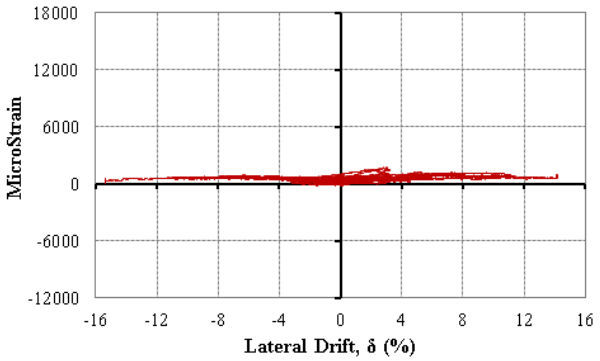

NH (-5)

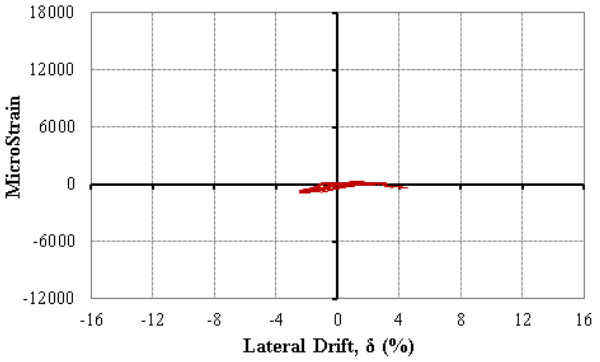

EH (-5)

Figure 11.10: Lateral drift-steel tube microstrain relation at 5 inch below the top of the footing
N: north, S: south, E: east, W: west, V: vertical, and H: horizontal

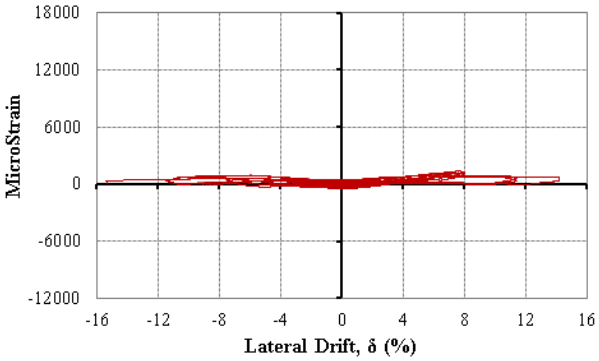

EV (-10)

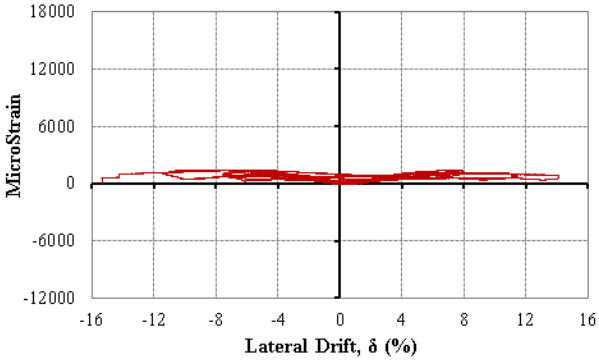

WV (-10)

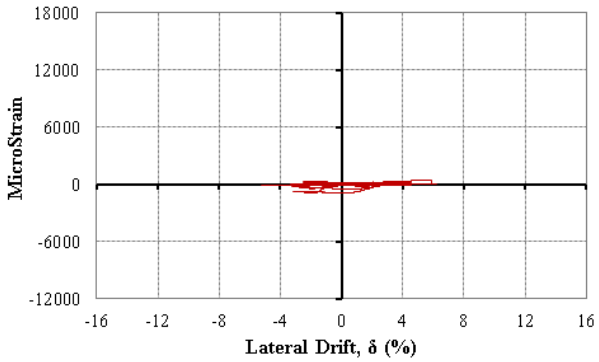

NH (-10)

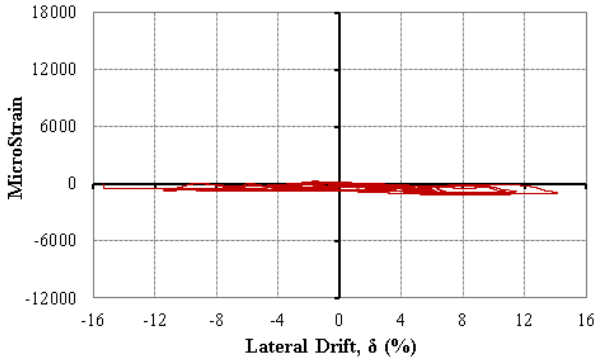

EH (-10)

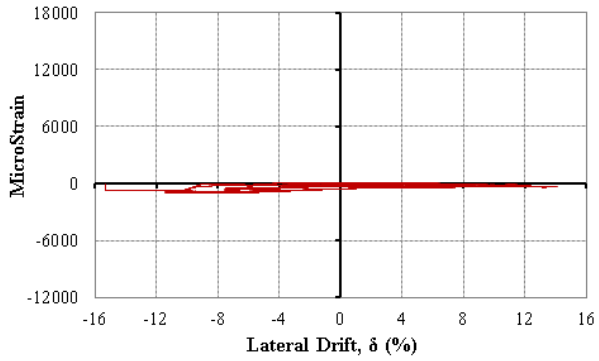

WH (-10)

Figure 11.11: Lateral drift-steel tube microstrain relation at 10 inch below the top of the footing
N: north, S: south, E: east, W: west, V: vertical, and H: horizontal

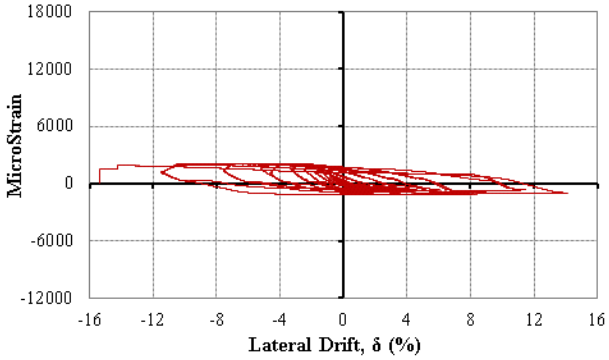

SV (-15)

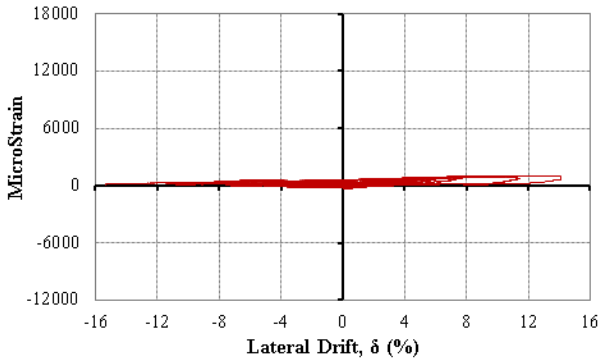

WV (-15)

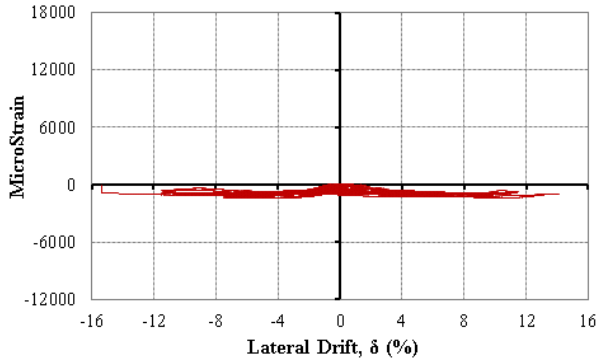

WH (-15)

Figure 11.12: Lateral drift-steel tube microstrain relation at 15 inch below the top of the footing
N: north, S: south, E: east, W: west, V: vertical, and H: horizontal

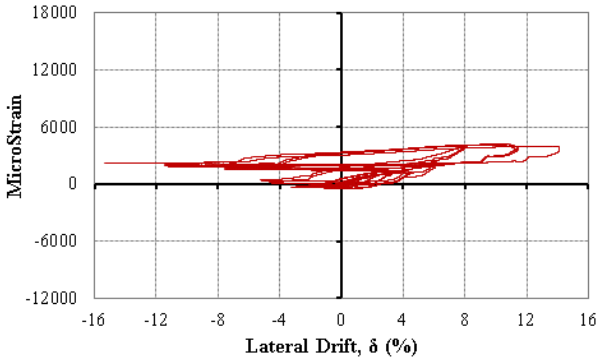

NV (-20)

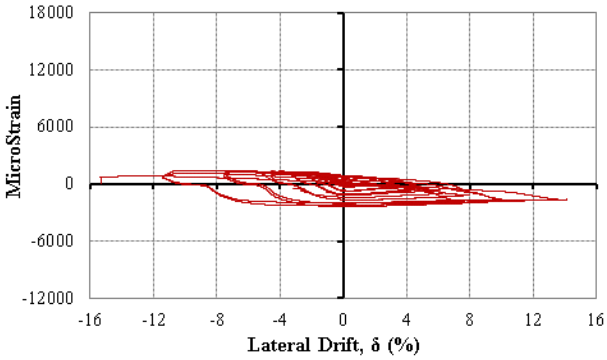

SV (-20)

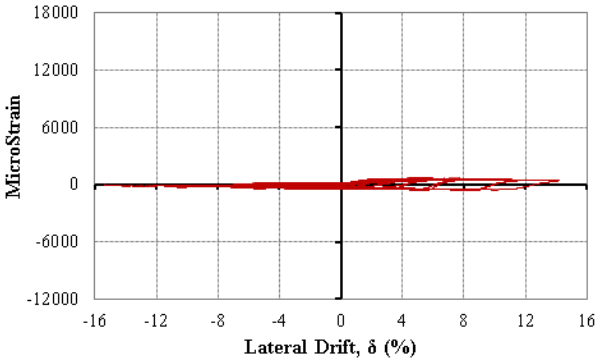

EV (-20)

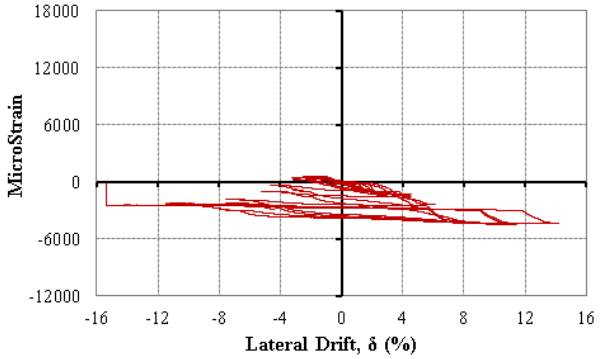

NH (-20)

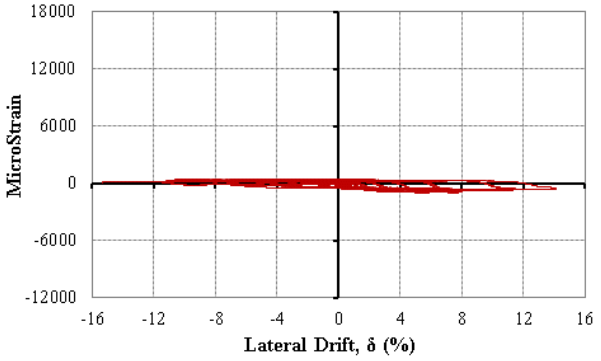

EH (-20)

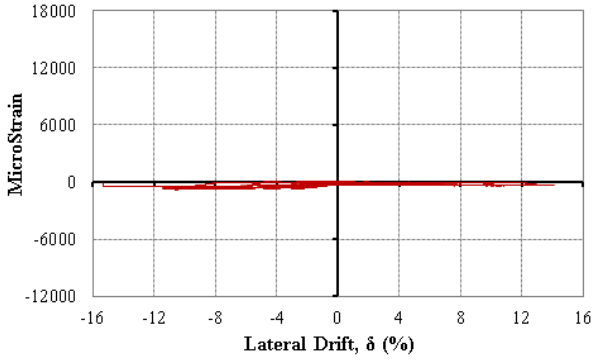

WH (-20)

Figure 11.13: Lateral drift-steel tube microstrain relation at 20 inch below the top of the footing
N: north, S: south, E: east, W: west, V: vertical, and H: horizontal

11.2.3 Lateral drift-FRP strain relations

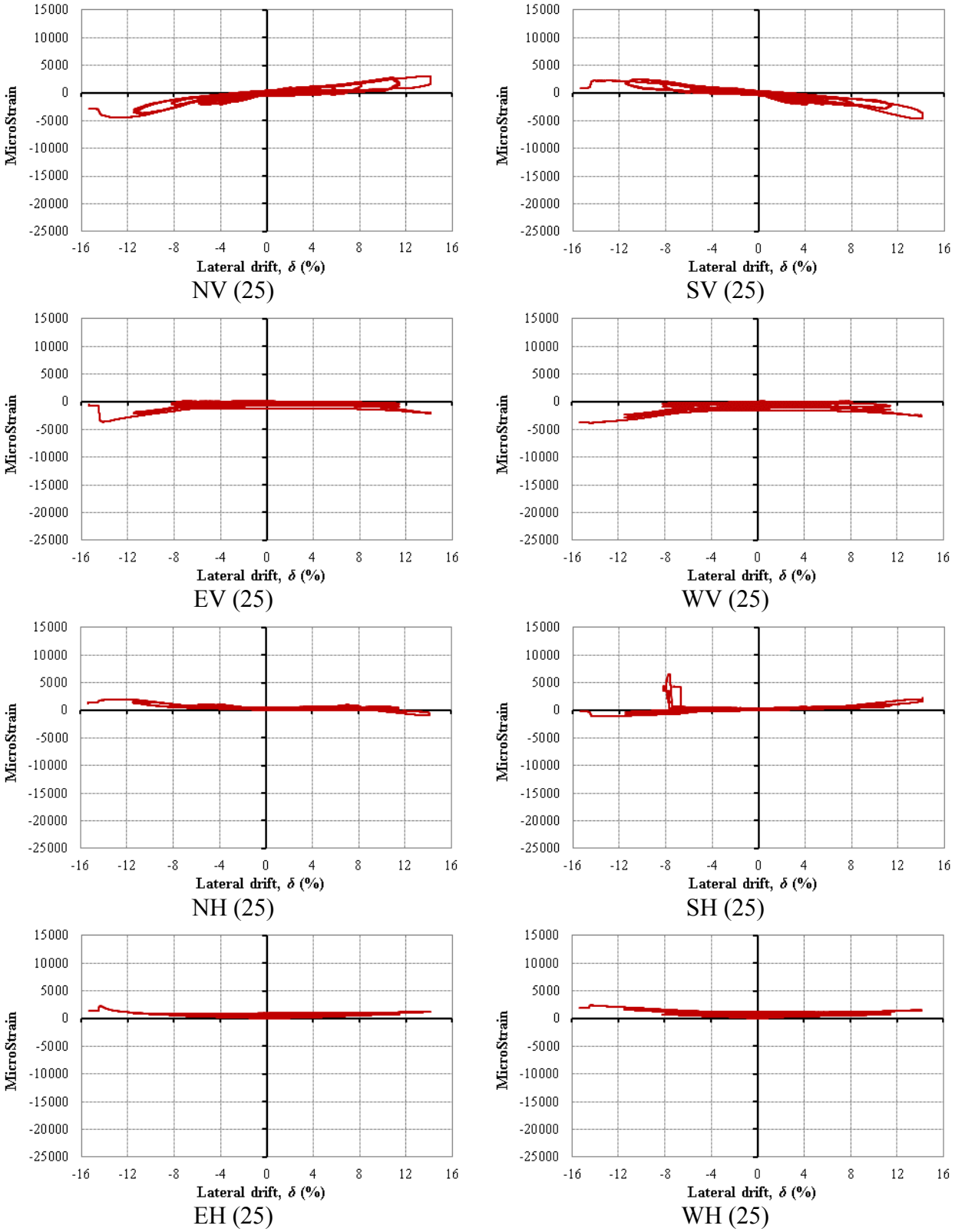

Figure 11.14: Lateral drift- FRP tube microstrain relation at 25 inch above the top of the footing
N: north, S: south, E: east, W: west, V: vertical, and H: horizontal

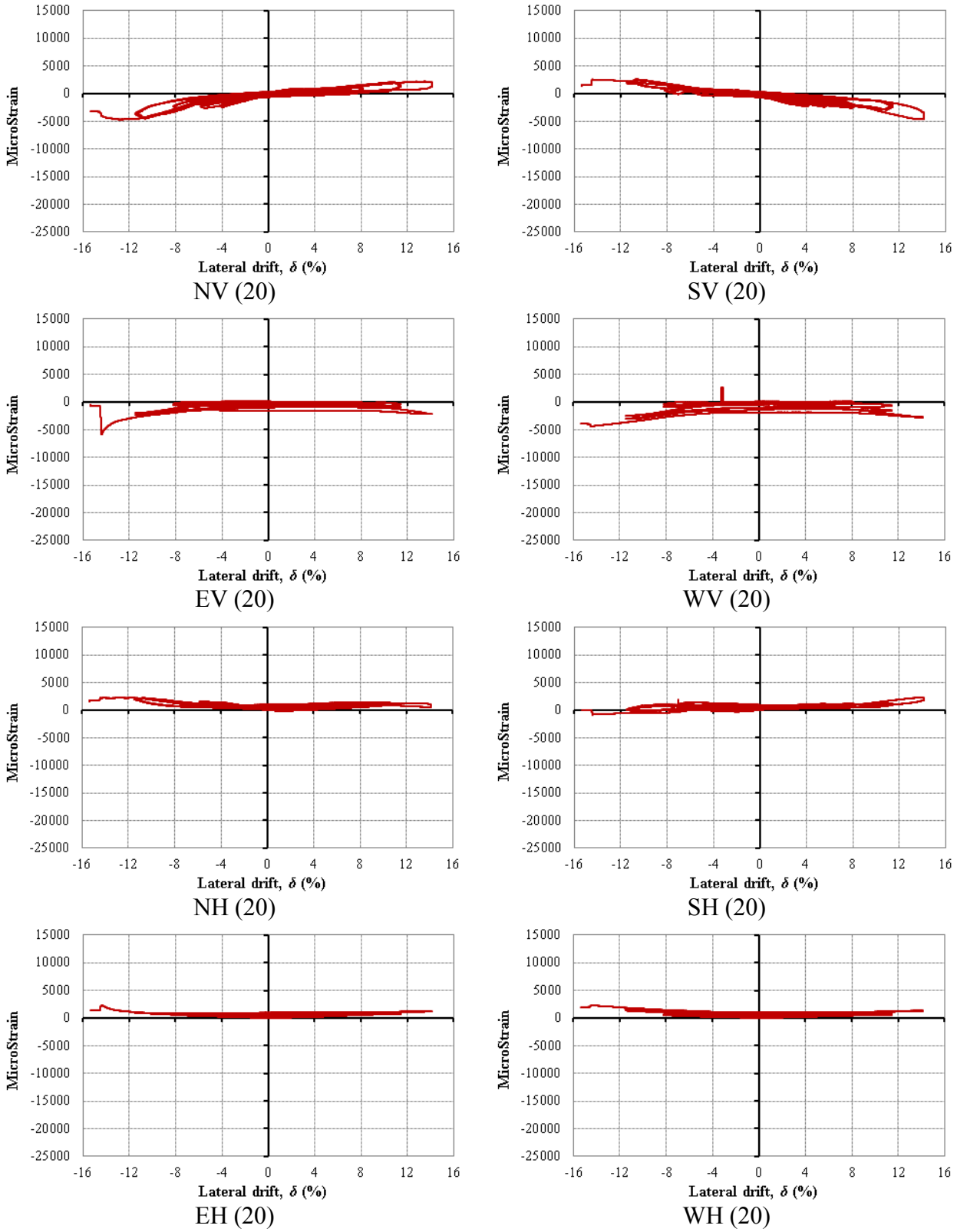

Figure 11.15: Lateral drift- FRP tube microstrain relation at 20 inch above the top of the footing

N: north, S: south, E: east, W: west, V: vertical, and H: horizontal

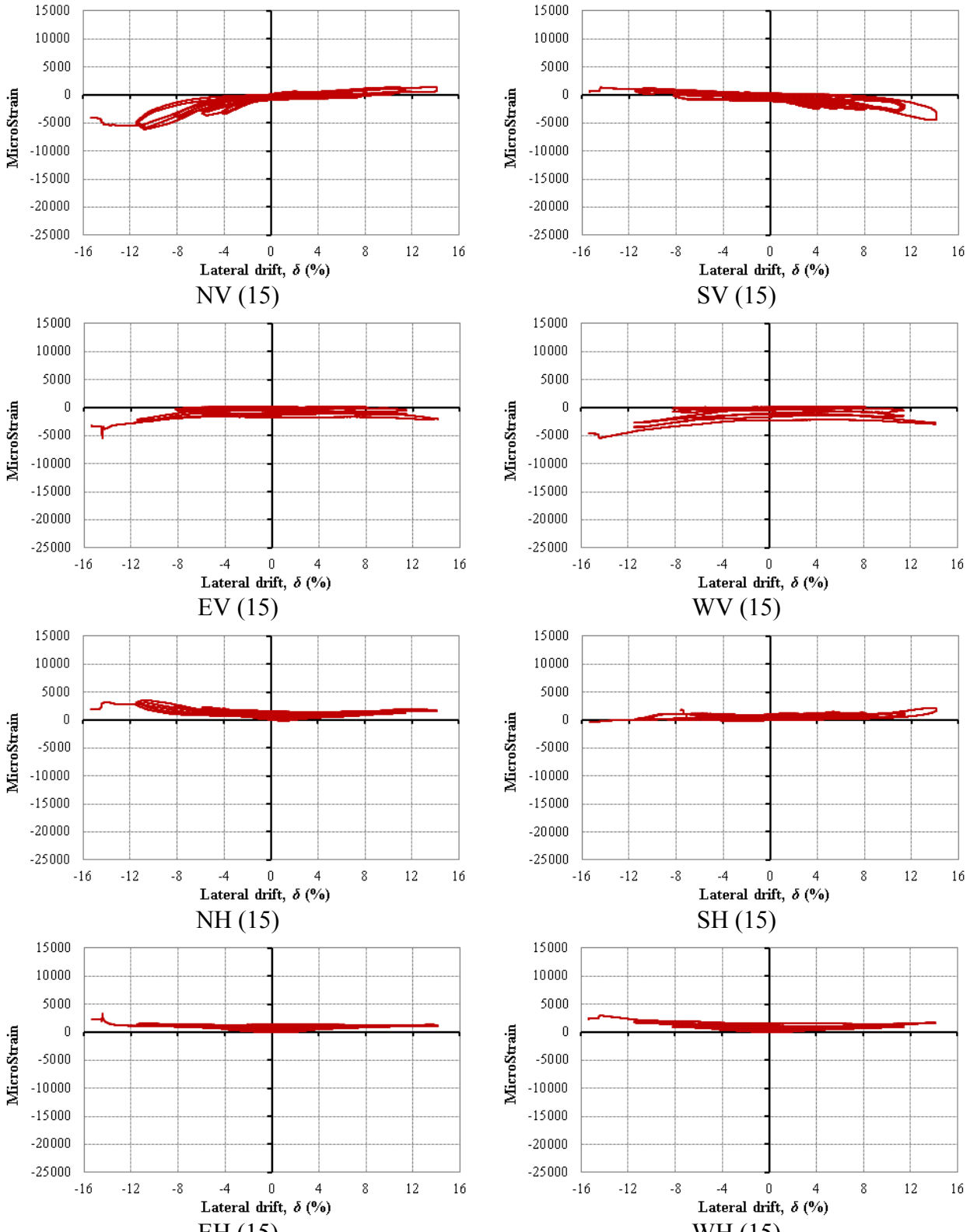

Figure 11.16: Lateral drift- FRP tube microstrain relation at 15 inch above the top of the footing

N: north, S: south, E: east, W: west, V: vertical, and H: horizontal

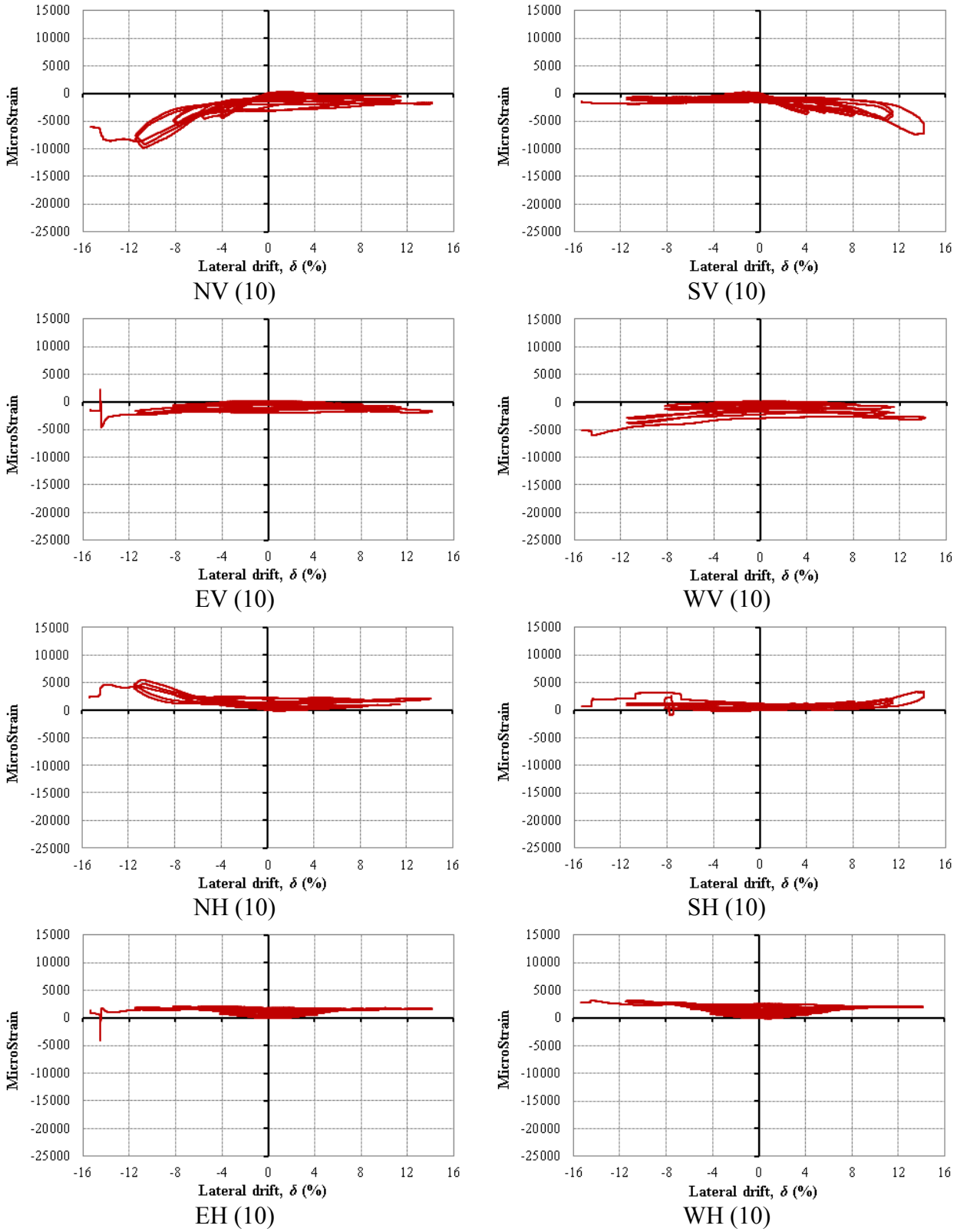

Figure 11.17: Lateral drift- FRP tube microstrain relation at 10 inch above the top of the footing

N: north, S: south, E: east, W: west, V: vertical, and H: horizontal

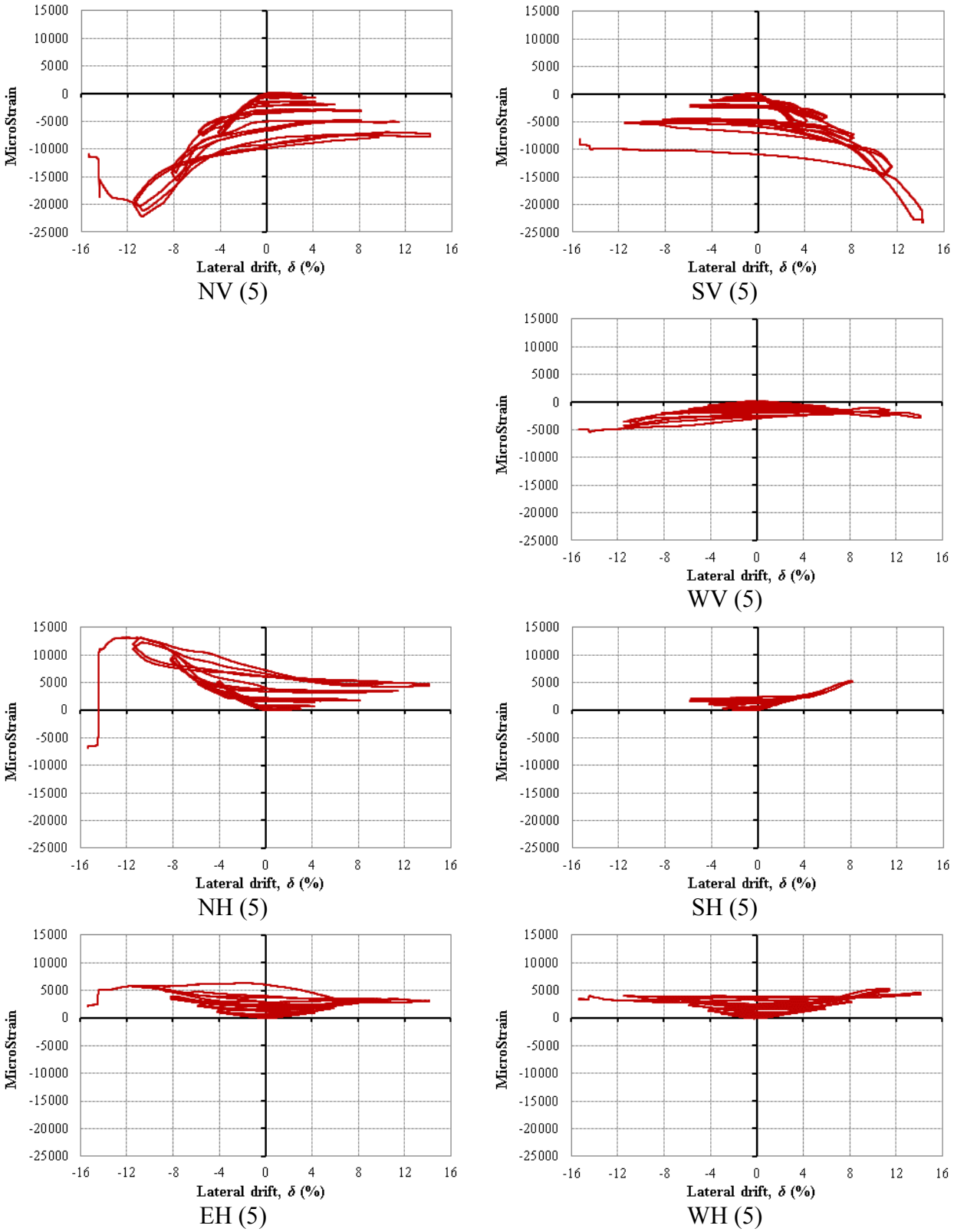

Figure 11.18: Lateral drift-FRP tube microstrain relation at 5 inch above the top of the footing

N: north, S: south, E: east, W: west, V: vertical, and H: horizontal

11.3 F4-24-P124 column

11.3.1 Force-curvature relations

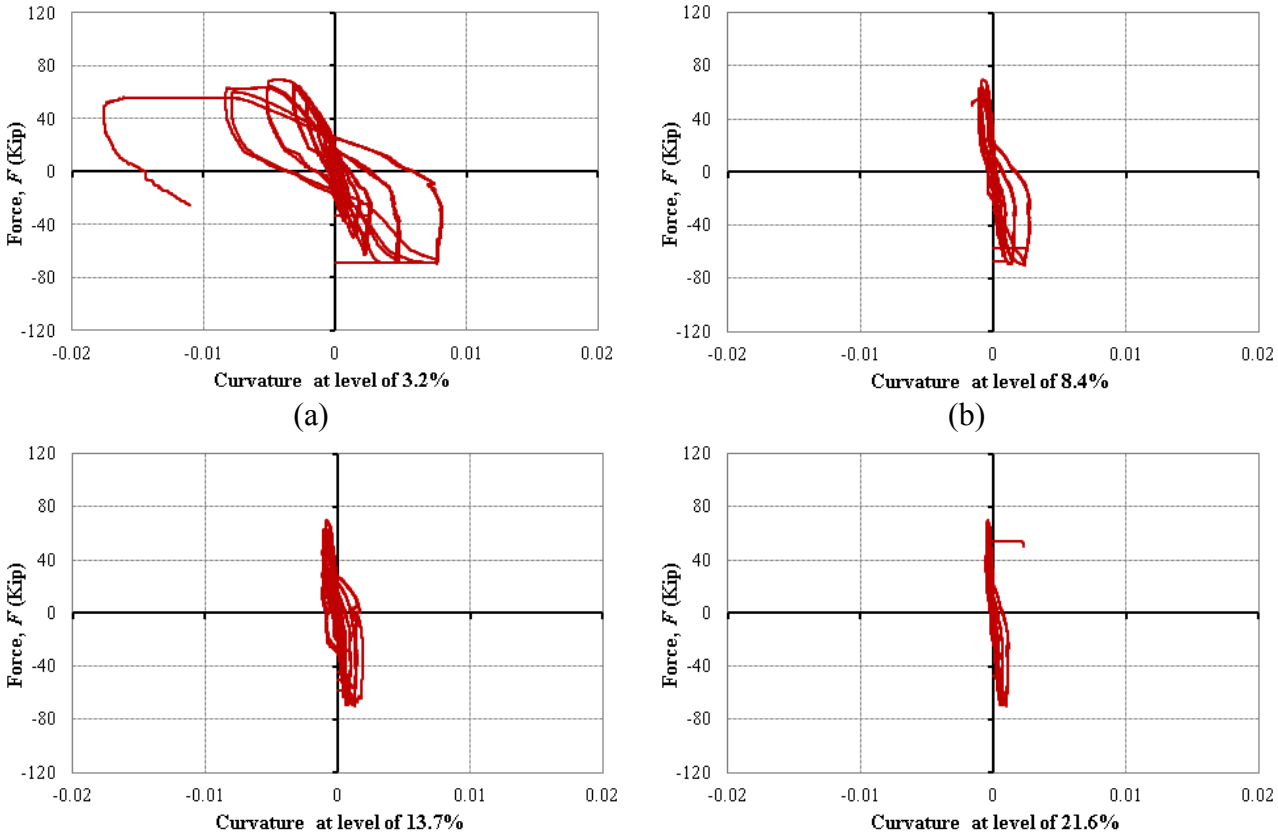

Figure 11.19: Force-curvature relation of the F4-24-P124 column: (a) at level of 3.2% of the column's height, (b) at level of 8.4% of the column's height, (c) at level of 13.7% of the column's height, and (d) at level of 21.6% of the column's height

11.3.2 Lateral drift-steel strain relations

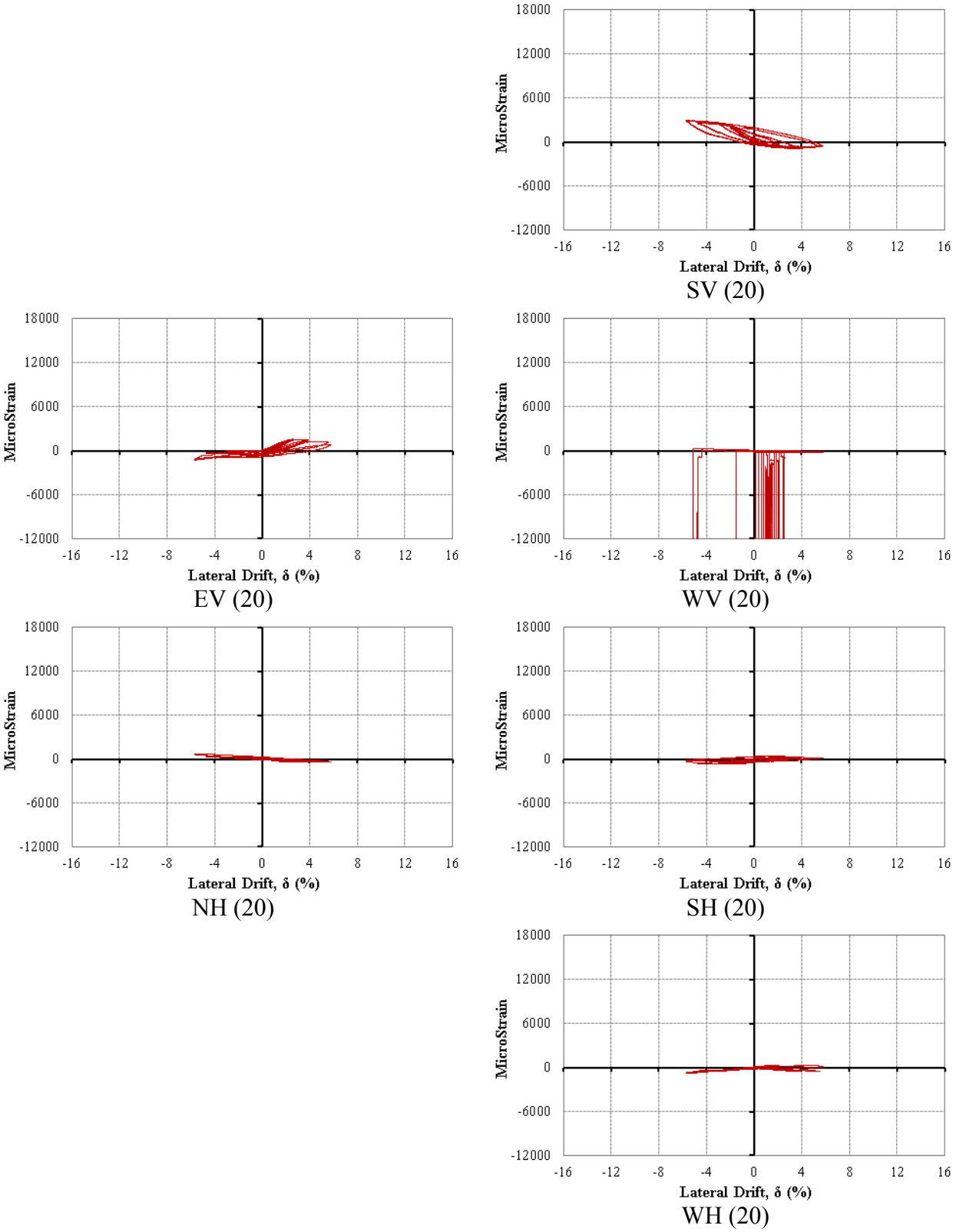

Figure 11.20: Lateral drift-steel tube microstrain relation at 20 inch above the top of the footing
N: north, S: south, E: east, W: west, V: vertical, and H: horizontal

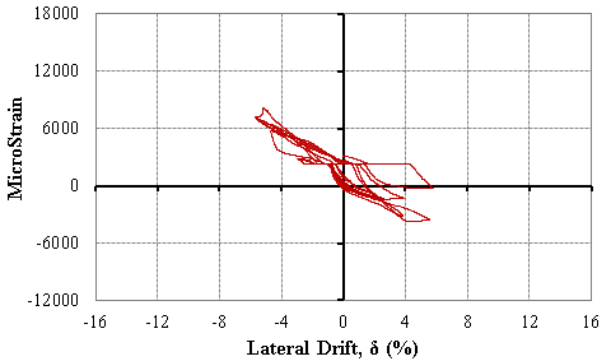

SV (15)

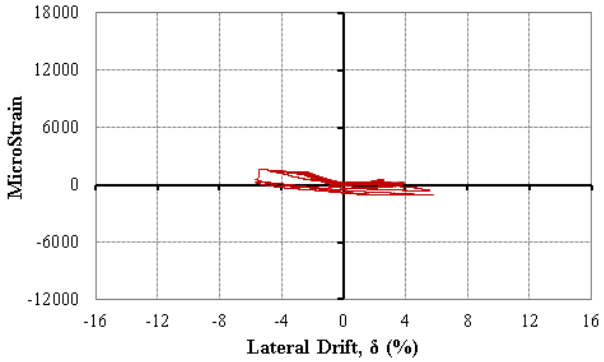

WV (15)

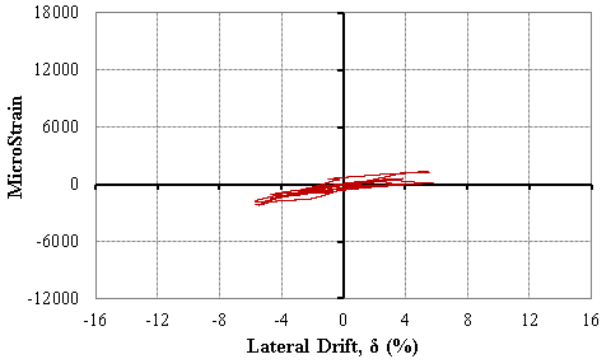

SH (15)

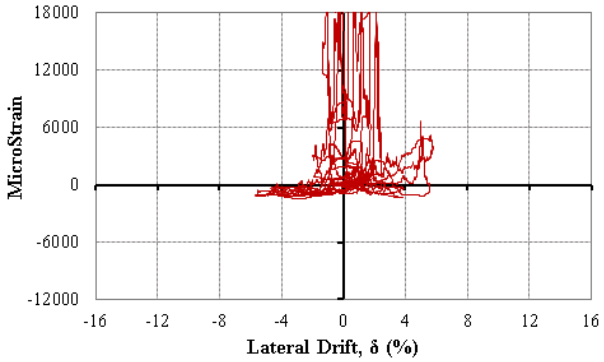

WH (15)

Figure 11.21: Lateral drift-steel tube microstrain relation at 15 inch above the top of the footing
N: north, S: south, E: east, W: west, V: vertical, and H: horizontal

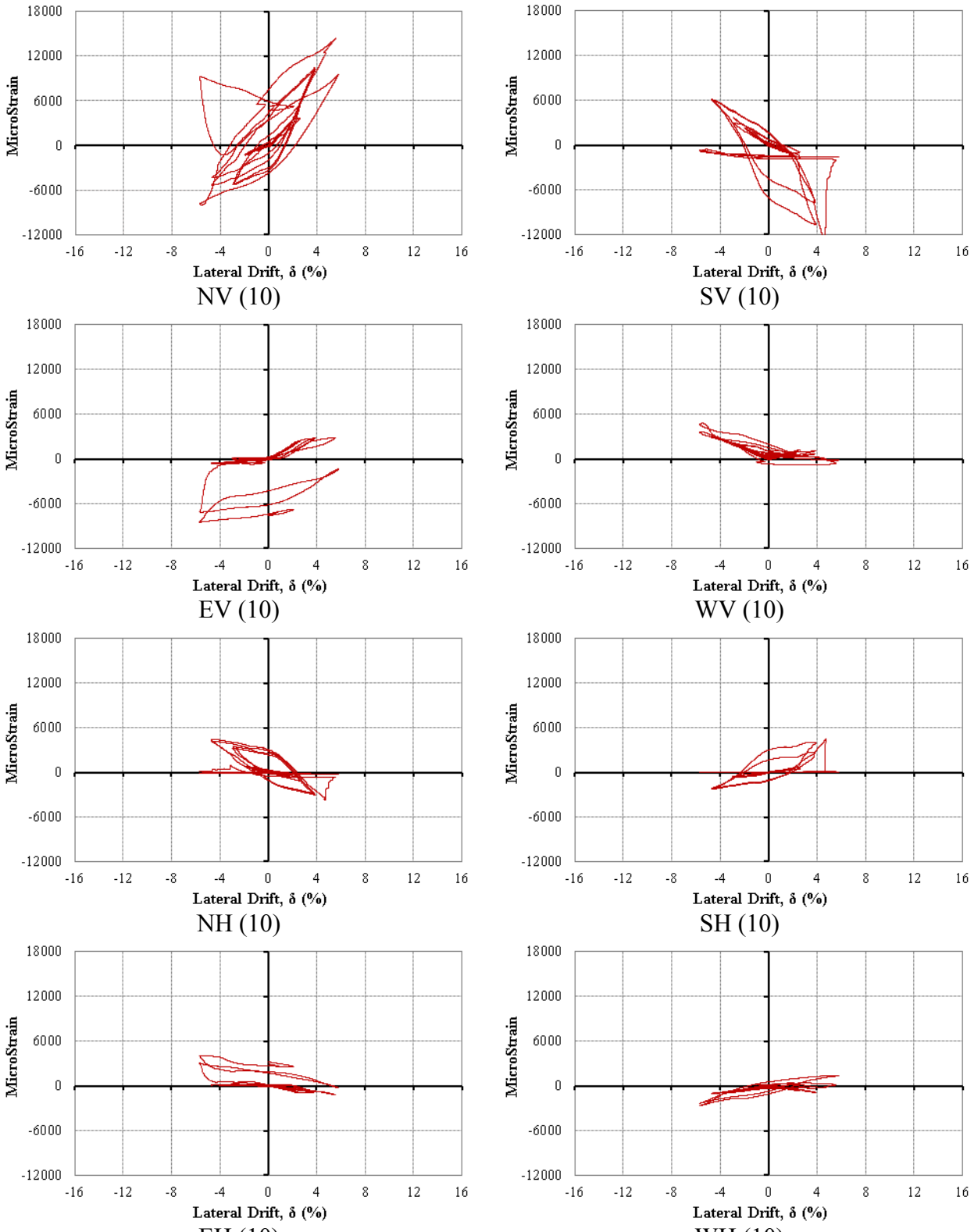

Figure 11.22: Lateral drift-steel tube microstrain relation at 10 inch above the top of the footing
N: north, S: south, E: east, W: west, V: vertical, and H: horizontal

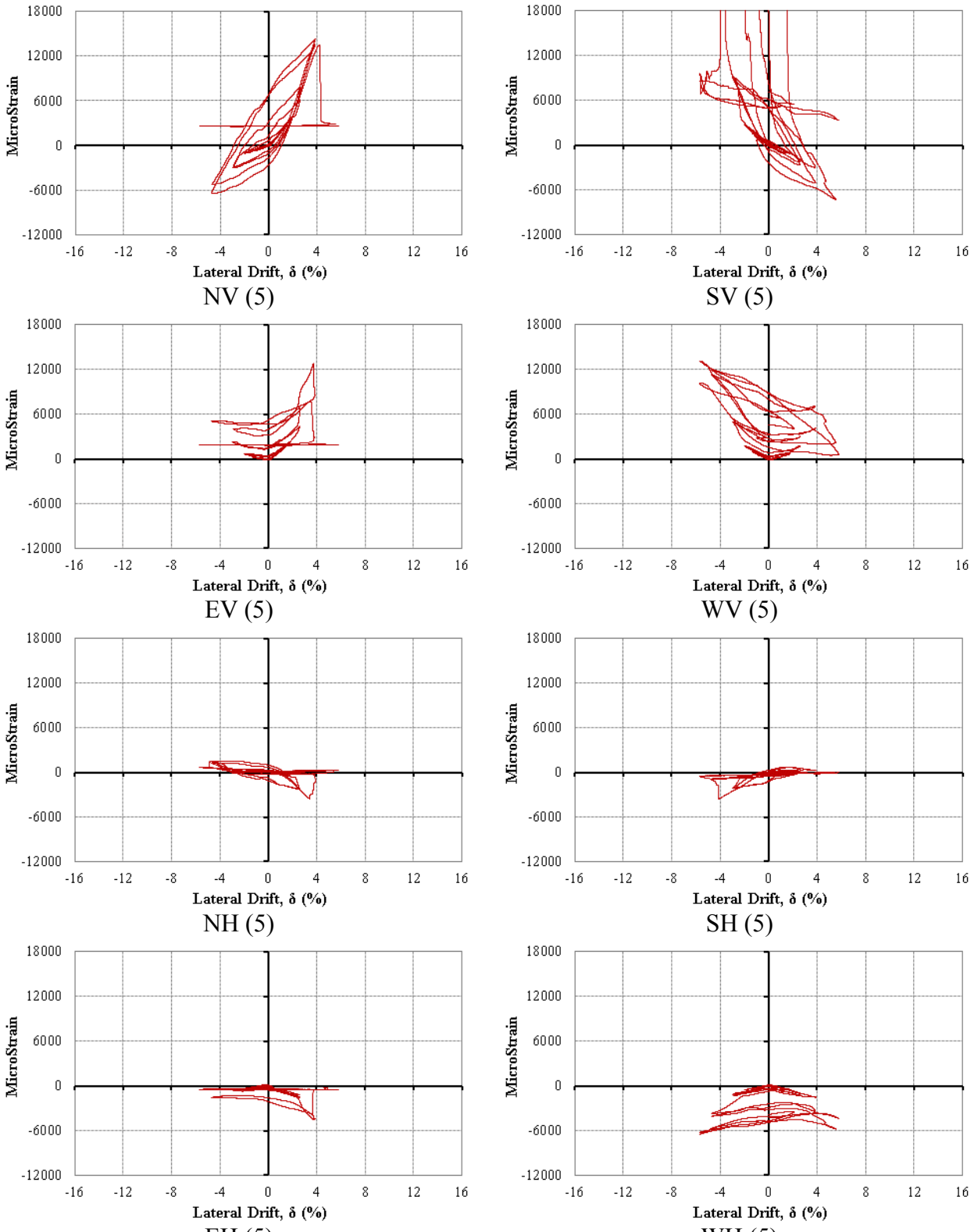

Figure 11.23: Lateral drift-steel tube microstrain relation at 5 inch above the top of the footing
N: north, S: south, E: east, W: west, V: vertical, and H: horizontal

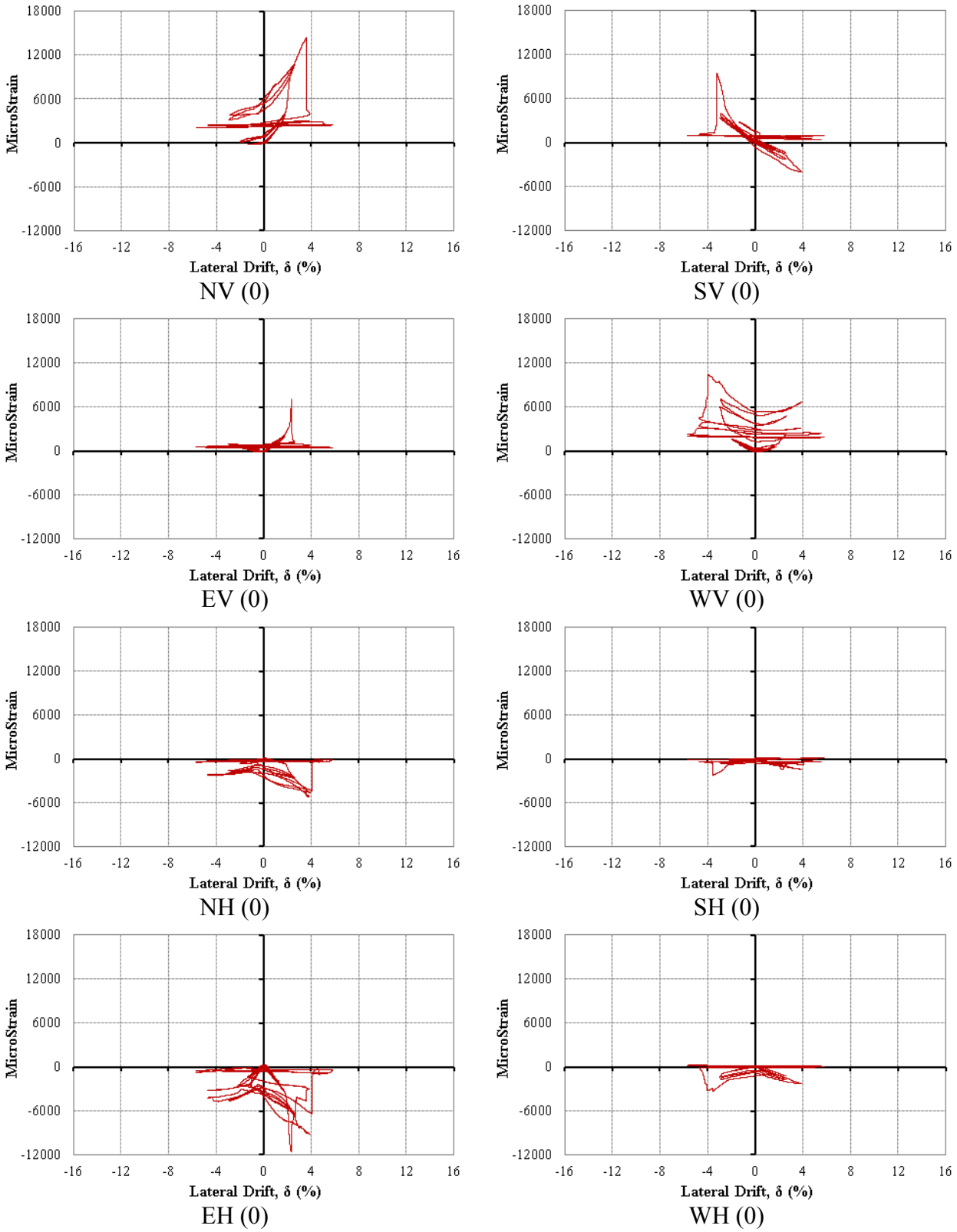

Figure 11.24: Lateral drift-steel tube microstrain relation at the level of the top of the footing
N: north, S: south, E: east, W: west, V: vertical, and H: horizontal

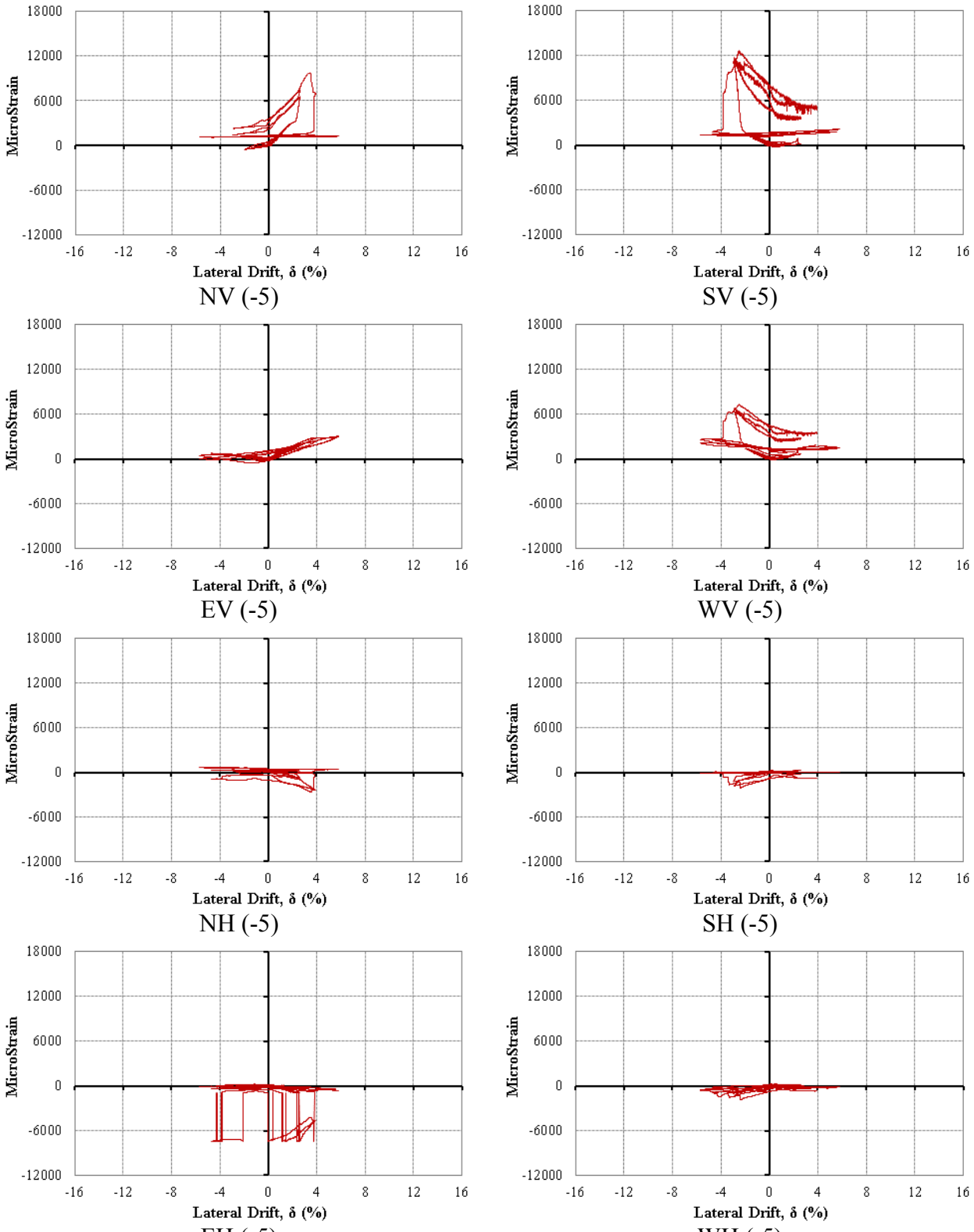

Figure 11.25: Lateral drift-steel tube microstrain relation at 5 inch below the top of the footing
N: north, S: south, E: east, W: west, V: vertical, and H: horizontal

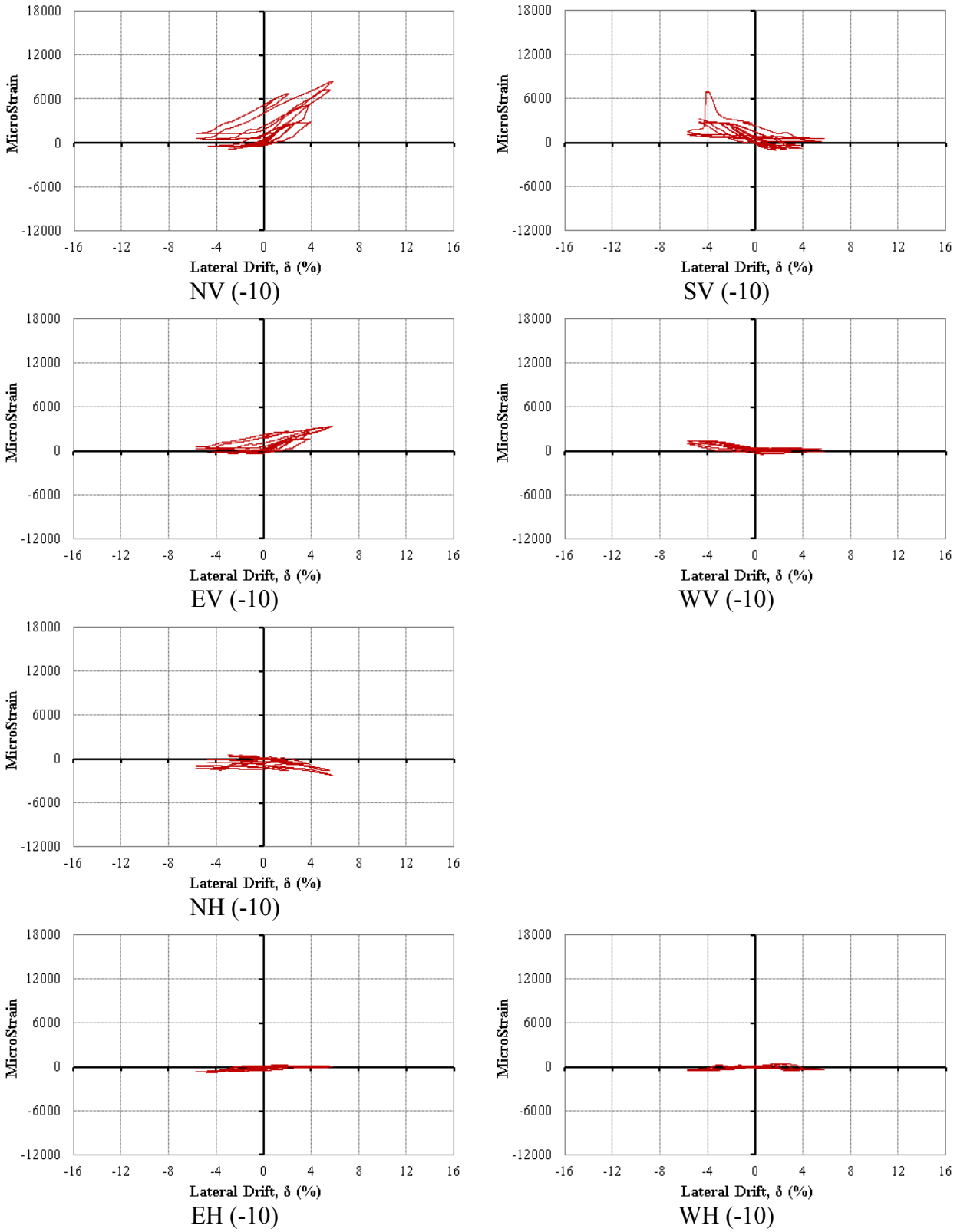

Figure 11.26: Lateral drift-steel tube microstrain relation at 10 inch below the top of the footing
N: north, S: south, E: east, W: west, V: vertical, and H: horizontal

11.3.3 Lateral drift-FRP strain relations

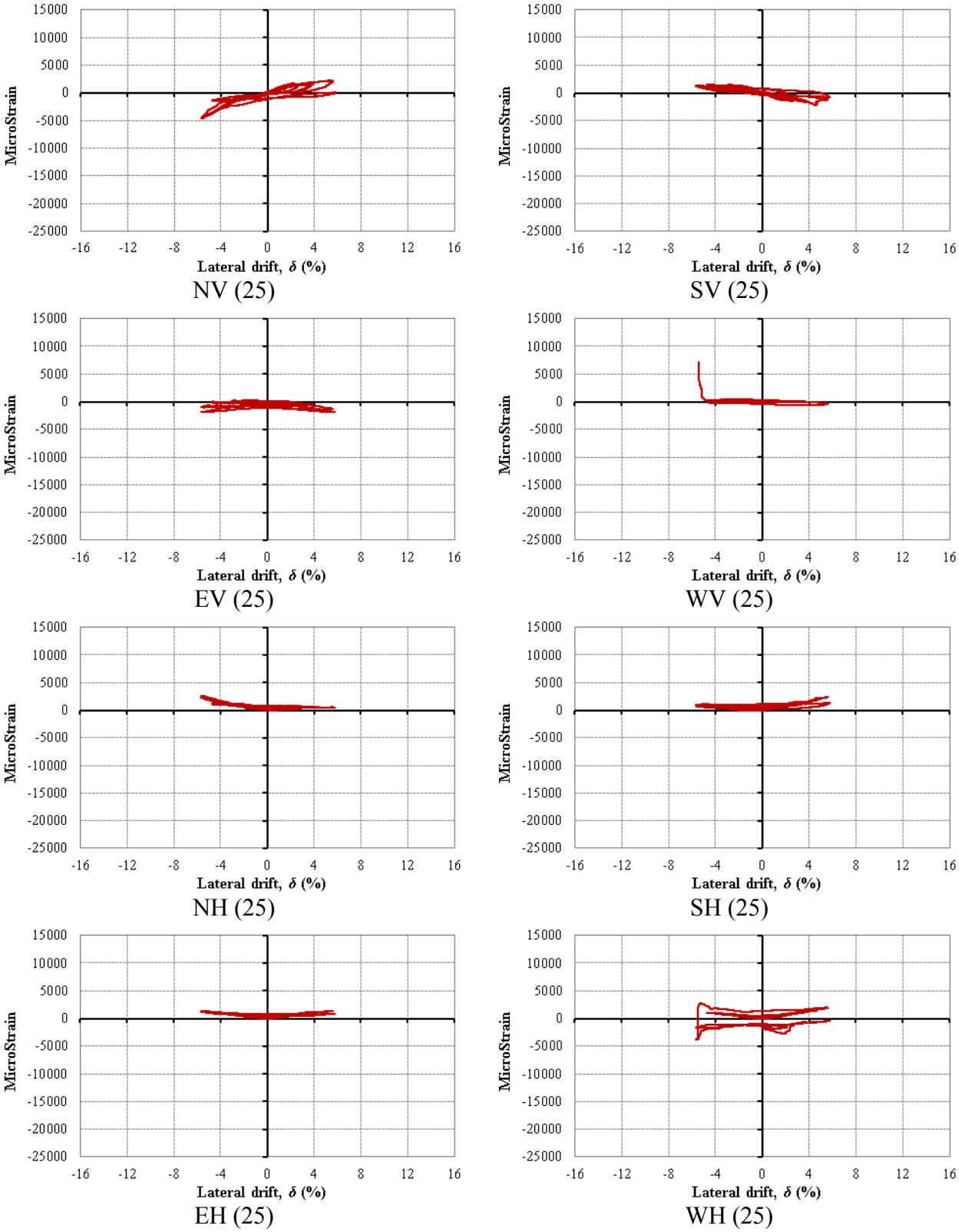

Figure 11.27: Lateral drift-FRP tube microstrain relation at 25 inch above the top of the footing
N: north, S: south, E: east, W: west, V: vertical, and H: horizontal

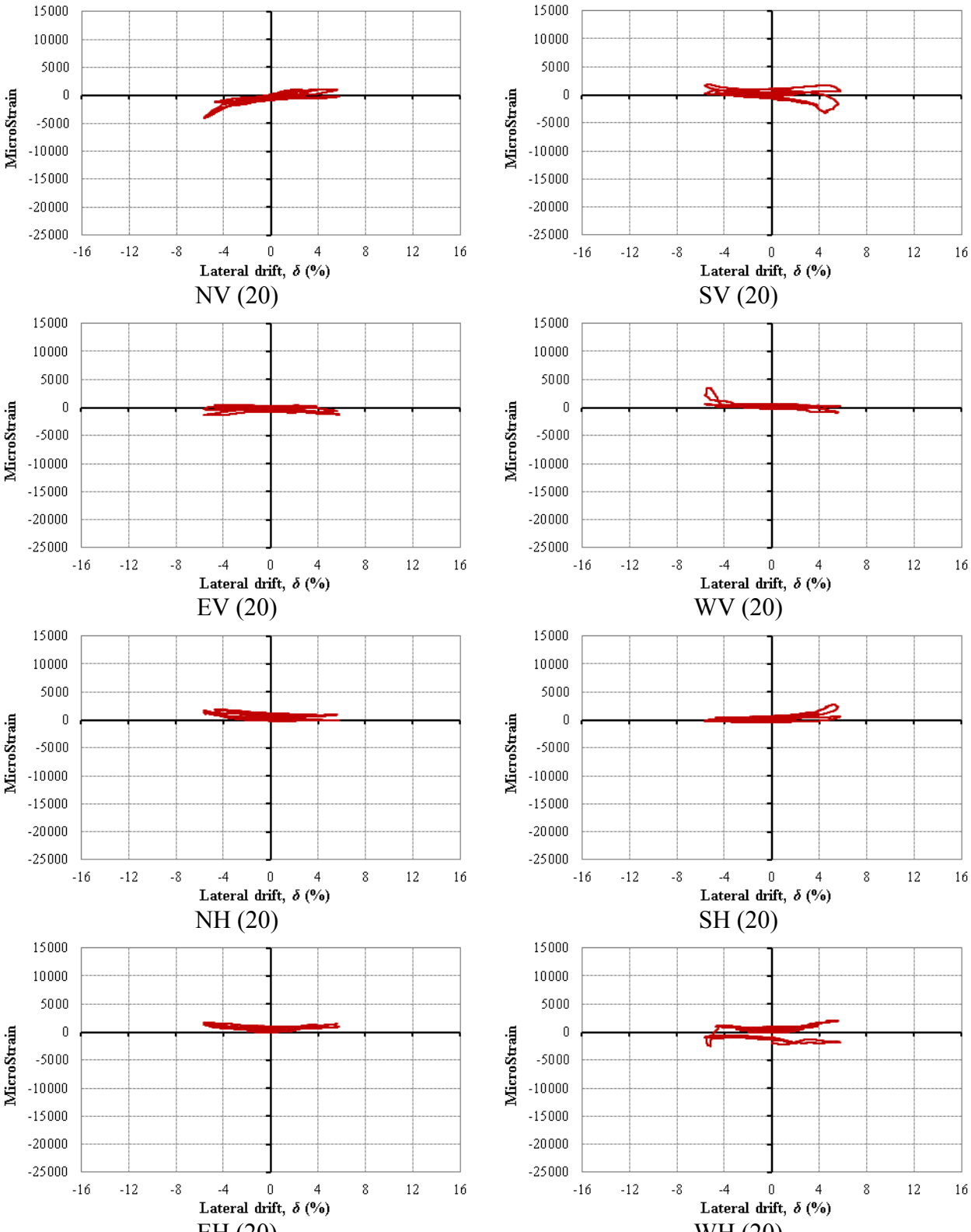

Figure 11.28: Lateral drift-FRP tube microstrain relation at 20 inch above the top of the footing

N: north, S: south, E: east, W: west, V: vertical, and H: horizontal

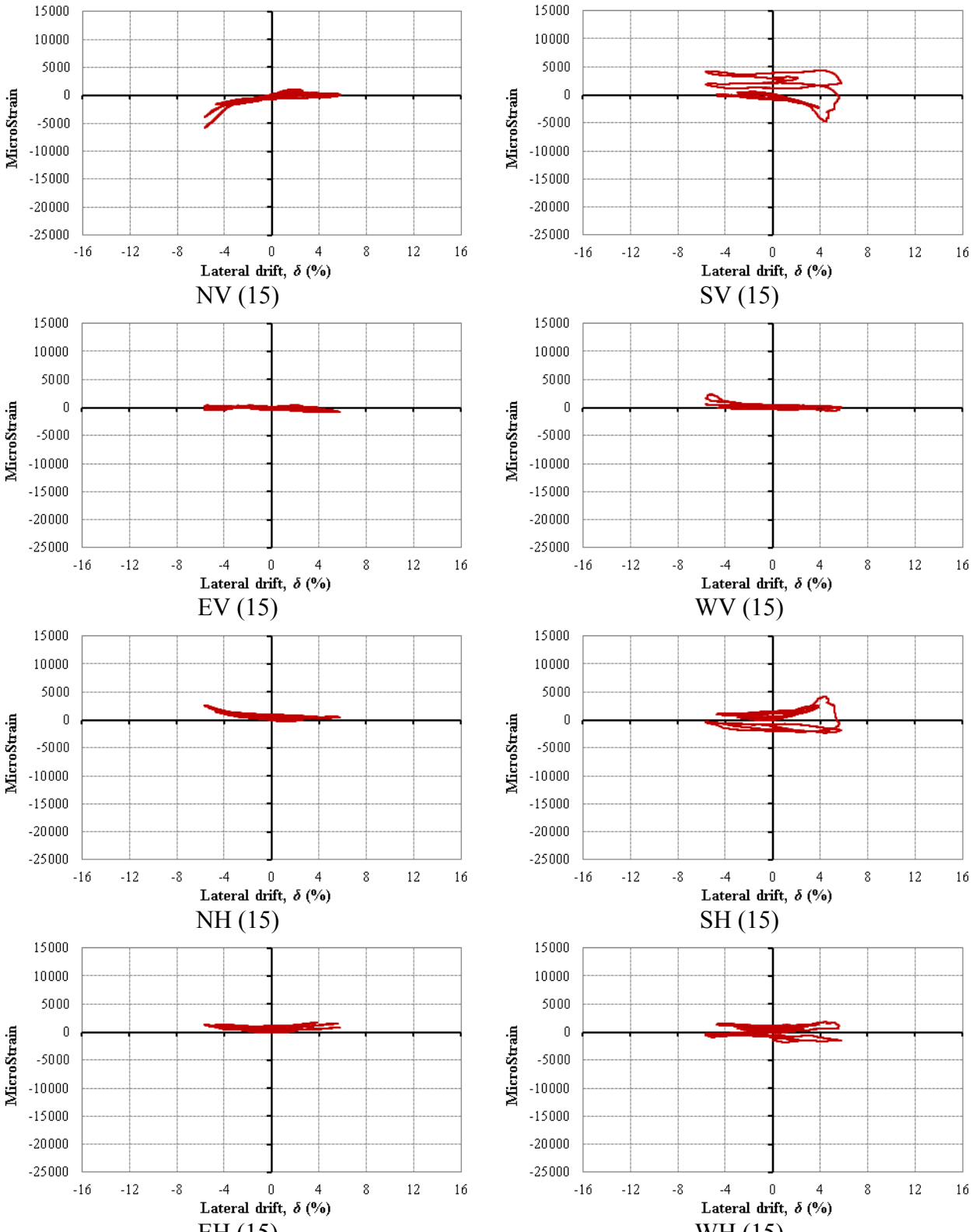

Figure 11.29: Lateral drift- FRP tube microstrain relation at 15 inch above the top of the footing

N: north, S: south, E: east, W: west, V: vertical, and H: horizontal

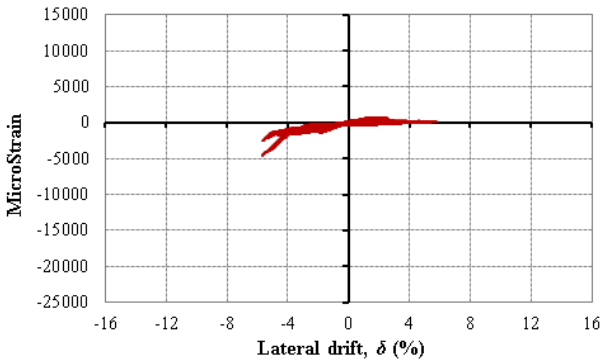

NV (10)

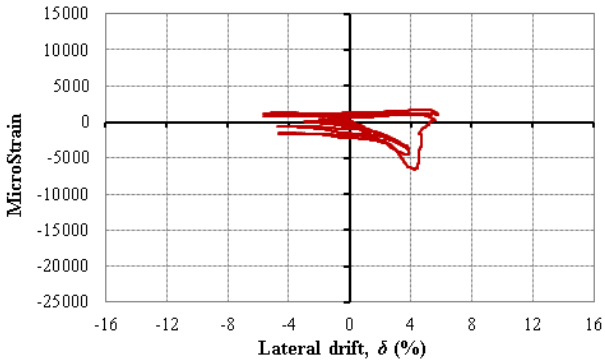

SV (10)

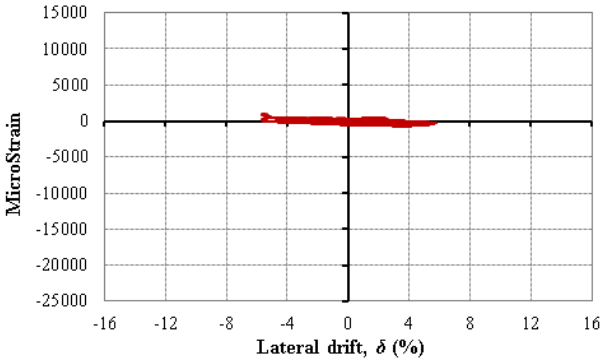

EV (10)

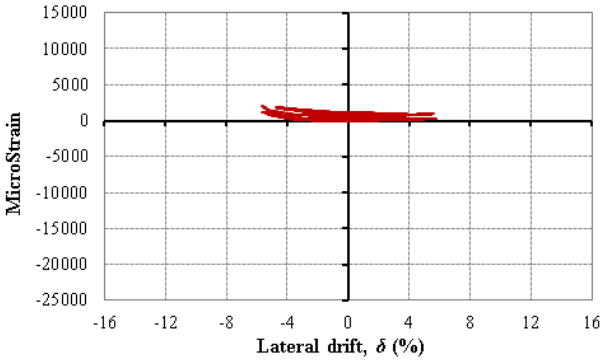

NH (10)

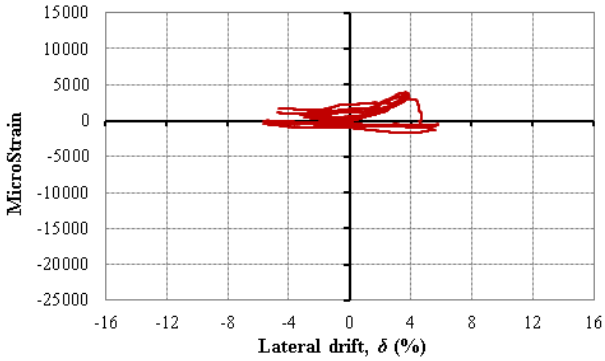

SH (10)

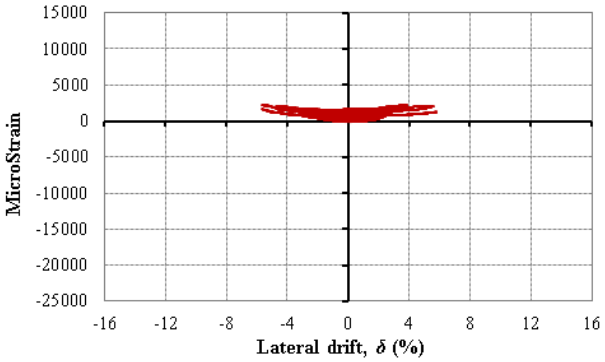

EH (10)

Figure 11.30: Lateral drift- FRP tube microstrain relation at 10 inch above the top of the footing

N: north, S: south, E: east, W: west, V: vertical, and H: horizontal

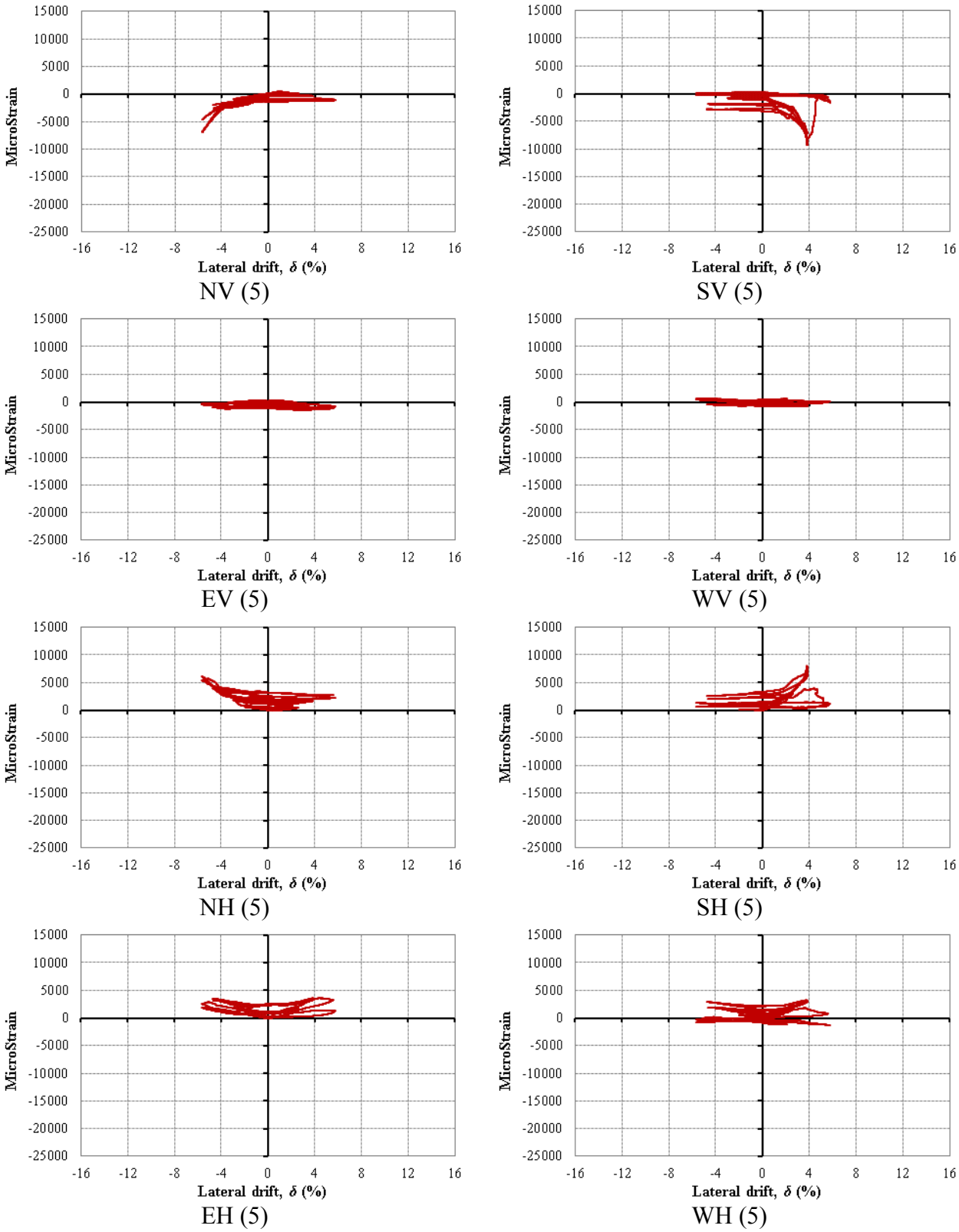

Figure 11.31: Lateral drift- FRP tube microstrain relation at 5 inch above the top of the footing

N: north, S: south, E: east, W: west, V: vertical, and H: horizontal

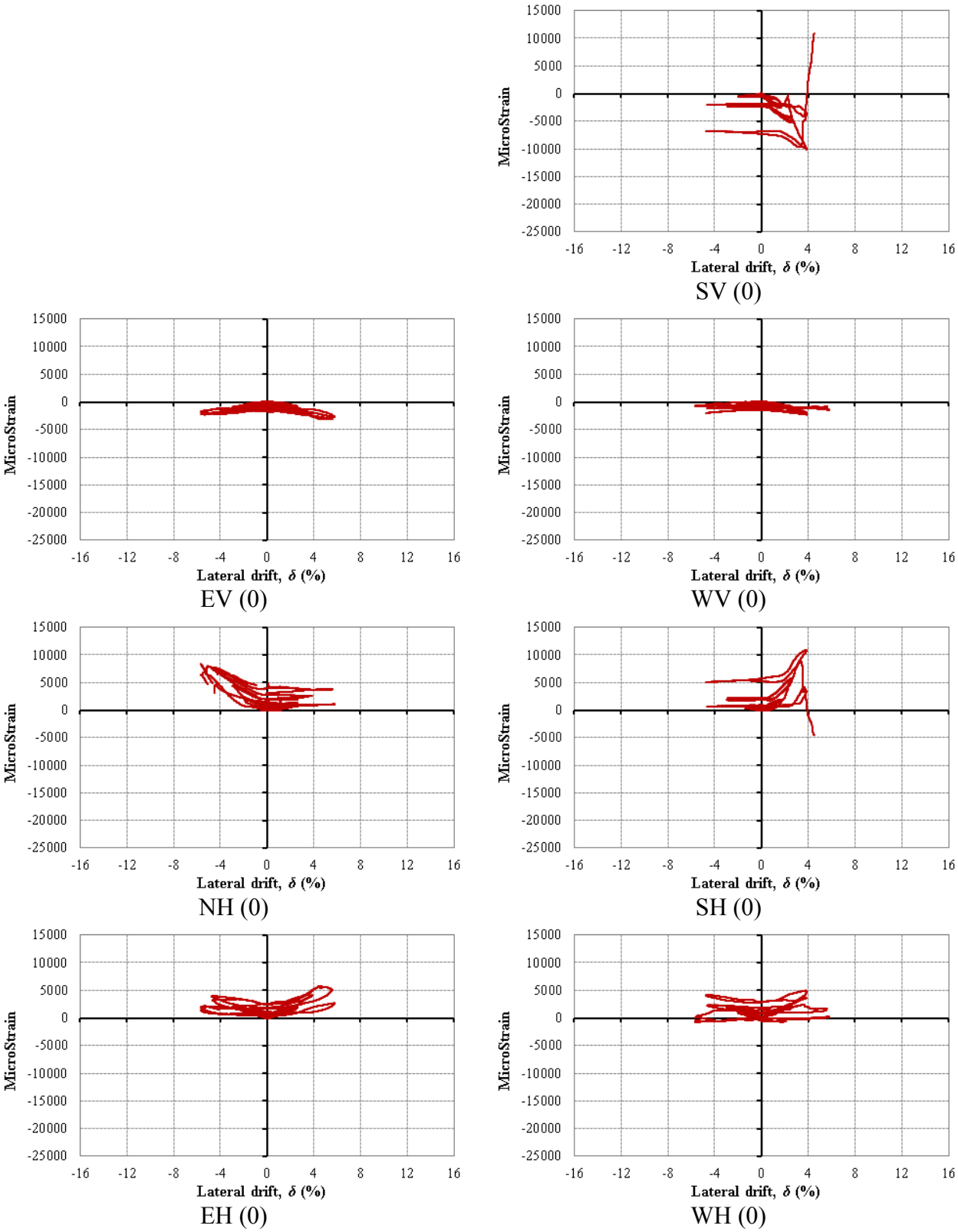

Figure 11.32: Lateral drift- FRP tube microstrain relation at the top of the footing
N: north, S: south, E: east, W: west, V: vertical, and H: horizontal

11.4 F4-24-E344 column

11.4.1 Force-Curvature relations

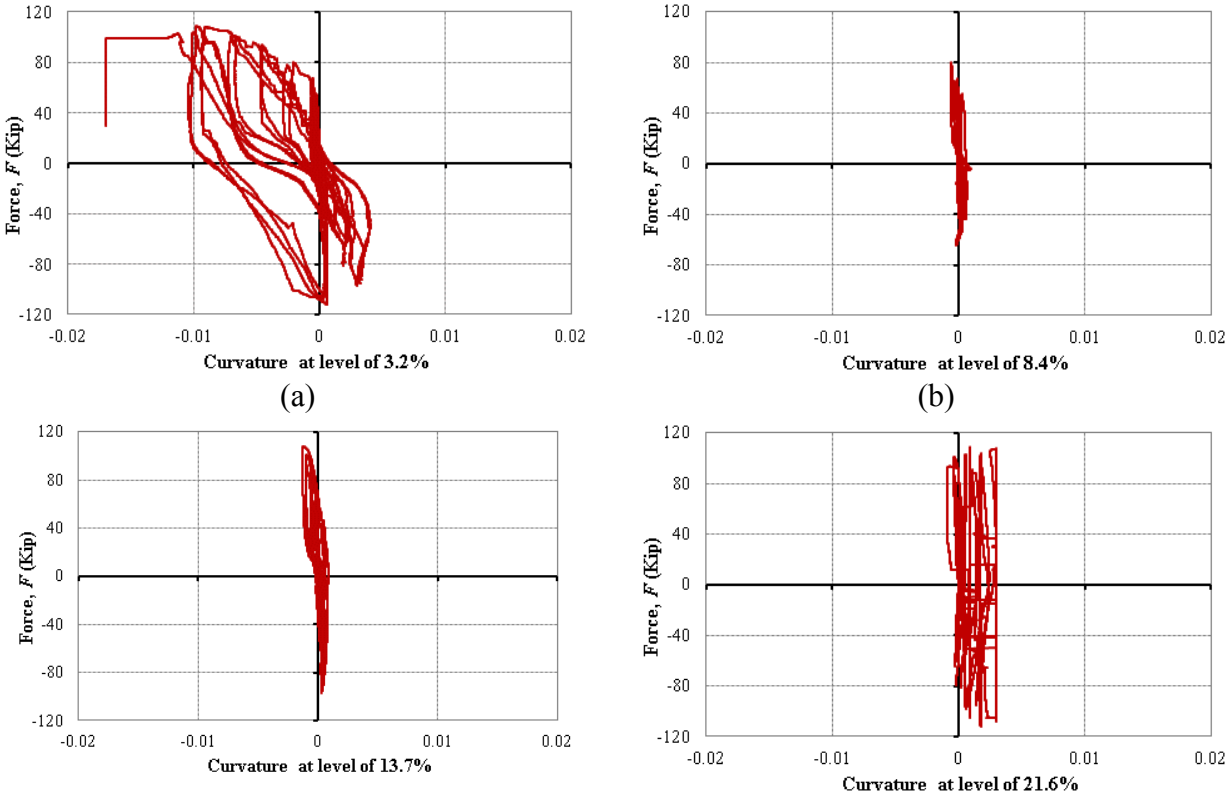

Figure 11.33: Force-curvature relation of the F4-24-P124 column: (a) at level of 3.2% of the column's height, (b) at level of 8.4% of the column's height, (c) at level of 13.7% of the column's height, and (d) at level of 21.6% of the column's height

11.4.2 Lateral drift-steel strain relations

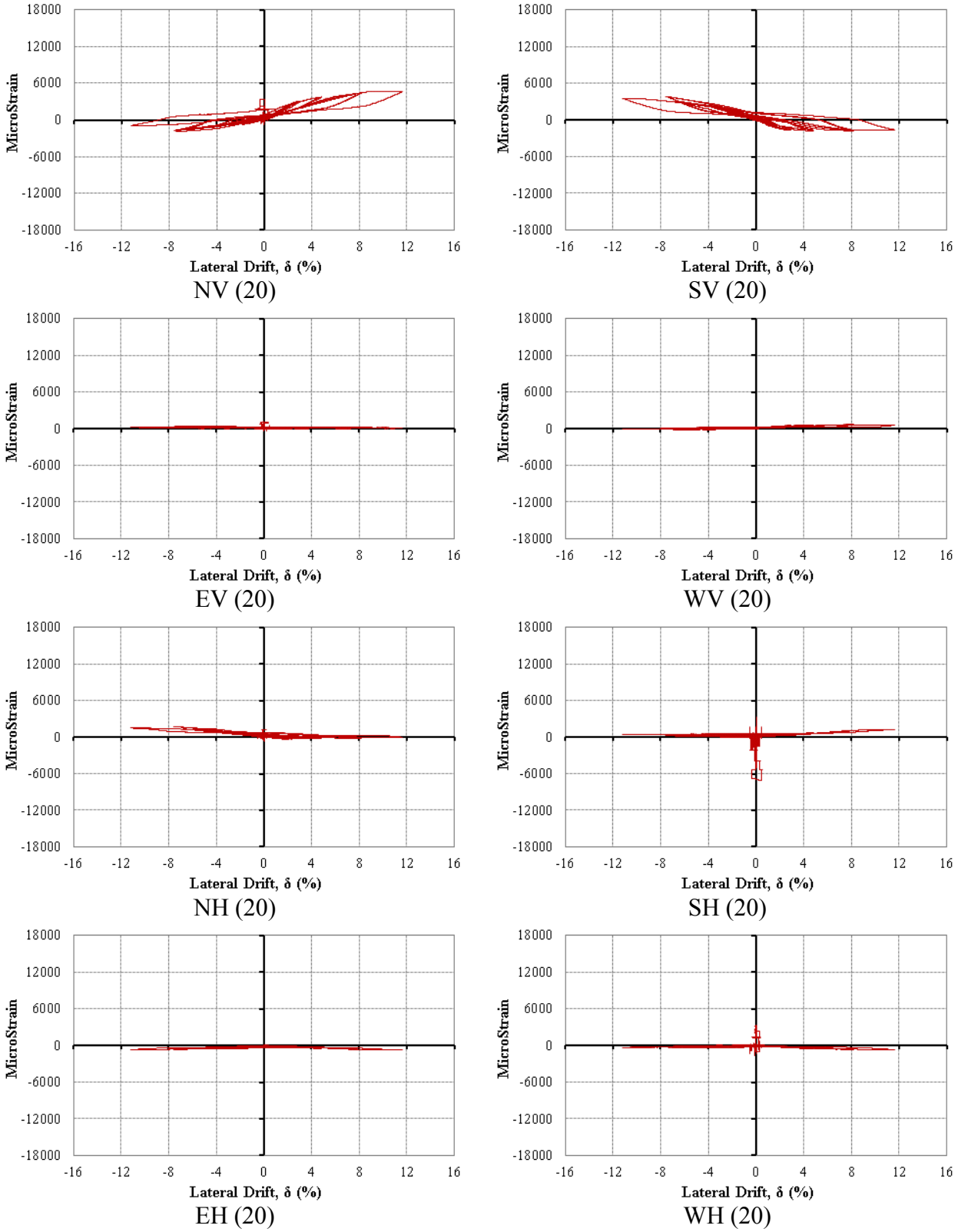

Figure 11.34: Lateral drift-steel tube microstrain relation at 20 inch above the top of the footing
N: north, S: south, E: east, W: west, V: vertical, and H: horizontal

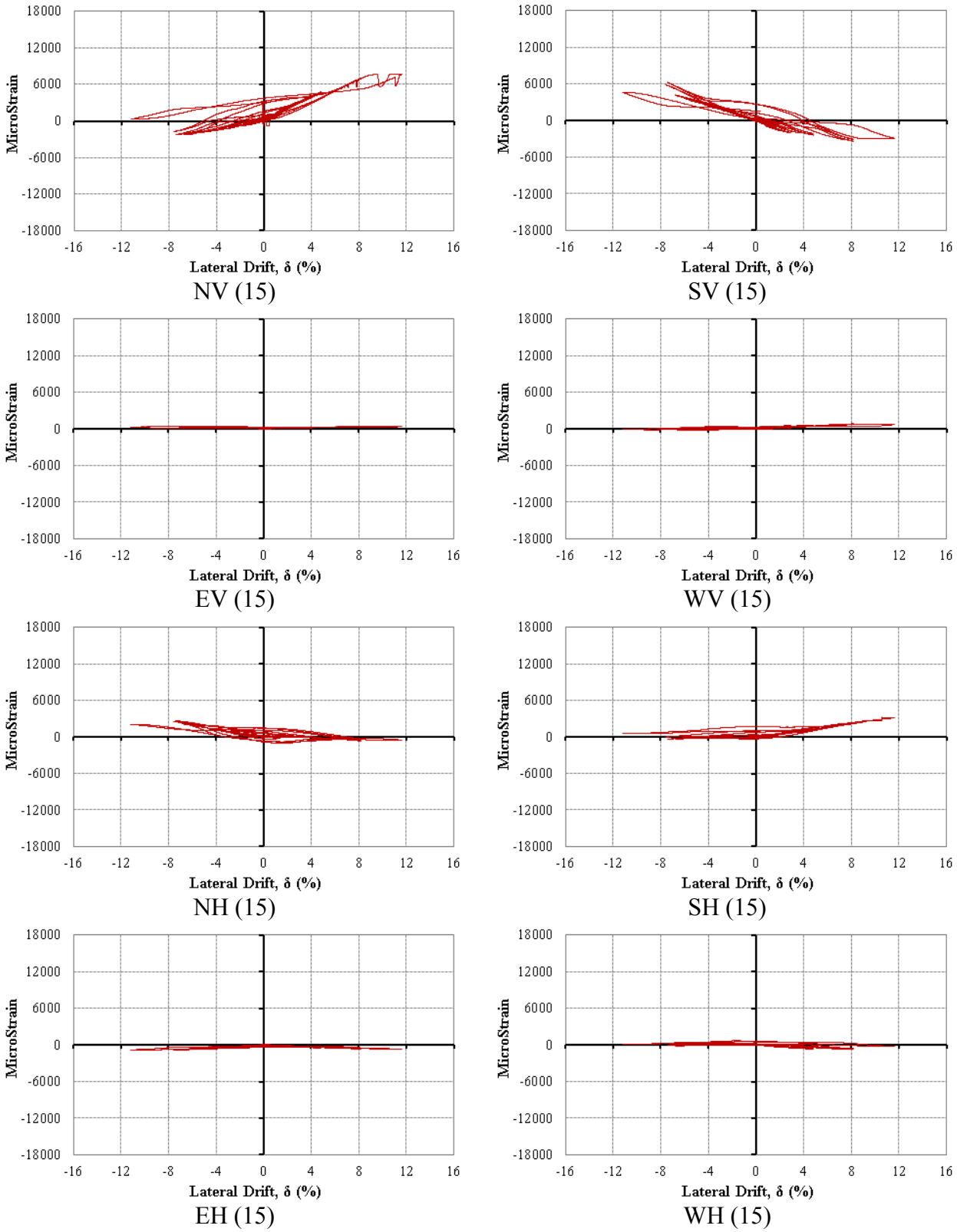

Figure 11.35: Lateral drift-steel tube microstrain relation at 15 inch above the top of the footing
N: north, S: south, E: east, W: west, V: vertical, and H: horizontal

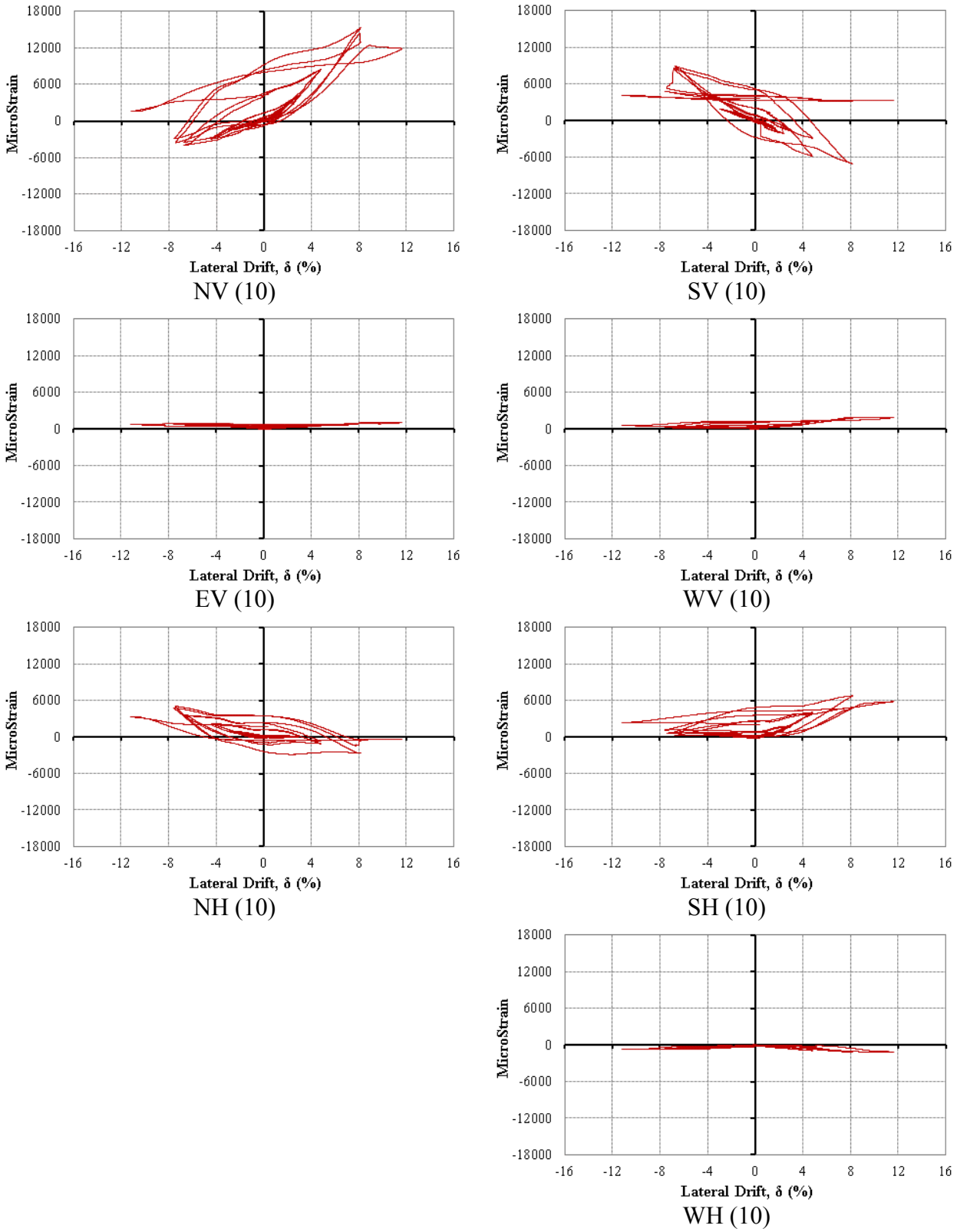

Figure 11.36: Lateral drift-steel tube microstrain relation at 10 inch above the top of the footing
N: north, S: south, E: east, W: west, V: vertical, and H: horizontal

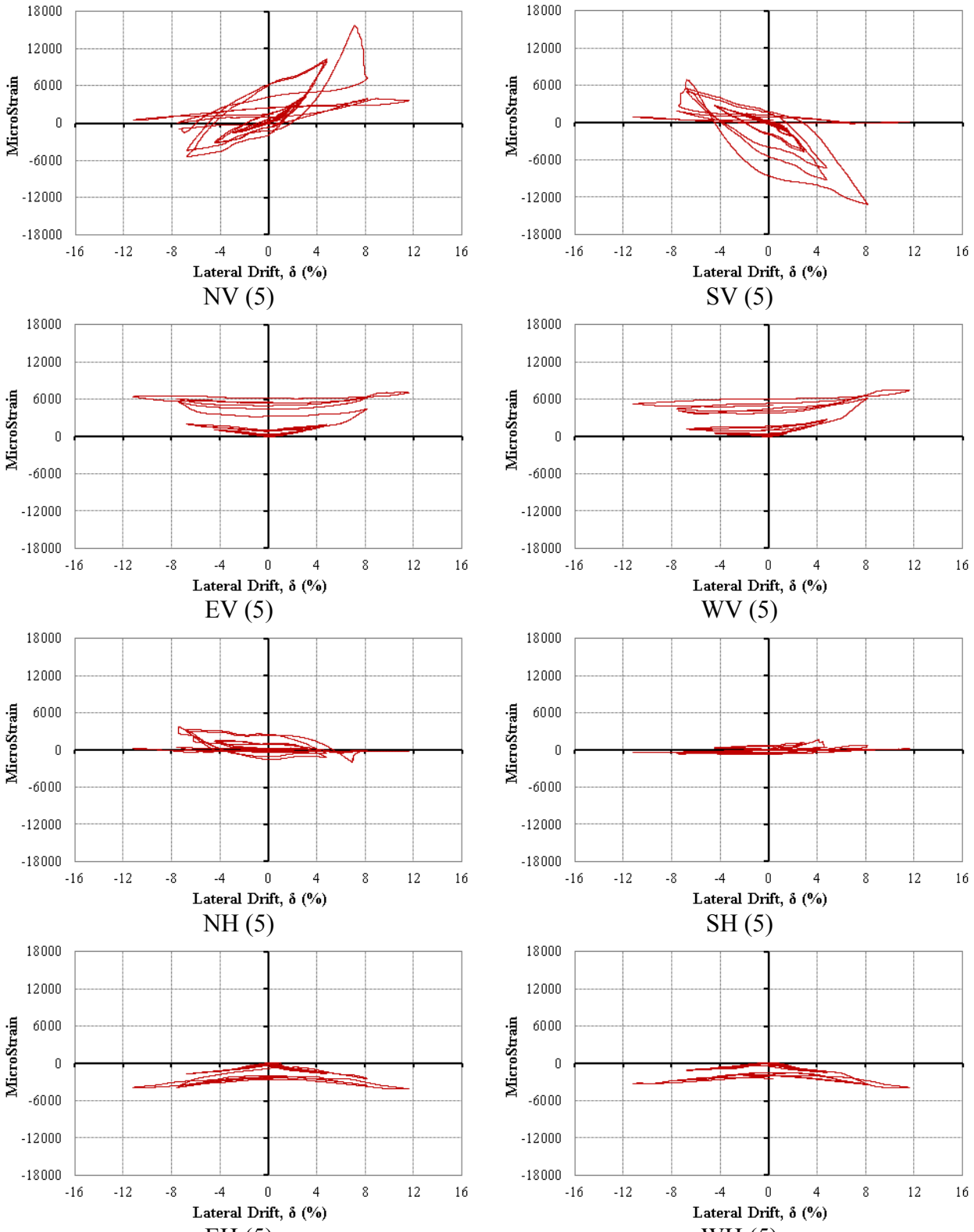

Figure 11.37: Lateral drift-steel tube microstrain relation at 5 inch above the top of the footing
N: north, S: south, E: east, W: west, V: vertical, and H: horizontal

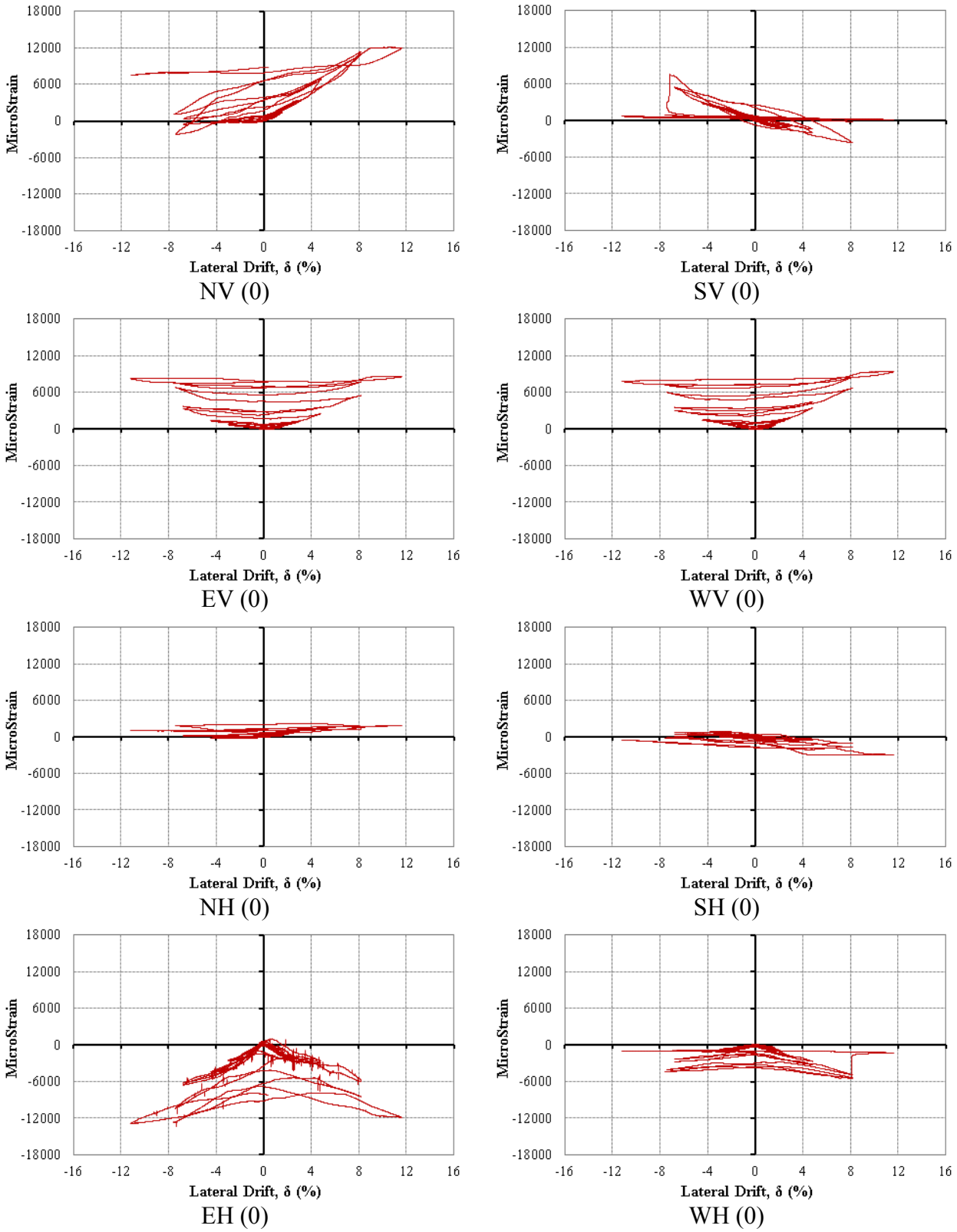

Figure 11.38: Lateral drift-steel tube microstrain relation at the level of the top of the footing
N: north, S: south, E: east, W: west, V: vertical, and H: horizontal

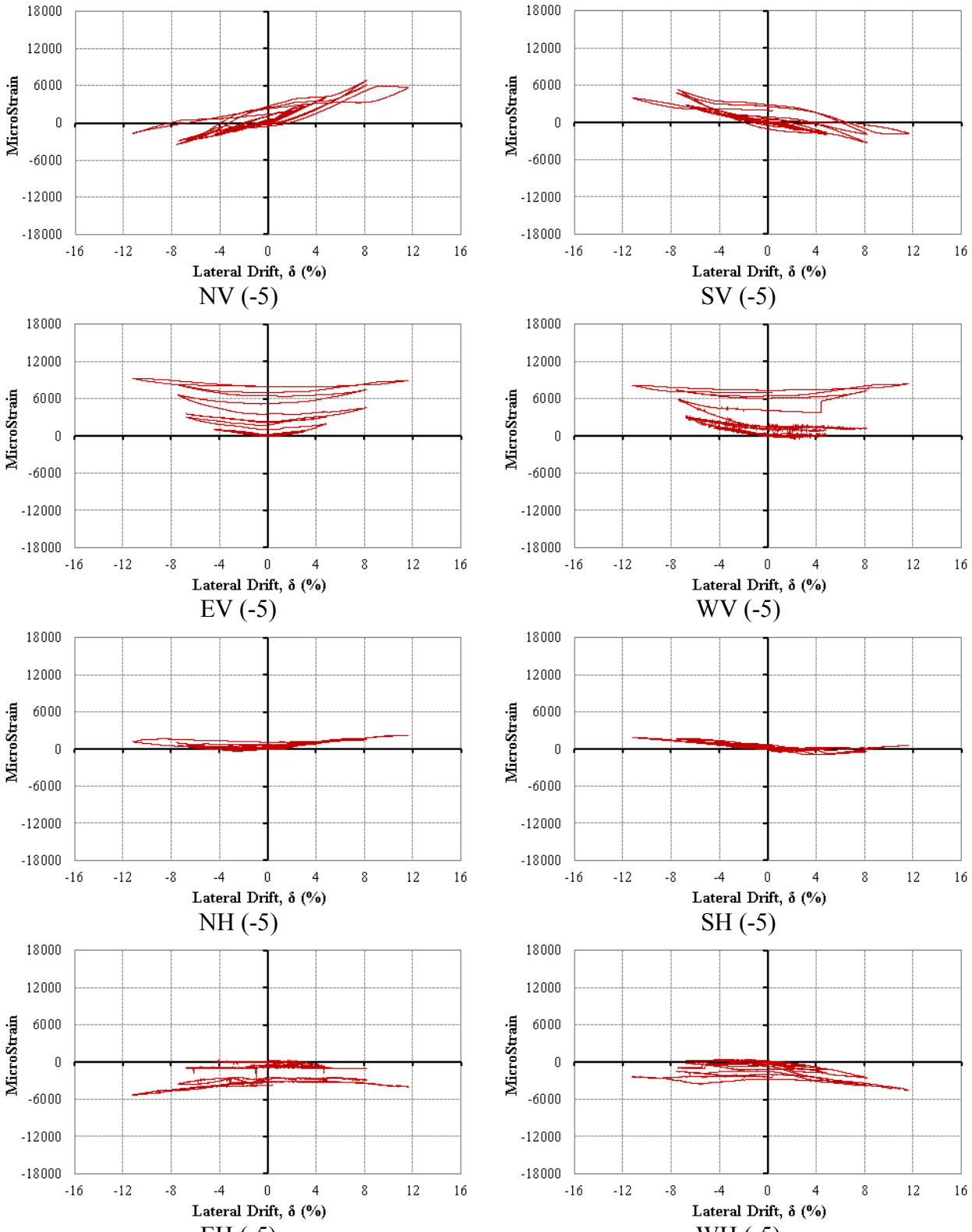

Figure 11.39: Lateral drift-steel tube microstrain relation at 5 inch below the top of the footing
N: north, S: south, E: east, W: west, V: vertical, and H: horizontal

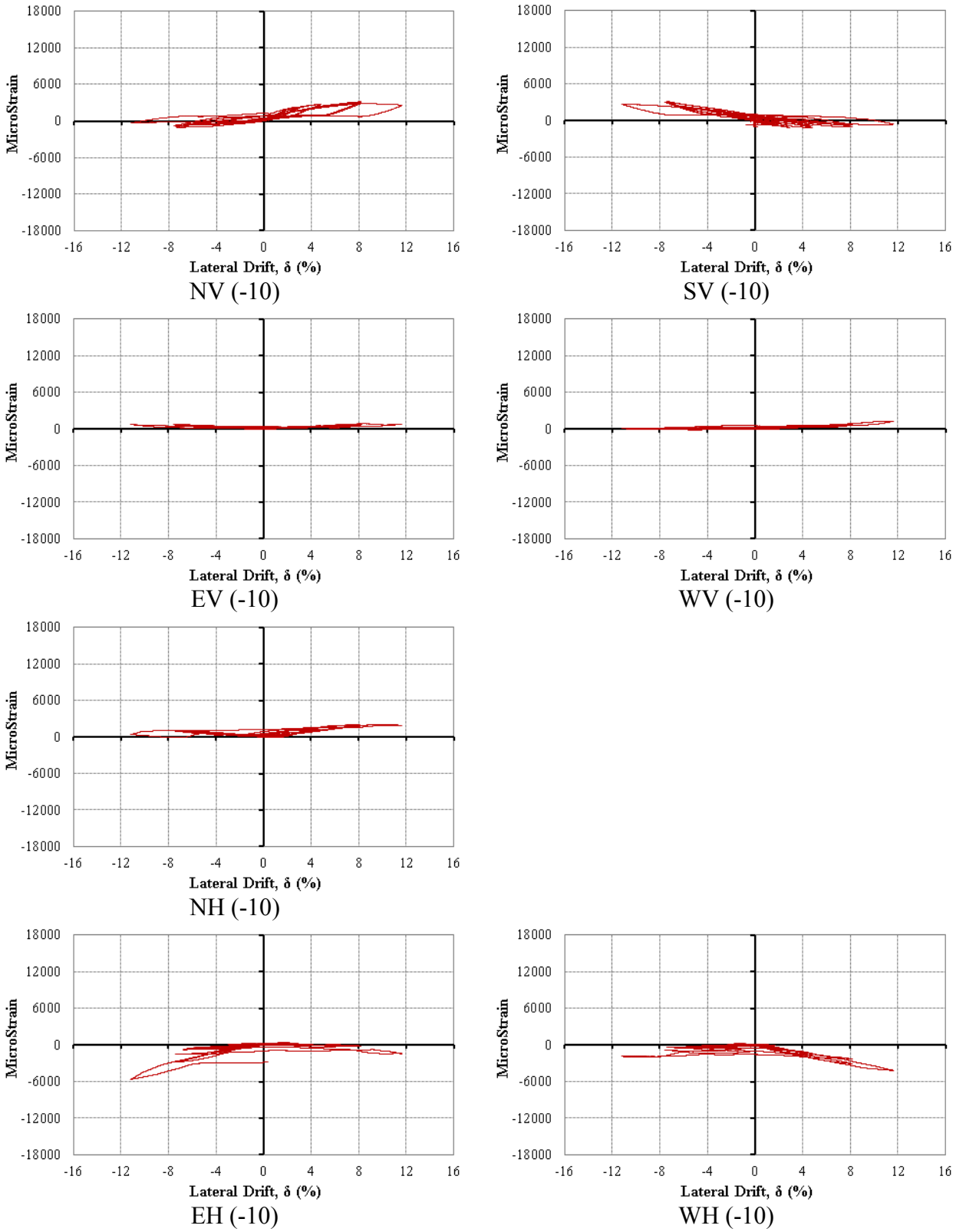

Figure 11.40: Lateral drift-steel tube microstrain relation at 10 inch below the top of the footing
N: north, S: south, E: east, W: west, V: vertical, and H: horizontal

11.4.3 Lateral drift-FRP strain relations

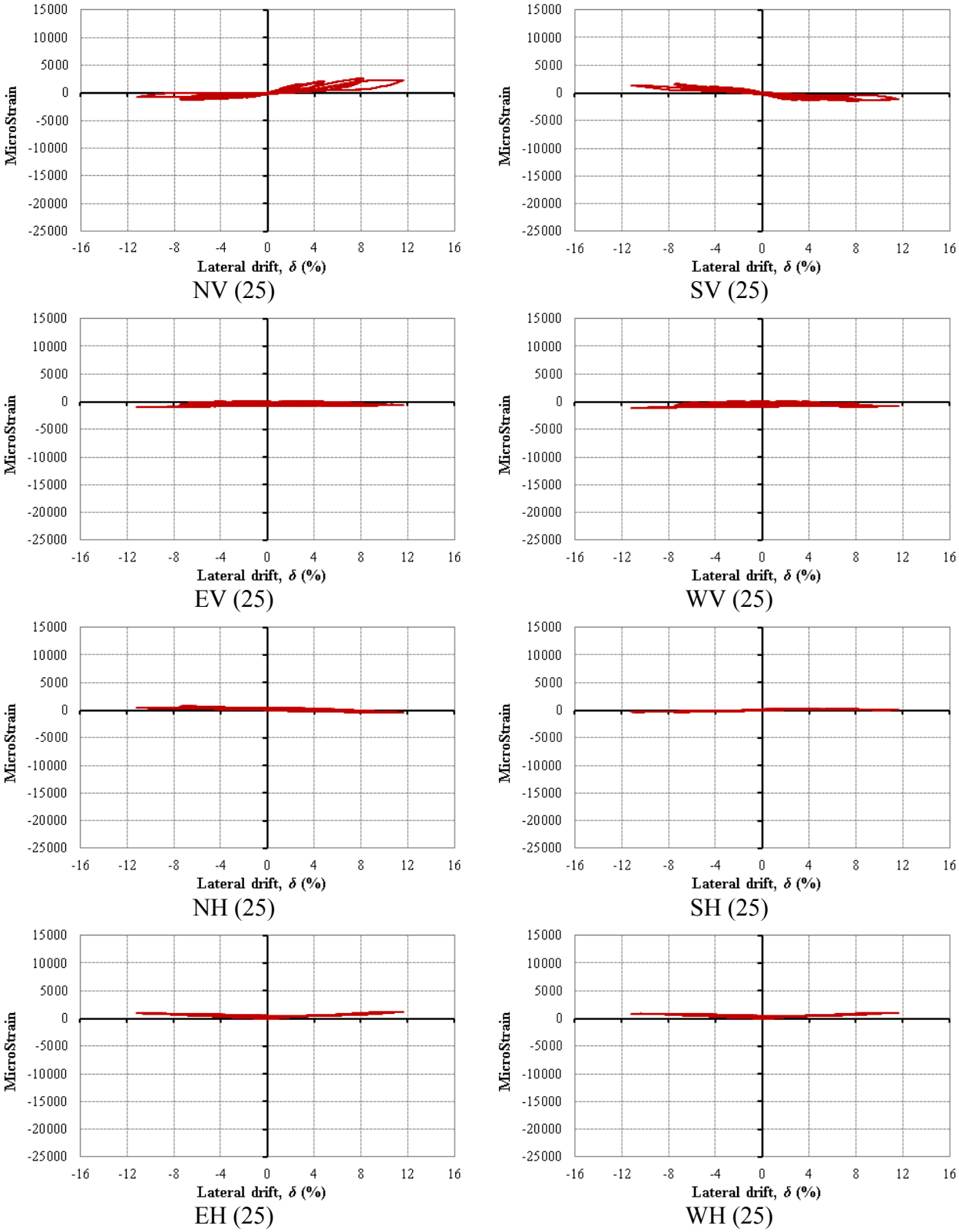

Figure 11.41: Lateral drift-FRP tube microstrain relation at 25 inch above the top of the footing
N: north, S: south, E: east, W: west, V: vertical, and H: horizontal

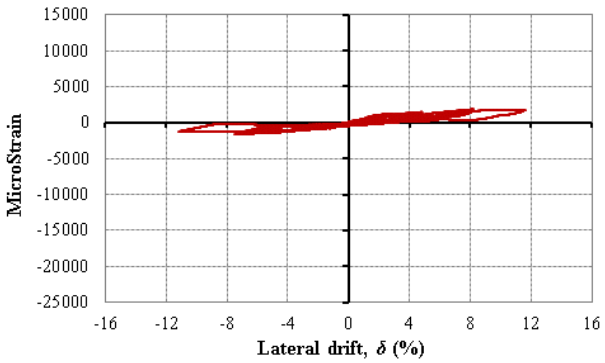

NV (20)

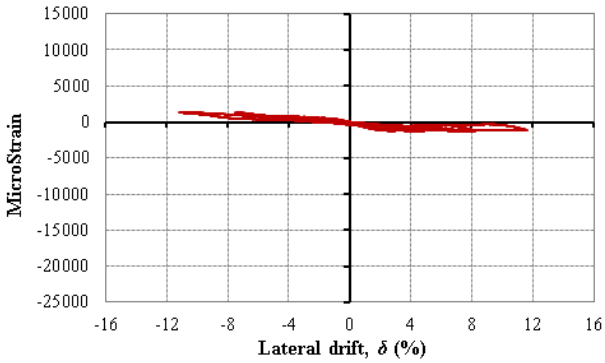

SV (20)

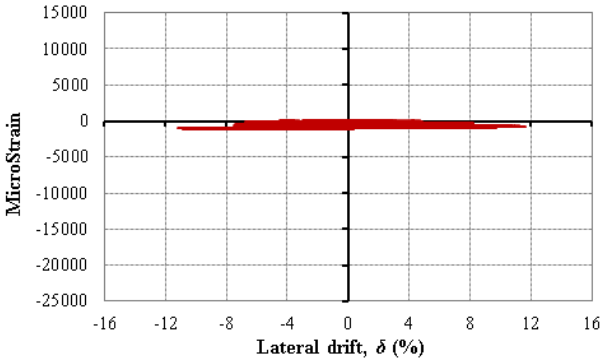

EV (20)

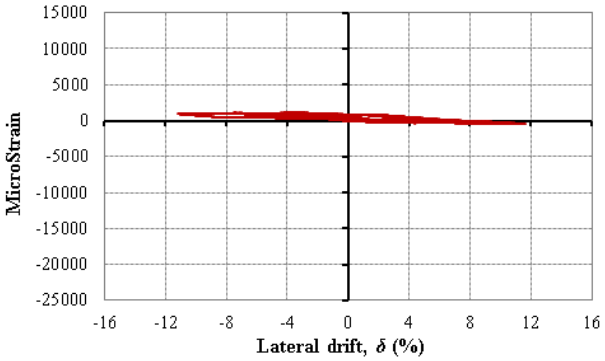

NH (20)

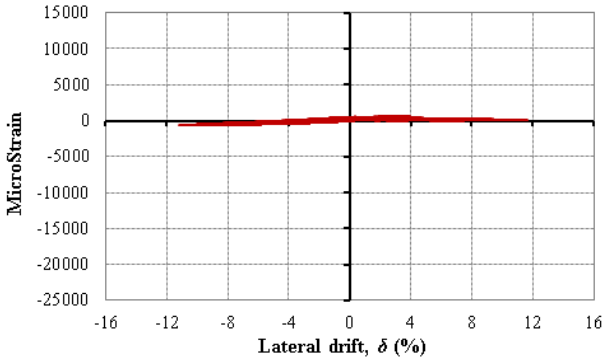

SH (20)

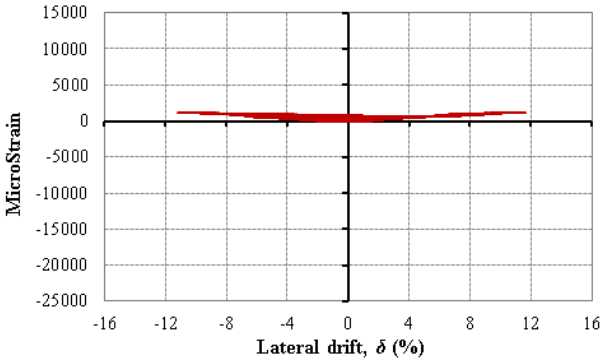

EH (20)

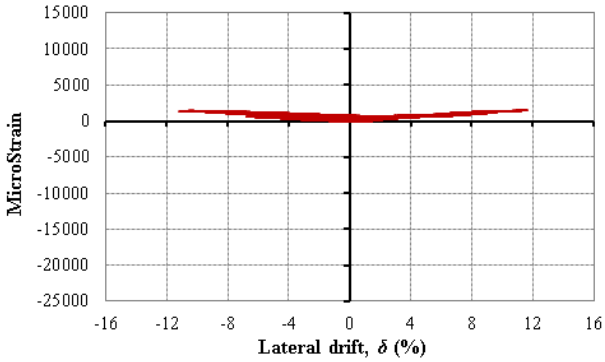

WH (20)

Figure 11.42: Lateral drift-FRP tube microstrain relation at 20 inch above the top of the footing

N: north, S: south, E: east, W: west, V: vertical, and H: horizontal

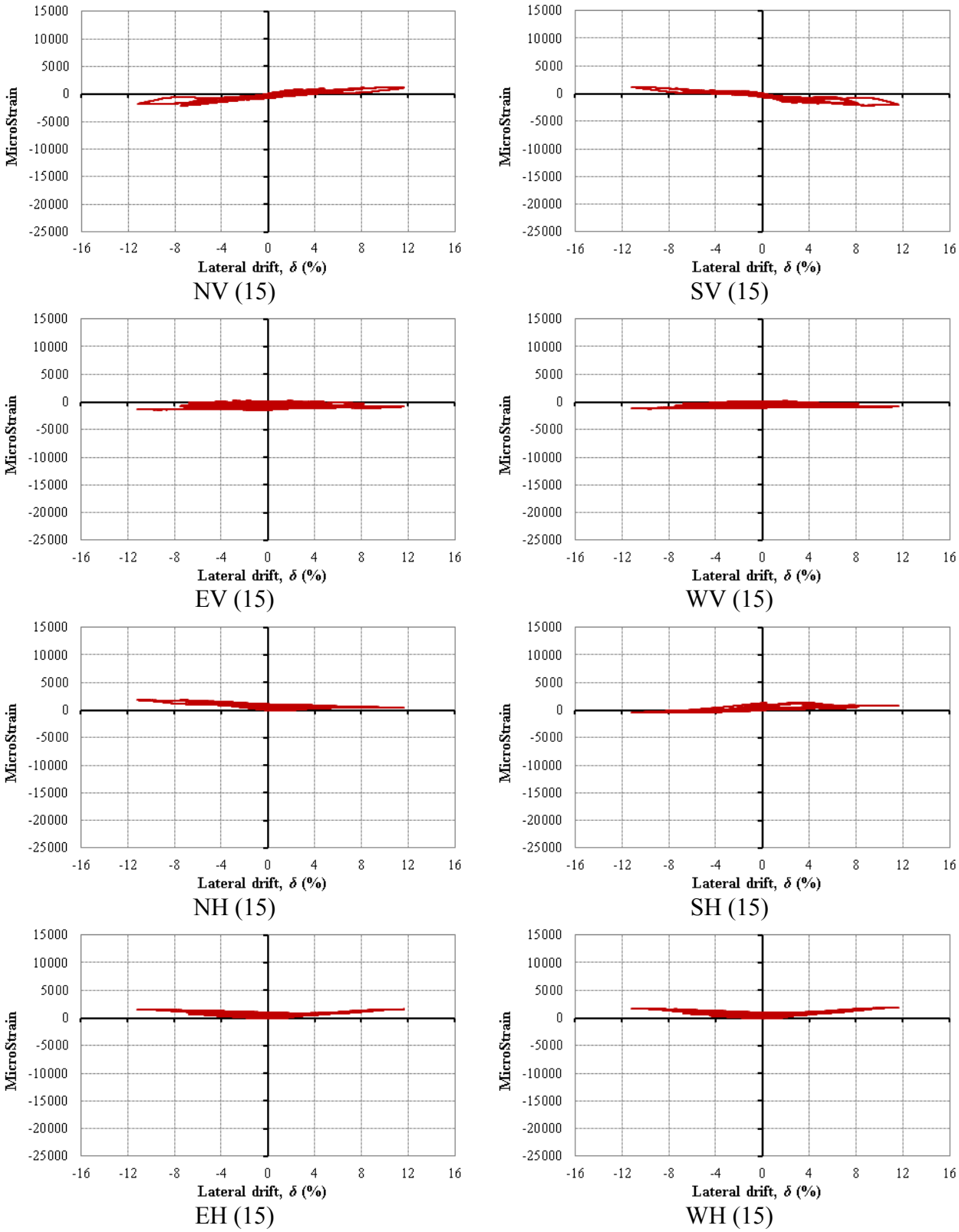

Figure 11.43: Lateral drift- FRP tube microstrain relation at 15 inch above the top of the footing

N: north, S: south, E: east, W: west, V: vertical, and H: horizontal

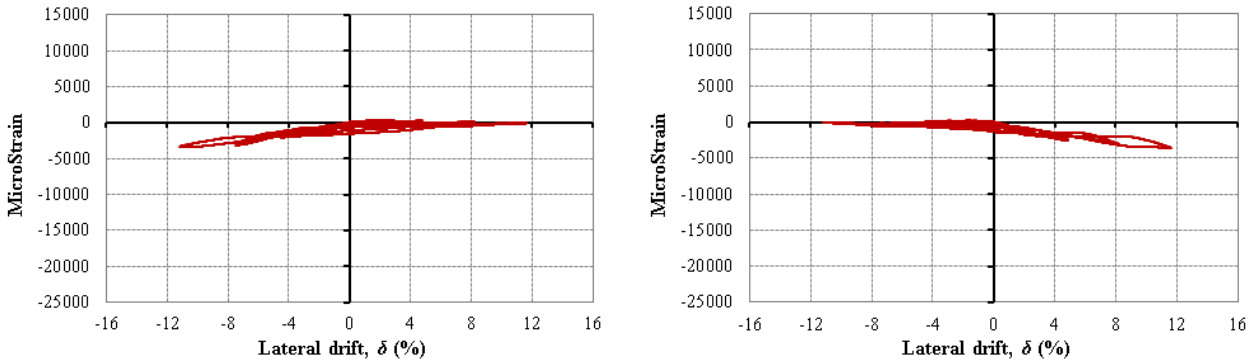

NV (10)

SV (10)

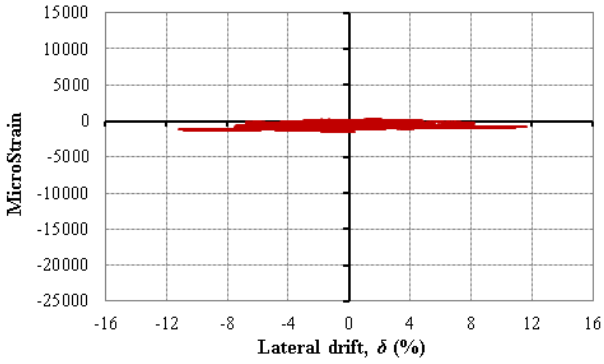

EV (10)

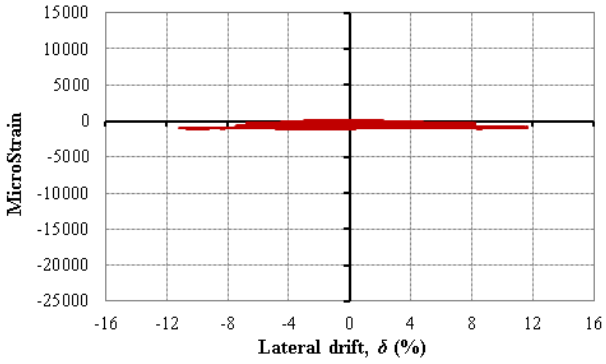

WV (10)

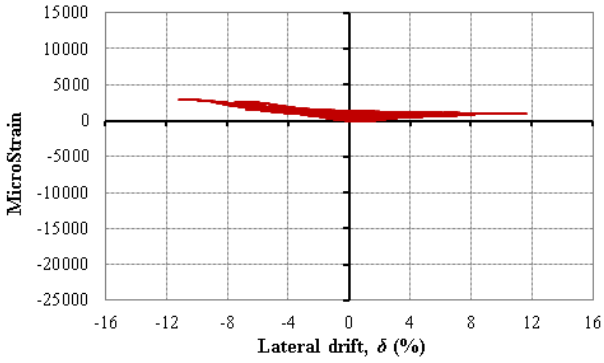

NH (10)

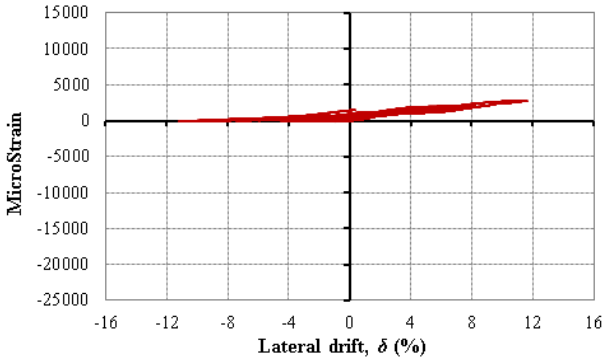

SH (10)

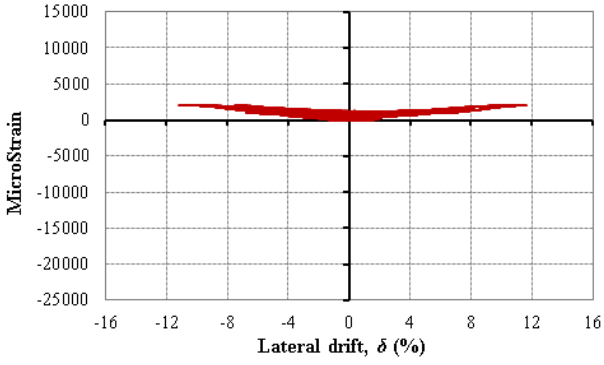

EH (10)

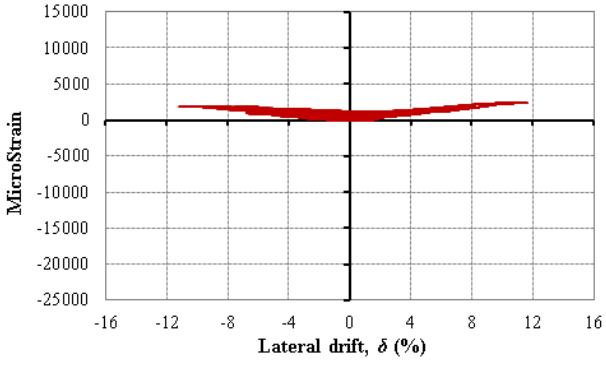

WH (10)

Figure 11.44: Lateral drift- FRP tube microstrain relation at 10 inch above the top of the footing

N: north, S: south, E: east, W: west, V: vertical, and H: horizontal

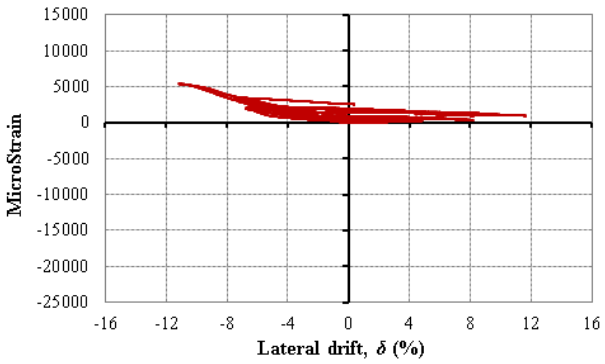

NV (5)

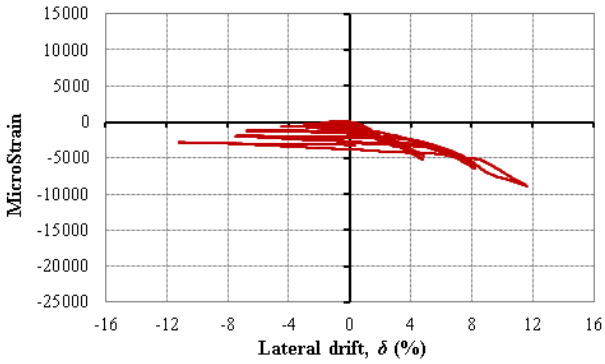

SV (5)

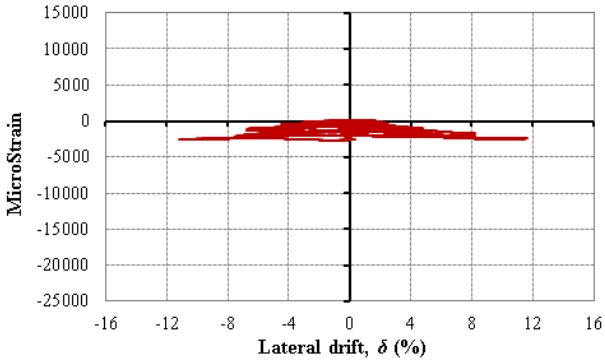

WV (5)

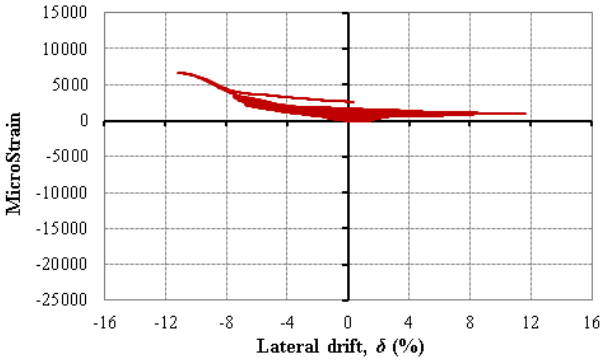

NH (5)

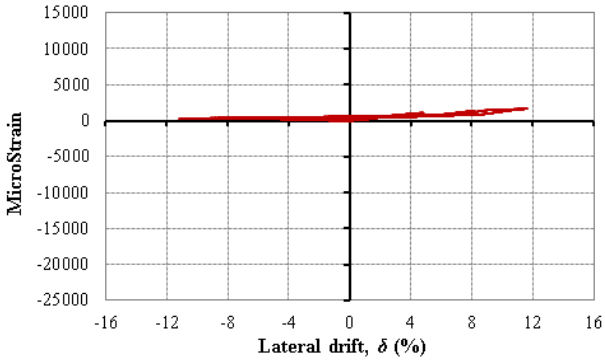

SH (5)

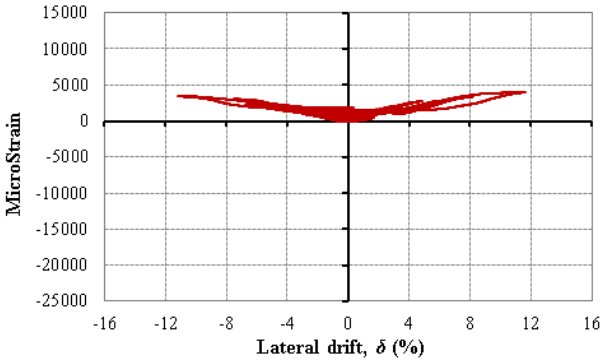

EH (5)

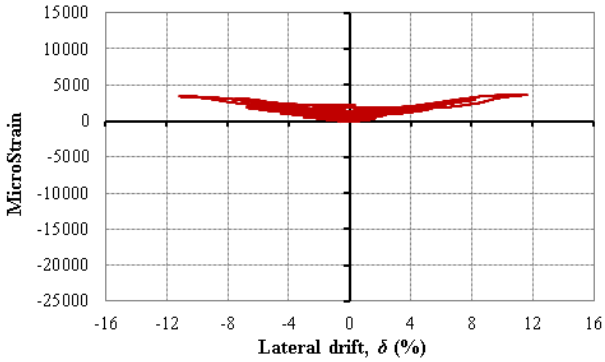

WH (5)

Figure 11.45: Lateral drift- FRP tube microstrain relation at 5 inch above the top of the footing

N: north, S: south, E: east, W: west, V: vertical, and H: horizontal

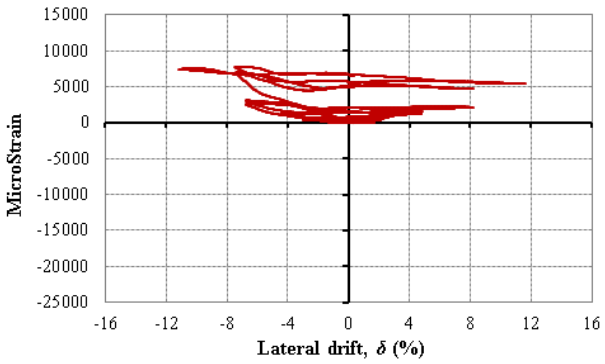

NV (0)

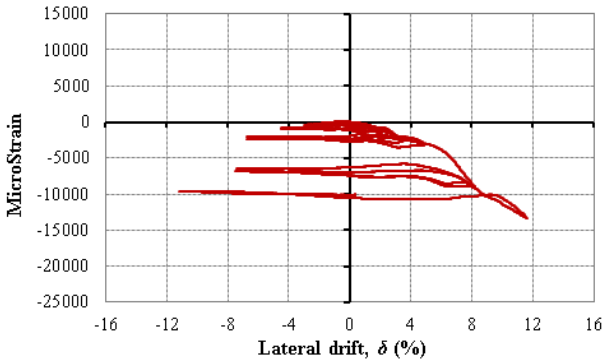

SV (0)

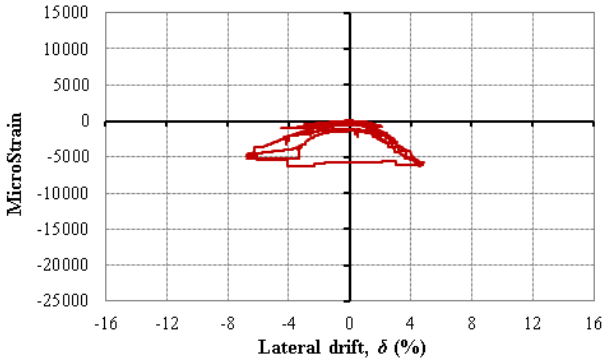

WV (0)

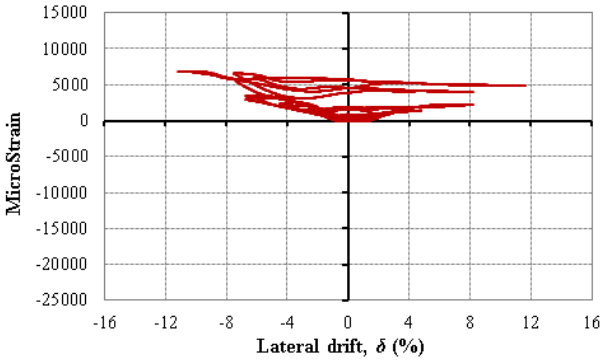

NH (0)

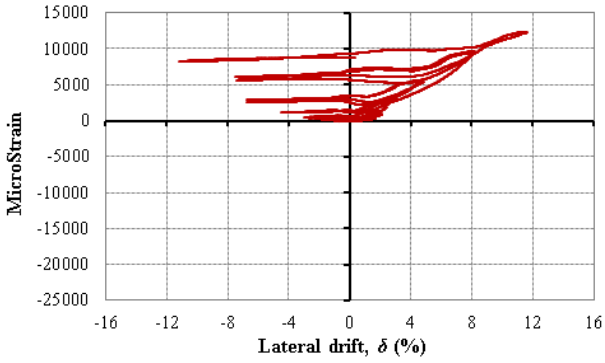

SH (0)

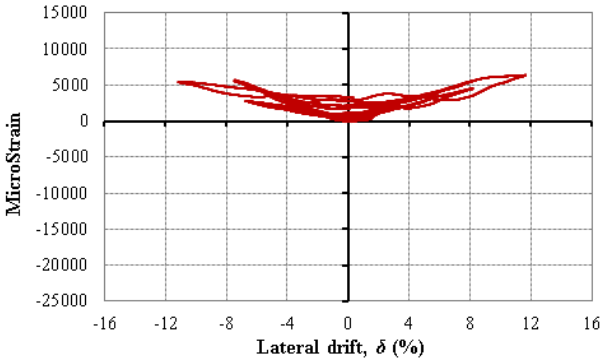

EH (0)

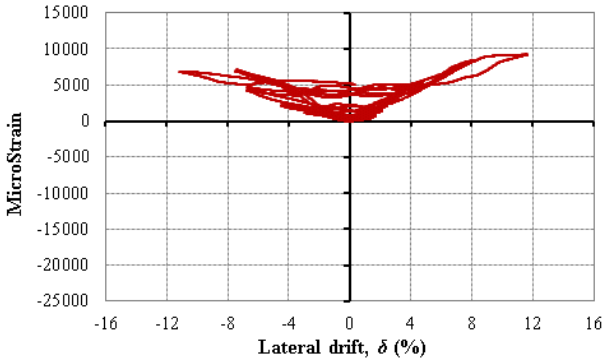

WH (0)

Figure 11.46: Lateral drift- FRP tube microstrain relation at the top of the footing
N: north, S: south, E: east, W: west, V: vertical, and H: horizontal